Andreas Rühl

On the Time and Temperature Dependent Behaviour of Laminated Amorphous Polymers Subjected to Low-Velocity Impact

Springer Vieweg

Mechanik, Werkstoffe und Konstruktion im Bauwesen

Band 47

Institutsreihe zu Fortschritten bei Mechanik, Werkstoffen, Konstruktionen, Gebäudehüllen und Tragwerken.

Andreas Rühl

On the Time and Temperature Dependent Behaviour of Laminated Amorphous Polymers Subjected to Low-Velocity Impact

Springer Vieweg

Andreas Rühl
Institute of Mechanics and Materials
Technische Hochschule Mittelhessen
Germany

Danksagung

Die vorliegende Arbeit ist in meiner Zeit als wissenschaftlicher Mitarbeiter am Institut für Mechanik und Materialforschung der Technischen Hochschule Mittelhessen in Gießen in Kooperation mit dem Institut für Statik und Konstruktion der Technischen Universität Darmstadt entstanden.

Zuerst möchte ich mich bei Professor Stefan Kolling für die Übernahme des Referats sowie die hervorragende fachliche Betreuung bedanken. Durch zahllose und stets fruchtbare Diskussionen konnte die Arbeit in einem sehr angenehmen Arbeitsumfeld und in einer auf ihre Weise schönen Stadt reifen.

Ebenso möchte ich Professor Jens Schneider herzlich danken, der mir mit der Übernahme des Referates die kooperative Promotion über seinen Lehrstuhl an der TU Darmstadt ermöglichte und darüber hinaus auch jederzeit fachlicher Ansprechpartner in Darmstadt war. In seiner Arbeitsgruppe und am ganzen Institut für Statik und Konstruktion bin ich sehr wohlwollend aufgenommen worden und konnte jederzeit auf offene Türen vertrauen.

Weiterhin gilt mein Dank den Mitarbeitern und studentischen Hilfskräften des Instituts für Mechanik und Materialforschung, insbesondere meinen langjährigen Weggefährten Christian Alter und Manuel Roth.

Ein weiteres großes Dankesehr möchte ich der Evonik Industries AG aussprechen, die mich mit kontinuierlichen Materiallieferungen unkompliziert unterstützte. Hier möchte ich insbesondere Herrn Bernd Kiesewetter hervorheben, der mir auch bei fachlichen Fragen mit Rat und Tat zur Seite stand.

Abschließend gilt mein Dank meinen Eltern Ursula und Dieter, auf deren bedingungslose und uneingeschränkte Unterstützung ich jederzeit vertrauen konnte.

Gießen, im Februar 2017   *Andreas Rühl*

Abstract

The substitution of conventional glass products with polymeric structures bears a huge weight reduction potential for the automotive and aviation industry. Against this background, a polymeric laminate consisting of poly(methyl methacrylate) (PMMA) and thermoplastic polyurethane (TPU) was investigated experimentally and numerically with regard to its impact behaviour and applicability.

Basic experiments with PMMA and TPU were used to identify the thermomechanical characteristics of the monolithic materials. Furthermore, PMMA-TPU-PMMA laminates were subjected to impact loadings at velocities up to 5 m/s using three-point bending and dart impact tests. The principle behaviour, characterized by a distinct post-breakage capacity, was examined. A significant heating of the highly strained interlayer was measured in the post-breakage phase.

Based on the experimental basis, different material models for the Finite Element simulation are presented. These material models are able to capture the temperature and time dependent behaviour of the laminate. Further studies regarding modelling techniques for characteristics of laminated structures were conducted.

A final validation experiment, consisting of head-dummy impacts at 10 m/s on automotive side windows, was conducted for PMMA and the laminate to investigate their applicability as glass substitution products. The corresponding simulations showed very high agreement to experimental results and exhibited as reliable prediction tools for future developments.

Zusammenfassung

Der Austausch von konventionellen Glasprodukten durch Kunststoffmaterialien beinhaltet ein großes Potential an Gewichtseinsparung für die Automobil- und Luftfahrtindustrie. Vor diesem Hintergrund wurde ein Polymerlaminat bestehend aus den Materialien Polymethylmethacrylat (PMMA) und thermoplastischem Polyurethan (TPU) im Hinblick auf sein Impaktverhalten experimentell und numerisch untersucht.

Grundlegende Experimente an PMMA und TPU wurden verwendet, um das thermomechanische Verhalten der monolithischen Materialien zu identifizieren. Weiterhin wurde ein PMMA–TPU–PMMA Laminat im Durchstoß– und Biegeimpaktversuch bei Geschwindigkeiten bis 5 m/s geprüft. Hierbei wurde eine signifikante Temperaturerhöhung der in der Nachbruchphase hoch gedehnten Zwischenfolie gemessen.

Basierend auf dieser experimentellen Basis wurden verschiedene Materialmodelle für die Finite-Elemente Simulation untersucht. Die präsentierten Materialmodelle waren in der Lage, das temperatur- und zeitabhängige Verhalten des Laminats sehr gut wiederzugeben. Weitere Teile der Arbeit beschäftigen sich mit Untersuchungen zur Modellierungstechnik des charakteristischen Verhaltens eines Laminats.

Ein finaler Validierungsversuch, welcher aus dem Aufprall eines Kopfimpaktors bei 10 m/s auf eine Automobilseitenscheibe besteht, wurde für PMMA und das Laminat durchgeführt. Die zugehörigen Simulationen stimmten sehr gut mit experimentellen Ergebnissen überein und erwiesen sich als zuverlässige Vorhersagemethode für zukünftige Entwicklungen.

Contents

Glossaries

Abbreviations

DIC	digital image correlation
DMA	dynamic mechanical analysis
DMTA	dynamic mechanical thermal analysis
DSC	differential scanning calorimetry
ECE	Economic Commission for Europe
EVA	ethylene-vinyl acetate
FE	Finite Element
FEM	Finite Element Method
FSP	fragment simulating projectile
IM	impact modified
Ipt	integration point
IR	infrared
IRT	infrared thermography
IUPAC	International Union of Pure and Applied Chemistry
JNCAP	Japan New Car Assessment Programme
LSG	laminated safety glass
LWIR	long wave infrared
MMA	methyl methacrylate
MWIR	mid wave infrared
NCAP	New Car Assessment Programme
NWIR	near wave infrared
PA	polyamide
PC	polycarbonate
PCL	polycaprolactone
PEVA	poly(ethylene-vinyl acetate)
PMMA	poly(methyl methacrylate)
PU	polyurethane
PVB	poly(vinyl butyral)
PVC	poly(vinyl chloride)
SD	standard deviation
SEM	scanning electron microscopy
SHPB	Split-Hopkinson pressure bar
SHTB	Split-Hopkinson tension bar
TPB	three-point bending
TPE	thermoplastic elastomer
TPS	transient plane source
TPU	thermoplastic polyurethane
TSG	toughened safety glass
VFT	Vogel-Fulcher-Tammann
VFTH	Vogel-Fulcher-Tammann-Hesse
WLF	Williams Landel Ferry
XFEM	extended Finite Element Method

Sub- and Superscripts

		iso	isochoric
0	engineering, initial	kin	kinetic
a	axial	l	lateral
amb	ambient	ov	overstress
c	critical	pl	plastic
cr	creep	pot	potential
d	dynamic	ref	reference
dev	deviatoric	rel	relaxation
el	elastic	s	specimen
f	flexural	vol	volumetric
fail	failure	vM	von Mises
h	hydrostatic	y	yield
in	inelastic	∞	infinite

Symbols

		F	force
$\mathbf{1}$	unity tensor	$\mathbf{F}$	deformation gradient
a_T	shift factor	$\dot{\mathbf{F}}$	material velocity gradient
A	cross section area	G	shear modulus
a	plane distance	G_{IC}	critical fracture energy
b	specimen width	G'	storage modulus (shear)
c	heat capacity	G''	loss modulus (shear)
c_R	Rayleigh wave speed	G^*	complex shear modulus
c_{sw}	shear wave speed	$\mathbf{H}$	displacement gradient tensor
C_1	WLF constant 1	I	invariant
C_2	WLF constant 2	J	Jacobian determinant, compli-
$\mathbf{C}$	Right Cauchy Green strain		ance modulus
	tensor	J_2	second invariant of deviatoric
$\mathbb{C}$	elasticity tensor		stress tensor
d	diameter	k	thermal conductivity
E	elastic modulus, energy	k_B	Boltzmann constant
E_A	activation energy	K	bulk modulus
E'	storage modulus	l	length
E''	loss modulus	$\mathbf{L}$	spatial velocity gradient
E^*	complex modulus	m	mass
$\mathbf{E}$	Green-Lagrange strain tensor	n	refractive index
f	frequency	$\vec{n}$	normal vector

p	hydrostatic pressure	β	decay coefficient
P	power	γ_0	intrinsic fracture energy
$\vec{q}$	Cauchy heat flux vector	$\dot{\gamma}$	shear strain rate
r	heat supply	δ	phase angle
R	radius	δ_t	crack opening displacement
$\bar{R}$	ideal gas constant	$\tan\delta$	loss factor
$\mathbf{R}$	rotation tensor	ε	strain, true strain, emissivity
s	displacement, entropy	$\dot{\varepsilon}$	strain rate
$\dot{s}$	entropy rate	$\boldsymbol{\varepsilon}$	Hencky's strain tensor
$\mathbf{S}$	second Piola-Kirchhoff stress tensor	η	viscosity
t	time, thickness	κ	thermal diffusivity
$\vec{t}$	stress vector	λ	stretch
T	temperature	ν	Poisson's ratio
T_g	glass transition temperature	ξ	Quinney-Taylor parameter
$\mathbf{U}$	right stretch tensor	ρ	mass density
$\vec{U}$	displacement field vector	σ	stress, true stress
v	velocity, volume	$\boldsymbol{\sigma}$	Cauchy stress tensor
$\vec{v}$	velocity vector	τ	shear stress, relaxation time, transmissivity
V	volume		
W	work, strain energy	χ	triaxiality factor
α	linear coefficient of thermal expansion	ψ	free energy
		ω	angular frequency

1 Introduction

1.1 Motivation

Amorphous polymers are a widespread alternative for conventional glass due to their low density and easy formability. These polymers are employed in various fields that differ significantly in application and loading situation. The material has to resist weather effects and show high-degree transparency, while at the same time it has to be evaluated in terms of scratch resistance, structural applicability, or crash performance. Diverse examples, like protective eyewear, aircraft canopies, transparent building constructions, or vehicle glazing only represent a small amount of possible utilization of amorphous polymers in daily life.

Weight reduction is one of the most important aims in the development and design of vehicles. Today's car light housings are already composed of amorphous (glassy) polymers, like polycarbonate (PC) and poly(methyl methacrylate) (PMMA). PMMA, in particular, shows good optical properties, weatherability, and a brittle fracture behaviour, which makes its behaviour similar to that of conventional glass. However, the vast majority of today's car windows are still made of conventional toughened safety glass (TSG) or laminated safety glass (LSG).

A replacement by polymeric alternatives appears advantageous, but involves complex processes and high efforts. Hence, approaches to substitute side and front windows by polymers, as performed for the race car in Figure 1.1 (a), are rare and have not reached commercial production yet. The reservations in the application of glassy polymers are of various nature, like reduction of the car's torsion stiffness, temperature dependence, or

(a) (b) (c)
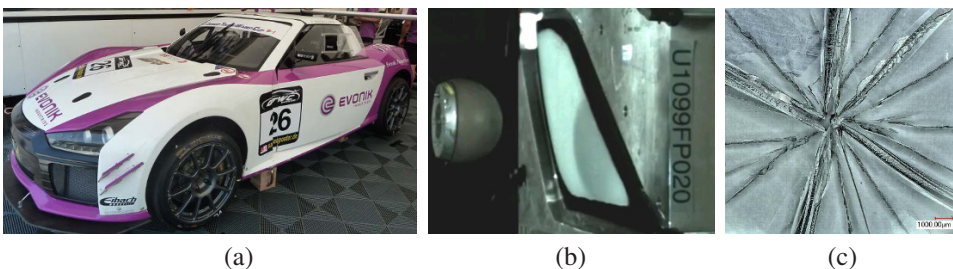
Figure 1.1 PMMA: (a) glazing of high performance cars (b) head impact test (c) fracture pattern.

expensive certification experiments (Figure 1.1 b) with partially unknown outcome and number of test cycles. TSG undergoes a special heat treatment during production that can not be directly applied to PMMA. Therefore, a direct substitution of TSG with monolithic PMMA exhibits post-breakage disadvantages due to bigger fragments. This makes PMMA attractive that is combined with a highly elastic interlayer material, like poly(vinyl butyral) (PVB) or thermoplastic polyurethane (TPU), to form a laminated structure. The resulting laminate combines the stated advantages of PMMA with a high deformation and post-breakage capacity as well as an improved fracture pattern.

The reduction of time-consuming and costly experiments raises the demand for accurate prediction methods of the thermomechanical behaviour of polymers and polymeric laminates. In terms of numerical simulations, one of the most conventional methods is the Finite Element Method (FEM). When proposing models for the FEM, not only the proper model set ups and correct boundary conditions, but also the adequate modelling of the material plays an important role for the validity and trustworthiness of numerical simulations. For the material modelling of polymers, standard mechanical properties like strength and failure behaviour (Figure 1.1 c) have to be taken into account on the one hand. On the other hand, polymers show a coupled dependence on time and temperature that has to be considered additionally when proposing such computational models.

Simulations of laminated structures, in particular, are a complex topic that covers various engineering disciplines. Therefore, basic experimental and numerical investigation is required to carve out the current possibilities and limitations in structural applicability and computational methods. Simulations of polymeric laminates are still subject to current investigation and models that are capable of accurate and trustworthy simulations are scarce. Consequently, high-confidence simulation models would contribute significantly to the acceptance and trustworthiness of laminated glassy polymer substitutes.

1.2 State of the Art

In this section, the current state of the art regarding the experimental and numerical research of PMMA-TPU laminates or similar structures is given. For an adequate description of the laminate, the state of the art considering the monolithic components PMMA and TPU has to be reviewed first. For limiting the extent, the focus is set to TPU in its interlayer form. Concluding, the literature concerning the laminate or comparable structures is evaluated.

Poly(methyl Methacrylate) (PMMA)

PMMA was subject to multiple examinations and only few representative works are treated in the present work. For a thorough review of the mechanical behaviour of PMMA the reader is referred to further literature, for example KINLOCH (2013).

PMMA was frequently investigated together with PC because both materials represent very conventional transparent polymers for glass substitution. Various investigation regarding the time dependent mechanical behaviour focused on the compressive area because the material behaves plastically with distinct higher strains than in the tensile area (KOLSKY, 1949; BAUWENS-CROWET, 1973; BLUMENTHAL et al., 2002; MULLIKEN et al., 2006). This allows observations of effects that occur only subordinately under tension. Further test data are presented in RICHETON et al. (2006), who performed uniaxial compression tests at wide ranges of temperature and strain rate. ARRUDA et al. (1995) as well LI et al. (2001) investigated the thermomechanical heating of PMMA due to plasticity. RITTEL (2000) used a cyclic loading to observe the same effects. Basic conclusion from these works are that PMMA has a significant rate dependence under compressive loads and distinct plasticity combined with heat generation and a ductile to brittle failure transition depending on temperature and strain rate.

Experimental effort regarding the tensile region of PMMA was carried out less frequently. Experimental results are presented in IMAI et al. (1976), CHEN et al. (2002), and WU et al. (2004). When no local or optical evaluation method was available, crosshead data and an incompressible evaluation of stress (IMAI et al., 1976) was used, which approaches the true stress-strain behaviour at small strains. With optical methods like extensometers, the influence of "parasitic deformations" (BAUWENS-CROWET et al., 1969) is reduced and the true material stress-strain behaviour was approached more accurately. Concluding from these works, the tensile behaviour is characterized by smaller failure strains with increasing strain rate (CHEN et al., 2002), dependence on environment and temperature (IMAI et al., 1976), and a change of fracture surface with strain-rate (WU et al., 2004). In contrast to compression, significantly smaller failure strains with a mainly brittle failure and minor plasticity were observed.

The impact behaviour of PMMA was investigated intensively because of its frequent application as protective goggles or aircraft canopies. Categorization of experiments can be performed in terms of the loading rate into low, intermediate and shock wave impacts (TEKALUR et al., 2010). Intermediate velocities, typically realized by a gas gun, and shock waves induced by explosives are not in the focus of the present work and only low velocity impacts with velocities roughly up to 20 m/s are considered subsequently. LIU et al. (2009) used an instrumented drop-weight impact machine at different temperatures for the low velocity impact on casted PMMA with a 16 mm tup. OGIHARA et al. (1998) performed low and high velocity impact tests on PMMA in order to determine the fracture behaviour and the perforation energy as a function of thickness. PEARSON et al. (2007) conducted quasi-static and low velocity impact tests using a screw-driven universal testing machine and an instrumented drop weight tower respectively. They were able to measure strains locally on the surface of the specimens and detected locally high strains near the impact point that decrease rapidly in radial direction.

The thermomechanical behaviour of PMMA using dynamic mechanical thermal analysis (DMTA) in different setups was investigated and discussed extensively (PEREZ et al., 1999; DE DEUS et al., 2004; IONITA et al., 2015). The material was found to behave viscoelastically, with an α-relaxation (glass transition) around $110\,°C$ and a β-relaxation roughly around room temperature. Different time-temperature shift equations were applied to PMMA as the material can be approached as thermorheologically simple for the most part and the generation of master curves was performed successfully (IONITA et al., 2015).

Failure of PMMA plates occurs similarly to that of conventional glass, which is tensile dominated because of its high compressive strength (DIN EN 1288-1, 2000). Here, PMMA differs significantly from PC in its energy dissipation method. PMMA dissipates energy through cracks, whereas PC can perform high plastic strains to absorb energy. The capability of performing high compressive plastic strains (BAUWENS-CROWET, 1973, ARRUDA et al., 1995, BLUMENTHAL et al., 2002) makes even small tensile portions decisive, which leads to a predominantly brittle failure of PMMA plies under impact. WEERASOORIYA et al. (2006) used a new Split-Hopkinson pressure bar (SHPB) technique to determine the fracture toughness of PMMA. They found a significant rate sensitivity and higher values at increasing strain rates. Furthermore, the failure of PMMA is temperature dependent, which was investigated by FLECK et al. (1990), who described the torsion strength as a function of temperature.

Several material models were proposed for PMMA and similar amorphous polymers in general. Most of the developments are based on compression tests to account for plasticity and thermomechanical coupling. The work by BOYCE et al. (1988) treats a micromolecular motivated approach to account for strain-rate and temperature dependence. BUCKLEY et al. (1995) proposed a constitutive model for amorphous polymers by combining several aspects of polymer theory to assure physical consistency. RICHETON et al. (2006) and RICHETON et al. (2007) developed an elastic-viscoplastic rheological approach for large inelastic impact loadings. They used a rate and temperature dependent linear spring in series with a parallel dashpot-spring structure.

Regarding the temperature behaviour of PMMA, ARRUDA et al. (1995) enhanced the model by BOYCE et al. (1988) using temperature dependent elastic constants with good correlation between simulation and uniaxial compressive experiments. RICHETON et al. (2007) included Williams Landel Ferry (WLF) shift parameters to account for the dependence of the yield strength on temperature and strain rate. Similar to this, BUCKLEY et al. (1995) used the Vogel-Fulcher-Tammann-Hesse (VFTH) shift approach for temperatures above the glass transition temperature T_g and the Arrhenius approach below T_g.

Modelling of fracture and failure has often been studied in the context of crack propagation. Here, the most conventional method in the explicit FEM is the element deletion, but also the extended Finite Element Method (XFEM) and node-splitting techniques, which requires additional node generation, were applied (SONG et al., 2008). Without claim of

completeness, a node-skipping technique (BAASER et al., 1999) can be used, for example, in implicit Finite Element (FE)-analysis. STICKLE et al. (2011) used a tensile stress criterion and a shear stress criterion within the Johnson-Cook fracture model. ANTOINE et al. (2014) modelled the brittle failure of PMMA within a laminate with a maximum tensile stress criterion considering temperature and strain rate and a strain based failure criterion for the ductile area.

Thermoplastic Polyurethane (TPU) Interlayers

The mechanical behaviour of TPU was investigated in several works for the compressive area (YI et al., 2006; QI et al., 2005; BUCKLEY et al., 2010). QI et al. (2005) examined TPU in terms of the time-dependent, large stress-strain behaviour and Mullins' effect related observations. Additionally, YI et al. (2006) and SARVA et al. (2007) conducted compression experiments at a large range of strain rates for different TPUs. They observed different time- and temperature dependent relaxation zones. SHPB experiments were conducted by SHARMA et al. (2002) likewise, who observed high strain-rate dependence for polyurethane (PU).

The temperature- and strain rate dependent behaviour of PU was confirmed by SARVA et al. (2007), EKEREN et al. (2011), and ZHANG et al. (2015) using either DMTA or differential scanning calorimetry (DSC) experiments. Compressive setups were applied far more frequently than tensile setups because of their increased complexity (ZHANG et al., 2015). The stress state in interlayers within a laminated structures under bending, however, becomes increasingly tensile with higher strains.

ZHANG et al. (2015) used the Split-Hopkinson tension bar (SHTB) setup to produce experimental tensile data over a large area of strain rates and temperature. Here, isochoric stress-strain curves were obtained by assuming incompressible material behaviour. SHTB were also conducted by FAN et al. (2015), who found a change of mechanical behaviour with strain rate. At quasi-static loading rates the material behaved rubber-like, while under high loading rates an elasto-plastic behaviour with a hardening branch was found. Furthermore, they discussed indications of cracks originating from crazes and the interaction between the two mechanisms using scanning electron microscopy (SEM) recordings. The high-strain tensile behaviour of TPU at different strain rates using a servo-hydraulic testing machine with digital image correlation (DIC) was investigated in KUNTSCHE (2015), who found a distinct nonlinear stress-strain behaviour that depends on strain rate.

Application in a laminate creates further parameters that may influence the behaviour of the TPU and the laminate significantly. TOQUEBOEUF et al. (1997) examined the behaviour of a PU within a polymeric laminate and determined that a multiaxial prestress and lateral confinement induced by the laminated structure have to be considered. MACALONEY et al. (2007) found a permanent change in mechanical behaviour for TPUs treated above a certain temperature that is within the range of typical lamination temperatures.

The deformation-induced thermomechanical interlayer heating was found to be small (ANTOINE et al., 2014) and of minor influence on the mechanical behaviour of the laminate and eventually neglected. KUNTSCHE (2015) mentioned a need for further investigation, but no published work has treated interlayer heating during impact loadings extensively yet.

ANTOINE et al. (2015) modelled the interlayer as a nearly-incompressible rubber-like material following an Ogden strain energy density in combination with a Prony series. QI et al. (2005) used a similar approach by using a nonlinear hyperelastic part and a viscoelastic-plastic overstress addition with parameters motivated from the molecular structure. ZHANG et al. (2015) used the thermo-viscoelastic Zhou-Wang-Tan (ZWT) model (WANG et al., 1992) to describe the strain- and temperature dependence of interlayers in structures designed for bird strikes. Due to the high strain behaviour a reliable stress or strain for failure is difficult to determine. Furthermore, the failure of TPU is expected to exhibit strain rate and temperature dependent. Here, engineering approaches by modelling the failure with a constant maximum tensile stress criterion (ANTOINE et al., 2014; RICHARDS et al., 1999) appeared to be sufficient for practical applications.

PMMA-TPU Laminates and Similar Structures

Experimental investigation of laminates was mostly conducted in terms of impact performance respectively energy absorption and their corresponding force-time and force-displacement behaviour. Laminated PMMA structures with a thickness of a few millimeters and in combination with PC or glass were subject to few investigation so far (ILLINGER et al., 1975; STENZLER et al., 2011; ANTOINE et al., 2014).

Laminates of greater thickness, roughly above 10 mm are used for ballistic protection. PATEL et al. (2006) executed ballistic impact tests on monolithic and multi-layered 12 mm PMMA, which exhibited an inferior ballistic performance of the multi-layered structure. They conducted further tests with glass-PMMA-PC structures and found a huge potential for weight reduction in protective structures. FOUNTZOULAS et al. (2009) subjected polymeric laminates to fragment simulating projectile (FSP) impact and found an increase in penetration resistance induced by the presence of TPU.

STENZLER et al. (2011) conducted medium-velocity gas-gun impact experiments on different PMMA-PC-TPU structures and examined the influence of the interlayer material on the overall impact performance. GUNNARSSON et al. (2011) used the DIC to investigat the behaviour of various PMMA and PC laminates at impact velocities up to 50 m/s. One laminate used a PU interlayer, together with PC plies. TEKALUR et al. (2010) investigated the crack pattern of layered PMMA and PC plates after impact loading. They found that multi-layered structures showed a very good impact energy absorption.

ANTOINE et al. (2014) used the FEM to study the impact behaviour of PMMA-PC-adhesive structures using the material model by BOYCE et al. (1988) and co-workers. They

could confirm a "sacrificial" role of PMMA plies on the impacted side by protecting the other plies. Furthermore, they found that the main energy dissipation mechanisms were the plastic deformation of PC and cracking of PMMA. Delamination, viscosity, and temperature softening were found to be only minor effects.

Another group of laminates is LSG, which is the standard application in automotive windshields. Here, the interlayer is predominantly PVB (KOLLING et al., 2015). Due to their parallels in structure and behaviour to LSG, some conclusion may be prescinded to polymeric laminates. LSG was subjected to numerous investigation (ALTER et al., 2013; FRANZ, 2015; KUNTSCHE, 2015) and is still an intensively investigated topic (KOLLING et al., 2015).

HOESS et al. (2009) introduced a laminate consisting of two PMMA plies in combination with a TPU interlayer in order to minimize the thermal stress induced by different coefficients of thermal expansion. This laminate already fulfills the requirements of the ball impact test specified in Regulation 43 of the Economic Commission for Europe Economic Commission for Europe (ECE) (UNECE NO. 43, 2012). The production and composition of these kind of laminates is still subject to current research and development (HOESS et al., 2016). By the knowledge of the author, numerical investigation considering the PMMA-TPU-PMMA laminates as proposed in HOESS et al. (2009) have firstly been undertaken in the course of the present work. Early stages of development are partially published in KOLLING et al. (2012), RÜHL et al. (2012b), and LOPEZ-RUIZ et al. (2015).

1.3 Aim and Structure of the Present Work

Applications of a PMMA-TPU-PMMA laminated structure as proposed in HOESS et al. (2009) have neither been subject to published experimental nor to numerical investigation. Hence, a comprehensive investigation regarding possibilities, capabilities, and limitations in the applicability and simulation of this laminate is the main subject of the present work. This will be supported by an experimental part and a numerical contribution.

The first aim is the creation of a broad experimental basis for evaluation and discussion of the behaviour of the laminate under dynamic loadings, predominantly represented by low velocity impacts. Although PMMA is a very well investigated polymer, the wide range in production type and additives may change its behaviour significantly. Therefore, some basic investigation of the exact PMMA used in the present work are required. For TPU, not only the temperature- and strain rate dependent mechanical behaviour is experimentally investigated but also a deeper insight into the thermomechanical coupling is given supported by DIC and infrared thermography (IRT).

The second aim is the development of computational models for the PMMA-TPU laminate. This contains the modelling of the thermomechanical behaviour of both materials with suitable material models and their validation by FE-simulations in comparison to

experimental results. Besides the mechanical behaviour, approaches for the modelling of temperature dependence within coupled thermomechanical simulations require investigation. A concluding evaluation of the simulation's predictability confidence leads to conclusions for topics of future investigation.

The structure of the present work is illustrated in Figure 1.2. Consecutively to this introductory chapter, fundamental definitions and theory required for understanding and discussion of experimental and computational results are given in Chapter 2. Chapter 3 contains three experimental sections for PMMA (Section 3.2), TPU (Section 3.3), and the PMMA-TPU laminate (Section 3.4).

These experimental results are used in the corresponding Chapters for the material modelling of PMMA (Chapter 4), TPU (Chapter 5), and combined for the laminate in Chapter 6. A final validation test is presented in Chapter 7 consisting of a head impact experiment on a side window is used for a concluding validation and discussion of the presented models. The main findings of the present work are summarized in Chapter 8 followed by a short overview of propositions for future topics of investigation.
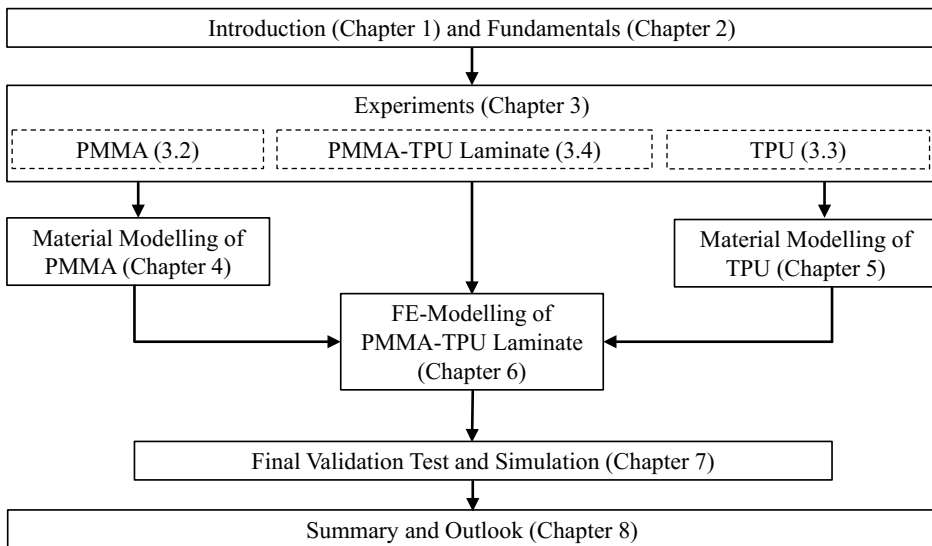
Figure 1.2 Structure of the present work.

2 Fundamentals

For an adequate description of the experimental procedures from Chapter 3, the material modelling of Chapter 4 and Chapter 5 as well as the numerical models from Chapter 6 and Chapter 7, the theoretical basis is provided in this chapter. In what follows, the fundamentals regarding the description of solid continua and polymer material modelling are given. In the last sections, the investigated polymers PMMA and TPU are introduced with respect to their chemical basis, mechanical and thermal behaviour as well as their production and processing. Concluding, the application of both materials in a laminate is presented.

The following tensor nomenclature is used within the present work: For convenience, the conventional superscript arrow is used for vectors, while tensors of second order are written in bold letters. Tensors of higher order are printed in blackboard-bold letters ($\mathbb{C}$). For tensor operations, a double scalar product is depicted with a colon. No operator between two tensors represents the tensor product. For vectors, the scalar product is depicted without any operator. This chapter is based on the work by several fundamental books, to which for deeper insight the reader is referred to (OGDEN, 1997; HOLZAPFEL, 2000; BECKER et al., 2013).

2.1 Continuum Mechanics

2.1.1 Kinematics

Continuum mechanics is used for the description of continuum bodies that consist of small particles, which define its mass and volume. A continuum is described by macroscopic quantities like temperature T and density ρ. Figure 2.1 shows the usual approach to describe a continuum, its movement, and deformation. The basis of a three-dimensional Eucledian space is given by three linearly independent, orthogonal vectors $\vec{e}_1$, $\vec{e}_2$, and $\vec{e}_3$. With an arbitrary origin, they define a right-handed coordinate system to describe any point P with its position vectors $\vec{X}$ or $\vec{x}$ respectively. This is used to formulate the displacement and deformation, which changes from a reference, initial configuration at a time t_0 to a deformed, translated and rotated configuration at a time $t_1 > t_0$, which is referred to as the current configuration. Quantities referring to the current configuration are written in small letters, those in reference configuration in capital letters.
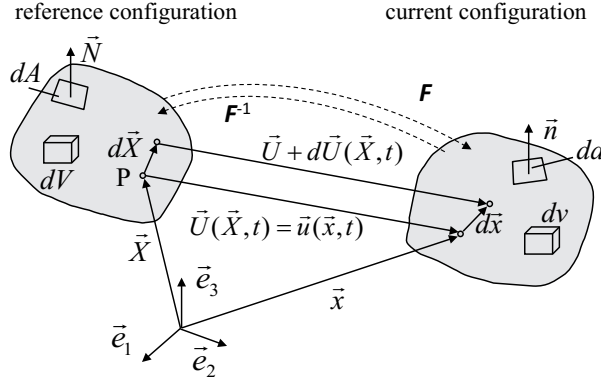
Figure 2.1 Reference and current configuration for the description of a continuum.

A displacement field vector $\vec{U}$ is composed of three components and expressed in the Lagrangian description by

$$\vec{U}(\vec{X},t) = \vec{x}(\vec{X},t) - \vec{X}. \tag{2.1}$$

The relative displacement between two points is described by the displacement gradient tensor $\mathbf{H}$ that is defined by

$$\mathbf{H}(\vec{X},t) = \frac{\partial \vec{U}(\vec{X},t)}{\partial \vec{X}} = \text{Grad}\,\vec{U}(\vec{X},t). \tag{2.2}$$

The linear mapping $\mathrm{d}\vec{x} = \boldsymbol{F}\mathrm{d}\vec{X}$ defines the deformation gradient

$$\mathbf{F}(\vec{X},t) = \frac{\partial \vec{x}(\vec{X},t)}{\partial \vec{X}} = \text{Grad}\,\vec{x}(\vec{X},t) \tag{2.3}$$

and the inverse deformation gradient

$$\mathbf{F}^{-1}(\vec{x},t) = \frac{\partial \vec{X}(\vec{x},t)}{\partial \vec{x}} = \text{grad}\,\vec{X}(\vec{x},t), \tag{2.4}$$

respectively. Hereby, $\mathbf{F}$ is connected to $\mathbf{H}$ through

$$\mathbf{H}(\vec{X},t) = \mathbf{F}(\vec{X},t) - \mathbf{1}, \tag{2.5}$$

where $\mathbf{1}$ represents the second order unity tensor. These tensors are central quantities for the description of nonlinear deformations of continuum bodies (HOLZAPFEL, 2000, p.71). For convenience, the dependencies of the single values are from now on only depicted,

when perceived as helpful. The components of the non-symmetric deformation gradient $\mathbf{F}$ are governed by

$$
\mathbf{F} = \begin{bmatrix} \dfrac{\partial x_1}{\partial X_1} & \dfrac{\partial x_1}{\partial X_2} & \dfrac{\partial x_1}{\partial X_3} \\[2mm] \dfrac{\partial x_2}{\partial X_1} & \dfrac{\partial x_2}{\partial X_2} & \dfrac{\partial x_2}{\partial X_3} \\[2mm] \dfrac{\partial x_3}{\partial X_1} & \dfrac{\partial x_3}{\partial X_2} & \dfrac{\partial x_3}{\partial X_3} \end{bmatrix}. \tag{2.6}
$$

Different properties can be deducted from the mathematical behaviour of $\mathbf{F}$. The deformation of a body is called homogeneous if $\mathbf{F}$ is independent of the Eulerian coordinates $\vec{x}$ (HOLZAPFEL, 2000, p.71). No deformation leads to $\mathbf{F=1}$, no motion to $\vec{x} = \vec{X}$ additionally.

The deformation gradient contains rigid body rotations that do, in fact, not contribute to deformation. Therefore, several additional strain descriptions have been created in either the reference or the current configuration that contain a polar decomposition of $\mathbf{F}$ in order to achieve rotation-free deformation quantities. Convenient strain tensors that are used in the reference configuration are summarized in Table 2.1. Polar decomposition is performed with the introduction of the right stretch tensor $\mathbf{U}$ and the rotation tensor $\mathbf{R}$ by

$$
\mathbf{F} = \mathbf{R\,U} \quad \text{with} \quad \mathbf{R}^\mathsf{T}\,\mathbf{R} = \mathbf{1} \quad \text{and} \quad \mathbf{U} = \mathbf{U^T}. \tag{2.7}
$$

With $\mathbf{U}$, the frequently used Right Cauchy Green tensor $\mathbf{C}$ is defined by

$$
\mathbf{C} = \mathbf{U}^2 = \mathbf{U^T U} = \mathbf{F^T F}. \tag{2.8}
$$

Nonlinearities in the stress-strain behaviour of a specimen, are either of material or geometric nature. Material nonlinearities are treated in Section 2.2. Geometric nonlinearities

Table 2.1   Convenient stretch and strain tensors.

Name	Symbol	Definition
Right stretch tensor	$\mathbf{U}$	$\mathbf{U} = \mathbf{R}^{-1}\,\mathbf{F}$
Right Cauchy-Green strain tensor	$\mathbf{C}$	$\mathbf{C} = \mathbf{F}^\mathsf{T}\,\mathbf{F}$
Green-Lagrange strain tensor	$\mathbf{E}$	$\mathbf{E} = \frac{1}{2}\left(\mathbf{F}^\mathsf{T}\,\mathbf{F} - \mathbf{1}\right)$
Hencky strain tensor	$\boldsymbol{\varepsilon}$	$\boldsymbol{\varepsilon} = \ln \mathbf{U}$

become dominant for higher deformation and are best visualized by the Green-Lagrange strain tensor $\mathbf{E}$ yielding a formulation with the spatial deformation gradient tensor $\mathbf{H}$ in

$$\mathbf{E} = \frac{1}{2}\left(\mathbf{F}^{\mathrm{T}}\mathbf{F} - \mathbf{1}\right) = \frac{1}{2}\left[(\mathbf{H}+\mathbf{1})^{\mathrm{T}} \ (\mathbf{H}+\mathbf{1}) - \mathbf{1}\right] = \frac{1}{2}\left(\mathbf{H} + \mathbf{H}^{\mathrm{T}} + \mathbf{H}^{\mathrm{T}} \ \mathbf{H}\right) \ . \qquad (2.9)$$

Here, the part $\mathbf{H}^{\mathrm{T}}\mathbf{H}$ considers geometric nonlinearities. For small strains this term can be neglected, which leads to

$$\mathbf{E} \approx \frac{1}{2}\left(\mathbf{H} + \mathbf{H}^{\mathrm{T}}\right) =: \boldsymbol{\varepsilon}_0 \ , \qquad (2.10)$$

where $\boldsymbol{\varepsilon}_0$ is defined as the (linearized) infinitesimal strain tensor. From an experimental point of view, materials are mostly characterized by uniaxial tensile or compressive experiments. Under one-dimensional uniaxial deformation and for small strains, the strain is evaluated either with respect to the initial length (engineering strain ε_0) or to the current length (true, logarithmic or Hencky's strain ε). Both strain measurements are related by

$$\varepsilon = \int_0^\varepsilon \mathrm{d}\bar{\varepsilon} = \int_{l_0}^l \frac{\mathrm{d}\bar{l}}{l} = \ln\left(\frac{l}{l_0}\right) = \ln\left(1 + \varepsilon_0\right) = \ln(\lambda), \qquad (2.11)$$

where λ represents the principal stretch, which is also a frequently used strain measurement. The engineering strain ε_0 is the linearized Taylor-series approach of the true strain ε. For small values of ε, the engineering strain ε_0 exhibits as a good approximation. If the lateral contraction is measured, Poisson's ratio v can be obtained, which is defined for small strains as

$$v = -\frac{\varepsilon_{\mathrm{l}}}{\varepsilon}, \qquad (2.12)$$

where ε_{l} represents the lateral strain. To compare different deformation states, equivalence formulations are required. A conventional quantity is the von-Mises equivalent strain $\varepsilon_{\mathrm{vM}}$, which is defined for isotropic materials in principal strains as

$$\varepsilon_{\mathrm{vM}} = \frac{1}{1+v}\sqrt{\frac{1}{2}[(\varepsilon_1 - \varepsilon_2)^2 + (\varepsilon_2 - \varepsilon_3)^2 + (\varepsilon_3 - \varepsilon_1)^2]}, \qquad (2.13)$$

where the strain components ε_{i} represent the main diagonal elements of the strain tensor. For the development of material models, it is helpful to use quantities of deformations that fulfill the requirement of material objectivity, which are referred to as invariants. The

three invariants of the Right Cauchy-Green deformation tensor $\mathbf{C}$ expressed by principal stretches are

$$I_C = \lambda_1^2 + \lambda_2^2 + \lambda_3^2 \tag{2.14}$$

$$II_C = \lambda_1^2\,\lambda_2^2 + \lambda_2^2\,\lambda_3^2 + \lambda_1^2\,\lambda_3^2 \tag{2.15}$$

$$III_C = \lambda_1^2\,\lambda_2^2\,\lambda_3^2. \tag{2.16}$$

The relative change in volume is expressed by the Jacobian determinant

$$J = \frac{v}{V} = \det\mathbf{F}, \tag{2.17}$$

where v and V are the current and the initial volume respectively. With $J{=}1$ an isochoric material behaviour is given. In terms of computational mechanics, a split into volumetric (dilatational) and deviatoric (distortional) deformation is conventional. Hereby, deviatoric parts are expressed by the modified deformation gradient $\bar{\mathbf{F}}$ and the modified Right Cauchy Green tensor $\bar{\mathbf{C}}$, marked by a superscript bar, which are defined in

$$\mathbf{F} = J^{1/3}\bar{\mathbf{F}} \qquad \text{and} \qquad \mathbf{C} = J^{2/3}\bar{\mathbf{C}}. \tag{2.18}$$

Besides the description of absolute values of deformation, the rate at which changes of state occur is a further important aspect. The velocity $\vec{V}$ of a point within a continuum is given in the reference configuration by

$$\vec{V} = \dot{\vec{X}}. \tag{2.19}$$

The corresponding material velocity gradient is calculated by

$$\dot{\boldsymbol{F}} = \text{Grad}\,\vec{V}(\vec{X},t). \tag{2.20}$$

In the current configuration the spatial velocity is obtained by

$$\boldsymbol{L} = \text{grad}\,\vec{v}(\vec{x},t). \tag{2.21}$$

Both velocity measurements $\dot{\mathbf{F}}$ and $\boldsymbol{L}$ are used for kinematic description of time dependent problems.

2.1.2 Stress

The most convenient stress expression is the Cauchy stress, which is defined in Cauchy's relation as

$$\vec{t} = \boldsymbol{\sigma}\, \vec{n} = \begin{bmatrix} \sigma_{11} & \sigma_{12} & \sigma_{13} \\ \sigma_{12} & \sigma_{22} & \sigma_{23} \\ \sigma_{13} & \sigma_{23} & \sigma_{33} \end{bmatrix} \begin{bmatrix} n_1 \\ n_2 \\ n_3 \end{bmatrix}, \tag{2.22}$$

where $\boldsymbol{\sigma}$ symbolizes the symmetric second order Cauchy stress tensor and $\vec{t}$ denotes the stress vector of a cross section area defined by the normal vector $\vec{n}$. For material objectivity, invariants of the Cauchy stress tensor are defined corresponding to Equations (2.14) to (2.16) as

$$\mathrm{I}_\sigma = \mathrm{tr}\,\boldsymbol{\sigma} \tag{2.23}$$

$$\mathrm{II}_\sigma = \frac{1}{2}\left[(\mathrm{tr}\,\boldsymbol{\sigma})^2 - \mathrm{tr}\left(\boldsymbol{\sigma}^2\right)\right] \tag{2.24}$$

$$\mathrm{III}_\sigma = \det\boldsymbol{\sigma}. \tag{2.25}$$

For material modelling, the Cauchy stress is frequently split into a hydrostatic and a deviatoric part according to

$$\boldsymbol{\sigma} = \boldsymbol{\sigma}_{\mathrm{h}} + \boldsymbol{\sigma}_{\mathrm{dev}} = \begin{bmatrix} -p & 0 & 0 \\ 0 & -p & 0 \\ 0 & 0 & -p \end{bmatrix} + \begin{bmatrix} \sigma_{11}+p & \sigma_{12} & \sigma_{13} \\ \sigma_{12} & \sigma_{22}+p & \sigma_{23} \\ \sigma_{13} & \sigma_{23} & \sigma_{33}+p \end{bmatrix}, \tag{2.26}$$

with p representing the hydrostatic pressure

$$-p = \frac{1}{3}(\sigma_{11} + \sigma_{22} + \sigma_{33}) = \frac{1}{3}\mathrm{tr}\,\boldsymbol{\sigma}. \tag{2.27}$$

To evaluate a stress state, which is often a mixture of shear stress τ and normal stress σ and, henceforth, possibly oriented into several directions, different equivalent stress measures can be used. The von-Mises equivalent stress is defined for an arbitrary stress tensor as

$$\sigma_{\mathrm{vM}} = \sqrt{\frac{1}{2}\left[(\sigma_{11} - \sigma_{22})^2 + (\sigma_{22} - \sigma_{33})^2 + (\sigma_{33} - \sigma_{11})^2 + 6\left(\sigma_{23}^2 + \sigma_{31}^2 + \sigma_{12}^2\right)\right]} \tag{2.28}$$

and forms to

$$\sigma_{vM} = \frac{\sqrt{2}}{2}\sqrt{(\sigma_1 - \sigma_2)^2 + (\sigma_2 - \sigma_3)^2 + (\sigma_3 - \sigma_1)^2} \tag{2.29}$$

by using principal stress quantities. Because of the correlation

$$\sigma_{vM} = \sqrt{3J_2} \, , \tag{2.30}$$

where J_2 is the second invariant of the deviatoric stress tensor $\boldsymbol{\sigma}_{dev}$, the application of the von-Mises stress in plasticity theory is often referred to as the J_2-plasticity. As a measurement for the spatial stress condition, the triaxiality factor χ can be defined as

$$\chi = -\frac{p}{\sigma_{vM}} = \frac{I_\sigma}{3\sqrt{3J_2}}, \tag{2.31}$$

where the hydrostatic pressure p can be expressed by the first invariant with $-1/3 I_\sigma$. With this definition, a uniaxial tensile stress state then corresponds to the value χ=1/3, while equibiaxial compression would lead to χ=-2/3. Different stress states can be illustrated in the Burzyński-plane (BURZYNSKI, 1929) for convenient categorization of triaxial experiments. Besides the Cauchy stress $\boldsymbol{\sigma}$, which is defined in the current configuration, the asymmetric first Piola-Kirchhoff stress tensor

$$\boldsymbol{P} = J\boldsymbol{F}^{-1}\boldsymbol{\sigma} \tag{2.32}$$

can be used to further define the symmetric second Piola-Kirchhoff stress tensor

$$\boldsymbol{S} = J\boldsymbol{F}^{-1}\boldsymbol{\sigma}\boldsymbol{F}^{-T} \, , \tag{2.33}$$

which relates to the initial configuration.

Engineering, Isochoric, and True Stress

A conventional approach for small strain tensile tests is the evaluation of engineering values. Here, the measured force F is used to calculate the uniaxial engineering stress σ_0 corresponding to the initial cross section of the specimen A_0 with

$$\sigma_0 = \frac{F}{A_0} = \frac{F}{b_0 t_0}, \tag{2.34}$$

where b_0 and t_0 represent the width and thickness of a rectangular specimen. This evaluation method contains no information about the contraction of the specimen and the resultant change in stress. At higher deformations, engineering values increasingly deviate

from real ones. The isochoric stress σ_{iso} is a quantity to approach the true stress by assuming Poisson's ratio $\nu = 0.5$ in

$$\sigma_{\mathrm{iso}} = \sigma_0 \ (1 + \varepsilon_0) = \frac{F}{A_0} \left(1 + \frac{\Delta l}{l_0} \right) = \frac{F}{A_0 \exp(-\varepsilon)} \ . \tag{2.35}$$

For rubber-like materials with Poisson's ratio close to 0.5, the approach is usually suitable for estimating the true stress. If the lateral contraction is measured, the true stress σ can be directly calculated for a transverse isotropic material with

$$\sigma = \frac{F}{A} = \frac{F}{bt} = \frac{F}{A_0 \exp(2\varepsilon_{\mathrm{l}})} = \frac{F}{A_0 \exp(-2\varepsilon\nu)} \ , \tag{2.36}$$

where the measured lateral contraction ε_{l} allows a conversion from engineering to true stress. In the course of the present work, materials are assumed to be transverse isotropic and σ from Equation (2.36), is referred to as the true stress henceforth. σ_0 and σ_{iso} are widespread stress measurements and in many cases sufficient. The true stress σ, however, is the most accurate, yet hardest to determine stress measurement because additional measurements of the lateral contraction have to be performed.

2.2 Polymer Materials Theory

2.2.1 Linear Elasticity

A linear relationship between stress and strain for small strains is expressed by the fourth order elasticity tensor $\mathbb{C}$ in

$$\boldsymbol{\sigma} = \mathbb{C} : \boldsymbol{\varepsilon}, \tag{2.37}$$

which is known in one dimension as Hooke's law. It can also be expressed by using the elastic strain energy density $W = {}^1\!/2 \, \boldsymbol{\varepsilon} : \mathbb{C} : \boldsymbol{\varepsilon}$ in

$$\boldsymbol{\sigma} = \frac{\partial W}{\partial \boldsymbol{\varepsilon}} = \frac{1}{2} \frac{\partial (\boldsymbol{\varepsilon} : \mathbb{C} : \boldsymbol{\varepsilon})}{\partial \boldsymbol{\varepsilon}} = \mathbb{C} : \boldsymbol{\varepsilon}. \tag{2.38}$$

Elasticity for small strains and isotropic material behaviour is described by Hooke's law with the elastic modulus E and Possion's ratio ν. The linear correlation between E, the shear modulus G, and the bulk modulus K is given by Poisson's ratio ν with

$$G = \frac{E}{2(1+\nu)} = \frac{3K(1-2\nu)}{2(1+\nu)} \tag{2.39}$$

and

$$K = \frac{E}{3(1 - 2\nu)}. \tag{2.40}$$

Note that for a perfectly incompressible material behaviour the bulk modulus K would become infinite. G and K are conventionally used for constitutive relations using the volumetric-deviatoric split, as defined in Equation (2.26). However, most polymers deviate from a linear elastic behaviour due to effects like nonlinear elasticity, viscoelasticity, and plasticity.

2.2.2 Hyperelasticity

Most elastic rubber-like polymers show a nonlinear stress-strain correlation, which is frequently described with hyperelasticity. The hyperelastic theory presumes the existence of a strain-induced elastic potential. Then, a strain energy W can be formulated as either a function of strain, the three invariants for material objectivity, or the three principal stretches according to

$$W = W(\boldsymbol{C}) \tag{2.41}$$

$$W = W(\mathrm{I}_C, \mathrm{II}_C, \mathrm{III}_C) \tag{2.42}$$

$$W = W(\lambda_1, \lambda_2, \lambda_3). \tag{2.43}$$

The strain energy function W derived with respect to the Green-Lagrange strain tensor $\mathbf{E}$ or the Right Cauchy Green strain tensor $\mathbf{C}$ yields the Second Piola Kirchhoff stress

$$\boldsymbol{S}(\mathbf{E}) = \frac{\partial W}{\partial \boldsymbol{E}} = 2\,\frac{\partial W}{\partial \boldsymbol{C}}. \tag{2.44}$$

A formulation in terms of invariants is given by

$$\mathbf{S}(\mathbf{C}) = 2\left(\frac{\partial W}{\partial I_C}\frac{\partial I_C}{\partial \mathbf{C}} + \frac{\partial W}{\partial II_C}\frac{\partial II_C}{\partial \mathbf{C}} + \frac{\partial W}{\partial III_C}\frac{\partial III_C}{\partial \mathbf{C}}\right), \tag{2.45}$$

which uses the second Piola-Kirchhoff stress tensor $\mathbf{S}$ and the right Cauchy-Green tensor $\mathbf{C}$. A concluding formulation for the Cauchy stress tensor is obtained using principal stretches in the component form with

$$\sigma_i(\lambda_i, \lambda_j, \lambda_k) = \frac{1}{\lambda_j \lambda_k} \frac{\partial W}{\partial \lambda_i}. \tag{2.46}$$

The formulation with deviatoric-based strain energies simplifies Equation (2.42) to a dependence on the first and second invariant. Further simplified models additionally omit dependence on the second invariant, which often shows to be sufficient for certain stress-states.

Various energy function formulations exist for the huge variety of different material behaviour. Frequently, the material is assumed to be incompressible (J=1), and only the hydrostatic parts are considered. For volumetric work, an additional dilatational work term is usually introduced. The strain energy is then composed of a linear combination of a deviatoric part W_{dev} and a hydrostatic term $W_{\mathrm{h}}(J)$ following

$$W = W_{\mathrm{dev}} + W_{\mathrm{h}} \tag{2.47}$$

to take account of compressibility. To prevent volumetric work from contributing to the deviatoric parts, the modified invariants $\bar{\mathrm{I}}_C$ and $\bar{\mathrm{II}}_C$ are introduced and marked with a superscript bar. Their correlation to the invariants of the Right Cauchy Green tensor are given by

$$\bar{\mathrm{I}}_C = \frac{\mathrm{I}_C}{\mathrm{III}_C^{1/3}} \qquad \text{and} \qquad \bar{\mathrm{II}}_C = \frac{\mathrm{II}_C}{\mathrm{III}_C^{2/3}}. \tag{2.48}$$

A corresponding formulation for the modified stretches is defined as

$$\bar{\lambda}_i = \frac{\lambda_i}{J^{1/3}}, \tag{2.49}$$

where J is the Jacobi determinant. A selection of frequently applied hyperelastic function is presented subsequently. An early extension of linear elasticity was the Neo-Hooke function (RIVLIN, 1948 and others) that uses only one parameter C_{10}. TRELOAR (1944) found by statistical consideration validity of

$$W_{\mathrm{dev}}^{\mathrm{NH}} = C_{10}(\bar{\mathrm{I}}_C - 3) \approx \frac{1}{2} N k_B T (\bar{\mathrm{I}}_C - 3), \tag{2.50}$$

where N represents the number of molecular chains, k_{B} the Boltzmann constant and T the temperature in Kelvin. By adding terms of higher order, the strain energy function by YEOH (1990) is obtained, which is defined as

$$W_{\text{dev}}^{Y} = C_{10}(\bar{I}_C - 3) + C_{20}(\bar{I}_C - 3)^2 + C_{30}(\bar{I}_C - 3)^3. \tag{2.51}$$

Terms of higher order enable a more accurate modelling with more inflection points but under the cost of higher effort for parameter identification. The $\bar{I}_C$-models, however, lack the ability of modelling other deformation states than uniaxial tension accurately (BS 903-5, 2004). Therefore, more complex models are required that consider $\bar{I}_C$ and $\bar{II}_C$ simultaneously and are able to cover a wider range of stress states more accurately. The Mooney-Rivlin model (MOONEY, 1940) is a Taylor series expansions of a model given in RIVLIN et al. (1951) with

$$W_{\text{dev}}^{MR} = \sum_{i,j=0}^{\infty} C_{ij}(\bar{I}_C - 3)^i (\bar{II}_C - 3)^j \,. \tag{2.52}$$

Herein, the shear modulus G is defined for small strains as

$$G = 2\sum_{i,j} C_{ij} \,. \tag{2.53}$$

Neo-Hooke, Yeoh and the Mooney function (MOONEY, 1940) are special derivatives of Equation (2.52). Furthermore, Neo-Hooke and Mooney-Rivlin are certain cases of the model by OGDEN (1972), that uses the volumetric independent principal stretches

$$\bar{\lambda}_k = J^{-1/3}\lambda_k \tag{2.54}$$

instead of invariants to formulate the strain energy

$$W_{\text{dev}}^{O} = \sum_{i=1}^{n} \frac{\mu_i}{\alpha_i} \left(\bar{\lambda}_1^{\alpha_i} + \bar{\lambda}_2^{\alpha_i} + \bar{\lambda}_3^{\alpha_i} - 3 \right), \tag{2.55}$$

where n is frequently set to three. μ_i and α_i are material parameters fulfilling

$$\frac{1}{2}\sum_{i}^{n} \mu_i \alpha_i = G \,, \tag{2.56}$$

where G is the frequency independent shear modulus. The strain energy function by
BLATZ et al. (1962), which is a coupled function of volumetric and an isochoric parts,
is defined as

$$W^{\mathrm{BK}} = f\frac{G}{2}\left[\mathrm{I}_C - 3 + \frac{1}{\beta}\left(\mathrm{III}_C^{-\beta} - 1\right)\right] + (1-f)\frac{G}{2}\left[\frac{\mathrm{II}_C}{\mathrm{III}_C} - 3 + \frac{1}{\beta}\left(\mathrm{III}_C^{\beta} - 1\right)\right]$$

(2.57)

where G represent the shear modulus, β a material parameter, and f serves as an interpola-
tion parameter. There are several further energy functions, for example the Arruda-Boyce
model (ARRUDA et al., 1993), which is motivated by micromechanical considerations,
or the Frazer-Nash model, where the polynomial structure allows distinct modelling of
complex stress-strain curves. However, the principle proceeding remains the same for all
hyperelastic strain energy formulations.

2.2.3 Viscoelasticity

Most solid materials show elastic behaviour for small strain and stress. If this behaviour
is linear it is called a linear elastic material, which follows Hooke's law. Fluids show a
viscous behaviour; strains are inelastic and the corresponding stress-strain rate behaviour
is either linear (Newtonian fluid) or nonlinear (non-Newtonian fluid). The combined be-
haviour of elasticity and viscosity is called viscoelasticity, and applies for most polymers.
It is characterized by creep, relaxation, and a hysteresis loop at unloading, which is gov-
erned by energy dissipation. To exhibit the basic principle of viscoelasticity, it is sufficient
to give the following equations in a uniaxial description.

2.2.3.1 Linear Viscoelasticity

Viscoelasticity is characterized by the observation of creep at boundary conditions of con-
stant stress ($\sigma \neq 0$) and relaxation at constant strain ($\varepsilon \neq 0$). This behaviour is depicted in
Figure 2.2 (a), where the continuous line shows the creep behaviour of the strain ε of a
viscoelastic model under a constant, instantaneous applied stress.

Basic formulations of viscoelasticity relate to the relaxation or creep behaviour, which
is depicted in Figure 2.2 (a) for a uniaxial tensile creep (σ=constant, continuous line) and
relaxation test (ε=constant, dashed line). The difference between the instantaneous stress
σ_1 and the infinite limit stress σ_∞ is called overstress and represents the stress resulting
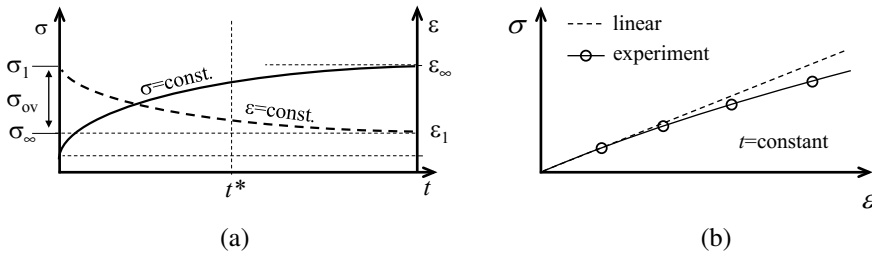
Figure 2.2 (a) Creep and Relaxation. (b) Typical creep isochrone.

from the viscous part of the material behaviour. The creep modulus and the relaxation modulus are defined by

$$E_{\mathrm{cr}}(t,T) = \frac{\sigma}{\varepsilon(t,T)} \qquad \text{and} \qquad E_{\mathrm{rel}}(t,T) = \frac{\sigma(t,T)}{\varepsilon} \,. \tag{2.58}$$

They describe the creep and relaxation behaviour and are central quantities in the theory of viscoelasticity. Their inverse values are referred to as the compliance creep modulus $J_{\mathrm{cr}}(t,T)$ and compliance relaxation modulus $J_{\mathrm{rel}}(t,T)$. Further quantities regarding the relaxation and creep behaviour are defined in DIN 53441 (1984) and DIN EN ISO 899-1 (2003).

Linear viscoelasticity is characterized by a linear isochronous stress-strain behaviour (OGORKIEWICZ, 1970). For illustration, Figure 2.2 (b) shows a typical creep behaviour of an isochrone under creep for a polymer. With increasing strain and stress, deviations from a linear behaviour become dominant and linear viscoelasticity does not represent the material behaviour accurately.

Therefore, the theory of linear viscoelasticity is valid within the linearity limits of stress σ and strain ε (SCHWARZL, 1990), which are approximately 0.5 % for uncrosslinked amorphous polymers (BUCKLEY et al., 1995). The mathematical description of linear viscoelasticity can be performed by integral or differential approaches.

Integral Formulation

The integral operator representation is based on the Boltzmann superposition principle, which states that stress resulting from deformations at different times sums up to the total stress and overstress from different loads is independently relaxed. The principle shows likewise validity for strain creeping resulting from stress.

In the integral formulation of viscoelasticity, a series of step functions approach the viscoelastic behaviour. Relaxation and creep follow the correlations

$$\sigma(t) = \int_{-\infty}^{t} E(t-s)\frac{\partial \varepsilon(s)}{\partial s}\,\mathrm{d}s \qquad \text{and} \qquad \varepsilon(t) = \int_{-\infty}^{t} J(t-s)\frac{\partial \sigma(s)}{\partial s}\,\mathrm{d}s, \qquad (2.59)$$

where $\varepsilon(t)$ and $\sigma(t)$ represent the strain and stress respectively. $J(t)$ stands for the creep function that relates the strain $\varepsilon(\sigma)$ to a constant stress σ in a creep experiment. $E(t)$ describes the relaxation function.

$E(t-s)$ and $J(t-s)$ represent the memory functions that consider the history of the material (FINDLEY et al., 2013). Equation (2.59) only applies for the linear area of the material, where creep and relaxation function are load-independent. Approaches to represent nonlinear viscoelastic behaviour in an integral approach were proposed by different authors, for example by LEADERMAN (1941), SCHAPERY (1969), or GREEN et al. (1997). The approach by LEADERMAN (1941) replaces the stress or strain respectively in Equation (2.59) by a function to form

$$\sigma(t) = \int_{-\infty}^{t} E(t-s)\frac{\partial f(\varepsilon)}{\partial s}\,\mathrm{d}s \qquad \text{and} \qquad \varepsilon(t) = \int_{-\infty}^{t} J(t-s)\frac{\partial g(\sigma)}{\partial s}\,\mathrm{d}s, \qquad (2.60)$$

where $f(\varepsilon)$ and $g(\sigma)$ respectively enable a nonlinear modelling.

Integral formulations, however, bear the disadvantage of complex mathematical terms with parameter identification that requires high experimental effort. Hence, they appear to be scarcely used in engineering practice compared to the much more frequently applied differential approach.
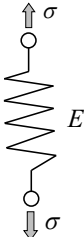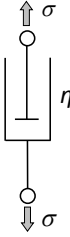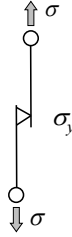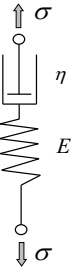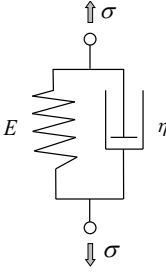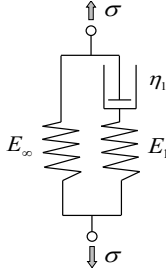
Differential Formulation

The differential formulation stems from the analogy observations of rheological spring-dashpot models and viscoelastic material behaviour. Rheological models are used to approximate the material behaviour and to create possibilities of calculation. Table 2.2 gives an overview of the basic rheological models in the first row and viscoelastic models in the second row.

The three basis elements (elastic) Hooke element, (viscous) Newton element and (plastic) St. Venant element, which is also reffered to as Coulomb element. These elements are conventionally referred to as spring, dashpot and friction elements respectively. Their behaviour is characterized by one parameter. For the spring, this is the elastic modulus E respectively the shear modulus G, for the dashpot the viscosity η and for the friction element

Table 2.2 Basic rheological elements and models.

elements		
Hooke element	Newton element	St. Venant element

models		
Maxwell model	Kelvin-Voigt model	standard linear solid model

the yield strength σ_y. A relaxation time τ is defined as the time, where $1 - 1/e \approx 63.2\,\%$ of the overstress after a sudden loading is decayed. The relationship

$$\tau = \frac{\eta}{G} \tag{2.61}$$

uses this relaxation time to describe the parameters for the viscous part of rheological models. The decay coefficient

$$\beta = \tau^{-1} = \frac{G}{\eta}, \tag{2.62}$$

which is the inverse of the relaxation time, is used alternatively. Combination of spring and dashpot elements in parallel or in series leads to viscoelastic models. The basic models models are known as the Maxwell- and Kelvin-Voigt models. With increasing complexity of the viscoelastic material behaviour, complex models are usually needed. For every

additional basic elements, one unknown parameter adds to the system of equations, which increases the complexity of the model. The central task for an adequate application of rheological models is the correct determination of parameters.

Uniaxial Analytical Solution

The one-dimensional differential Equation for the standard linear solid model from Table 2.2 under uniaxial deformation is given by

$$\dot{\sigma} + \frac{E_1}{\eta}\sigma = (E_\infty + E_1)\dot{\varepsilon} + \frac{E_\infty E_1}{\eta}\varepsilon, \tag{2.63}$$

which can be solved according to

$$\frac{\mathrm{d}}{\mathrm{d}t}\left[\sigma \exp\left(\frac{E_1}{\eta_1}t\right)\right] = E_\infty \frac{\mathrm{d}}{\mathrm{d}t}\left[\varepsilon \exp\left(\frac{E_1}{\eta_1}t\right)\right] + E_1 \frac{\mathrm{d}\varepsilon}{\mathrm{d}t}\exp\left(\frac{E_1}{\eta_1}t\right). \tag{2.64}$$

Integration with respect to time and application of the boundary conditions $\sigma(0) = 0$ and $\varepsilon(0) = 0$ (RANZ, 2007) yields

$$\sigma(t) = \int_0^t \left[E_\infty + E_1\exp\left(\frac{E_1}{\eta_1}(\bar{t} - t)\right)\right]\dot{\varepsilon}\,\mathrm{d}\bar{t}. \tag{2.65}$$

Solved for the stress $\sigma(\varepsilon, \dot{\varepsilon})$ by assuming a constant strain rate, which gives the time with $t = \varepsilon/\dot{\varepsilon}$, Equation (2.65) can be formed to

$$\sigma(\varepsilon, \dot{\varepsilon}) = E_\infty \varepsilon + \dot{\varepsilon}\eta_1 \left[1 - \exp\left(-\frac{E_1}{\eta_1}\frac{\varepsilon}{\dot{\varepsilon}}\right)\right]. \tag{2.66}$$

Equation (2.66) can be used for the identification of the parameters E_∞, E_1 and η form uniaxial tensile tests, which is performed in Section 4.1.

For a higher complexity of the material response and a better resolution of the stress-strain behaviour at different strain rates, an extension of the conventional viscoelastic models is frequently performed. This is, for example, realized with a generalized Maxwell model, which is shown in Figure 2.3 (a) and is often referred to as a Prony series. The standard linear solid model is extended by an arbitrary number n of parallel Maxwell models. Corresponding to Equation (2.66), the stress-strain behaviour is calculated by

$$\sigma(\varepsilon, \dot{\varepsilon}) = E_\infty \varepsilon + \sum_{i=1}^{n} \dot{\varepsilon}\frac{E_i}{\bar{\beta}_i}\left[1 - \exp\left(-\bar{\beta}_i\frac{\varepsilon}{\dot{\varepsilon}}\right)\right]. \tag{2.67}$$
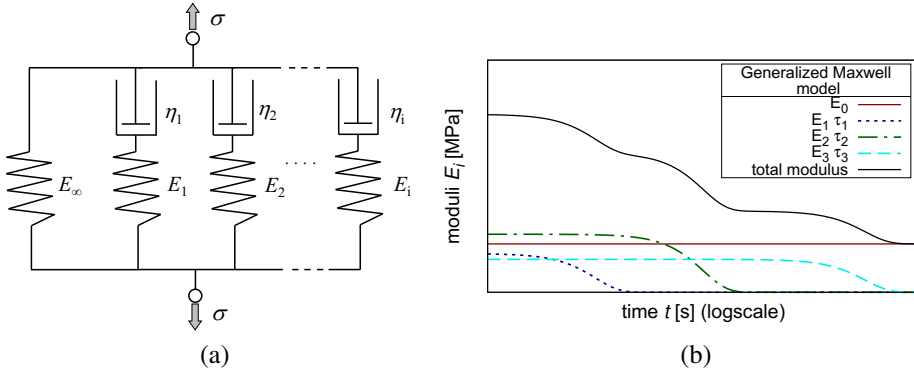
Figure 2.3 (a) Generalized Maxwell model and (b) relaxation of the generalized Maxwell Model.

Here, the decay constant $\bar{\beta}$ is defined as E/η. The principle behaviour of this model is depicted in Figure 2.3 (b). Here, an arbitrary set of parameters for four parallel Maxwell elements with different elastic moduli and different relaxation times is shown. After sudden deformation and $\dot{\varepsilon}=0$ for $t>0$, the dynamic moduli relax with increasing time, while the elastic modulus remains constants. At $t\to\infty$ the total modulus equals the elastic modulus. To follow thermodynamically consistency, the equations have to comply to the Clausius-Duhem inequality. This can be simplified to the limitation that the viscosity η has to fulfill $\eta \geq 0$.

Figure 2.4 shows the principle behaviour of a linear viscoelastic model under uniaxial tension for constant strain rates. With increasing strain rate $\dot{\varepsilon}$, the complete material answer is the sum of the elastic stress σ_∞ and the overstress σ_{ov}. The typical behaviour is then characterized by parallel stress-strain curves for different constant strain rates. The magnitude of the parallel translation is governed by

$$x = \frac{2(1+v)G_1}{\beta_1} \; . \tag{2.68}$$
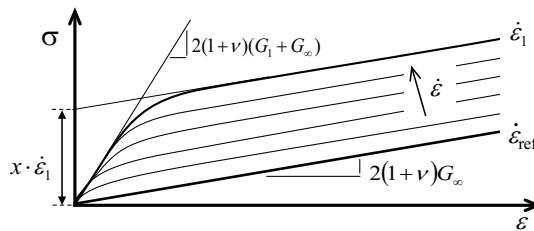
Figure 2.4 Linear viscoelastic stress-strain behaviour at different constant true strain rates.

2.2.3.2 Nonlinear Viscoelasticity

Nonlinearities in viscoelastic material behaviour can either result from the elastic or the viscous part. In terms of rheology, this would mean that the elastic springs do not follow Hooke's law but instead a nonlinear stress-strain behaviour, for example a hyperelastic one. A nonlinear viscosity means a non-Newtonian behaviour of the dashpot elements. Correspondingly, the viscosity η could be strain as well as strain rate dependent or follows an exponential correlation to the strain rate.

From an experimental point of view, nonlinear viscoelasticity is characterized by the deviation from linear creep isochrones, which is depicted in Figure 2.2 (b). At higher strains, geometrical nonlinearity becomes apparent, which additionally contribute to a nonlinear behaviour, but are not part of material nonlinearities. Geometrical nonlinearities result from higher-order terms in strain formulations and are included with the choice of nonlinear strain tensors, like the Green-Lagrange strain tensor. They can also be observed in linear viscoelastic models at higher strains.

The modelling of nonlinear viscoelasticity is, caused by its complexity, still subject to current investigation and development (WANG et al., 1992; MICHAELI et al., 2006; EFFIN-GER et al., 2014). For exmaple, MICHAELI et al. (2006) implemented an isotropic material model with transient adjustment of the damping coefficients at simultaneously constant Maxwell spring elasticities. The Zhou-Wang-Tan (ZWT) model (WANG et al., 1992) is able to capture nonlinearities with a nonlinear spring that additionally exhibits a quadratic dependence on the strain. The infinite modulus E_∞ and the dynamic moduli E_i are additionally temperature dependent.

Further integral formulations like a nonlinear extension of Equation (2.59) exist in SCHAPERY (1969). For commercial FE-solvers this material behaviour is mostly not fully functionally implemented and due to its complex parameter identification and model structure scarcely applied in engineering practice.

2.2.4 Time-Temperature Superposition

In order to determine the elastic and viscous parts of the stress-strain behaviour, the material is frequently subjected to sinusoidal loads, and a corresponding typical viscoelastic material answer is shown in Figure 2.5 (a). A material that behaves viscoelastic and is loaded with an oscillating sinusoidal displacement $s(t)$ or force $F(t)$ (curve a) reacts with a phase-delay (d), characterized by the phase angle δ.

The reaction can be split into an in-phase, instantaneous response (b) and a $90°$-shifted out-of-phase, viscous response (c). The elastic response is characterized by the storage modulus G', the viscous response by the loss modulus G''. Both properties are used to calculate the loss factor

$$\tan \delta = \frac{G''}{G'}, \tag{2.69}$$

which describes the viscously dissipated energy within the system. Both moduli are summarized to the complex modulus G^* by

$$G^* = G' + iG'' \qquad \text{and} \qquad |G^*| = \sqrt{G'^2 + G''^2}, \tag{2.70}$$

which is depicted in the complex number plane in Figure 2.5 (b). $\tan \delta$ changes with temperature and peak values are described as viscoelastic relaxation or transition points. The calculation of the moduli is given (SCHWARZL, 1990) with

$$G'(\omega) = G_\infty - \int_0^\infty g(\tau) \frac{1}{1 + \omega^2 \tau^2} \, d\tau \tag{2.71}$$

and

$$G''(\omega) = \int_0^\infty g(\tau) \frac{\omega \tau}{1 + \omega^2 \tau^2} \, d\tau, \tag{2.72}$$

where ω is the angular frequency, τ the relaxation time, and $g(\tau)$ is the relaxation spectrum. Formulation for discrete relaxation spectra leads to

$$G'(\omega) \approx G_\infty + \sum_{i=1}^n \frac{G_i \tau_i^2 \omega^2}{1 + \tau_i^2 \omega^2} = G_\infty + \sum_{i=1}^n \frac{G_i \omega^2}{\beta_i^2 + \omega^2} \tag{2.73}$$

(a)   (b)
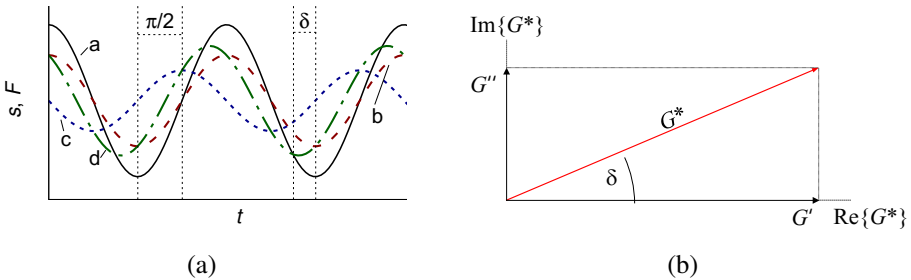
Figure 2.5 (a) Viscoelastic material response under cyclic loading. a: displacement; b: in-phase response; c: out-of-phase response; d: complex response. (b) moduli in the complex number plane.

and

$$G''(\omega) \approx \sum_{i=1}^{n} \frac{G_i \tau_i \omega}{1 + \tau_i^2 \omega^2} = \sum_{i=1}^{n} \frac{G_i \omega}{\beta_i + \omega^2 / \beta_i} \,. \tag{2.74}$$

The above relationships are utilized in dynamic mechanical analysis (DMA) in order to characterize viscoelastic material behaviour.

If a temperature change equals a shift of the relaxation curve of a material along the time axis to obtain a continuous connection of different isothermal relaxation curves, the material behaviour is referred to as thermorheologically simple. The resulting composite master curve can be used to describe the material over a wide range of frequency and time respectively. The shifts can be approached by different equations.

WILLIAMS et al. (1955) recognized a relationship between temperature and time for polymers that follows

$$\log a_{\mathrm{T}}(T, T_{\mathrm{ref}}) = -\frac{C_1(T - T_{\mathrm{ref}})}{C_2 + T - T_{\mathrm{ref}}}, \tag{2.75}$$

where a_T is the shift factor and T_{ref} is an arbitrary chosen reference temperature. C_1 and C_2 represent two material parameters that depend on T_{ref}. Further details about the WLF function are given in FERRY (1980). With the help of the WLF parameters, the logarithmic midpoint of the glass transition area can be estimated by using the relationship

$$\log t_{\mathrm{g}}(T) = 1.20 + \log a_T = C_0 + \frac{C_1 C_2}{T - T_\infty}, \tag{2.76}$$

where $C_0 = 1.20 - C_1(T_{\mathrm{softening}})$ and T_∞ is known as the Vogel temperature (VOGEL, 1921). $T_{\mathrm{softening}}$ refers to the midpoint of the glass transition area (SCHWARZL, 1990). The Vogel temperature is used in the VFTH or Vogel-Fulcher-Tammann (VFT) relationship, which describes the viscosity η of glassy materials as

$$\eta = \eta_0 \exp\left(\frac{-B}{T - T_\infty}\right), \tag{2.77}$$

where B is an activation energy related material parameter. The parameters of the VFT equation are connected to the WLF equation by $B = \ln(10)\, C_1 C_2$ and $T_\infty = T_{\mathrm{ref}} - C_2$. Both relationships are mathematically equivalent expressions. Under the presumption that no transformation within the material takes places, a further formulation, which is based on the Arrhenius kinematic is defined as

$$\log a_{\mathrm{T}}(T, T_{\mathrm{ref}}) = \frac{0.43 E_{\mathrm{A}}}{\bar{R}}\left(\frac{1}{T} - \frac{1}{T_{\mathrm{ref}}}\right). \tag{2.78}$$

This shift equation relates to secondary relaxation processes that are initiated by an activation energy and follow an Arrhenius kinematic. Here, E_A is the activation energy for the observed relaxation process and $\bar{R}$ represents the ideal gas constant.

Both approaches have approved to model the time-temperature shift of thermoplastic polymers. While the Arrhenius approach shows better results for the energy elastic area, the WLF Equation is more suitable for the entropy-elastic area. Alternatively, phenomenological approaches, like the arctan-approach (WOICKE et al., 2004), have been formulated and show likewise validity for certain materials and temperature areas. With the temperature dependent shift factor gained from Equations (2.75) and (2.78), the frequency shift governed by

$$\log a_T(T, T_{\text{ref}}) = \log \frac{\omega_{\text{ref}}}{\omega} \tag{2.79}$$

is used to obtain a so-called master curve for extrapolation to a wide range of frequencies. This master curve can then be further processed to obtain parameters for viscoelastic models and predict the material behaviour for a wide range of frequencies and temperatures and is a central tool for further analysis of viscoelastic material behaviour.

2.2.5 Numerical Treatment of Viscoelasticity

For spatial numerical calculations, stress is split according to Equation (2.26) into a deviatoric and a volumetric part. It is usually assumed that only the deviatoric part contributes to the viscoelastic behaviour (WRIGGERS, 2013). For the linear standard body of viscoelasticity (Table 2.2), corresponding strain measurements can be defined as shown in Figure 2.6.
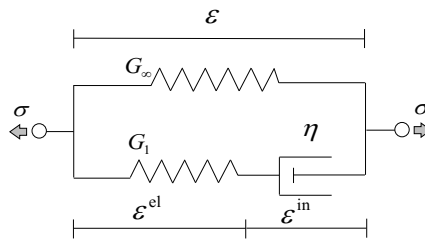
Figure 2.6 Standard body of viscoelasticity: strain definitions.

The stress can then be expressed by

$$\boldsymbol{\sigma}(t) = K \text{tr}\, \boldsymbol{\varepsilon} \mathbf{1} + 2G \left[(1 - \alpha)\bar{\boldsymbol{\varepsilon}} + \alpha \bar{\boldsymbol{\varepsilon}}^{\text{el}} \right]. \tag{2.80}$$

Here, **1** represents the unity tensor, the superscript "el" the elastic part of the Maxwell element. The superscript bar denotes the quantity's deviatoric part, α describes the ratio between the modulus of the infinite spring G_∞ and the spring of the Maxwell element G_1. Addition of both moduli yields G. The evolution of $\bar{\boldsymbol{\varepsilon}}$ is described by

$$\dot{\bar{\boldsymbol{\varepsilon}}}(t) = \frac{1}{\tau}\bar{\boldsymbol{\varepsilon}}^{\mathrm{el}} + \dot{\bar{\boldsymbol{\varepsilon}}}^{\mathrm{el}} = \beta\,\bar{\boldsymbol{\varepsilon}}^{\mathrm{el}} + \dot{\bar{\boldsymbol{\varepsilon}}}^{\mathrm{el}}, \tag{2.81}$$

where τ and β represent the dashpot parameters relaxation time and decay constant respectively. The stress at the end of a time step n+1 can then be obtained by conventional FE integration rules. With the Euler implicit algorithm this yields (WRIGGERS, 2013)

$$\boldsymbol{\sigma}_{n+1} = K\,\mathrm{tr}\,\boldsymbol{\varepsilon}_{n+1}\,\mathbf{1} + 2\,G\left[\left(1 - \alpha\frac{\Delta t}{\tau + \Delta t}\right)\bar{\boldsymbol{\varepsilon}}_{n+1} + \alpha\frac{\tau}{\tau + \Delta t}\left(\bar{\boldsymbol{\varepsilon}}_n^{\mathrm{el}} - \bar{\boldsymbol{\varepsilon}}_n\right)\right], \tag{2.82}$$

where Δt is the time step. In the present work, the explicit FE-solver LS-DYNA is used for computations. Here, the deviatoric co-rotated form of the viscoelastic stress rate is used and expressed by

$$\frac{\partial}{\partial t}\hat{\bar{\boldsymbol{\sigma}}}^{\mathrm{in}} = \sum_{i=1}^{n} 2G_i\hat{\bar{\boldsymbol{L}}} - \sum_{i=1}^{n} 2\beta_i G_i\int_0^t e^{-\beta_i(t-s)}\hat{\bar{\boldsymbol{L}}}(s)\mathrm{d}s, \tag{2.83}$$

where the circumflex stands for the co-rotated form and $\hat{\bar{\boldsymbol{L}}}$ for the deviatoric co-rotated rate of deformation. The co-rotated form is worthwhile for shell elements in order to achieve the vanishing of a normal stress through thickness. Time Integration of Equation (2.83) leads to the deviatoric co-rotated viscoelastic stress (LS-DYNA, 2016)

$$\hat{\bar{\boldsymbol{\sigma}}}^{\mathrm{in}} = \sum_{i=1}^{n} 2G_i\int_0^t e^{-\beta_i(t-s)}\hat{\bar{\boldsymbol{L}}}(s)\mathrm{d}s. \tag{2.84}$$

2.2.6 Thermoviscoelasticity

To describe thermal effects within a constitutive model, thermomechanical consistency has to be fulfilled by following the dissipation inequality

$$\gamma = \dot{s}(\vec{X},t) + \frac{1}{\rho_{\mathrm{ref}}}\mathrm{Div}\left(\frac{\vec{q}_{\mathrm{ref}}}{T}\right) - \frac{r}{T} \geq 0, \tag{2.85}$$

which is the second law of thermodynamics expressed by continuum mechanical variables and is also known as the Clausius-Duhem inequality. Here, $\dot{s}$ represents the entropy rate, ρ_{ref} the mass density in the reference configuration, and r the heat supply per unit mass. For a thermoelastic material the local energy balance leads to the Equation of heat conduction given in HAUPT (2002) with

$$c\dot{T} = T\frac{\partial^2\psi}{\partial T\partial\mathbf{E}}\,\dot{\mathbf{E}} - \frac{1}{\rho_{\text{ref}}}\operatorname{Div}\vec{q}_{\text{ref}} + r, \qquad (2.86)$$

where c represents the heat capacity at constant deformation, $\dot{T}$ the temperature rate, $\dot{\mathbf{E}}$ the time derivative of the Green-Lagrange strain tensor and $\vec{q}$ the heat flux vector. HAUPT (2002) identifies the term $T\dfrac{\partial^2\psi}{\partial T\partial\mathbf{E}}\,\dot{\mathbf{E}}$ as the part that represents the thermoelastic coupling effect. The free energy ψ, the stress $\mathbf{S}$, the entropy s, the heat flux vector $\vec{q}$ and the associated evolution equations are required in order to completely describe a thermomechanically consistent viscoelastic material behaviour (HAUPT, 2002). Additionally, the fulfillment of the dissipation inequality (2.85) leads to a stress relation

$$\frac{1}{\rho_{\text{ref}}}\mathbf{T} = \frac{\partial}{\partial\mathbf{E}}\psi(\mathbf{E}, T, q_1, ..., q_k) \qquad (2.87)$$

and an entropy relation

$$s = -\frac{\partial}{\partial T}\psi(\mathbf{E}, T, q_1, ..., q_k), \qquad (2.88)$$

where q_1 to q_k represent equilibrium solutions for certain states of strain and temperature. Both Equations (2.87) and (2.88) are the basis for the calculation of the thermomechanical stress-strain behaviour and the temperature for every state fulfilling Equation (2.85).

2.2.7 Adiabatic Heating

The work by TAYLOR et al. (1934) revealed for metals that a large part of plastic strain energy is converted into heat. This applies not only to metals but also to polymers, which behave in general viscoelastic, viscoplastic, or both. Viscoelastic material behaviour is characterized by a hysteresis loop, which indicates energy dissipation, while for plastic materials a remaining strain is caused by plastic dissipation. For calculating a heat flux and a resulting temperature rise of a body, the conversion of a certain amount of the plastic work into heat W is governed by

$$W = \xi\int\boldsymbol{\sigma} : \mathrm{d}\boldsymbol{\varepsilon}^{\text{pl}}, \qquad (2.89)$$

where $\boldsymbol{\sigma}$ is the stress and $\boldsymbol{\varepsilon}^{\text{pl}}$ stands for the plastic strain. ξ is referred to as the Quinney-Taylor parameter and is mostly assumed to be close to 1. However, ξ was found to vary significantly with strain and strain rate for metals (HODOWANY et al. (2000)) and polymers (RITTEL, 1999) likewise.

Furthermore, polymers show not only inelastic strains resulting from plasticity but also from a viscoelastic behaviour. To describe the heating process caused by dissipation of strain energy within the inelastic dashpots, a formulation of an inelastic strain energy density has to be performed. JOHNSON et al. (2005) investigated the viscoelastic heating of rubbers under high strains modelled with Maxwell elements. They set up a calculation model with the energy dissipation following

$$r(t) = \frac{(E^{\text{v}}\varepsilon^{\text{v}})^2}{\eta} = \frac{2\left(\frac{1}{2}E^{\text{v}}(\varepsilon^{\text{v}})^2\right)}{\eta/E^{\text{v}}} = \frac{2W^{\text{v}}}{\tau} = \frac{(\sigma^{\text{v}})^2}{E^{\text{v}}\tau} \geq 0 \tag{2.90}$$

where the superscript v stands for viscous or inelastic response. Following ANTOINE et al. (2015), the dissipated energy is calculated in a three-dimensional constitutive model with

$$r(t) = \sum_{k=1}^{m}\left(\frac{\beta_k}{2G_k}\boldsymbol{\sigma}_k^{\text{v}} : \boldsymbol{\sigma}_k^{\text{v}}\right), \tag{2.91}$$

where, according to general numerical formulations of viscoelasticity, only the deviatoric stress and strain parts contribute to viscoelastic overstress and, therefore, to the viscous dissipation. Plasticity, modelled with friction elements, and viscosity, modelled with dashpot elements, are the two main mechanisms of energy dissipation and thus thermomechanical heat generation. However, their experimental separation and quantitative determination are complex.

2.3 Materials and Laminated Setup

In what follows, an overview of the investigated materials PMMA and TPU regarding their chemical basis and production as well as their engineering applications, mechanical and thermal behaviour, and their combination in a laminate is presented.

2.3.1 Poly(methyl Methacrylate) (PMMA)

PMMA is an amorphous thermoplastic and together with PC a widespread glass substitution because of their very good optical properties and advantageous processing and production parameters. As a comparatively old plastic, PMMA has been the subject of numerous research and applications. First basic investigation was undertaken in the 19th

century already (FITTIG et al., 1877) but commercial production and application started in the 1930s. In particular, PMMA was used early for outdoor applications like signs or windows because of its good weatherability and optical properties. Already in the 1930s and 1940s, PMMA was frequently applied in aircraft glazing due to significant weight reduction and easy formability. Modern engineering applications are, amongst many others, ballistic protective eyewear (KELLY, 2001), aircraft canopies (ZHANG et al., 2015), or transparent building constructions (LEONHARDT et al., 1973).

In Germany, the development was decisively expedited by Otto Röhm, who established the trade name Plexiglas®, which today is marketed by Evonik Industries AG and Arkema. Other tradenames for PMMA are Acrylite® (Evonik Cyro LLC), Perspex® (Lucite International), or Oroglas® (Rohm and Haas). PMMA is frequently referred to as one of its trade names or as acrylic. An overview of some Plexiglas® materials is given in Table 2.3. In the present work, predominantly extruded Plexiglas® 8N was used for experiments.

Except the failure strain $\varepsilon_{\text{fail}}$, mechanical properties of conventional PMMA (H and N) show only slight variation in their mechanical properties. Nomenclature "H" of Table 2.3 stands for high-molecular material, which is used for extrusion molding, while "N" represents low-molecular material, typically used for injection molding. Most mechanical properties vary only subordinately, whereas some thermal properties, like the softening temperature, show higher deviations. Plexiglas® Resist AG100 refers to an impact modified PMMA with significantly higher energy absorption potential and prolonged failure strains. When impact modified, which is performed by adding rubbery components to the mixture, the elastic modulus E is usually reduced significantly. Comparison to other works is difficult when materials are provided by different companies. Within these companies, further PMMA mixtures exist that may deviate decisively from the PMMA used in the present investigation.

Chemical Structure

Conventional PMMA is created by radical polymerization of methyl methacrylate (MMA) with a suitable initiator, which results in an atactic and amorphous structure. The amorphous structure of PMMA is caused by the bulky molecular components that prevent

Table 2.3 Plexiglas® material properties according to their data sheets.

	6N	7N	8N	7H	8H	Resist AG100
ρ [kg/m³]	1190	1190	1190	1190	1190	1160
E [N/mm²]	3200	3200	3300	3200	3300	2200
$\varepsilon_{\text{fail}}$ [-]	0.03	0.035	0.055	0.055	0.055	0.45
α [10^{-6}/K]	80	80	80	80	80	110

crystallization (OGORKIEWICZ, 1970), which leads to a highly transparent thermoplastic. With special catalyses it is also possible to create either isotactic or syndiotactic PMMA (SCHWARZL, 1990, p.79). The standardized name according to the International Union of Pure and Applied Chemistry (IUPAC) is Poly(methyl 2-methylpropenate), its chemical basis unit is shown Figure 2.7 (a).

The nuclear composition, tacticity and its structure determine the material behaviour. The average length of the polymer chains is determined by pressure, temperature and duration of the polymerization process. According to SCHWARZL (1990, p.84), the single polymers chains of amorphous polymers show entanglement, as sketched in Figure 2.7 (b), but no chemical bonding. The thermoplastic behaviour is accompanied by effects like complete thermoformability and crack healing above T_g.

(a)   (b)

Figure 2.7   (a) repeating unit of MMA ($CH_2 = C(CH_3)COOCH_3$); (b) molecular structure of PMMA.

Thermomechanical Properties

The elastic modulus of conventional PMMA in literature ranges between 3000 MPa (LIU et al., 2009) and 3400 MPa (CHAUDHRI, 2004), while Poisson's ratio is usually located between 0.3 and 0.4. Elasticity and Poisson's ratio show rate- and temperature dependence, which are effects of the viscoelastic character of polymers. The strain linearity limit, until which linear elasticity shows validity, is at around 0.6 % (OGORKIEWICZ, 1970). Above this limit PMMA exhibits nonlinear characteristics, like strain softening and tension-compression asymmetry (BUCKLEY et al., 1995).

Under impact, PMMA with a typical non-ballistic window thickness of a few millimeters, shows brittle behaviour and impact energy is mainly absorbed due to the generation of cracks. In contrary, PC offers huge potential of energy absorption due to high plasticity. Applications as transparent armors are frequent because of a high specific impact performance (RADIN et al., 1988) in which case the typical thickness is above 10 mm (HSIEH et al., 2004). Here, local plasticity plays a major role caused by a decisive three-dimensional stress state. In compressive load cases, PMMA is capable of performing high plastic strains with significant heating of the material (RITTEL et al., 2000).

Changes in the molecular structure at certain temperature areas lead to significant variation of the material behaviour. These areas are defined as relaxation areas or temperatures respectively. The α-relaxation of PMMA, generally associated with the glass transition temperature T_g, is located around $110\,^\circ$C (IONITA et al., 2015; SWALLOWE et al., 2003). It stems from rotations of MMA molecules and molecular chains leading to the most significant relaxation effect, whereas other relaxations refer to more localized rotations or movement of side-chains.

It is widely recognized that the β-relaxation occurs due to intramolecular methyl ester side group (COOR) rotations around the CC bond (TETSUTANI et al., 1982; HAWARD, 2012). While the β-relaxation occurs roughly around room temperature (SCHWARZL, 1990), its exact value shows noticeable scattering in literature. This is caused by a merging of α- and β-relaxation (HAWARD, 2012), which is also referred to as cooperative $\alpha\beta$-relaxation (IONITA et al., 2015; DIONÍSIO et al., 2000). At small temperatures, additional γ- and δ-relaxation areas were observed (DE DEUS et al., 2004).

Thermal Properties

At room temperature, the thermal conductivity k of PMMA is $0.19\,$W/(m K), the heat capacity c $1500\,$J/(kg K) and the thermal diffusivity χ $0.108\,$mm^2/s (SCHWARZL, 1990). Generally, the thermal conductivity for amorphous polymers shows a high dependence on temperature at small temperatures and a maximum around the glass transition temperature, after which the conductivity decreases. In this area, a significant change in heat capacity occurs, which is utilized in the calorimetric determination of the glass transition area.

Optical Properties

Transmissivity in the visible electromagnetic spectrum is important for the use in transparent applications and is provided by the amorphous structure of PMMA. At wavelengths above the visible light, the transmissivity decreases rapidly. Absorption in the near wave infrared (NWIR)-area is mainly based on the absorption bands of hydrogen-oscillations (DOMININGHAUS, 1975, p.238). The CO-group of the esters causes absorption bands at $2.1\,\mu$m to $2.3\,\mu$m, while the CH$_{3-}$ and CH$_{2-}$ show various absorption bands within in the NWIR area (DOMININGHAUS, 1975, p.238). Following DOMININGHAUS (1975, p.193) further, conventional PMMA products vary insignificantly in their absorption bands.

At a thickness above 1 mm, PMMA changes its transmissive behaviour to highly absorbing in the mid wave infrared (MWIR) and long wave infrared (LWIR) area. Therefore, it can be subjected to infrared (IR) surface temperature measurements. The refractive index n for PMMA, which is with approximately 1.492 (DOMININGHAUS, 1975, p. 195) close to that of soda lime-silica glass, shows only a small dependence on the incident angle up to $50\,^\circ$.

Fracture and Failure

The theoretical tensile strength of PMMA, which is calculated based on the separation of planes on an atomic level, is given in KINLOCH (2013) with 300 MPa. Generally, the theoretical tensile strength σ_{theo} required to separate two planes can be expressed as a function of the plane distance a_0 in

$$\sigma_{\text{theo}} = \sqrt{\frac{E\gamma_0}{a_0}}, \tag{2.92}$$

where E is the elastic modulus and the intrinsic fracture energy γ_0 can be considered as a threshold energy for the creation of new surfaces and, consequently, cracks.

Due to imperfections, the real tensile strength is generally about one to two decades below the theoretical value. KINLOCH (2013) gives the tensile strength with 50 MPa, OGORKIEWICZ (1970) the failure stress with 74 MPa. In a conventional thickness of a few millimeters, the failure of PMMA is brittle and the qualitative behaviour appears to be somewhat insensitive to thickness variations (KINLOCH, 2013). Compared to other glassy polymers like PC, plasticity plays a minor and more localized role under tensile loadings. The transition whether a glassy polymer behaves brittle or ductile, is determined by the competition between crazing (damage) and shear bands (yield) (ESTEVEZ et al., 2000).

Crazing can be seen as the initiator for cracks (FAN et al., 2015), while shear yielding causes ductility (KINLOCH, 2013; ESTEVEZ et al., 2000). Crack propagation velocity is limited by the sound velocity (2750 m/s; CARLSON et al., 2003), but is actually significantly below that value (600 m/s to 800 m/s in CHAUDHRI, 2004 and 715 m/s in LIU et al., 2009). Above a critical propagation velocity $c_c \approx 0.4 c_R$, where c_R is the Rayleigh wave speed, a distinct change in the crack propagation behaviour is observed. Above this limit, cracks become instrinsically unstable and frustrated microbranching occurs (FINEBERG et al., 2003).

The critical fracture energy G_{IC} was found to depend significantly on the crack velocity (KINLOCH, 2013). The critical crack opening displacement δ_{tc}, however, appears to be constant for a wide temperature range (KINLOCH, 2013). Though the tensile region of PMMA appears to be macroscopically dominated by elastic respectively viscoelastic behaviour, concentrated plasticity occurs around the crack tips (KINLOCH, 2013). A typical microscopic image of the crack edges of a splinter is given in Figure 2.8 (c).

Fabrication and Processing

Conventional PMMA is mostly extruded or formed by casting or injection molding. According to HAGAN et al. (1961), molded specimens exhibit a higher influence of the molecular orientation than extruded ones. However, glassy polymers are not as strongly dependent on fabrication methods than other polymer groups (KINLOCH, 2013). After forming

of the basic geometry, specimens are usually machined out of plain material with a given thickness. Alternatively, specimens can be gained by laser- or waterjet-cutting.

While machining shows higher mechanical loading at the edges, laser cutting bears high temperature-induced loads on the cutting edges. Both processes may contribute to preliminary stress that can influence stress-strain behaviour as well as the fracture process. Figure 2.8 show the edges of PMMA specimens for dart impact tests. Images were taken with a light-optical microscope. Specimens are viewed from the side with an angle of $60°$ and have a thickness of 3 mm. The machined specimen edge, depicted in Figure 2.8 (a), shows a significantly higher surface roughness, whereas the laser cut edge (Figure 2.8 b) shows a smooth surface because of the melting of the material. In the course of the present work, both types of processed specimens were subject to investigation and compared eventually.

Influence of Conditioning and Environment

Different peripheral media may lead to a significant change in mechanical behaviour. Although PMMA exhibits a high resistance against a number of chemicals, some influences remain. One known effect is the stress-solvent crazing, which is induced by the stress-state combined with a solvent like alocohols or ketones (OGORKIEWICZ, 1970). Another effect is the absorption of water. HAMOUDA (2002) found a significant increase of the impact resistance as well as an increase of admissible deformation in tensile test for commercial PMMA with increasing moisture. BURCHILL (1989) correlated a reduction of the yield strength of 10 MPa to each per cent absorbed water. He found that the maximum mass percent absorption of water was at 0.8% after conditioning up to 45 days. Absorption of water leads to a reduction of the glass transition temperature T_g presumably due to hydrogen bonding to the carbonyl groups as stated by HAMOUDA (2002).

According to the data sheet of Plexiglas® XT (EVONIK INDUSTRIES AG, 2008), water absorption for a 24 hour conditioning at $23°C$, as regulated in DIN EN ISO 62 (2008), leads to a mass related percentage of water absorption of 0.48 %. Concluding, water absorption effects of environmental humidity are of minor importance compared to polymers like polyamide (PA), which has humidity absorption in the magnitude of 9 % off mass (PATERSON et al., 1992).

| (a) | (b) | (c) |
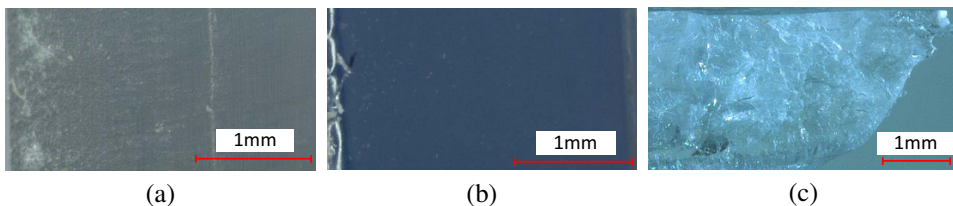
Figure 2.8 PMMA: surface after (a) machining and (b) laser cutting. (c) Microscopic view of splinter.

2.3.2 Thermoplastic Polyurethane (TPU)

TPU is a polymer with a two-phase microstructure, which combines the properties of rubbers and plastics. In the present work, only the interlayer form will be considered, which is delivered in extruded roll forms as shown in Figure 2.9 (a). Specimens are then conventionally generated by die cutting, which is depicted in Figure 2.9 (b).

In terms of laminated safety glass and comparable substitutes, the popular interlayer materials are the standard safety glass interlayer PVB as well TPU, and poly(ethylene-vinyl acetate) (PEVA), frequently referred to as ethylene-vinyl acetate (EVA). Every interlayer material can be modified for special application and are available in various thicknesses. A comparison between and classification of different interlayer materials can be found in KUNTSCHE (2015). TPUs are, due to their two-phase microstructure, increasingly used as interlayer materials for laminated structures. Besides the ability of performing very high strains, further main characteristics are viscoelastic behaviour, high abrasive resistance and easy formability. Furthermore, it exhibits good adhesion in laminates (XIBAO et al., 2014; HOESS et al., 2016) within a broad temperature range for engineering applications (XIBAO et al., 2014).

In order to combine the properties of elastomers and thermoplastics, first commercial production of TPU materials began in the 1950s in Germany and the United States of America. Trade names for TPU are, amongst others, Desmopan® (Bayer MaterialScience AG / Covestro AG), Elastollan® (BASF Polyurethanes GmbH), or Krystalflex® (Huntsman). The product name of the TPU investigated in the present work is Elastollan® L785 A10 and was provided by BASF Polyurethanes GmbH.

Chemical Basis

TPU belongs to the group of thermoplastic elastomer (TPE), and is created by the polyaddition of di- and polyols with diisocyanates. This is performed by the linkage between the short-chained diols and long-chained polyols by a PU unit, which is illustrated in

(a)   (b)
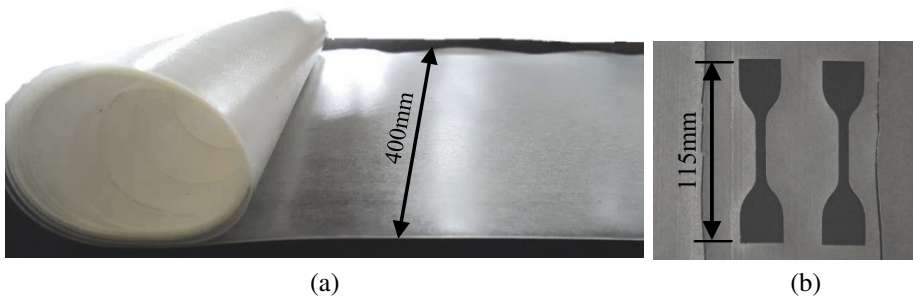
Figure 2.9   TPU: (a) Interlayer in rolled form. (b) Specimen extraction by die cutting.

Figure 2.10. Therefore, it can also be referred to as a block copolymer. The chemical difference and incompatibility of the single components lead to a two-phase microstructure of hard and soft segments, which is sketched in Figure 2.10. Here, sidled, pointed and continuous lines represent the residues of long-chain diols, short-chain diols and diisocyanate respectively, while the urethane group is depicted by points. The combination of isocyanates with the short-chained diols forms the hard segments, while the soft segment is caused by the polyester (COO) part. Hard segments tend to form ordered hard domains, while the soft segments represent the amorphous part (QI et al., 2005). Depending on the ratio of the domains, phase separation may not be perfect and for TPUs with a low hard segment part, hard segments may be isolated within soft domains (ESTES et al., 1971).

Short- and long-chain diols exhibit different areas for energy- and entropy elasticity, which is used for modification of material properties like the glass transition temperature T_g by variation of their compound ratio. T_g shifts with a higher amorphous part (soft segments) to a lower T_g and simultaneously narrows the transition temperature range (BASF POLYURETHANES GMBH, 2011). The hard segment shows generally glass transition temperatures above typical operating temperature (YI et al., 2006).

Elastollan L785 A10, in particular, is an aliphatic polyester-based TPU, with a hard segment part of 38 % and a shore hardness of 85. According to HOESS et al. (2016), it is based on polycaprolactone (PCL) as polyol, 1,4-butanediol as chain lengtheners and dicyclohexylmethane-diisocyanate ($H_{12}MDI$). Additionally, the material is combined with anti-oxidants, hydrolysis-, and UV-stabilizers. Creation of the final product is performed by extrusion with cylindrical or lenticular granules. The resulting product shows very good optical properties caused by its comparatively high amorphous parts.

Mechanical behaviour

The general behaviour of TPU is governed by strong viscoelastic behaviour, nonlinearities, hysteresis and softening (QI et al., 2005). It is, furthermore, referred to as highly flexible and elastic, resistant to abrasion and impact, and with good weatherability (YI et al., 2006). Representative mechanical properties regarding engineering values are summarized in Table 2.4. These properties show a dependence on various parameters, which
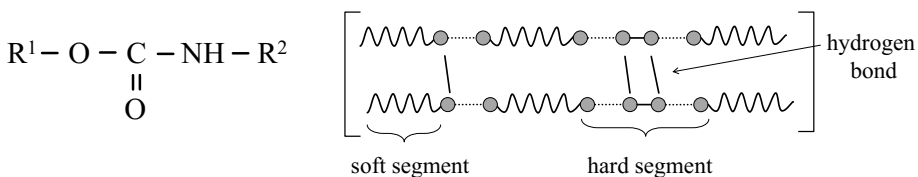
Figure 2.10 TPU: (a) basis unit (b) structure (BASF POLYURETHANES GMBH, 2011, QI et al., 2005).

are, amongst others, the processing condition and type as well as temperature, moisture content and pre-experimental conditioning. Furthermore, a huge variation in mechanical response can be reached by additives.

The TPU investigated in the present work is designed for good mechanical properties and chemical resistance. A comparatively high failure strain and tensile strength as well as good damping properties are its distinguishing characteristics. TPU shows high resistance against hydrolysis, which makes it less sensitive to environmental influences than other interlayer materials like PVB.

ZHANG et al. (2015) states that for laminated structures the bonding strength between PMMA, PVB and PC is weak, especially at low temperatures. That is why TPU interlayers are more frequently used in some applications, which is reported to have remarkably good adhesive properties (HOESS et al., 2016) in combination with PMMA. The surface contour of certain TPU interlayer is still visible in laminated specimens after cracking of the PMMA plies. This enables to estimate the extend of delamination by the clearly distinguishable surface of delaminated and laminated TPU.

Table 2.4 Properties of Elastollan® L785 A10 according to BASF POLYURETHANES GMBH (2013).

density ρ	eng. failure strain $\varepsilon_{0,\text{fail}}$	tensile strength σ_{ts}
1180 kg/m³	7.0	45 MPa
σ_0 at ε_0=0.1	σ_0 at ε_0=1.0	σ_0 at ε_0=3.0
3.5 MPa	6.0 MPa	11.0 MPa

Influence of Conditioning and Loading History

Comparable interlayer materials like PVB or EVA show a significant influence of moisture content. According to the producer, this effect is of subordinate importance for TPU. Following KHAJEHSAEID et al. (2014), the Mullins' effect (MULLINS et al., 1957 and related works) occurs for most elastomers, which is still subject to investigation and remains not fully understood (QI et al., 2005). The Mullins' effect leads to a softening of the equilibrium stress-strain curve with every load cycle. QI et al. (2005) and BUCKLEY et al. (2010) found occurrence of the Mullins' effect for TPU materials and proposed a modelling technique with a deformation history variable. After several loading cycles a curve is reached that does not significantly deviate from the previous curves, which they refer to as the stabilized test curve.

It is important to notice, that the lamination process using an autoclave may change the interlayer material behaviour significantly. A permanent altering of the material at higher temperatures, as observed by MACALONEY et al. (2007) for various TPUs between 60 °C and 100 °C, is immanent of the autoclave process. However, a reproducible method for

separation of an interlayer from the laminate plies without altering respectively damaging the interlayer is a sophisticated task. Therefore, testing of the final interlayer material after the lamination process can hardly be performed in a reproducible way. Consequently, the interlayer investigated in the present work is tested using the "virgin" supply state.

2.3.3 PMMA-TPU Laminate

Polymeric laminates are conventionally used in the aviation (WANG et al., 2010) and for ballistic protection (KELLY, 2001). These laminates mostly consist of multiple layers that consist of glass, PMMA, PC, and different interlayer material in various arrangements. In the automotive industry, car side widows are made of TSG and the windshields of LSG for the most part. A direct replacement of these windows with amorphous polymers is not directly possible. Conventional PMMA will show too brittle behaviour in a crash situation and, moreover, tends to fail into bigger fragments than TSG with hazardous potential for occupants and pedestrians. In order to counter this, impact modified PMMA is used with a hardcoating layer for an improved scratch resistance.

However, an impact-modified PMMA shows increased strength, which possibly conflicts requirements like emergency breakage. This modifies the mechanical properties of the impact modified material to a partly unknown extent. Moreover, the windshield is an integral part of automobiles that contributes to the torsion stiffness of the vehicle, which would be clearly decreased by polymers because of smaller elastic moduli. Therefore, substitution of vehicular windshields is currently not at disposition, whereas replacement of glass side windows with polymers appears to be a reasonable midterm aim for the automotive industry.

Combinations of PMMA and TPU to a laminated structure leads to a synergetic effect of their characteristics. The result is a comparatively stiff laminate with a distinct post-breakage behaviour and a huge potential for impact energy absorption. Without claim of correct crack representation, the principle behaviour under impact is shown in Figure 2.11. In the case of failure of one or more of the PMMA layers, the high failure strain of TPU allows significant deformation with the adhered PMMA splinters. Moreover, wedging of PMMA splinters that are adhered to the TPU layer are thought to increase the post-breakage stiffness by tilting. The adhesive bonding reduces injury risks by preventing splinters from loosening from the structure.

Inhomogeneous laminates, like PMMA-PC (STENZLER et al., 2011) or PMMA-glass structures (PATEL et al., 2006), lead to heterogeneous thermal expansion, which has to be overcome by the interlayer. PATEL et al. (2006) states for transparencies of armored vehicles that a thick additional layer acts as a crack propagation barrier. With increasing thickness of such interlayers differences of thermal expansion can be neutralized more effectively. Compared to inhomogeneous multi-material laminates, a PMMA-interlayer-

PMMA laminate exhibits less potential for internal stress due to different coefficients of thermal expansion (HOESS et al., 2009).

TPU shows to be very suitable as an interlayer material and is finding increased application in this function (ZHANG et al., 2015). When combining TPU between two PMMA plies, different purposes are fulfilled. PMMA gives the compound its basic elasticity as well as using its good weatherability and scratching resistance which may be further improved by hardcoating. However, PMMA exhibits brittle failure behaviour with only small failure strains and tensile dominated load cases. In the case of an impact, the TPU layer overcomes these disadvantages. Its ability of performing huge strains, which are located significantly above 100 %, increases the impact performance of the laminate significantly.

In the present work, the PMMA products Plexiglas® 8N or Plexiglas® 7H were investigated that showed only small differences in mechanical properties but enabled a huge variety of specimen forms. For the sake of completeness, Tables A.1 and A.2 in the Appendix give an overview of which material was used in each experiment. A non-symmetric structure with two PMMA plates of 2.0 mm and 1.5 mm adhered by a 0.5 mm TPU interlayer was used for experiments of the present work. The thicker PMMA ply was always the side subjected to impact.

intact   cracked   post-breakage
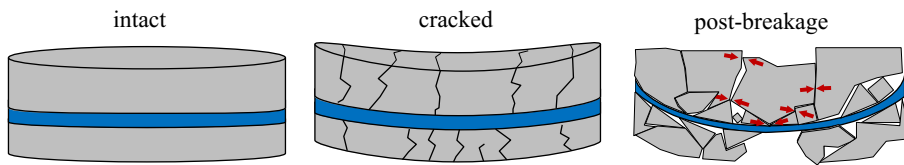
**Figure 2.11**   Principle load carriage of laminate.

Production

Following HOESS et al. (2009), the production of the laminate is performed by hot pressing of two PMMA layers with the TPU layer in between. The press temperature is given with 80 °C to 140 °C with a heating time from 30 to 60 seconds. The applied pressure can vary between 10 kN to 100 kN for a time range between 20 to 60 seconds. Alternatively, the laminate can be produced by coextrusion, which is currently under development with promising results for the mechanical behaviour compared to its laminated counter-part (HOESS et al., 2016). With coextrusion, the automated production becomes significantly simplified because lamination processes can be omitted.

The good adhesion between PMMA and TPU is realized by a number of cumulated effects inherent of the TPU interlayer (PIZZI et al., 2003): Besides a wetting of hydrogen bonding to a substrate's surface, the small-sized molecules can permeate into porous sub-

strates. Furthermore, covalent bondings are formed to the adhesion partner, which creates a strongly adhered laminate.

The laminate of the present work is not attached with any hardcoating and all experiments refer to the material treated in the previous chapters. Photographs of the laminate are given in Figure 2.12. The non-symmetric structure is clearly visible in Figure 2.12 (b), where the upper side has a thickness of 2.0 mm. An exemplary specimen after dart impact testing with total failure is depicted in Figure 2.12 (b). The localized failure and the adherent PMMA splinters can be observed.


(a)   (b)
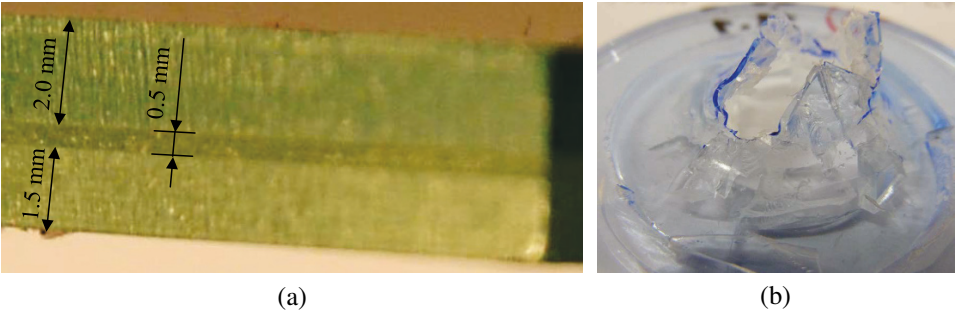
Figure 2.12 PMMA-TPU laminate: (a) Structure of the laminate investigated in the present work. (b) Failed laminate after impact.

3 Experimental Investigation

The following sections present experimental results regarding the mechanical and thermal material behaviour of PMMA, TPU, and both materials combined in a laminated setup. Experiments were chosen in order to cover a wide range of tensile dominated load cases. Sections are arranged according to materials. The experimental setup is always described the first time it appears, to which in subsequent sections is referred to. General experimental procedures, like the specimen treatment or frequently used methods like the DIC or IR thermography, are given beforehand.

Thermal properties were investigated using the transient plane source (TPS) method in order to provide basic characteristics. The link between temperature and time dependence for both materials was examined with DMTA experiments, which were used to determine the glass transition temperature T_g, parameters for the time-temperature superposition, and a master-curve. The mechanical behaviour of PMMA and TPU was subjected to uniaxial and biaxial (only TPU) tensile tests for basic characteristics. For PMMA and the PMMA-TPU laminate, three-point bending (TPB) tests (Sections 3.2.4) and dart impact tests (Section 3.2.5) were conducted at different velocities and temperatures. Figure 3.1 gives an approximate overview of the triaxiality factors roughly covered by the experiments of the present work. Here, the slope of every stress state is given by the triaxiality factor from Equation (2.31).
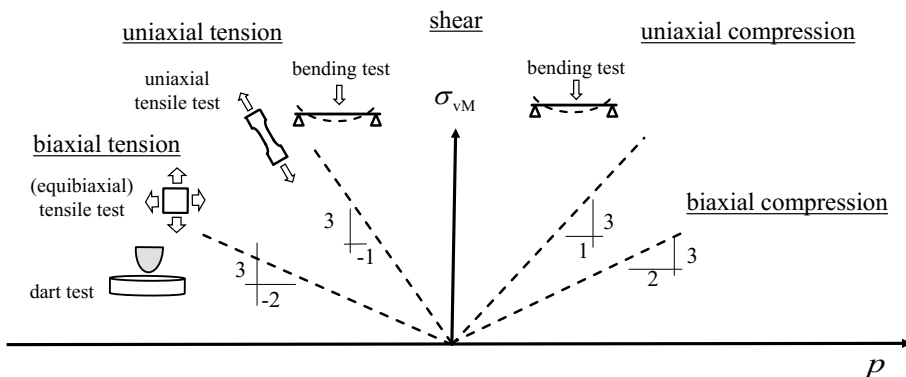
Figure 3.1   Stress states in experiments depicted in the Burzyński-plane.

3.1 General Experimental Procedures

3.1.1 Specimen Preparation

The general specimen preparation is documented subsequently. Experimental procedures that used different specimen preparations are explicitly marked in the corresponding section. An overview of the materials used in the experiments is given in Table A.1 of the Appendix.

PMMA

PMMA (Plexiglas® 8N or 7H) specimens were provided by Evonik Industries AG. The final specimen geometries were created by machining or laser cutting from extruded plates of approximately 300 mm edge length. Specimens were taken at a minimum distance of approximately 10 mm from the edges to reduce inhomogeneities from production. After processing, specimens were conditioned between 80 °C to 90 °C, which is about 80 % of the glass transition temperature for PMMA for at least one day to facilitate relaxation processes and reduce possible internal stress resulting from production and processing.

TPU

TPU specimens (Elastollan® L785 A10) were provided by BASF Polyurethanes GmbH. Tensile geometries were extracted by die cutting in extrusion direction ($0°$) at the centre position of a 86 mm width roll with a thickness of 0.35 mm and 0.50 mm respectively. Air humidity absorption is of minor importance for TPU as it is for example for PVB. Therefore, no additional measures to regulate the air humidity were undertaken. It has to be noted that all monolithic experiments were conducted with virgin materials, which means no conditioning, preloading, or heat treatment – except otherwise stated – was performed. This may be particularly important because of the known occurrence of Mullins' effect (QI et al., 2005) and entropy-related effects (MACALONEY et al., 2007), which result in an altering of the mechanical behaviour. Tensile specimens were additionally prepared with a spray pattern for DIC evaluation. Preliminary measurements exhibited no influence of the spray pattern on the mechanical behaviour.

PMMA-TPU Laminate

Specimens for all tests were provided by Evonik Industries AG. The production was performed by adhering two PMMA plates with a TPU interlayer using an autoclave. Detailed information regarding the production of these laminates can be found in Section 2.3.3 as well as HOESS et al. (2009) and HOESS et al. (2016). Laminated specimens were stored for at least one day inside a climate chamber at 60 °C to facilitate relaxation effects. Higher temperatures were not applied because of possible hazard to the laminate's adhesion. In

order to limit the extent of the present work, only one structure was investigated for all shown experiments, which is a PMMA-TPU-PMMA combination with a corresponding 2.0 mm- 0.5 mm-1.5 mm thickness. The 2.0 mm ply was always the side subjected to impact, except stated otherwise. The thickness of the specimens varied within the range 4.0 mm ±0.1 mm.

3.1.2 Digital Image Correlation

Evaluation of the testing machine data like the crosshead movement and the calculation of engineering strain and stress data is not sufficient to describe the local material behavior. At small strains, an evaluation of engineering values using traverse displacement can be trustworthy to some extent, but the influence of „parasitic deformations" (BAUWENS-CROWET et al., 1969), like the machine's stiffness, can still not be extinguished. Since optical measurement methods like extensometer and DIC for local strain evaluation have become frequently applied, these influences can be reduced. For the local evaluation of strains, the DIC method was used in the present work.

The general setup of two cameras and the corresponding illumination is shown in Figure 3.2 (a). The DIC uses an algorithm that calculates the relative movement of a pattern of the facets, which enables to correlate to the surface strain of a specimen. The specimens are prepared with a black-white spray pattern as shown in Figure 3.2 (b). Size, shape and overlapping of the facets (Figure 3.2 c) have to be chosen according to the size of spray pattern in order to capture the facet's characteristics. This way, the strain field for each image taken can be measured and visualized (Figure 3.2 d).

In the present work, an Aramis system from the company Gesellschaft für Optische Messtechnik (GOM) (GOM ARAMIS, 2013) is used for the strain and deformation evaluation of uniaxial, biaxial, and bending tests. Further information about the DIC can be found in WINTER (1993).
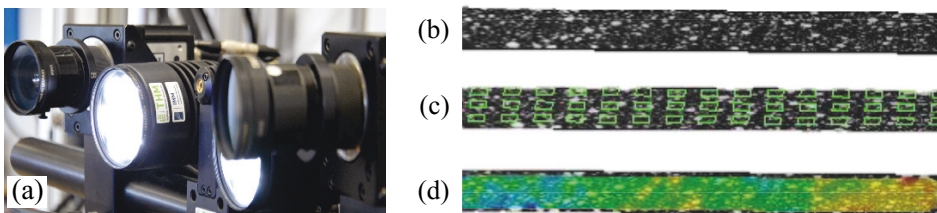
Figure 3.2 3D-GOM Aramis measurement system (left) and principle of DIC (right).

3.1.3 Infrared Surface Temperature Measurements

For test evaluation, an emissivity ε=0.9 was chosen for PMMA and TPU for every thickness, which is a typical value for plastic materials. The remaining 0.1 are assumed to be composed of transmitted and reflected blackbody radiation with an average ambient temperature of 23 °C. IR measurements were performed using the highspeed IR camera ImageIR 5325 from the company Infratec GmbH. The camera operates in the MWIR area (3.7 µm to 4.8 µm) and is able to reach a frame rate of 1600 Hz at a resolution of 80x64 IR pixels at an integration of 480 µm. Using this calibration time, the camera was calibrated to an uncertainty of ±1 K or ±1 % in the temperature range from 0 °C to 80 °C.

The assumption of ε=0.9 appears to be reasonable for PMMA considering the transmissivity spectrum given in Figure 3.3. However, the same assumption for TPU may exhibit greater potential for errors in measurement. Preliminary experiments revealed some transparency of the material at a thickness of 0.35 mm. Furthermore, the thickness decreases with high strains, which leads to more transparency of the material. No measurements of the transmissivity of the interlayer were performed in the course of the present work. Therefore, the model of Figure 3.3 was used for emissivity assumptions.

Uniaxial tensile test specimens were prepared with the black-white spray paint used for the DIC evaluation, which is assumed to have high emissivity values. The other side, which was filmed by the IR-camera remained untreated. Therefore, the electromagnetic radiation reaching the IR-detector array is a mixture of predominantly TPU material, the spray paint at direct contact with the TPU, as well as some remaining ambient radiation through the effect of remaining transmissivity. As the electromagnetic radiation travels through the specimen with the temperature T_1 it is continuously absorbed, which leads to a decrease in transmissivity. Another part of the radiation is absorbed by the paint with the temperature T_2 applied on the opposite side to the IR detector. Radiation, which is not absorbed by the TPU or the paint is assumed to be 10 % (ε=0.9). This value may be
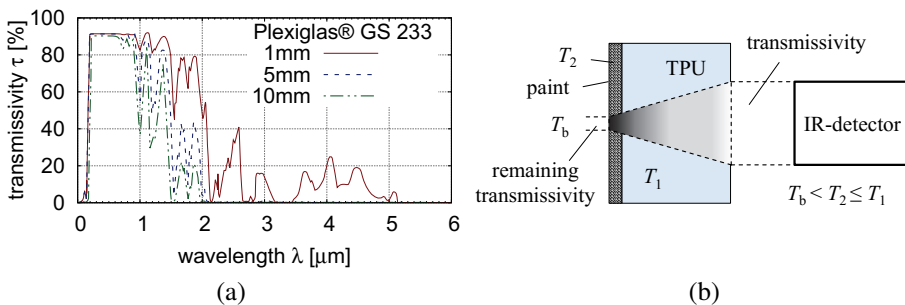
Figure 3.3 PMMA: (a) Electromagnetic transmissivity of PMMA, data from Evonik Industries AG (unpublished). (b) Transmissivity model for TPU specimens spray pattern on back.

adjusted when further transmissivity measurements were undertaken and new results can be obtained by a linear scaling with a new ε.

This way, it is ensured that the test setup is reproducible with the named possible error sources included, but for every test to the same extent. Consequently, IR measurements are not primarily meant to cover the total amount of temperature rise but to determine the minimum temperature rise because of the radiation mixture with the cooler background temperature T_b.

3.1.4 Sensors and Signal Processing

Different sensors were used for the variety of experiments. Mostly, these sensors were inherent of the instrumented experimental setup and required no further adjustment except for regular calibration. The sensors of the drop tower consist of a photocell for the triggering of data acquisition and the measurement of initial or impact velocity and a strain-gauge sensor to acquire tup forces. The strain gauge is placed above the tup. For the *4a* Impetus pendulum system, different acceleration sensors up to 200 g were available that have increasing absolute uncertainties with increasing maximum measurable acceleration. Where possible, these different sensor types were compared by preliminary testing and showed very high agreement.

For most dynamic experiments, determination of the initial contact point had to be processed manually. Experiments were processed automatically with a developed subroutine. Therein, an average value of the first 600 neutral values (no contact to specimen) was subtracted from the force signal to determine the zero force signal. Data acquisition rates for all signals varied between 200 kHz and 2000 kHz, depending on the haul-off speed. High-speed photography was performed for the dart tests in order to interpret the force-displacement behaviour. The high-speed camera's synchronization signal was recorded by the same transient recorder that was used for the strain gauge and trigger signal measurement in order to assign every frame the corresponding time and force point.

Naturally, dynamic experiments undergo oscillations induced by the impact, which can be seen in the upcoming experiments using the instrumented drop weight tower and the *4a* Impetus pendulum system. Similar magnitudes of oscillations can be seen in PEARSON et al. (2007) and TEKALUR et al. (2010). No uniform approach exists for handling these oscillations, for example by filtering the signal. When filters are applied it is immanent to carefully examine any change in quantity and quality of the signal. Therefore, filters were scarcely applied on the results of the present work, and are always mentioned explicitly.

3.2 Experimental Investigation of PMMA

3.2.1 Transient Plane Source Method Experiments

Temperature dependent thermal properties for PMMA are already published in numerous works. However, properties for PMMA products of different producers may vary significantly. Furthermore, for the use in numerical simulations, discrete values obtained directly from experiments at different temperatures will increase the accuracy of the results. For the determination of the thermal conductivity k and heat capacity c, the TPS method (GUSTAFSSON, 1991) was applied according to DIN EN ISO 22007-1 (2012). The used machine was a TPS 1500 from the company HotDisk AB. The experimental setup is shown in Figure 3.4.

The Hot Disk method is composed of a combined sensor and heat source that is based on a Wheatstone bridge. From the sensor's temperature increase it is possible to determine the thermal conductivity k, the volumetric heat c_{vol}, and the thermal diffusivity κ (GUSTAVSSON et al., 1994) of the specimens. These specimens are assumed to be infinite in their dimensions, so that a limit of measurement in terms of duration and heating power is given by specimen geometries as soon as the boundaries interact with the measurement. The ideal probing depth Δ_p is given in GUSTAVSSON et al. (1994) with

$$\Delta_p = 2\sqrt{\kappa t}, \tag{3.1}$$

with t representing time and the thermal diffusivity κ given by

$$\kappa = \frac{k}{\rho c}, \tag{3.2}$$

which contains the three major thermal properties: thermal conductivity k, mass density ρ, and heat capacity c. Further details can be found in HOT DISK (2015). The TPS-sensor was positioned between two quadratic PMMA specimens with an edge length of 250 mm

(a)   (b)

Figure 3.4 TPS experimental setup: (a) Setup with climate chamber. (b) Measurement of PMMA.

and of 25 mm (specimen a) thickness. A second specimen geometry with 100 mm edge length and 20 mm thickness (specimen b) was used for counter-checking the results. To create a defined contact pressure between the sensor and the specimens, an additional defined steel mass of 5 kg was applied on top. The setup was positioned in a climate chamber and measurements were performed between -50 °C and 130 °C in 10 °C temperature steps. Every temperature step included eight to fourteen measurements with a waiting period of 120 min to 180 min between each measurement to ensure thermal equilibrium.

Results of the thermal conductivity k are depicted in Figure 3.5 (a). They show very high reproducibility for every temperature. k increases steadily with temperature until reaching the area of the glass transition temperature, where a decrease with temperature is measured. The measurements reveal that k varies only slightly for the investigated temperature range with the lowest and highest average values determined with 0.1889 W/(m K) at -50 °C and 0.2244 W/(m K) at 90 °C. The determined values for k show close agreement to data from KNAPPE et al. (1969) and Evonik Industries, which is published in RÜHL et al. (2016).

The heat capacity is obtained by multiplying the volumetric heat capacity c_{vol} with the density ρ of the material. The density was calculated as a function of temperature under the assumption of a constant isotropic linear coefficient of thermal expansion $\alpha = 80 \cdot 10^{-6}$ 1/K. Assuming isotropy, a multiplication by three for the spatial consideration approaches the volumetric coefficient of thermal expansion to be $\alpha_{\mathrm{vol}} = 240 \cdot 10^{-6}$ 1/K. Calculations for the heat capacity are shown in Figure 3.5 (b) and show good reproducibility for every temperature, with a steady increase from 1135.39 J/(kg K) at -50 °C and 2201.15 J/(kg K) at 130 °C, which corresponds to an increase of 94 %. In comparison to earlier measurements by Evonik Industries, published in RÜHL et al. (2016), the obtained experiments are in very good agreement. A further investigation of the calorimetric behaviour exhibits a significant increase of the tangent between 100 °C and 120 °C, which corresponds well to the general glass transition temperature at approximately $T_{\mathrm{g}} = 117$ °C (EVONIK INDUSTRIES AG, 2015).
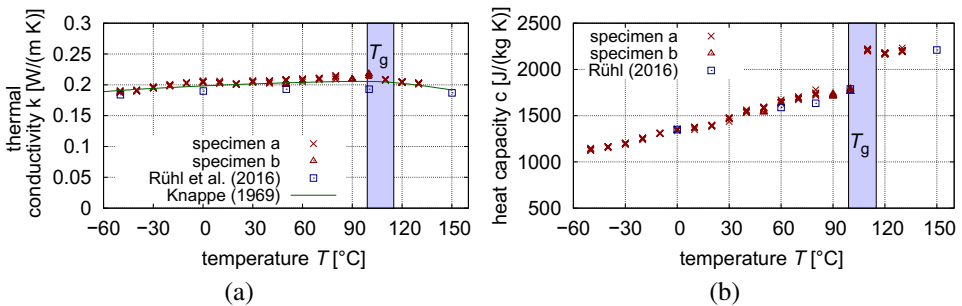

Figure 3.5 PMMA: (a) Thermal conductivity. (b) Heat capacity.

3.2.2 Dynamic Mechanical Thermal Analysis

DMTA experiments are based on regulations DIN EN ISO 6721-1 (2011) and ASTM D4065 (2012) and were conducted with the machine DMA/SDTA 861, which is produced by the company Mettler Toledo (Figure 3.6 a). Cooling was performed by liquid nitrogen. Experiments with the bulk material PMMA are usually conducted in tensile or bending experimental setups (IONITA et al., 2015) with frequencies below resonance. All experiments regarding PMMA were conducted in a three-point bending setup, which is depicted in Figure 3.6 (b). The specimen is visible in the centre of the photography between the support on both sides and the centred oscillating tup. Temperatures shown in the upcoming graphs, represent values that were obtained with the temperature sensor recognizable by a small metallic wire at the left support. Values obtained by bending tests represent a flexural elastic modulus E_f, which is a mixture of tensile and compressive elastic modulus. A difference between both moduli is typical for polymers, also referred to as compression-tension asymmetry, and some deviation to the tensile elastic modulus can be expected. Assuming small strains without rate effects, the flexural elastic modulus E_f is obtained by

$$E_f = \frac{4l^3 F}{sbt^3},$$
(3.3)

where l is the free length, F the measured load, s, b and t the displacement, the specimen width and thickness respectively. A beam with the geometry l=60 mm, b=10 mm, and t=3 mm was found to have an adequate geometry factor. DMTA bending tests require a preload to ensure no sign-change in bending direction. Preliminary tests revealed that the preload required to conduct the experiments had to be chosen carefully. Too small preloads led to a wrong calculation of the storage and loss modulus, too high preloads yielded nonlinear deformations of the specimen. Final parameters for the conducted tests are summarized in the appendix in Table A.4.

(a)   (b)   (c)
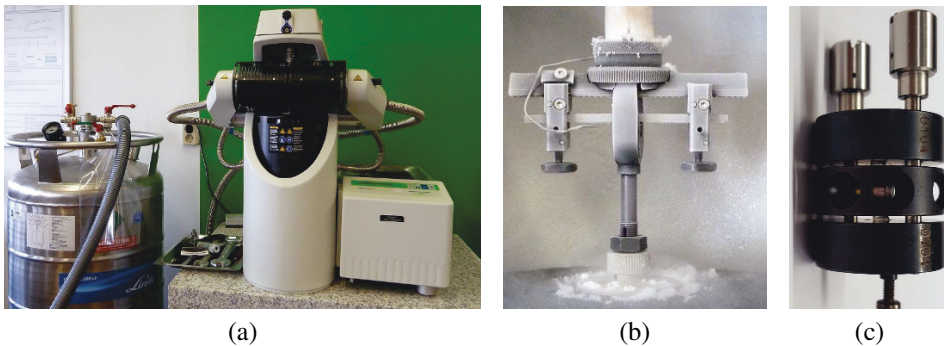
Figure 3.6   (a) DMA/SDTA 861. (b) Bending setup after nitrogen-cooling. (c) Double-shearing setup.

3.2.2.1 Reproducibility

The trustworthiness of the results are affirmed by comparison of different tests with the same setup. Figure 3.7 shows results for three temperature sweeps for PMMA with the same setup. Results for the storage modulus E' (a) and the loss modulus E'' (b) showed good reproducibility below the glass transition temperature, which affirms the validity of the bending tests for this area. Temperatures above the glass transition resulted in higher deviations.
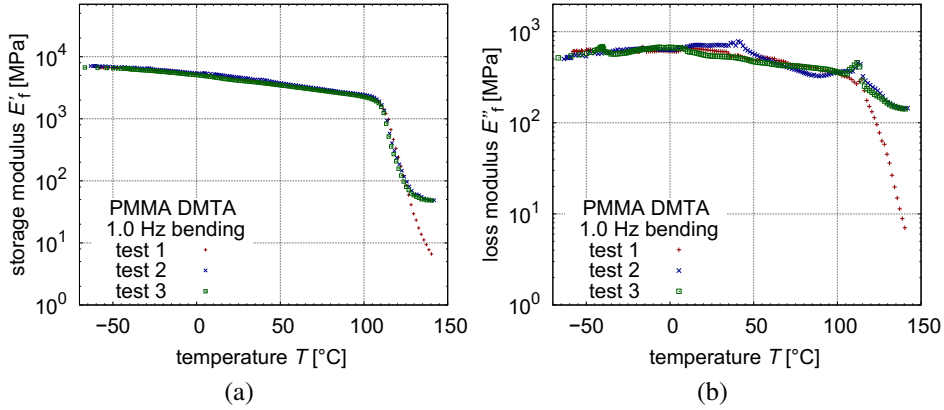

Figure 3.7 PMMA: reproducibility of DMTA test. (a) Storage modulus E'. (b) Loss modulus E''.

3.2.2.2 Temperature Sweep and Relaxation Processes

In a temperature sweep, the bending oscillation is performed at a constant frequency, usually 1.0 Hz, while the temperature changes. The temperature range was between -60 °C and 150 °C, to cover primary and secondary relaxation processes. Figure 3.8 shows the results of a temperature sweep on PMMA at 1.0 Hz. PMMA shows a high storage modulus, which decreases only slightly at low temperatures. When reaching the α-relaxation (glass transition) area E' and E'' show a sudden drop. The loss factor tan δ is approximately 0.1 until 100 °C. A clear maximum is observed at 130.3 °C. Different approaches for obtaining the glass transition temperature are given in DIN EN 6032 (2016). Using the T_g-onset method, the glass transition temperature was located at 108.5 °C. Other methods for the glass transition temperature evaluation are shown in Table 3.1 compared to results from IONITA et al. (2015).

Values for onset and max tan δ show close agreement to results from IONITA et al. (2015). β-relaxations are visible for the test 1.0 Hz temperature sweep between 0 °C and 10 °C. According to IONITA et al. (2015) they occur in the temperature region between -43 °C and 33 °C and according to KINLOCH (2013) around room temperature. For a more
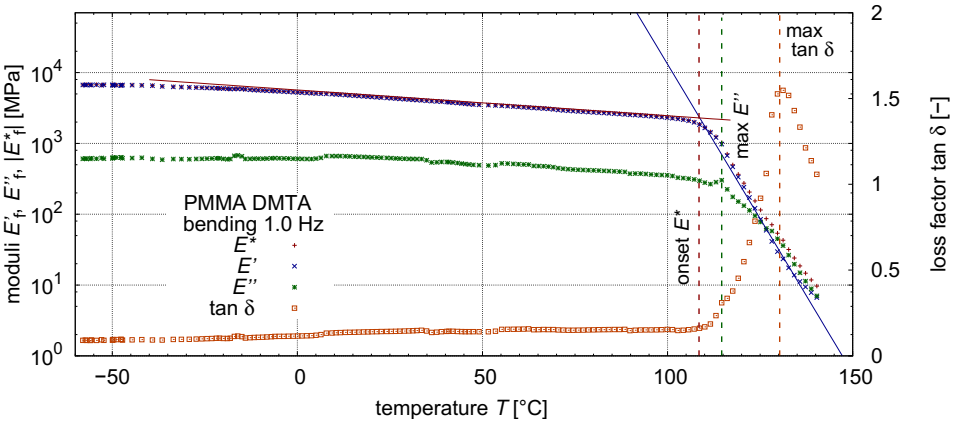
Figure 3.8   PMMA: DMTA. Temperature sweep at 1 Hz.

accurate determination of a β-relaxation reference temperature, results of temperature-frequency sweeps are discussed in the subsequent section.

Table 3.1   PMMA: DMTA. Glass transition temperatures.

source DIN EN 6032	onset $|E^*|$ T_{g} onset	E''_{peak}	max tan δ T_{g} peak
present work[a]	108.5 °C	114.6 °C	130.3 °C
MULLIKEN et al. (2006)[b]		114.9 °C	
IONITA et al. (2015)[a]	109.4 °C	111.4 °C	128.7 °C

[a] bending setup
[b] compressive setup

3.2.2.3   Temperature-Frequency Sweep and Master Curve

Figure 3.9 shows the result of a temperature-frequency sweep from -100 °C to 165 °C and 0.01 Hz to 100 Hz. Glassy and rubbery areas as well as the glass-rubbery-transition area are well visible. Isothermals at 0.01 Hz and 100 Hz are plotted to show the frequency induced shift of elasticity. Higher values for E_{f} are observed at higher frequencies due to higher overstress portions. The bending setup, in particular, appeared to be susceptible for inertia effects, and higher frequency parts were partially removed from the evaluation eventually.

The glass transition area is clearly visible for every frequency between approximately 100 °C and 115 °C. T_{g} increases slightly with increasing frequency, which corresponds to findings of IONITA et al. (2015), but appears to be of subordinate influence. Focus was set
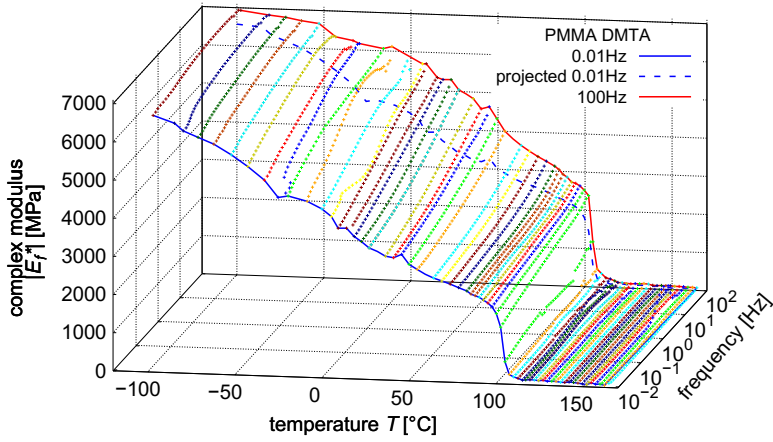
Figure 3.9 PMMA: DMTA data used for the master curve generation.

on the temperature range from small temperature until $60\,^{\circ}\text{C}$, which covers most technical applications of PMMA as glass substitutions. Therefore, the glass transition temperature will not be treated extensively, but the β-relaxation occurring around room temperature was central in this investigation. The Arrhenius shift approach, given in Equation (2.78), was applied for a master curve generation below glass transition T_g. At and above T_g, the WLF approach, given in Equation (2.75), shows to be a good approximation (BUCKLEY et al., 1995).

For the generation of a master-curve, thermorheological simplicity is assumed henceforth, although deviations were observed (PEREZ et al., 1999). Using the time-temperature superposition, the isothermal raw data curves in Figure 3.10 (a) are shifted within the frequency area to form the master curve for PMMA in Figure 3.10 (b). Solid red lines represent the manual shift process, while the blue dashed line depicts a shift using the Arrhenius approach with a beta-relaxation activation energy taken from IONITA et al. (2015). The shift factors are depicted in Figure 3.10 (c), compared to calculated values using Equation (2.78). The corresponding parameters are given in Table 3.2.

The Arrhenius approach is, according to its recommended application area, used for a shift in the secondary dispersion area only and, therefore, the according apparent activation energy E_A is used. "Apparent" signalizes that the value may deviate from the real, molecular-level β-relaxation because of different effects like mixture with other relaxation areas (IONITA et al., 2015, PEREZ et al., 1999).

Figure 3.10 (c) shows the manually determined shift factors compared to the Arrhenius fit using β-relaxation activation energies E_A from different authors. It is apparent that the Arrhenius shift approach from Equation (2.78) is able to reproduce experimental data well
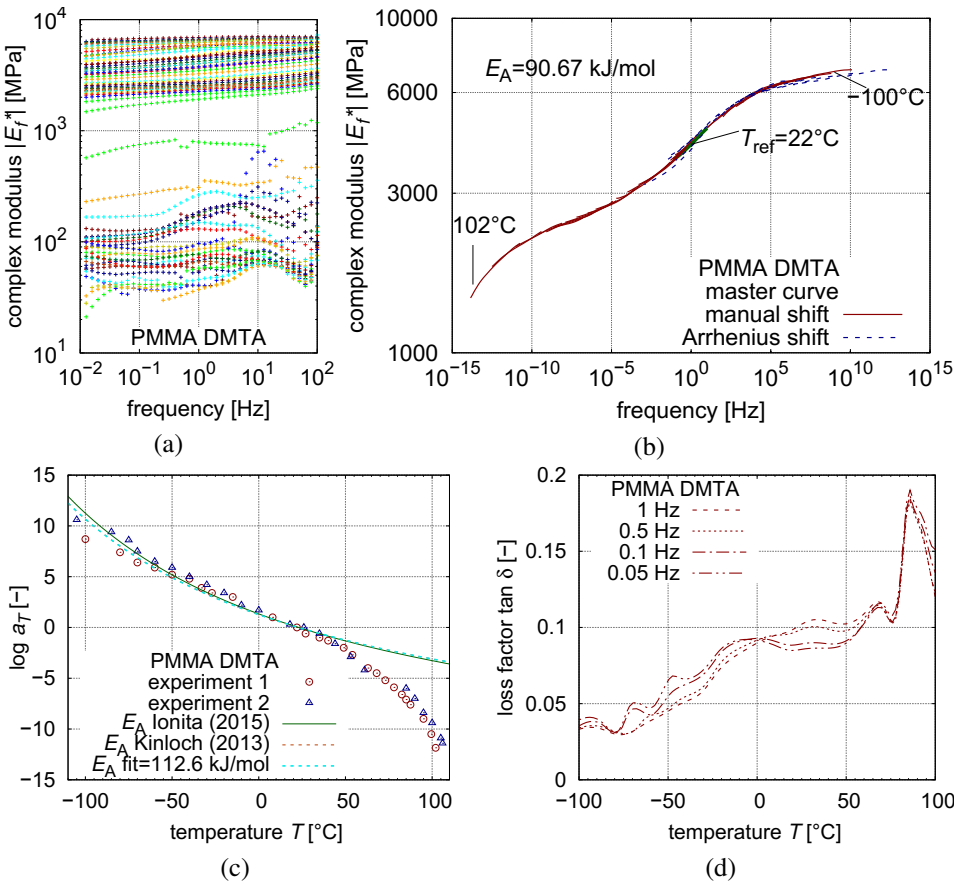
Figure 3.10 PMMA: DMTA. Master curve generation. (a) Raw data for master curve. (b) Manually shifted isothermal curves compared to an Arrhenius shift. (c) Shift factors compared to literature values. (d) β-relaxation in multifrequency plot.

Table 3.2 PMMA: Arrhenius shift parameters for (apparent) β-relaxation.

author	T_{ref} [°C]	E_A [kJ/mol]
KINLOCH (2013)		86
IONITA et al. (2015)		90.67
GARWE et al. (1996)		74
present work	22.0	112.6 (fitting value)

for low temperatures up to approximately $50\,°\text{C}$. Above this temperature, experimental data deviates from the Arrhenius shape. As shown in Figure 3.10 (d), form and position of

apparent α- and β-relaxations, marked by curve-crossing, correspond to experiments of IONITA et al. (2015). An overview of β-relaxation values for PMMA is given in Table 3.3.

Table 3.3 PMMA: β-relaxation temperatures.

source	E''_{peak}	max tan δ
present work[a]		5.0 °C
MULLIKEN et al. (2006)[b]	14.9 °C	
IONITA et al. (2015)[a]	7.0 °C	11.2 °C

[a] bending setup
[b] compressive setup

3.2.2.4 Determination of Viscoelastic Parameters

The master curve from Figure 3.10 can be used to obtain parameters for viscoelastic rheological models. Because of the cross-linked molecular structure a generalized Maxwell model with a time-temperature independent elastic spring was chosen. According to Equations (2.73) and (2.74), the parameters of the generalized Maxwell model can be obtained by summation of the storage and loss moduli and a concluding complex addition of both parts according to Equation (2.70).
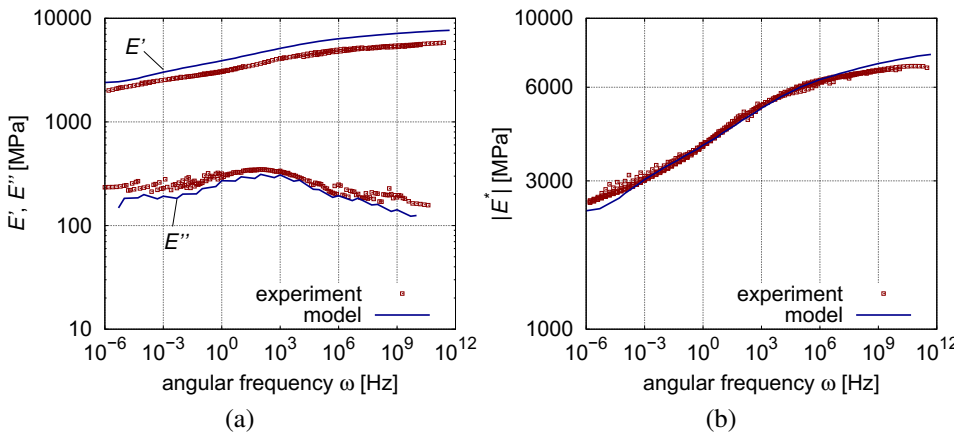
Figure 3.11 PMMA: viscoelastic parameter identification. (a) Storage modulus E' and loss modulus E''. (b) Complex modulus $|E^*|$.

For an accurate modelling of a wide spectrum of relevant frequencies, typically one Maxwell element per decade is sufficient (KUNTSCHE, 2015). The relaxation time τ was fixed at every decade, so that only the moduli had to be determined. Figure 3.11 (a)

shows the shifted portions of E' and E'' for the master curve from Figure 3.10 compared to their corresponding relaxation approaches. Model and experiment show a high correlation for E', E'', and $|E^*|$ and the material behaviour can be approached for a wide range of frequencies. The obtained Maxwell model is used henceforth in Section 4.1 for the numerical simulation of PMMA. The corresponding parameters can be found in Table A.5 of Appendix A.3.
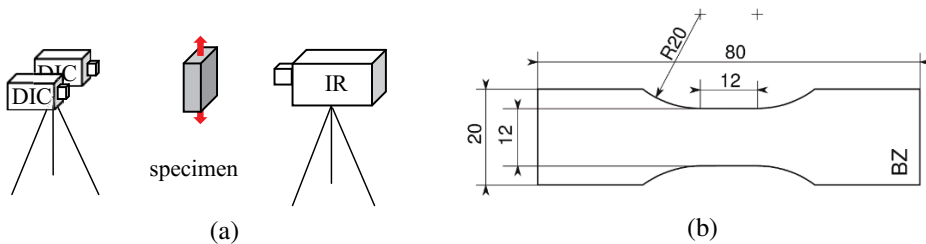
3.2.3 Uniaxial Tensile Tests

Tensile tests procedures are regulated in the ASTM standard ASTM D638 - 02A (2003), DIN EN ISO 527 - 1 (2012), and DIN EN ISO 527 - 2 (2012). Dynamic tensile tests were performed on a servo-hydraulic Zwick Roell HTM, quasi-static experiments on a servo-electric testing machine.

Initially, short-time relaxation tests at 1.0 mm/min and 5.0 mm/min were performed to determine overstress portions at quasi-static experimental velocities. Dynamic uniaxial tensile tests were then conducted at velocities of 1.0 mm/min, 0.1 m/s, 1.0 m/s, and 3.0 m/s at the German Institute for Polymers (DKI), Darmstadt. Experiments were performed with the specimen geometry "BZ", developed by BECKER (2009), which is shown in Figure 3.12 (b). The test configuration with DIC and IR measurements is shown in Figure 3.12 (a). The experiments were evaluated using the DIC for the determination of the true stress-strain behaviour and for one test series additionally with an IR camera for the measurement of adiabatic heating.

Figure 3.13 shows the results of the tensile test depicted in (a) with the true stress-strain behaviour, in (b) with the development of the strain rate, in (c) the results of the optical measurements for Poisson's ratio and in (d) results of strain-relief tests in order to approximate the equilibrium curve. Experiments in Figure 3.13 (a), (b) and (c) are evaluated according to their true stress-strain behaviour, as defined in Equation (2.36). The relaxation behaviour in Figure 3.13 is discussed with engineering values. The subjects elastic modulus E, strain-rate dependence, failure, development of strain rate $\dot{\varepsilon}$, Poisson's ratio ν, and equilibrium stress are discussed subsequently.

Figure 3.12 Tensile tests. (a) Experimental setup. (b) Geometry of BZ specimen (BECKER, 2009).
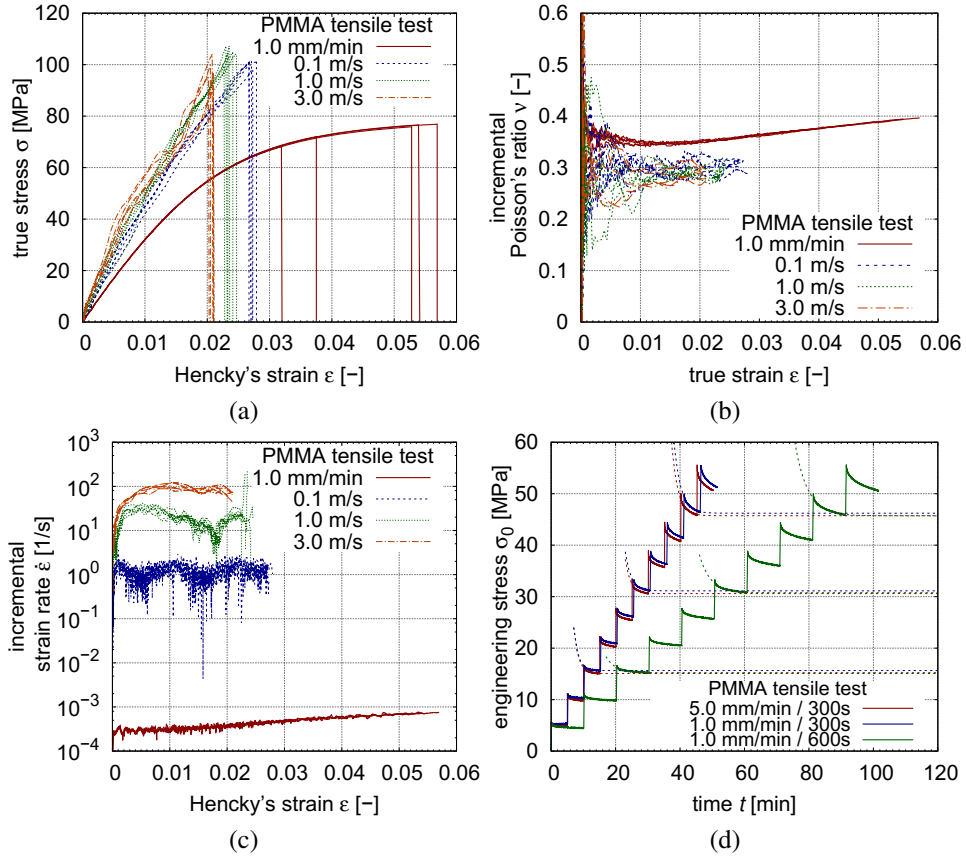
Figure 3.13 PMMA: uniaxial tensile tests. (a) True stress-strain behaviour. (b) Poisson's ratio. (c) Strain rate development. (d) Short-time relaxation behaviour.

Stress-Strain Behaviour and Elastic Modulus

The true stress-strain behaviour shows a distinct viscoelastic behaviour with a nearly linear slope in stress until failure for the dynamic tests. For the test at 1.0 mm/min, a strong nonlinear behaviour could be observed with increasing strain. Due to small overall strains in the experiment, the isochoric evaluation with Equation (2.35) leads to almost identical results in the stress-strain behaviour. Also, the difference between true and engineering strains is marginal for small values. Therefore, all three stress-strain evaluation methods from Section 2.1.2 show no major deviations.

With strain limits between ε=0.05 % and 0.5 % an elastic modulus of 3323.78 ± 6.6 MPa was obtained. This values ranges within the spread of values in literature, which are for example 3000 MPa (LIU et al., 2009), 3240 MPa (SONG et al., 2008), 3300 MPa (GRELL-

MANN et al., 2015), or 3400 MPa (CHAUDHRI, 2004). As per the producer, E of PLEX-IGLAS® 8N is located at 3300 MPa (Table 2.3, PLEXIGLAS® 8N). Detailed results of the experiments are given in Appendix A.4.

Material Failure

Failure was defined as the local force maximum, after which the force drops to 20 % of the maximum. An overview of the average failure stress and strain is given in Table 3.4. Failure points are depicted in Figure 3.13 as vertical lines. The average true failure strain at 1.0 mm/min is determined with 0.0471, the average true failure stress with 73.96 MPa. Very similar, OGORKIEWICZ (1970) specifies the failure stress of PMMA at 74 MPa. The quasi-static failure strain shows a significantly higher standard deviation than the failure stress. All dynamic tests show a failure stress at 100 MPa with standard deviations of a few per cent. Failure strains are significantly decreased compared to the experiments at 1.0 mm/min but also show less scattering. This shows two characteristics of the material: First, the uniaxial failure point of PMMA is dependent on the experiment velocity respectively the corresponding strain rate. An increase in strain rate leads to a decrease in failure strain. For higher strain rates, the true failure stress settles at around 100 MPa. Secondly, the scattering of the failure strain is distinctly higher for the quasi-static test than for the dynamic tests.

In the experiment at 1.0 mm/min, temperature changes below 1 °C were measured with surface IR surveillance. After failure, the breaking edges revealed increased temperatures, but a quantitative determination was not performed because of high uncertainties. Tensile tests at different haul-off velocities were also conducted by CHEN et al. (2002) and WU et al. (2004). CHEN et al. (2002) showed similar failure strains (3 % to 5 %), nonlinear behaviour at small strain rates. A high agreement to experimental results from WU et al. (2004) could be observed for dynamic tensile tests.

Table 3.4 PMMA: uniaxial tensile tests. Average true failure values with standard deviations.

test	strain rate at failure $\dot{\varepsilon}_{fail}$ [1/s]	failure stress σ_{fail} [MPa]	failure strain ε_{fail} [-]
1.0 mm/min	$6.4 \cdot 10^{-4}$	73.96 ± 3.68	0.0471 ± 0.0114
0.1 m/s	1.0	100.70 ± 1.15	0.0272 ± 0.0004
1.0 m/s	20.0	103.54 ± 3.03	0.0234 ± 0.0008
3.0 m/s	70.0	97.89 ± 4.92	0.0208 ± 0.0003

Strain Rate

Figure 3.13 (b) illustrates the development of the incremental strain rate based on true strain values as a function of true strain. In this section, the incremental true strain rate

is referred to as strain rate for convenience. All experiments show a small area at the beginning that is required to obtain a stable strain rate. After that, the experiments at 0.1 m/s, 1.0 m/s, and 3.0 m/s have nearly constant average strain rates of approximately 1 /s, 20 /s, and 70 /s. The 1.0 mm/min experiment shows a slight increase in strain rate and simultaneously the best reproducibility compared to the other velocities. This behaviour corresponds to the nonlinear stress-strain behaviour from Figure 3.13 (a) and is caused by localization effects.

All experiments at 1.0 m/s showed a strain rate between 20 /s and 30 /s until a true strain of approximately 1.7 %, where a decreases in strain rate to values below 10 /s occurs, followed by an increase in strain rate to the previous strain rate level. Experiments at 0.1 m/s and 3.0 m/s show a comparatively constant strain rate development. Concluding for all velocities, the strain rate remains around their engineering value, and effects of decrease in strain rate due to specimen prolongation can be neglected because of small true strains.

Poisson's Ratio

Poisson's ratio of PMMA is depicted in Figure 3.13 (c) as a function of strain for different experiment velocities and revealed as strain rate dependent. For the quasi-static test, Poisson's ratio ranges between 0.35 and 0.40. An average value by neglecting values at very small strains (< 0.001) was calculated with 0.36. This agree wells to values from literature that give Poisson's ratio generally between 0.3 and 0.4 (LIU et al., 2009; SONG et al., 2008; CHAUDHRI, 2004). With increasing experiment velocity Poisson's ratio decreases to values of 0.32 (0.1 m/s), 0.29 (1.0 m/s), and 0.26 (3.0 m/s) because of the increasing glass-like behaviour. This corresponds to general finding for amorphous polymers in BUCKLEY et al. (1995) as the material approaches a more glassy behaviour with higher strain rates.

Equilibrium Stress Condition

Figure 3.13 (d) shows the engineering stress in a stress-relaxation test for two different velocities (1.0 mm/min and 5.0 mm/min) with a stepwise increase of load and holding times of 300 s and 600 s. Exponential functions of the form

$$\sigma_0(t) = A + e^{B(t-C)} , \tag{3.4}$$

where A, B and C are fitting parameters were determined in a least-square fit with the data of the relaxation curves to approach the relaxation behaviour. The resulting relaxation approaches are depicted in dashed lines.

Portions of overstress can be observed at both experiment velocities, although these are often referred to as quasi-static. For both velocities, the overstress dissipated within the

holding times was between 6 % to 9 % for 1.0 mm/min and 9 % to 10 % for 5.0 mm/min. The long-time relaxation behaviour can not be investigated by these short holding times. It is, however, sufficient to take into account the longest relaxation processes taking place in experiments subjected in the experiments of the present work, which are deformations times of a few milliseconds to a few minutes.

Under the assumption that the relaxation curves continue to be governed by this exponential behaviour at higher relaxation times, the overstress occurring in experiments at conventional quasi-static strain rates is around 10 % of the total stress for PMMA. However, the elastic modulus E obtained from experiments at 1.0 mm/min will be seen as the equilibrium "infinite" elastic modulus E_∞, following the conventional evaluation practice. Yet, overstress and the corresponding relaxation still has a remarkable share of the overall stress.

3.2.4 Three-Point Bending Tests

Three-Point bending tests were conducted according to German regulation DIN EN ISO 178 (2013) and are subsequently referred to as bending tests for simplicity. Bending tests were to investigated the combined uniaxial tensile and compressive behaviour of the material. Specimens had a thickness of t=3 mm and a width of b=10 mm. Specimen length l and support distance varied between 35 mm to 50 mm and 45 mm to 60 mm, respectively. These values were adjusted to reduce oscillations as well as increasing the range of strain rates for later processing in material characterization.

Test velocities were 5.0 mm/min and 500.0 mm/min as well as the three dynamic velocities 1.0 m/s, 2.5 m/s, and 4.0 m/s. The former tests were performed on a servo-electric testing machine from *Hegewald & Peschke*, latter ones with the *4a* pendulum system. Both

(a)   (b)
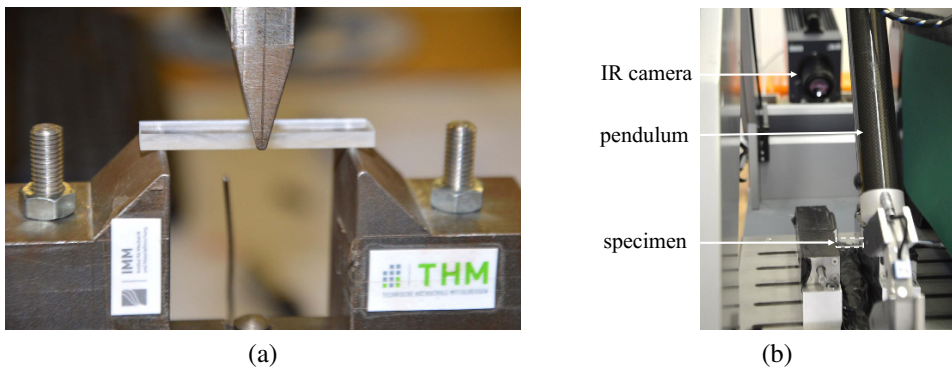
Figure 3.14 PMMA: bending tests. (a) Quasi-static experiments. (b) Dynamic experiments with the *4a* Impetus pendulum system.

Table 3.5 PMMA: bending tests. Experiment velocities and corresponding strain rates.

test velocity	support distance l_b [mm]	specimen length l [mm]	initial strain rate $\dot{\varepsilon}$ [1/s]
5.0 mm/min	50	60	$2.0 \cdot 10^{-3}$
500.0 mm/min	50	60	0.20
1.0 m/s	50	60	24.00
2.5 m/s	35	45	122.45
3.0 m/s	30	40	266.67
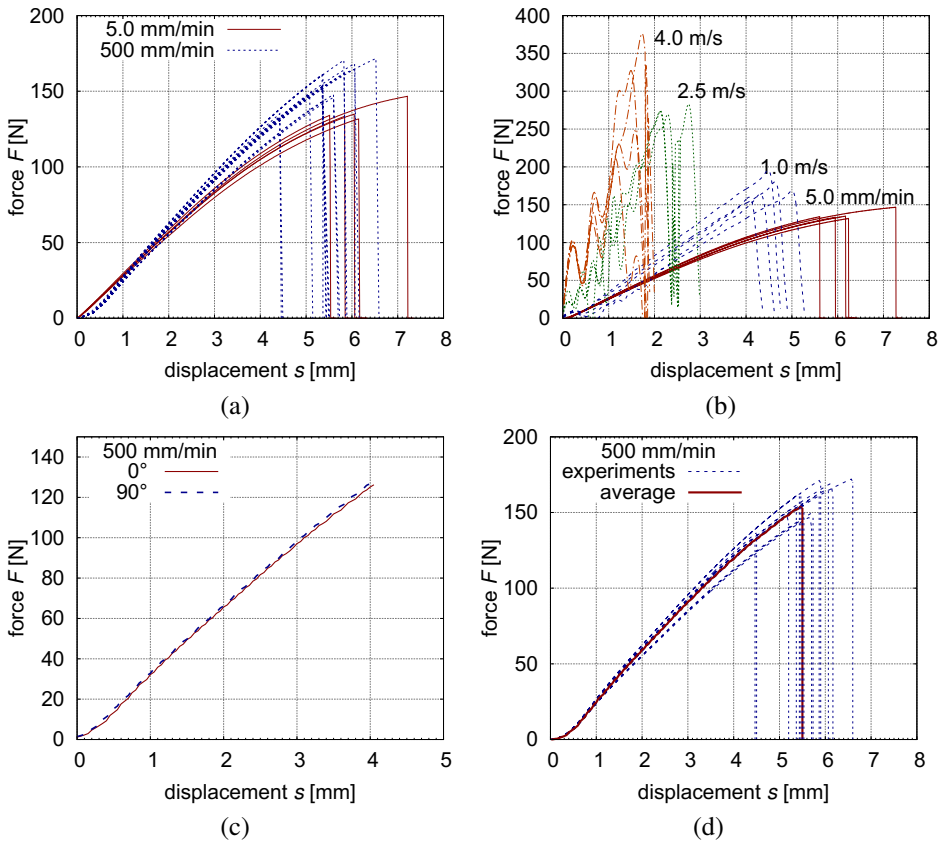
Figure 3.15 PMMA: bending tests. (a) quasi-static testing velocities (b) dynamic experiments compared to one quasi-static test (c) dependence on orientation (d) quasi-static failure spread.

setups are shown in Figure 3.14. The corresponding initial strain rate $\dot{\varepsilon}$ of each test at the surface fibre are calculated with the test velocity v according to

$$\dot{\varepsilon} = \frac{6b}{l^2} v \tag{3.5}$$

and are given in Table 3.5. For bending tests, the triaxiality factor χ is typically between 0.33 (uniaxial compression, impacted surface) and -0.33 (uniaxial tension, rear surface).

Experimental results of the two low velocity experiment series are shown in Figure 3.15 (a) in the form of force-displacement curves. Experiments at 500 mm/min were repeated 15 times in order to calculate the standard deviation of the failure displacement, which showed to be high for low velocities. The smallest test velocity was 5.0 mm/min and showed smaller maximum forces because of less overstress as well as a more linear behaviour.

Results of dynamic bending experiments are shown in Figure 3.15 (b). Experimental data of 2.5 m/s and 4.0 m/s were processed using a 2500 Hz and 4000 Hz lowpass filter respectively to treat high oscillations that are immanent of the testing system. Experiments at 2.5 m/s and 4.0 m/s show less scattering in their failure displacements. Direct comparison of the curves of Figure 3.15 (b) is misleading because of the different support distances, except for 5.0 mm/min and 1.0 m/s. Here, the viscoelastic character of the material can be observed.

Figure 3.15 (c) shows average values of three experiments each for specimens that were extracted in the direction of extrusion (0°) and perpendicular to that (90°). The force-displacement behaviour revealed a very close agreement of both direction and the assumption of isotropy appears reasonable.

Figure 3.15 (d) shows the average curve of the 15 experiments of the test at 500 mm/min. The high scattering from previous quasi-static experiments can be affirmed, and the average curve is assumed to fail at the average failure point. Detailed values and statistical evaluation of the experiments are given in Table A.13 in the Appendix.

3.2.5 Dart Impact Tests

The dart impact test is a standard experiment for the evaluation of the impact performance of structures and is regulated in the German regulations DIN ISO 7765-2 (2009) and DIN EN ISO 6603-2 (2002) as well as the American standard ASTM D5628-10 (2010). The PMMA disc specimens were 89 mm in diameter and had a thickness of 3 mm. For the quasi-static test, an Instron servo-electric testing machine model 5566, for the dynamic tests an Instron drop tower of the type Ceast 9350, which is shown in Figure 3.16 (a) and (b), was used. The tup used in both experimental setups was a steel hemisphere with a diameter of 20 mm.

For the temperature dependent tests, samples were stored for at least one hour inside the climate chamber at experimental temperature before testing. During specimen exchange, the door remained opened for a maximum of ten seconds. In order to establish temperature equilibrium, the waiting times between experiments were at least ten minutes. A falling mass of 25.5 kg was chosen in order to create a predominantly displacement-controlled deformation process. Resulting velocity after failure of the specimens deviated within

1 % to the initial velocity. Temperature dependent experiments were performed within the climate chamber shown in Figure 3.16.

Cooling below room temperature was performed with liquid nitrogen. The temperature was measured at the height of the specimen in the vicinity of the ventilation. A possible influence of the nitrogen environment on the mechanical behaviour of PMMA (KINLOCH, 2013) was not considered. Reference measurement regarding the climate chamber temperature taken at the ventilation system compared to a PT 100 temperature sensor positioned directly next to the specimen showed deviations between the two sensors below 1 K at thermal equilibrium.

The initial impact velocity is measured by a double-flag photocell. The development of the velocity $\vec{v}$ for every time point can be obtained by time integration of the reaction force subtracted by the gravitational force. This is numerically approximated by measured data at every time point i with the data sampling time $t_s = t_i - t_{i-1}$

$$v = \int \frac{F(t) - gm}{m} \mathrm{d}t \rightarrow v_i \approx v_{i-1} + \sum_{i=1}^{n} t_s \frac{\frac{F_i + F_{i-1}}{2} - gm}{m} \tag{3.6}$$

with $F(t)$ representing the actual measured force at the time t, g being the gravitation constant, and m the total falling mass containing the tup, the frame and additional masses. Based on Equation (3.6) the tup displacement at every time point i is calculated by double integration with respect to t and numerically approximated by

$$s = \int \int \frac{F(t) - gm}{m} \mathrm{d}^2 t \rightarrow s_i \approx s_{i-1} + \sum_{i=1}^{n} t_s \frac{v_i + v_{i-1}}{2} \tag{3.7}$$

Equations (3.6) and (3.7) show a crucial dependence on the correct measurement of the initial velocity.
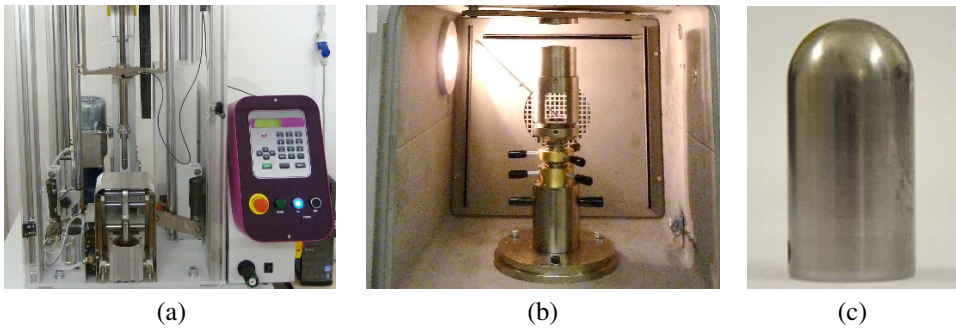
Figure 3.16 (a) Drop Tower CEAST 9350. (b) Support in climate chamber. (c) 20 mm tup.

Experimental Results

Two quasi-static experiment series were conducted in order to compare a possible influence of the specimen processing. Series one consisted of laser cut, series two of machined sp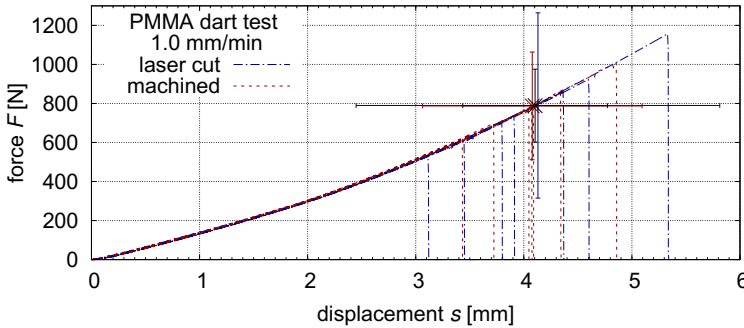ecimens. The force-displacement behaviour of both series is depicted in Figure 3.17. No influence of the machining process on the force-deflection or the failure behaviour is visible. The high variance in the failure displacement confirm the results of the quasi-static uniaxial tensile and bending tests.

Figure 3.17   PMMA: dart test at 1.0 mm/min. Errorbars represent the 95 % confidence interval of the mean.

Dynamic Experiments were conducted at four different temperatures for two velocities. Figure 3.18 shows the corresponding force-displacement behaviour. In each series, five experiments were repeated, except for the series of -30 °C and 5.0 m/s with three repetitions. Graphs on the left side of Figure 3.18 show experiments at 1.0 m/s, the ones on the right side at 5.0 m/s. All series showed good reproducibility of the force-displacement behaviour. The failure displacement of the 5.0 m/s experiments can not be determined as clearly as for the 1.0 m/s experiments because of higher oscillations and multiple contact points. Therefore, the force-displacement behaviour of an experiment at 5.0 m/s is discussed subsequently.

The crack propagation velocity c_{crack} for thin plates is given in LIU et al. (2009) with

$$c_{crack} \approx 0.8 c_R = \frac{0.696 + 0.896\nu}{1 + \nu} c_{sw} = \frac{0.696 + 0.896\nu}{1 + \nu} \sqrt{\frac{E}{2\rho(1 + \nu)}} \qquad (3.8)$$

with c_R, c_{sw}, ν, E and ρ represent the Rayleigh wave speed, shear wave speed, elastic modulus, Poisson's ratio, and density. With values for PLEXIGLAS® 8N given in Table 2.3 and a Poisson's ratio of 0.30 a crack velocity of 766 m/s is calculated. The factor 0.8 was determined experimentally in CHAUDHRI (2004). c_R and c_{sw} are given in RAVI-CHANDAR et al. (2000) with 947 m/s and 1014 m/s respectively. Obtained val-

ues correspond well to values given in LAMBROS et al. (1995) and SONG et al. (2008) (c_R=930 m/s).

A series of high-speed images for one experiment at 23 °C and 5.0 m/s together with the corresponding signal depicted in Figure 3.19. One photograph represents a certain time span of deformation, depending on the shutter time of the camera, which is depicted by the four yellow boxes in Figure 3.19.

After the first three maximum forces no cracks are visible on the high-speed images and the variation of the force signal can be related to multiple impacts respectively a loss
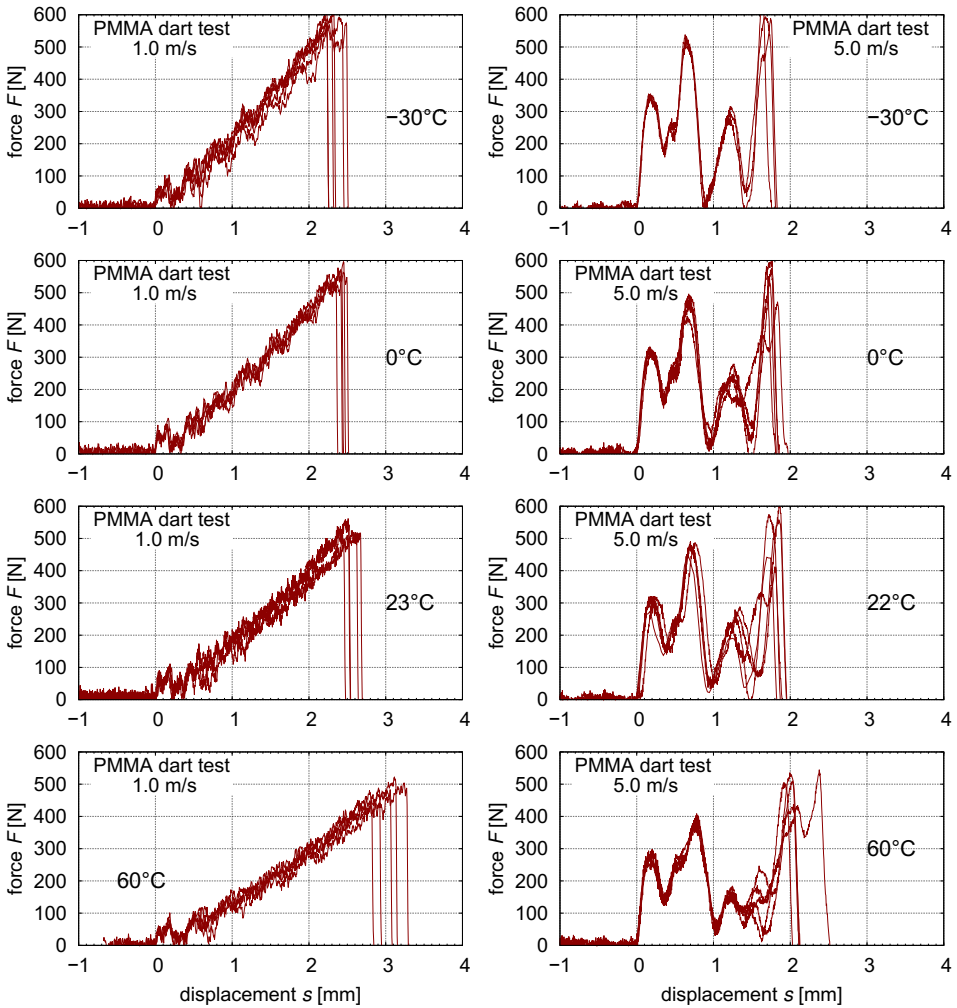
Figure 3.18   PMMA: dart impact tests at 1.0 m/s (left) and 5.0 m/s (right) for different temperatures.
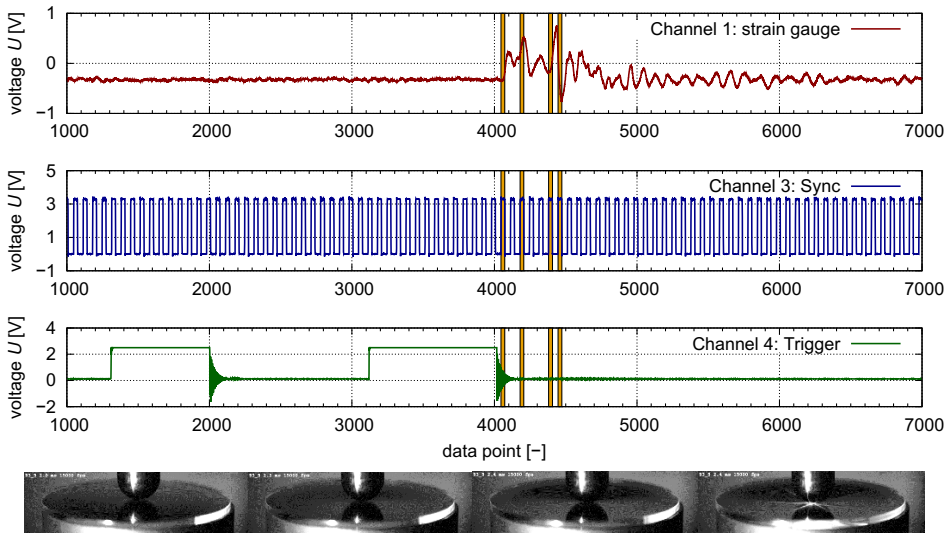
Figure 3.19 PMMA: dart impact test. Signals measured at 5.0 m/s and the corresponding high-speed photographs. Yellow boxes mark the shutter time of one picture of the high-speed camera with 15 kHz.

of contact between tup and specimen. Failure occurs at the fourth maximum, which is clearly visible by the sudden appearance of cracks in the right-hand side photograph of the image series.

The overall temperature dependence between -30 °C and 23 °C appears to be marginal at both velocities. Compared to results from room temperature, failure displacements at 60 °C are observed to be 19 % (1.0 m/s) and 15 % higher. This is due to the increasing proximity to the glass transition temperature.

Concluding, the influence of temperature on the dynamic mechanical behaviour of monolithic PMMA is a minor effect for low temperatures (-30 °C and 0 °C) and room temperature (23 °C). At higher temperature, softening effects become increasingly dominant, which leads to a reduction in maximum forces and a prolongation in failure displacement. Detailed values and statistical evaluation of the experiments are given in Table A.14 in the Appendix. For all investigated temperatures and velocities, the fracture pattern was reproducibly governed by a star-shaped crack propagation leading the specimen to depart into four to six parts. For low velocity impact loadings on cast PMMA, similar observations were made by LIU et al. (2009), who observed three to six cracks and star shaped radial cracks.

3.3 Experimental Investigation of TPU Interlayers

3.3.1 Transient Plane Source Method Experiments

Experiments were conducted according to the setup described in Section 3.2.1. TPU specimens were obtained by stacking 0.5 mm plies, as shown in Figure 3.20 (a), to a total thickness of approximately 13 mm in order to reach a sufficient thickness for TPS measurements. The stacked plies were stored under pressure for several days at temperatures up to 150 °C in order to reach sufficient merging of the plies leading to a thermal degradation of the material, visible in Figure 3.20 (b). The specimens were clamped to ensure a continuous contact to the sensor, which is depicted in Figure 3.20 (c).

(a) (b) (c)
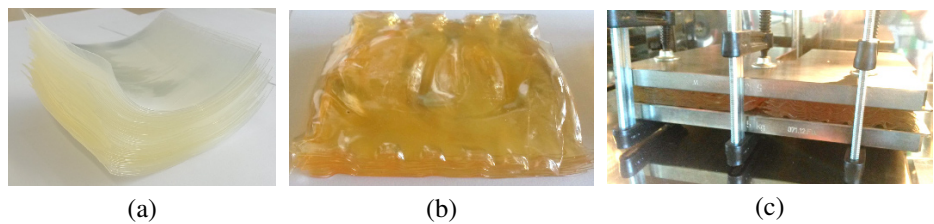
Figure 3.20 TPU: (a) Single plies. (b) Plies after annealing. (c) Clamped experimental setup.

Thermal properties were measured from -40 °C to 100 °C. Thermal conductivity k (Figure 3.21 a) shows a small decrease at around 10 °C. At 0 °C, which is located in the area of the glass transition (Section 3.3.2), k increases slightly. From 20 °C to 100 °C k remains approximately constant at 0.225 W/(m K). Heat capacity c (Figure 3.21 b) was determined corresponding to Section 3.2.1 and rises constantly with increasing temperature with a plateau between 0 °C and 20 °C. A higher grade is observed around 0 °C, which corresponds to the glass transition area. Concluding, the material behaves, similar to PMMA, like a typical amorphous thermoplastic with a thermal conductivity around 0.2 W/(m K) and an increase of heat capacity with temperature.

(a) (b)
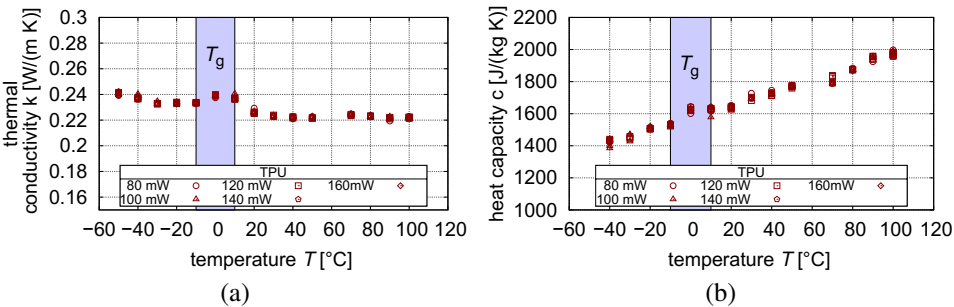
Figure 3.21 TPU: TPS measurements. (a) Thermal conductivity. (b) Heat capacity.

3.3.2 Dynamic Mechanical Thermal Analysis

3.3.2.1 Temperature Sweep and Relaxation Processes

The experimental setup from Section 3.2.2 was used. All experiments regarding TPU were conducted in a double shearing setup (Figure 3.6 c) with circular specimens that were 3 mm in diameter and 0.35 mm in thickness. Temperature sweeps were conducted at 0.5 Hz and 1.0 Hz. Results of the latter frequency are shown in Figure 3.22. Different methods for the determination of the glass transition temperature T_g according to DIN EN 6032 (2016) are applied and shown in Table 3.6. At low temperatures the scattering of G'' values is noticeable in the logarithmic view. This is most likely caused by small slippage of the specimens, which are constrained by friction.

Table 3.6   TPU: DMTA. Glass transition temperatures.

method DIN EN 6032	onset G^* T_g onset	max G'' T_g loss	inflection G'	max tan δ T_g peak
0.5 Hz T_g	$-5.00\,°C$	$-2.75\,°C$	$2.02\,°C$	$32.50\,°C$
1.0 Hz T_g	$2.7\,°C$	$-5.83\,°C$	$22.48\,°C$	$32.50\,°C$

The determination of the glass transition temperature was performed in a logarithmic scale of G^* and is summarized for different methods and two frequencies in Table 3.6. The glass transition zone can be located roughly in the range between -5 °C and 30 °C for 1 Hz. T_g shows dependence on the applied frequency and shifts to lower temperatures for higher frequencies. ZHANG et al. (2015) and YI et al. (2006) found an increase of T_g with frequency for a similar PU interlayer material. YI et al. (2006) revealed significantly deviating material behaviour for three different PU materials. The presented results show
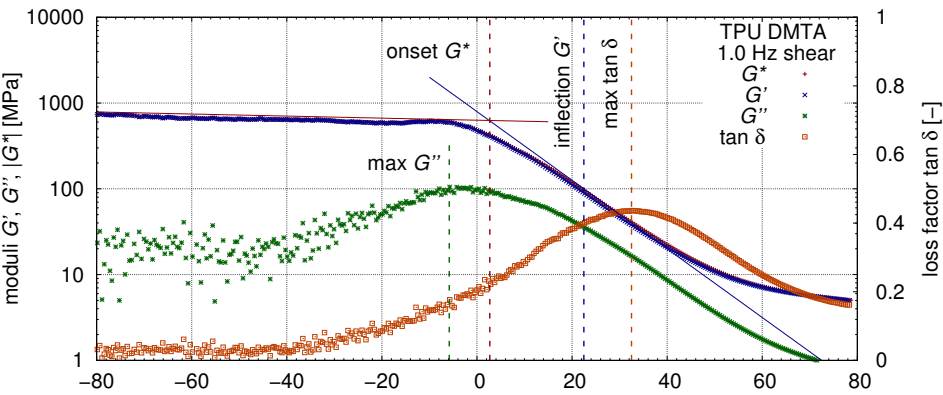
Figure 3.22   TPU: DMTA. Results temperature sweep at 1.0 Hz.

to be within the range of published DMTA results for different TPUs (MACALONEY et al., 2007; YI et al., 2006). However, YI et al. (2006) showed that their composition affects their behaviour in such a significant manner that T_g varied between -25 °C and 24 °C, which makes comparison of TPUs with different or unknown compositions unfeasible.

3.3.2.2 Temperature-Frequency Sweep and Master Curve

Figure 3.23 shows the results of a combined temperature-frequency sweep, with temperature and frequency ranging between -70 °C to 80 °C and 0.01 Hz to 100 Hz, respectively. Parameters of the experiment can be found in Appendix A.3. Assuming thermorheological
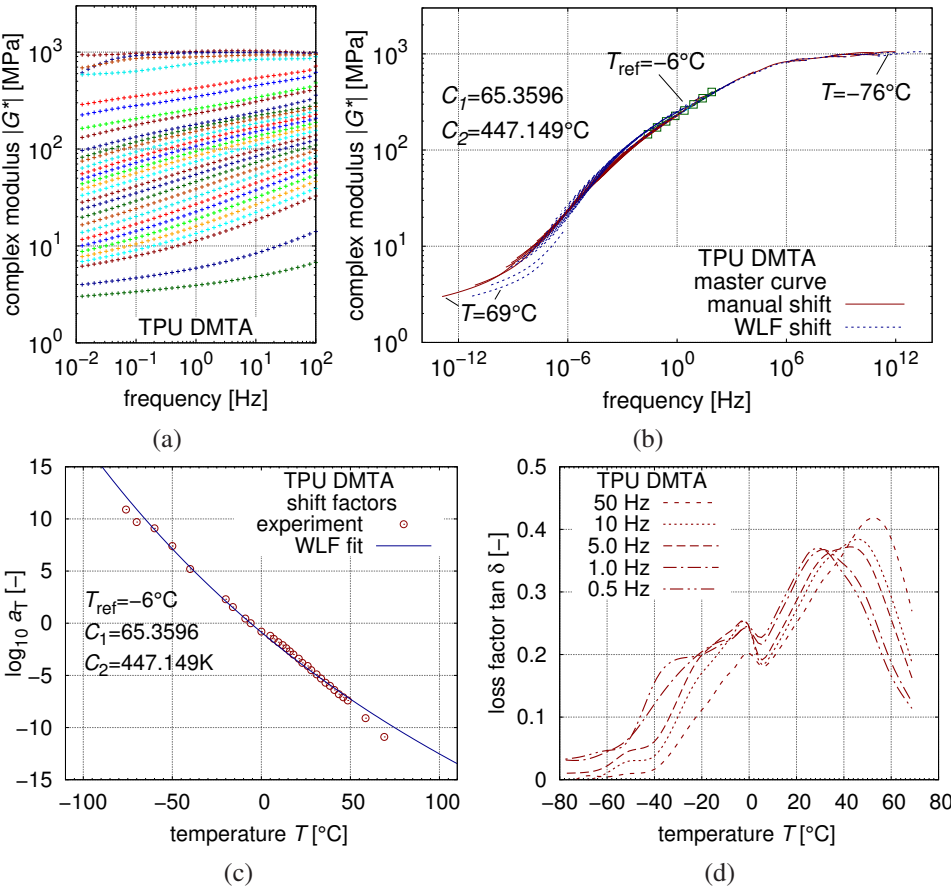
Figure 3.23 TPU: DMTA. Master curve generation. (a) Isothermal frequency sweep raw data. (b) Master curve with isothermal shift compared to a WLF-shift. (c) Shift factors with a WLF least square fit. (d) Multifrequency plot.

simplicity, the resulting isothermal raw data curves (a) were shifted according to the time-temperature superposition to form a master curve in Figure 3.23 (b). The resultant shift factors for each temperature were used to obtain parameters for a WLF-function (Table 3.7) with a least-square fit in Figure 3.23 (c). The superposition using these parameters is illustrated in Figure 3.23 (b) compared to the original shift and show good agreement. Figure 3.23 (d) depicts a multifrequency plot for the same experiment. Curve crossing is observed at around -20 °C, 0 °C, and 35 °C pointing to relaxation processes. The WLF shift approach proved to be capable to capture the time-temperature superposition.

Table 3.7   TPU: WLF shift parameters.

T_{ref}	C_1	C_2
$-6.0\,°C$	65.3596	$447.149\,°C$

3.3.3 Uniaxial Tensile Tests

The experimental setup, which is described in Section 3.2.3, was applied. The specimen geometry from DIN EN ISO 53504 (2015), geometry S1, was used due to its small width in the parallel area, which results in smaller traverse displacements until failure. The tests at 5.0 mm/min, 0.1 m/s, and 3.0 m/s were conducted at the German Institute for Polymers (DKI), Darmstadt.

Further experiments were performed regarding the extraction point and direction as well as conditioning to investigate possible anisotropy, influence of moisture and permanent endothermic effects as described in MACALONEY et al. (2007). Additionally, one test series was carried out at 500 mm/min in order to investigate adiabatic heating processes. Figure 3.24 (a) illustrates the isochoric stress-strain behaviour, (b) Poisson's ratio, (c) the development of the strain rate during the test, and (d) two different extraction directions. The main characteristics of this material of TPU is discussed subsequently by means of the presented results.

Stress-Strain Behaviour

The stress-strain behaviour for different velocities is shown in Figure 3.24 (a). Stress was evaluated according to Equations (2.36) and (2.35) for their isochoric and true values, depicted are average values additionally for clarity. For the most part, both stress evaluation shows only minor deviations. At higher strains the isochoric stress becomes slightly higher than the true stress, but the overall deviation remains small. The stress-strain correlation behaves highly strain rate sensitive. Experiments at 3.0 m/s exhibit roughly a ten times higher stress than the experiments at 5.0 mm/min. The experiments at 5.0 mm/min were
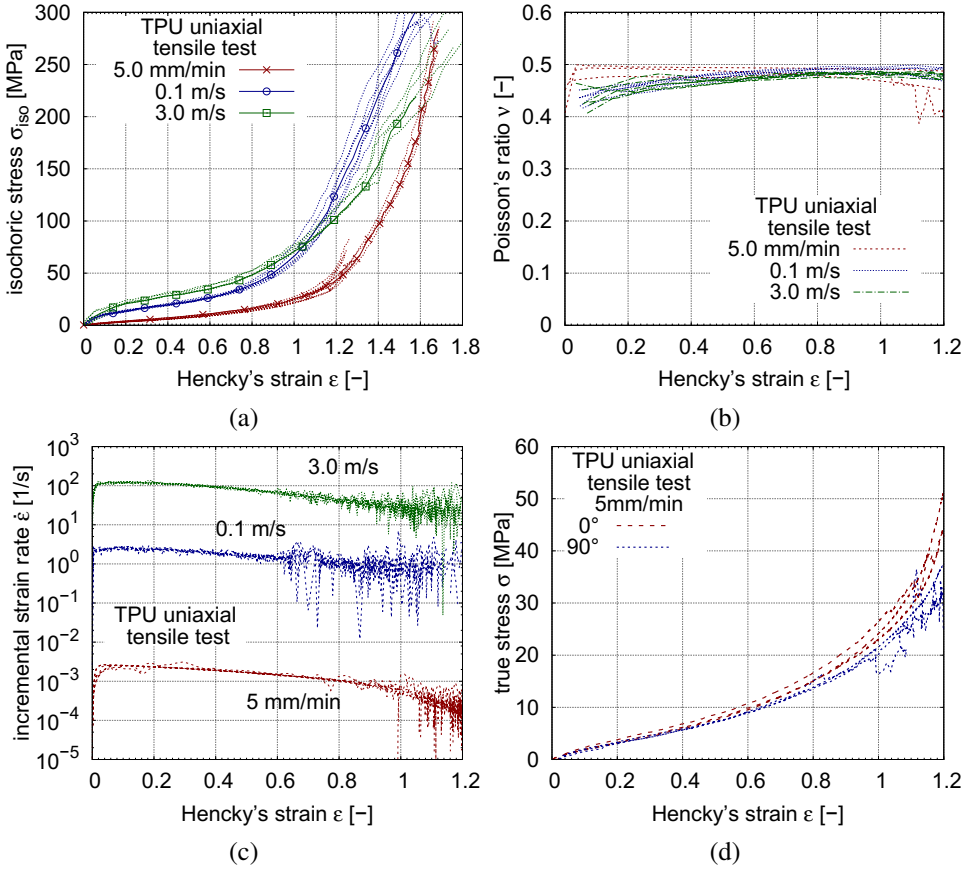
Figure 3.24 TPU: uniaxial tensile tests. (a) True stress-strain. (b) Poisson's ratio. (c) Development of strain rate. (d) Isotropy.

repeated in a second investigation and showed very high agreement to the results from DKI.

Stress-strain curves at 0.1 m/s and 3.0 m/s cross reproducible at approximately $\varepsilon=1$. This effect can not be explained by isothermal viscoelastic material behaviour. Similar effects were observed by KUNTSCHE (2015), who assumed specimen slippage as a possible explanation. Another explanation may be the heating of the interlayer due to inelastic dissipative effects. QI et al. (2005) names as dissipation sources for TPU amongst others breakage of hydrogen bonds between and within the hard domains as well as slipping and friction effects. The dissipation leads to heat generation within the specimen, which offers a further approach for the observed curve crossing.

Failure

Due to the very high strains a complete local analysis with DIC could not always be performed, and, therefore, exact failure strains could not be determined. It is, however, possible to state minimum values for the failure strain. For quasi-static tests, failure strain observed to be above a true strain of 1.6 ; for dynamic tests the true failure strain was above 1.5 . At least 275 MPa of isochoric stress was reached for every experiment before failure.

Strain Rate

True strain rate decreased for all experiments with increasing strain due to specimen elongation. For all experiments a decrease in strain rate of approximately one decade could be observed until the end of the experiment. At high strains, the measurement of the strain rate became more unstable because the DIC increasingly failed to find facettes within the spray pattern. Disregarding these instabilities, it appeared that at higher strains the strain rate of experiments at 0.1 m/s decrease less and got closer to the strain rate of 3.0 m/s. This lead to a further approach of the stress-strain curves of 0.1 m/s and 3.0 m/s, which abets the curve-crossing behaviour.

Poisson's Ratio

Poisson's ratio v was determined close to the isochoric value of 0.5 for all strains and experiment velocities, which is depicted in Figure 3.24. Assumption of isochoric material behaviour, therefore, exhibits as a good approximation.

Conditioning and Endothermic Effects

Results from Figure 3.24 (d) indicated a minor dependence on the extraction direction relatively to the extrusion direction. However, it may also be possible that the difference stem from the proximity to the edge of the TPU roll. For the small TPU rolls the 90° specimens contained areas that were significantly closer to the edges than those from 0° direction. To investigate this influence, specimens in 90° were extracted from another TPU roll with a width of 400 mm width. Two categories were made, one with specimens from the centre (c) and the other with specimens extracted close to the edges. The tensile test results can be seen in Figure 3.25 (a). No significant influence on the extraction point was observed in this test.

Using DSC, MACALONEY et al. (2007) observed a permanent endothermic reaction for different TPUs occurring when heating to temperatures between 60 °C and 100 °C. To investigate if this behaviour also applies to the TPU of the present work, uniaxial tensile tests on unconditioned "as-delivered" specimens as well as conditioned specimens were

conducted. The conditioning was performed in a climate chamber at $90\,°C$ and 10% relative humidity for $24\,h$. After that the specimens were stored for $48\,h$ at room conditions. The influence on the force-traverse displacement can be seen in Figure 3.25 (b).
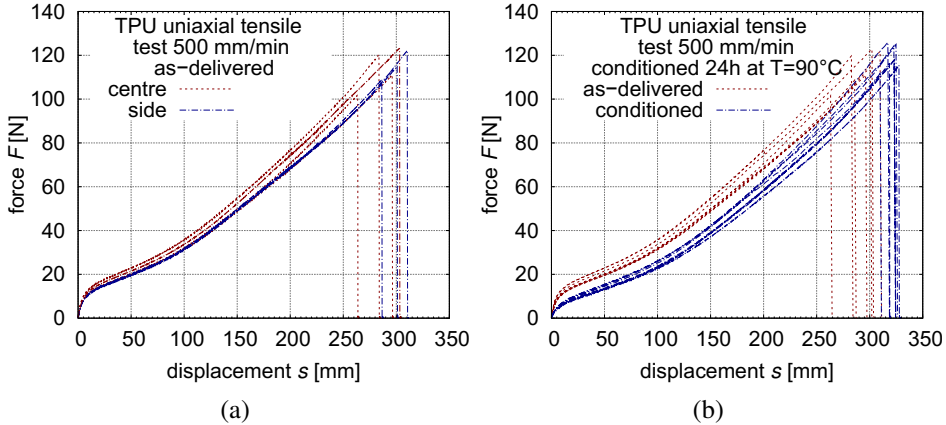
Figure 3.25   TPU: uniaxial tensile tests. (a) Influence of extraction point. (b) Influence of conditioning.

The conditioning resulted in a significant softer material response and the findings of MACALONEY et al. (2007) can be affirmed. It is, however, not further investigated to which extent this behaviour is of permanent nature. It is clear that TPU interlayers undergo this temperature range during the lamination process, but not to which extent the interlayer experiences the same change as in its not-laminated state. Investigation of the interlayer material outside of this section is always referred to the not-annealed material, "as-delivered" condition.

Residual Strains and Plasticity

Specimens that were loaded close to the failure strain (ε=1.5) and then unloaded showed residual strains after several days of unloading, which is depicted in Figure 3.26. After three months of unloading, residual strains were still between 0.2 and 0.3. These residual strains are caused by either material damage or plasticity. QI et al. (2005) specifies values between 0.02 and 0.062 for compression after strain loads up to 1.0. Concluding, the high strain behaviour is governed by dominant viscoelastic behaviour accompanied by a recognizable portion of plasticity. Both effects dissipate energy, which leads to a temperature rise of the specimen. An isolation of both inelastic effects from an experimental side of view can be estimated in a first approach by comparing residual strains to overall strains.
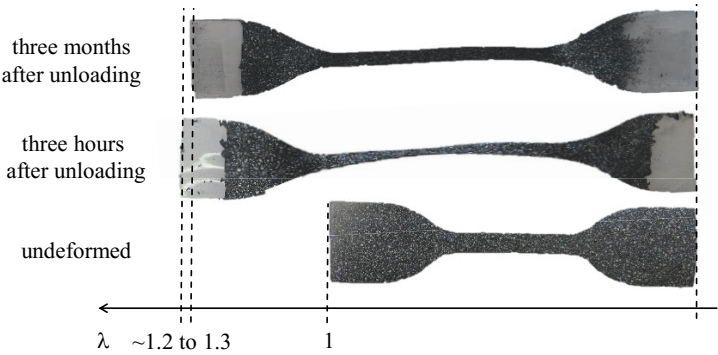
Figure 3.26　TPU: uniaxial tensile test. Inelastic global stretch after unloading.

Temperature-Strain Correlation

To investigate the temperature development of the TPU interlayer, uniaxial tensile tests with a constant traverse velocity of 500 mm/min were conducted, for which simultaneous optical stress-strain measurement with the DIC as well as a surface temperature measurements with an IR camera were performed. An analogue output signal of the DIC was used to synchronize the data acquisition of the DIC and IR systems. The DIC system filmed the front side of the specimen, which was prepared with a black-white spray pattern, while the IR camera filmed the unmodified rear side, which is discussed in Section 3.1.3.

Two methods for the temperature evaluation as shown in Figure 3.27 (right hand side) were performed. First, an average temperature along a static line in the centre of the specimen geometry was used. At the beginning of the test the line includes partly the
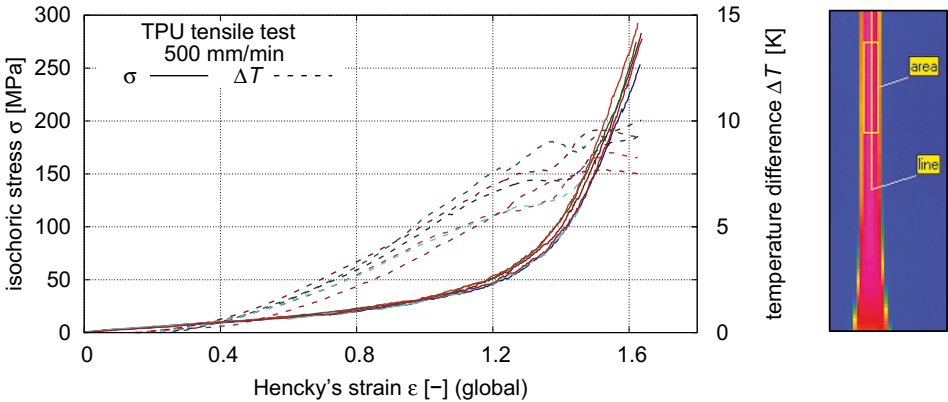
Figure 3.27　TPU: uniaxial tensile test. Correlation between strain and temperature at 500 mm/min.
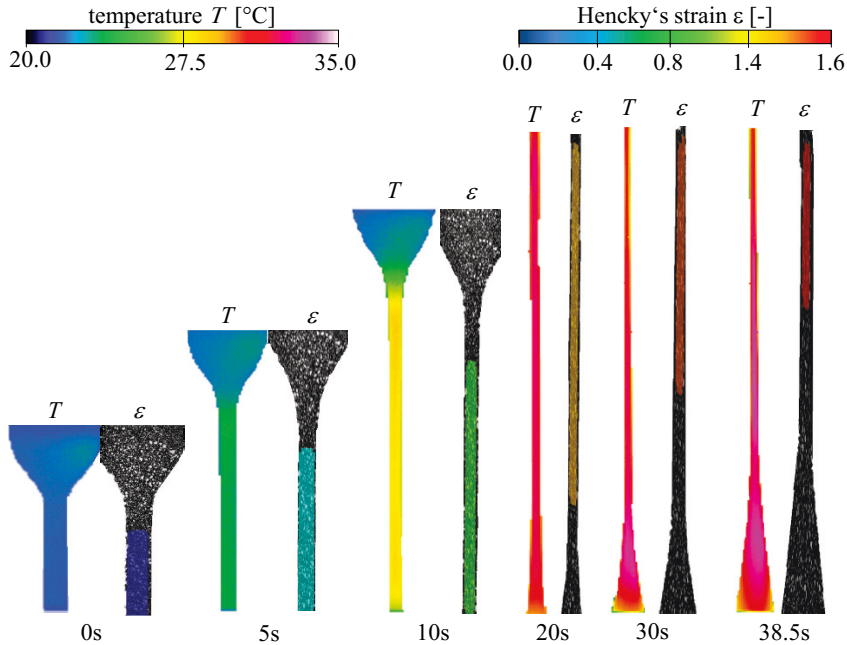
Figure 3.28 TPU: uniaxial tensile test. Image series of correlation between strain and temperature at 500 mm/min.

testing machine. However, it showed that the influence is only marginal because significant heating starts at strains above approximately 0.3 . Secondly, a static rectangle that covers only the specimen surface at all strains was used. Both methods showed well agreement and only minor deviations for the temperature development. The temperature shown in Figure 3.27 is evaluated with the rectangle and represents average temperature values of roughly 10 times 40 IR pixels.

Figure 3.27 shows an average temperature rise of 8.40 K and an average maximum temperature rise of 8.75 K. The average maximum temperature rise is composed of the difference between the maximum temperature at the beginning and the end of the averaged for all six experiments, detailed values are given in Table A.9 in the Appendix.

Figure 3.28 shows corresponding IR and DIC images for different times with increasing strains. Temperature and strain distribution appears to be homogeneously distributed within the parallel length. For higher strains (images above 20 s) parts of the parallel length move outside of the evaluable window. The image at 38.5 s is the last one taken before rupture of the specimen and no localization of the specimen can be observed. Therefore, a partial evaluation of the specimen for strain and temperature appears as a reasonable approach.

Concluding, the TPU interlayer exhibits thermomechanical heating at intermediate haul-off velocities. For higher velocities an increase in maximum temperature can be expected, which is likely to have an effect on the material behaviour due to thermal softening. The temperature development becomes dominant at strains above 0.3, and is, therefore, particularly important for high deformation processes.

3.3.4 Biaxial Tensile Tests

Dart impact experiments at high deformations and after failure of the PMMA plies alters the stress state within the interlayer from compressive to approximately uniaxial and biaxial tension. When using hyperelastic material laws that depend on more than one invariant, triaxiality plays a vital role for the determination of the parameters. Parameter identification with uniaxial data is not sufficient to model non-uniaxial strain states (JOHLITZ et al., 2011) and biaxial tensile tests can be used to enhance a hyperelastic model to cover the behaviour within the I_C-II_C-space more accurately, which is depicted in Figure 3.29 (a). It can be deducted that uniaxial tension a I_C-dominated deformation state, wheares for pure shear and equibiaxial tension II_C becomes increasingly influencial. For different triaxiality factors I_C or II_C are more or less dominant and have to be considered simultaneously.

For this purpose, equibiaxial (plane stress) experiments were conducted at Fraunhofer Ernst-Mach-Institut (EMI), Freiburg at an actuator velocity of 0.01 mm/s resulting in an axial velocity of 0.02 mm/s. The applied cruciform specimen is depicted in Figure 3.29 (b). The displacement was evaluated with a local and a global method. Global refers to the actuator displacements, while local means the distance between two points on the specimen close the support, which were evaluated with DIC as shown in Figure 3.30. As

(a)

(b)
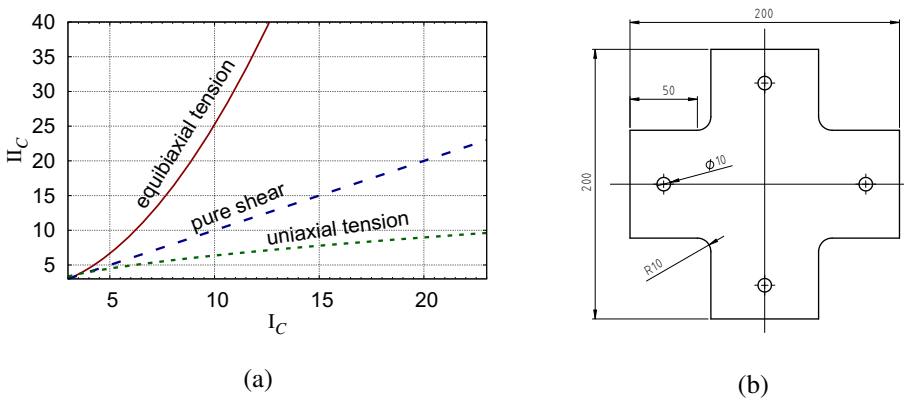
Figure 3.29 (a) I_C-II_C-plane for different strain states. (b) Biaxial tensile cruciform specimen from Fraunhofer EMI.

(a)

(b)

(c)

(d)
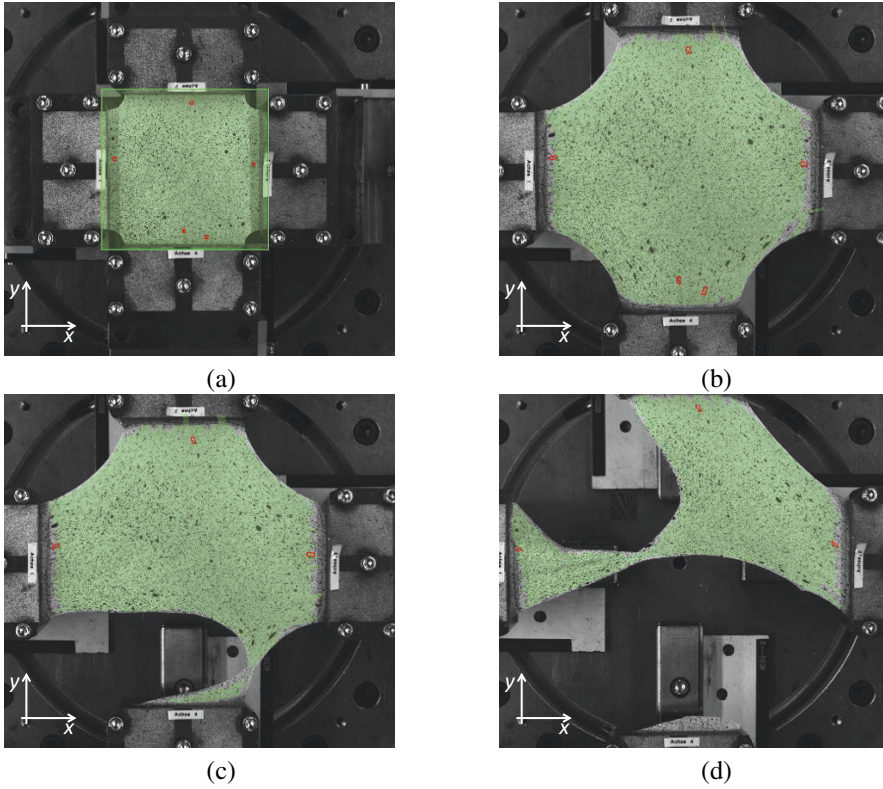
Figure 3.30 TPU: biaxial tensile test. Image series of experiments conducted at Fraunhofer EMI.

depicted in Figure 3.30 (c) and (d) rupture of the interlayer starts at the radius close to the support and can therefore not be considered as a biaxial failure point.

The force-displacement behaviour under biaxial tension is shown in Figure 3.31. The x- and y-axis forces are average values from both opposite actuators, while their displacements are summed. Figure 3.31 (a) shows that both axes provide the same force-displacement behaviour with scattering that lies within the magnitude of material uncertainties. The global and local evaluation of displacement is shown in Figure 3.31. Slightly higher values can be observed for the local evaluation. The difference, resulting from clearance and stiffness of the actuators shows also minor influence. The principle behaviour is characterized by two failure points, which can be seen in Figure 3.30 (c) and (d).

To obtain stress-strain curves from the force-displacement behaviour, the following assumptions are taken: The material behaves isotropically and incompressibly. Both presuppositions are reasonable for extruded TPU in its rubbery state. From Figure 3.31 (a) the isotropic assumption can be confirmed. The isochoric stress for each axis is calculated with Equation (2.35) and then further processed with Equation (2.28) to obtain the
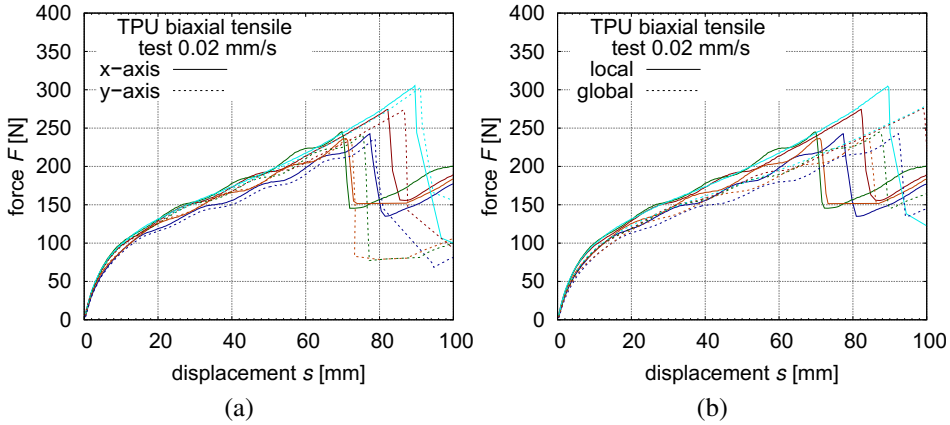
Figure 3.31 TPU: biaxial tensile test. (a) Comparison of x- and y-axis. (b) Comparison of local and global evaluation for x-axis values.

isochoric equivalent von-Mises stress $\sigma_{\mathrm{vM, iso}}$. Strains were evaluated locally in the centre of the specimen. Strain evaluation showed that shear strains are significantly below the two strains in x- and y-direction, which is shown in Figure 3.32 for one representative experiment. An equivalent von-Mises strain was calculated according to Equation (2.13) to compare uniaxial and biaxial stress-strain behaviour. Figure 3.32 (b) reveals a smaller equivalent stress response for the biaxial stress states at large strains. Considering the parameter identification of material models in future works, this entails further consideration of uniaxial, biaxial, and further stress states in order to represent the material behaviour accurately.
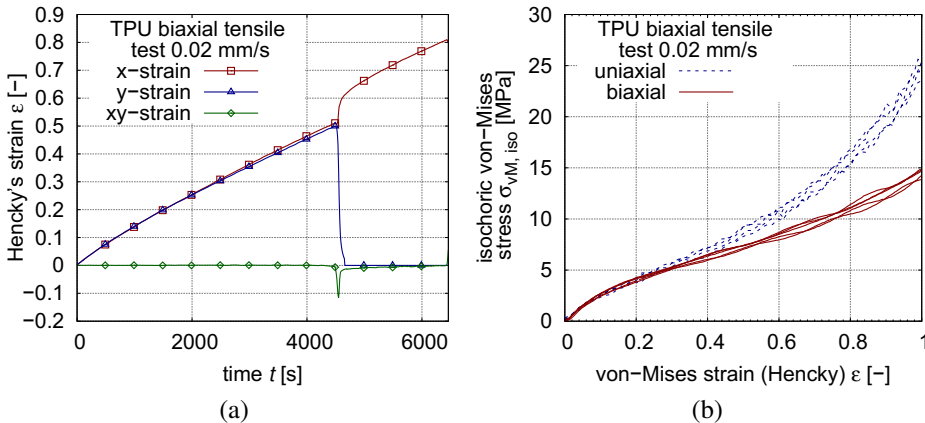
Figure 3.32 TPU: biaxial tensile test. (a) Strain components in the centre of the specimen. (b) Equivalent stress-strain compared to uniaxial tension.

3.4 Experimental Investigation of PMMA-TPU Laminates

PMMA-TPU laminates were investigated regarding their strain-rate and temperature de-pendent behaviour in low velocity impact events. Free and clamped bending tests were utilized to get a deeper insight in the high strain behaviour of the interlayer including adi-abatic heating effects after failure of the PMMA plies. Dart impact experiments at two different velocities and four different temperatures were conducted to investigate the com-bined temperature-strain-rate dependence of the laminate.

3.4.1 Three-Point Bending Test

PMMA-TPU laminates at different velocities were subjected to three-point bending tests, subsequently simply referred to as bending tests. Additional thermographic investigation was performed to examine the thermomechanical heating of the interlayer.

Experimental Setup

Quasi-static experiments were conducted on a servo-hydraulic Instron universal testing machine, dynamic ones on the *4a* Impetus pendulum system. Specimens were prepared by machining specimens with the geometry 60 mm x 10 mm x 4 mm from laminated plates. Test velocities were 5.0 mm/min (quasi-static), 1.0 m/s, 2.0 m/s, and 3.0 m/s. The support distance of the quasi-static tests was chosen with 40 mm because of greater protruding lengths given by an overall specimen length of 80 mm. The support distance of the dy-namic experiments was 50 mm.

Force-Displacement Behaviour

Figure 3.33 shows the force-displacement behaviour of the laminate under bending load-ing for different impact velocities. For the quasi-static test, it reveals initially linear be-haviour with increasing nonlinearities at higher strains. This is caused by the PMMA, which predominantly controls the behaviour of the laminate until first breakage, which is also represented in the scattering of quasi-static failure strain, which confirms previous quasi-static experiments of monolithic PMMA.

The dynamic tests exhibited significant oscillations, which are immanent of the experi-mental setup. Here, experiments at 3.0 m/s were processed with a SAE 3000 lowpass filter. Similar peak force values before failure were reproduced for all dynamic experiments. Af-ter breakage of the PMMA plies, the specimen is pulled through the support resulting in no significant post-breakage behaviour. For all experiments, the TPU interlayer showed no failure or damage.
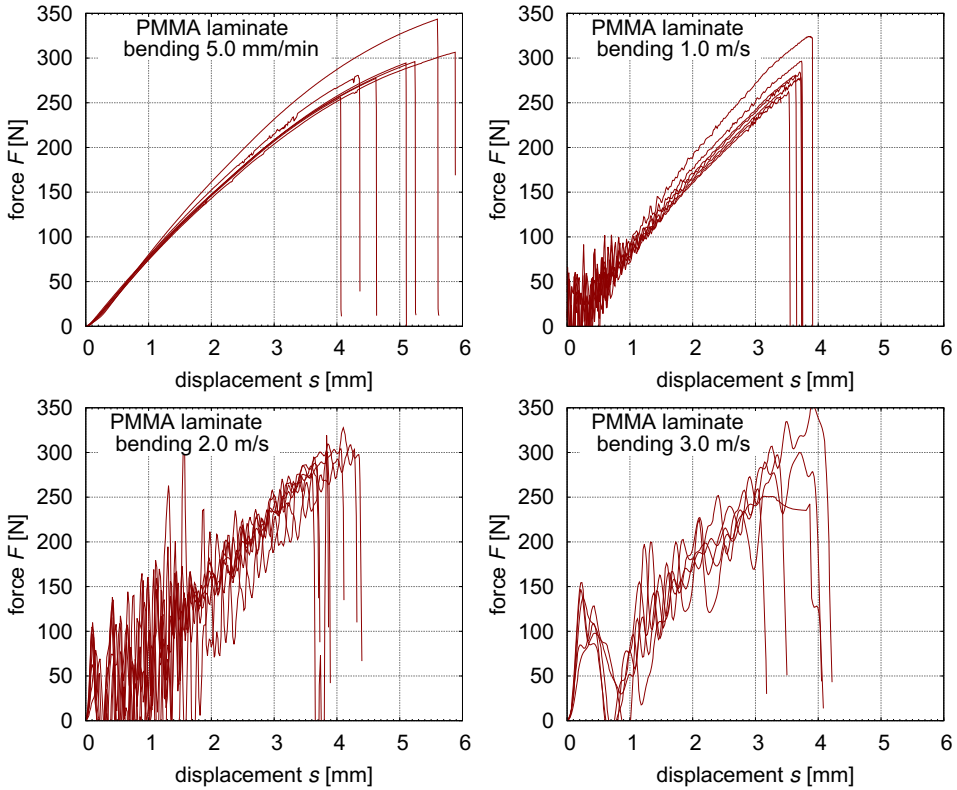
Figure 3.33 PMMA laminate: bending test. Force-displacement behaviour at 5.0 mm/min, 1.0 m/s, 2.0 m/s, and 3.0 m/s.

Interlaminar Deformation and Delamination

The experiment at 5.0 mm/min was additionally examined with DIC to investigate the initial deformation behaviour through thickness. At initial deformations, the TPU interlayer is compressed, accompanied by significant shear strains at intermediate deformations until PMMA failure. Figure 3.34 shows the planar shear strain ε_{xy} on the surface of the laminate at the last picture of the DIC before breakage of both PMMA layers. Because of the different shear behaviour of the single plies, the TPU interlayer can be differentiated distinctly.

It is clearly visible that the major part of the shear strain is performed by the TPU layer, whilst the PMMA undergoes comparatively small shear strains. This shows that both PMMA layers are separated from each other and no average monolithic behaviour can be assumed. Instead, there is a distinct heterogeneous deformation state consisting of the mixed tension-compression bending state for both PMMA layers. For the interlayer,

shear deformation are dominant in the intact state, which changes to a tensile state after failure of the PMMA layers. Furthermore, the homogeneous shear deformation can be seen as an evidence that, until failure of the PMMA plies, no significant delamination has occurred.

A postiori specimen inspection revealed that delamination occurred locally around the PMMA breakage point, which was below the fin. Areas that indicated no sign of breakage or cracks did not show any signs of delamination and no global delamination was observed.
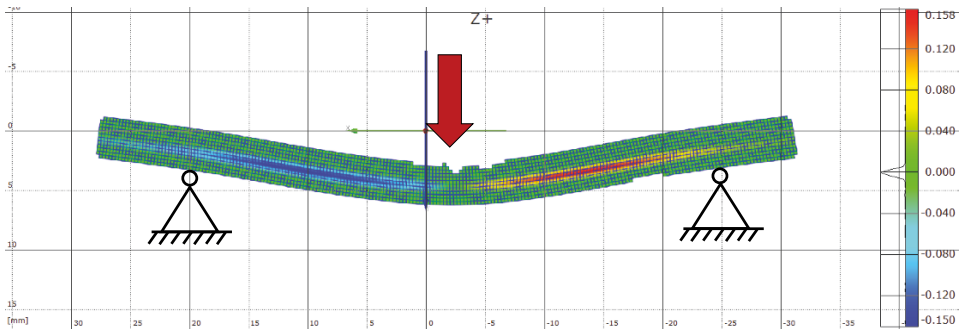
Figure 3.34   PMMA laminate: bending test. Shear strains ε_{xy} from DIC evaluation before first breakage in quasi-static test.

Temperature Measurements

Measurements were conducted in quarter-frame mode (80x64 IR pixels) at an integration time of 480 µs for quasi-static and two dynamic tests. For the quasi-static test, it can be stated that there is a measurable temperature rise within in the TPU interlayer after failure of the PMMA plies. This is remarkable because adiabatic heating is usually not considered in low velocity impact events, especially not under quasi-static loading. An isothermal approach appears to be correct only until failure occurs though.

For the dynamic tests, the setup with the *4a* Impetus enabled to conduct IR measurements at velocities of 1.0 m/s and 2.0 m/s. Temperature evaluation was performed first for a minimum and a maximum temperature respectively (each pixel evaluated) and secondly for the average temperature within a rectangular area to capture the global temperature change.

Figure 3.35 shows an image series of the specimen with 5.2 K temperature rise. Figure 3.36 shows a series of IR images, where a maximum local temperature rise of 24.94 K was measured. The first images of Figure 3.35 and Figure 3.36 taken immediately before the impact. The second image shows the last image before breakage and image three the

subsequent picture immediately directly after failure. Image four shows the image of the highest temperature measured, in vicinity to the highest deformations.

| 0.0 ms | 4.27 ms | 5.49 ms | 57.38 ms |
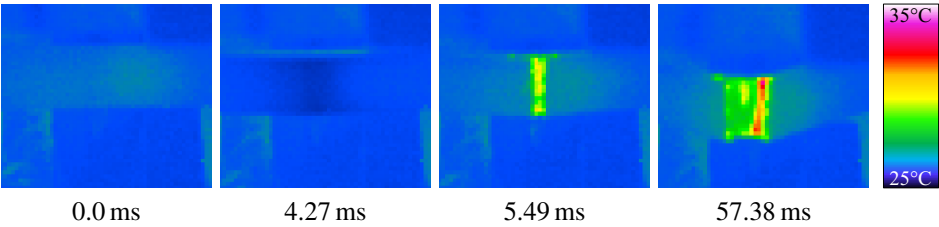
Figure 3.35 PMMA laminate: bending test. Series of IR images of specimen with small temperature rise at v=1.0 m/s.

| 0.0 ms | 4.27 ms | 5.49 ms | 57.38 ms |
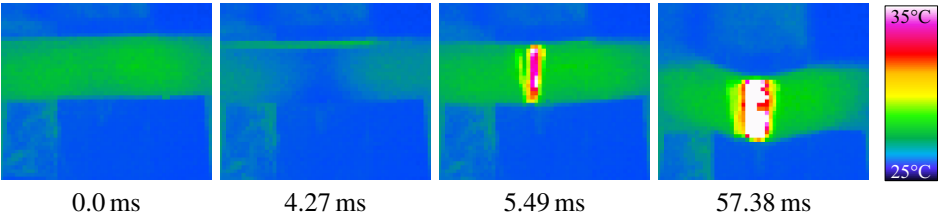
Figure 3.36 PMMA laminate: bending test. Series of IR images of specimen with high temperature rise at v=1.0 m/s.

The experimental results for the adiabatic temperature rise for both velocities are depicted in Figure 3.37. A high scattering in the measured temperature was observed for both ve-

(a)

(b)
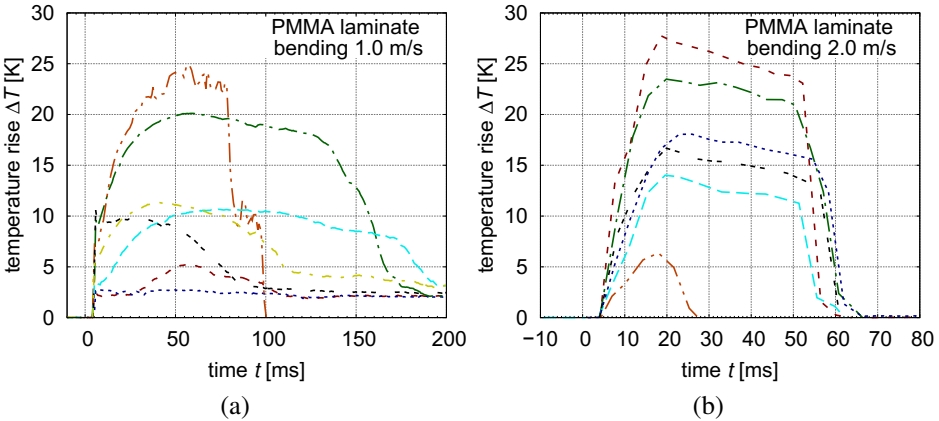
Figure 3.37 PMMA laminate: bending test. Adiabatic heating at 1.0 m/s and (b) 2.0 m/s. A high scattering can be observed for both velocities.

locities. For 1.0 m/s, two experiments showed a small temperature rise (2.7 K and 5.2 K), three experiments a medium temperature rise (9.5 K, 10.7 K, and 11.3 K), and two experiments a high temperature rise (20.1 K and 24.9 K). These great deviations stems from the undefined deformation behaviour after failure of the PMMA plies, which leads to an arbitrary pull-through of the specimen.

Concluding, a noteworthy heating of the interlayer takes place that is located in its maximum around 25 K. However, high scattering of the measured maximum temperature revealed that the present experimental setup with free edges of the beams was not definite enough to establish reproducible results. Therefore, a clamped bending setup was used in Section 3.4.2 for a more defined experiment.

3.4.2 Clamped Bending Tests

Clamped bending tests were conducted corresponding to the bending setup from Section 3.2.4 but with the specimen fully constrained at both supports, as depicted in Figure 3.38.

Preliminary experiments exhibited that at a support distance of l=60 mm and an overall specimen length of l_s=80 mm failure of the PMMA layers occurred at the impact point as well as on both supports. Therefore, a higher support distance was desirable and with a support distance l_s=120 mm shear loadings of l80 mm and an overall specimen length of at the support were reduced. Experiments were conducted at 1.5 m/s, 2.0 m/s, and 3.0 m/s and IR measurements were performed for all three experiments. Again, all acceleration based data showed some oscillations caused by the experimental setup.

Experimental results are shown in Figure 3.39. The left side represent the force-displacement behaviour, while the right side depicts the IR-temperature measurements. Experiments at 1.5 m/s showed no interlayer failure and exhibited clearly visible recovery. For two of the five experiments at 2.0 m/s the interlayer stayed intact, while for the other three a total laminate failure could be observed. Failure of the PMMA at the support occurred sometimes but not regularly. Furthermore, at some experiments only one side
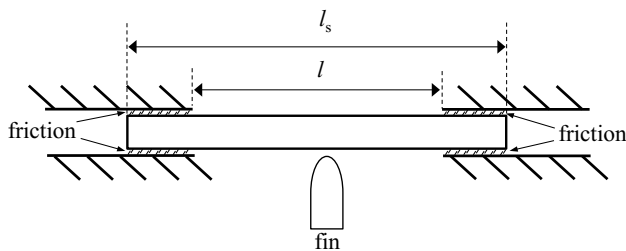
Figure 3.38   Principle of clamped bending tests.

failed, while the other stayed intact. The test can therefore roughly located at the failure threshold for the whole laminate. At 3.0 m/s the total laminate failed in each experiment including rupture of the interlayer under the fin.

Inspection of the tested specimens revealed that failure of the upper and lower PMMA layer did not always occur at the same point of the length axis for both support sides as
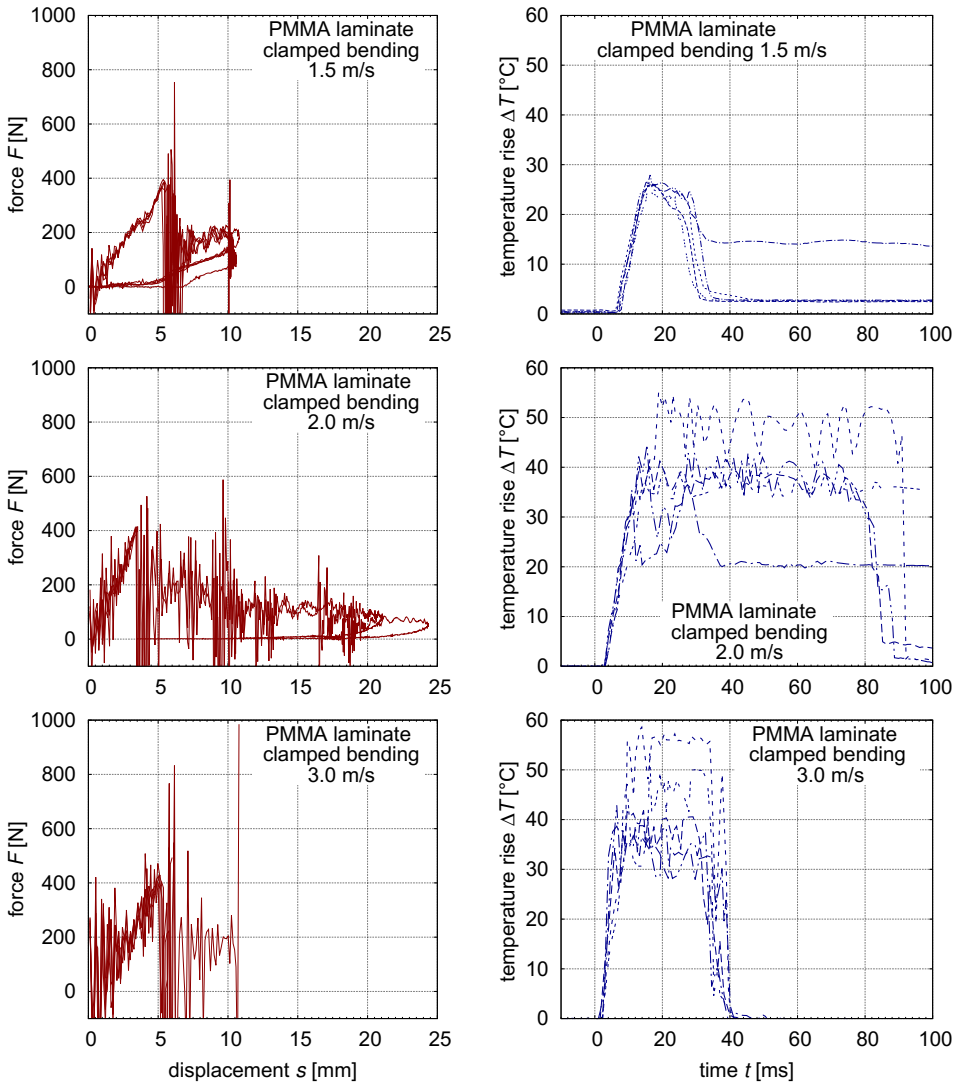
Figure 3.39 PMMA laminate: clamped bending test. Force-displacement and temperature-time behaviour.

well as the impacted point. Multiple force peaks can be observed, which corresponds to failure directly under the fin and at both edges of the clamped support. Experiments at 1.5 m/s showed significantly less maximum deformation than those 2.0 m/s, which is an effect of the prolonged support distance by 20 mm. The pattern on the specimens caused by the clamping led to the conclusion that no visible specimen on both sides could be affirmed. wslippage of the specimen occurred and the assumption of a fully constrained

Compared to the temperature rise of the free bending experiment (Figure 3.37), it is clearly visible that the maximum temperature shows significantly reduced spread, especially for a velocity of 1.5 m/s and 3.0 m/s. Some spreads remain because of the evaluation method of the IR images and the immanent material variance. Maximum temperature rise for experiments at 1.5 m/s is very reproducible at around 25 K. For 2.0 m/s and 3.0 m/s higher values were measured that varied between 35 K and approximately 50 K. The abrupt temperature decreases are not due to heat conduction but by either rupture of the interlayer (3.0 m/s), or the concealing of the interlayer by PMMA through recovery. As discussed in Section 3.1.3, the measurement of the TPU interlayer undergoes high uncertainties due to the unknown transmissivity, which is presumably not constant at high deformations because of thickness reduction.

Concluding, a distinct thermomechanical interlayer heating could be observed. A temperature rise between 25 K and 55 K has a significant effect on the mechanical behaviour, considering the experimental results from Section 3.3.2. The values given for the temperature, however, can only represent rough approximations of the real values, and quantitative interlayer heating measurements requires a deeper insight in future investigation.

3.4.3 Dart Impact Tests

Experiments of this section were performed corresponding to the setup described in Section 3.2.5. The dart impact test is used to investigate the temperature and strain rate dependent high deformation behaviour of the laminate including the total failure of the laminate. Specimens were 80 mm in diameter with a total thickness of 4 mm, according to the structure described in Section 2.3.3. Figure 3.40 shows the result of quasi-static dart tests on the laminate, which was positioned freely on a 70 mm-diameter support, as shown in Figure 3.42.

The experiment was conducted at 1.0 mm/min and was repeated nine times because of the high variation in failure displacement observed during preceding experiments. These experiments characterize the principle behaviour of laminated structures under local impact. First, a continuous slope can be observed until failure of at least one PMMA layer. This first area of deformation shows little scattering of the experimental results. However, the first failure displacement and the resulting force scatter significantly, in this experiment between 1025 N and 2629 N, which is a 156 % higher force related to the smallest max-

imum. This confirm the findings from previous experiments at quasi-static loading rates that quasi-static failure of PMMA specimens undergoes very high scattering.

Further examination reveals that two of the nine specimens (blue dashed lines) showed a second significant rise with a stiffness similar to the initial one. Two experiments failed at a similar early initial point (green chain line) but revealed no second force maximum in this magnitude. The force in all experiments drops to a local minimum between approximately 200 N and 500 N after failure of both PMMA plies. Here, the interlayer becomes dominant and leads to a reproducible post-breakage behaviour. Total failure occurs at very different points of displacement, two experiments showed no interlayer failure at all and reached the maximum possible traverse displacement.

Figure 3.41 depicts the force-displacement behaviour of the laminate under dynamic dart impact loading at 1.0 m/s and 5.0 m/s. Corresponding to the quasi-static test, the force-displacement behaviour of the laminate is characterized by an initial force peak at failure of both PMMA followed by second force peak. The wide scattering observed in the quasi-static experiments, did not occur and the experiments showed high reproducibility, which affirms the findings of Section 3.2.3, Section 3.2.4, and Section 3.2.5 for mono-lithic PMMA. The initial behaviour of the laminate at 5.0 m/s is characterized by multiple impacts leading to a non-continuous slope until first failure.

Experiments at -30 °C, where both materials are in their glassy state, showed a brittle behaviour of the complete laminate with only small post-breakage resistance. Between -30 °C and 0 °C a major change in the post-breakage behaviour can be observed, which can be assigned to the glass-rubbery transition of the TPU interlayer. At room tempera-ture, the post-breakage displacement is enlarged to approximately 35 mm at 1.0 m/s impact velocity. At 60 °C the tendency of higher post-breakage displacement is reversed and only
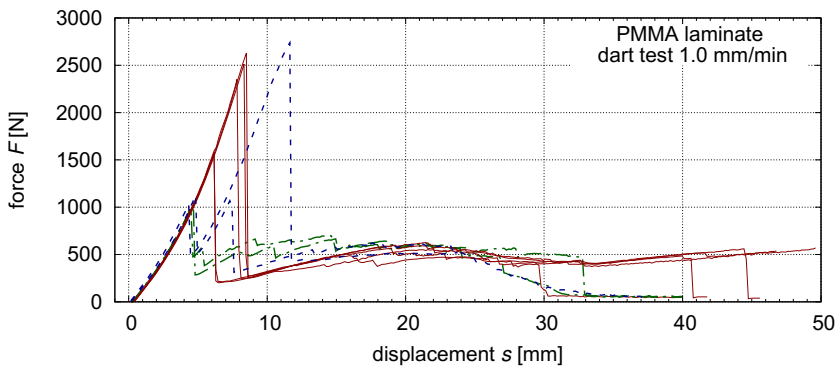
Figure 3.40 PMMA laminate: dart test. Force-displacement behaviour for nine identical specimens at 1.0 mm/min.
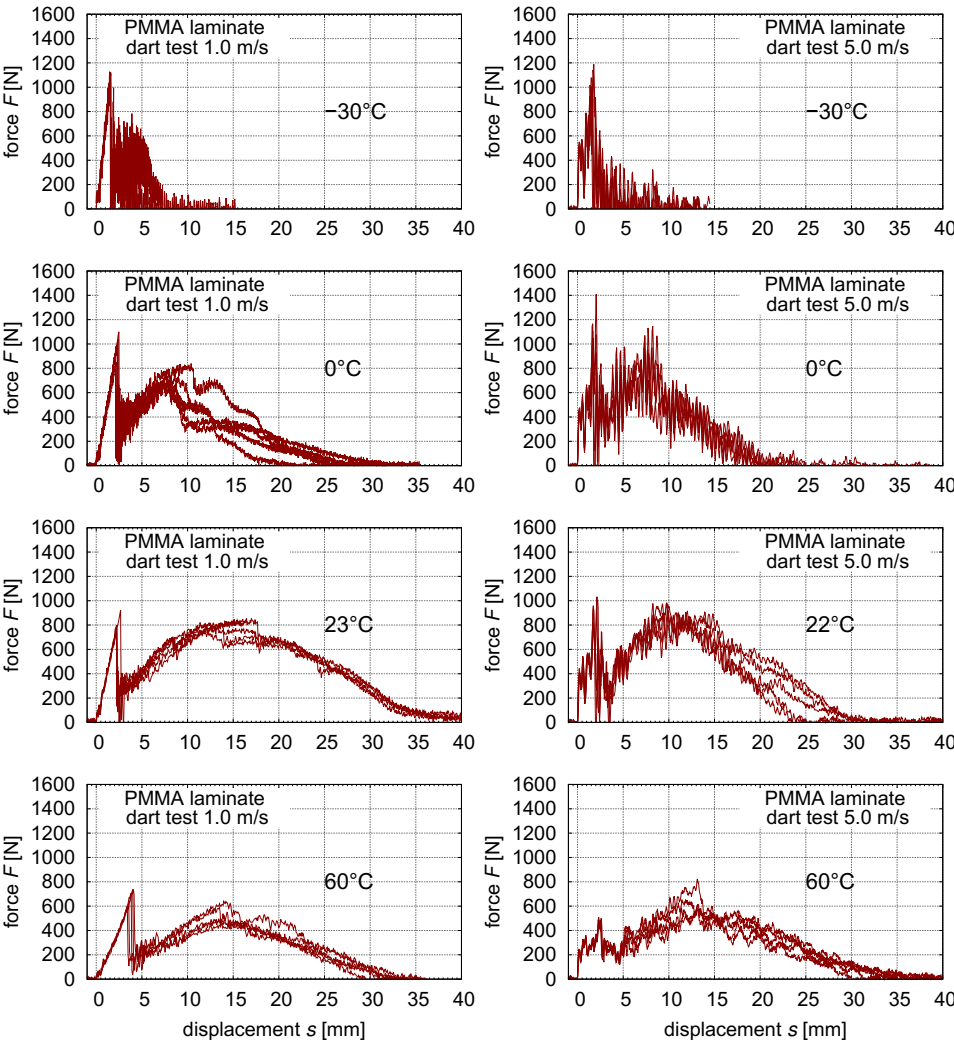
Figure 3.41 PMMA laminate: dart test. Force-displacement behaviour at different temperatures and velocities.
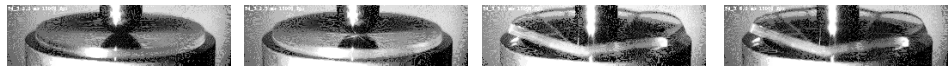
Figure 3.42 PMMA laminate: dart test. High speed images at 22 °C and 5.0 m/s. (1) First load peak, (2) initial cracks, (3) second load peak, (4) interlayer failure.

approximately 30 mm are reached at a generally lower force level, which is caused by the thermal softening of both materials.

Summarizing, the force displacement-behaviour of a laminated structure shows huge advantages compared to monolithic material in terms of post-breakage behaviour and energy-absorption. The specific laminate treated in the present work shows its best impact performance around room temperature. The glass transition area of TPU has a distinct effect on the overall laminate behaviour.

Impact Performance

The impact performance is characterized by the potential of energy absorption and the fracture behaviour of the laminate. Impact energy absorption is obtained by

$$W = \sum_{i=1}^{n} W_i + t_s \frac{F_i v_i + F_{i-1} v_{i-1}}{2}, \tag{3.9}$$

where i is the data point number, W the dissipated energy, t_s the sampling time between each data point and v the velocity. This formula gives respect to the change in velocity as well as the change in force. The difference energy can be formulated globally with the kinetic energy W_{kin} and the potential energy W_{pot} by

$$\Delta W = W_{kin}(t=0) - W_{kin}(t_{end}) - W_{pot}(s_{total}), \tag{3.10}$$

where s_{total} is the potential energy of the total distance the tup traverses. Both Equations show the same result as they use the same data basis. For the subsequent energy calculations Equation (3.10) is used. The energy evaluation of the dart impact experiments is given in Figure 3.43. They summarize the findings of the investigation of the force-displacement behaviour.

A maximum in energy absorption can be observed for the results at room temperature. Below this, breakage of PMMA and TPU shows increasing embrittlement, which leads to less energy absorption. At 60 °C, the reduction in stiffness becomes a more dominant factor, which leads to less energy absorption. Energy absorption shows no significant dependence on the impact velocity, which corresponds to the finding of HAGAN et al. (1961) that the impact strength of polymers for falling heights between 0.3 m (2.43 m/s) and 1.4 m (5.24 m/s) is not or only marginally changed.

Fracture and Delamination

Figure 3.44 shows representative disc specimens of the PMMA-TPU laminate after impact loading of the drop tower exemplarily for a test velocity of 1.0 m/s at different temperatures. The fracture behaviour crucially depends on the temperature. For the low temperatures at -30 °C and partially for 0 °C a brittle fracture was observed. At -30 °C, the parts
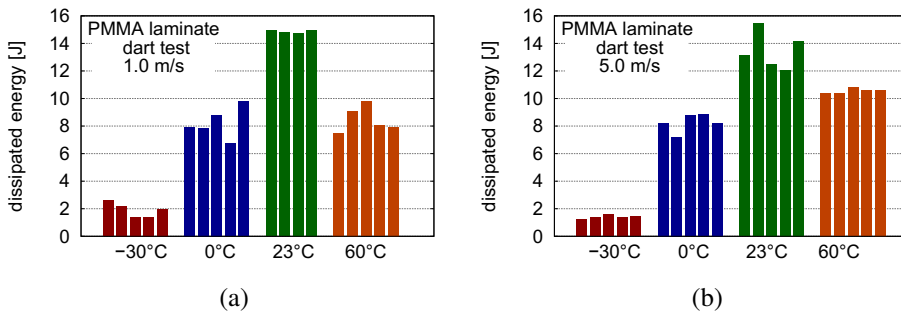
Figure 3.43 PMMA laminate: dart test. Temperature dependent energy absorption. (a) 1 m/s. (b) 5 m/s.

of the specimens were departed completely. For higher temperatures, a more local failure occurs and the laminate remained connected by extant interlayer parts. Furthermore, two kinds of cracks are visible on most specimens. Radial cracks induced by the tup that propagate towards the specimen edges and circular cracks at the support edges.

Delamination appears to increase slightly with higher temperature. Delamination of the laminate can be recognized by the appearance of a currogated interlayer surface, which is visible through the amorphous PMMA. Experiments show that delamination occurs locally around the cracks. Complete delamination of PMMA parts occurred very scarcely only at low temperature experiments. For two different velocities of 1.0 m/s and 5.0 m/s no principle change in fracture form or pattern is found and only fracture pattern from experiments at 1.0 m/s are present. Summarizing, fracture and delamination occur under dart impact testing. The extent and form is temperature dependent. The influence of the delamination on the force-displacement behaviour and, therefore, the impact performance has to be subject to further investigation. As already stated by STENZLER et al. (2011), a significant difference to monolithic material is the more localized failure instead of a global failure area.

3.5 Summary

Basic experiments regarding the mechanical and thermal behaviour of PMMA and TPU were performed. Thermal conductivity k, heat capacity c, and thermal diffusivity κ were determined as a function of temperature. DMTA measurements revealed the viscoelastic behaviour of PMMA and TPU and led to the identification of different relaxation areas, including the glass transition, as well the creation of a master curve. For PMMA, a discrete relaxation spectrum for application in a generalized Maxwell model was obtained.

Uniaxial tensile test at different haul-off velocities confirmed the viscoelastic behaviour observed in the DMTA measurements for both materials. The DIC was used to determine

1 mm/min   1 m/s

-30°C   0°C

23°C   22°C   60°C
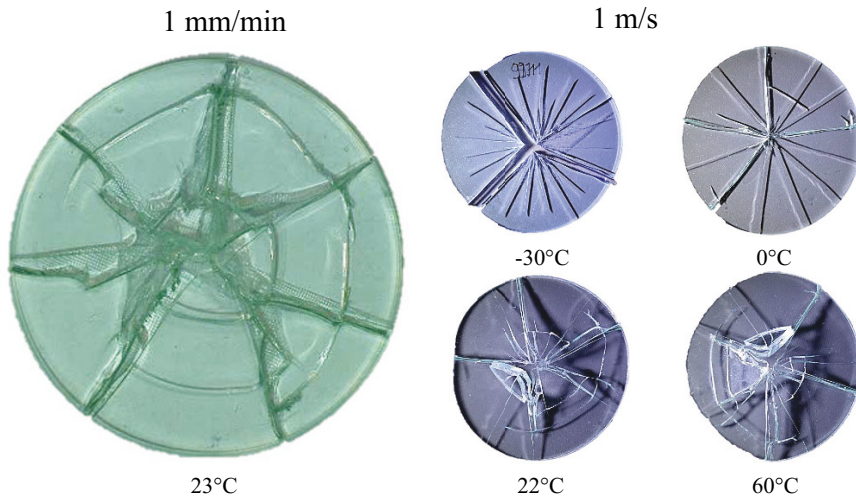
Figure 3.44   PMMA laminate: dart test. Fracture pattern for different velocities and temperatures.

the local stress and strain values as well as Poisson's ratio and the local strain rate, which changes with increasing strain. Failure of PMMA was found to scatter significantly under quasi-static loading rates with coefficients of variation of 0.24 in the tensile test, 0.09 in the bending test, and 0.15 in the dart test. The scattering was reduced for higher strain rates, which was reproducibly shown for uniaxial tensile tests, bending tests and dart tests. Failure strains and displacements decreased significantly with strain rate.

TPU exhibited very high strains until failure, which could not be identified exactly. The stress-strain behaviour, furthermore, exhibited as nonlinear. Two different dynamic uniaxial tensile velocities showed crossing stress-strain curves. A further investigation regarding the influence of permanent effects induced by higher temperatures, as observed by MACALONEY et al. (2007), showed a significant change of mechanical behaviour which is likely to apply to the interlayer used in a laminate. Biaxial plane-stress experiments revealed that the equivalent biaxial and uniaxial stress-strain behaviour deviate, which has to respected in the material modelling in order to consider multiaxial stress states accurately.

Bending and clamped bending tests were used to determine the flexural behaviour of PMMA and PMMA-TPU laminates. The adiabatic heating of the TPU interlayer was observed with high-speed IRT. Significant heating of the interlayer due to high localized strain deformation was observed. For the characterization of the temperature dependent impact performance, dart impact tests were conducted that revealed a high dependence of the absorbed energy on the temperature, where the glass transition of the interlayer has a major effect on the post-breakage behaviour of the laminate.

4 Material Modelling of PMMA

Experiments from Chapter 3 revealed central material characteristics of PMMA in tensile dominated stress states, which are summarized

(1) nonlinear quasi-static stress-strain relationship,

(2) linear viscoelastic behaviour,

(3) small failure strains, and

(4) time- and temperature dependent failure.

Geometries investigated in the present work can be considered as plane shells with thicknesses approximately one magnitude below other dimensions. Impact loadings on shell specimens leads to a tensile dominated specimen and, therefore, the focus is set on modelling the tensile area.

The following sections treat the modelling of the elastic and viscoelastic material response until failure. Subsequently, the temperature influence on the mechanical behaviour is taken into account by investigating the dependence on material constants and the application of the time-temperature superposition. The proposed models are validated with experiments from Section 3.2.

Material model validation was performed with FE-simulations using the commercial FE-solver LS-DYNA (LS-DYNA, 2007) in implicit and explicit calculation mode. Here, fully integrated shell elements (type 16) were used and compared to solid elements with selective reduced integration rule (type 2) in combination with a stiffness-based hourglass formulation (type 5).

Mesh dependence studies of all experiments for the elastic area until failure were carried out with three different mesh densities. Convergence was reached for the shown results and no significant difference between shell and solid elements was observed. Tensile test simulations were conducted with single elements as well as the specimen geometry with negligible deviations. Preliminary studies of the bending and the dart test were performed with quarter models, final simulation results with a full FE-model.

4.1 Linear Viscoelasticity

The conventional approach of modelling linear viscoelastic material behaviour is performed with rheological models, which are treated in Section 2.2.3. Two approaches with linear viscoelastic models are studied subsequently, which are shown in Figure 4.1. A generalized Maxwell model with a linear spring parallel to one respectively two Maxwell elements is referred to as a simplified engineering model. Experimental results from uniaxial tensile tests were used to identify the corresponding material model parameters.

The second approach is of the same type with a significantly raised number of parallel Maxwell elements to represent a wide area of relaxation times. Within this model, experimental data from DMTA results are used for identification of the material model parameters. This second model is referred to as the full linear viscoelastic model due to its additional coverage of the relaxation spectrum.
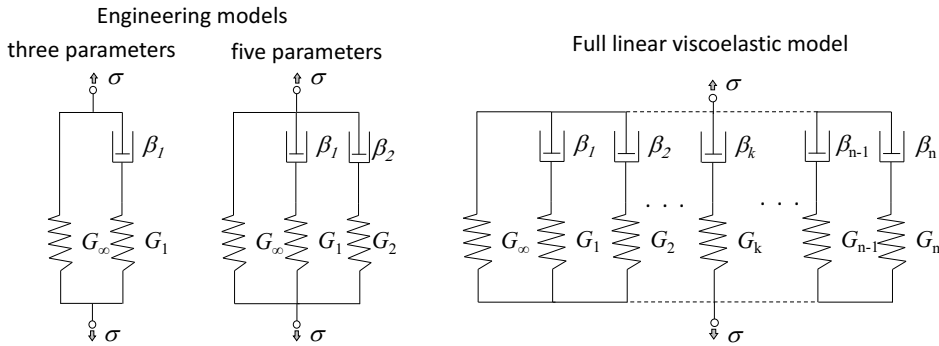
Figure 4.1   Linear viscoelastic models for modelling PMMA.

Engineering Models

Under uniaxial tension, PMMA performs strains up to approximately 6 % in quasi-static tests and 2 % to 3 % in dynamic tests. A linear viscoelastic approach appears appropriate, especially for the dynamic area, because geometric nonlinearities are of subordinate influence. Two engineering models, with of one three and five parameters, were examined.

The parameters of the three-parameter and five-parameter model, which are governed by Equation (2.66) and Equation (2.67), were determined with the least-square method with minimization of the quadratic error between the stress-strain results of uniaxial tensile experiments and simulations. The obtained parameters are given in Table 4.1. With a quasi-static Poisson's ratio (0.36) and an average dynamic Poisson's ratio (0.3), determined in Section 3.2.3, the corresponding bulk moduli of each Maxwell-model were calculated according to Equation (2.39) and assumed to relax with the same decay constant

as the associated shear moduli. This is possible because the FE-solver LS-DYNA enables an additional modelling of volumetric relaxation of the form

$$K(t) = \sum_{i=1}^{n} K_i e^{-\beta t}. \tag{4.1}$$

Therefore, the consideration of the real Poisson's ratio is possible by using the shear and bulk moduli to form a corresponding Poisson's ratio for every relaxation area.

Table 4.1 Parameters of the five parameter generalized Maxwell model for PMMA.

element number	shear modulus G_i	bulk modulus K_i	decay constant β_i
three parameter model			
1	1.84 GPa	2.75 GPa	
2	1.27 GPa	2.75 GPa	$0.129\,\text{ms}^{-1}$
five parameter model			
1	1.27 GPa	4.09 GPa	
2	0.55 GPa	1.19 GPa	$0.01891\,\text{ms}^{-1}$
3	2.92 GPa	6.33 GPa	$60.5913\,\text{ms}^{-1}$

Simulation results of both material models compared to uniaxial tensile tests at different velocities are shown in Figure 4.2 (a) for the three-parameter and (b) for the five-parameter engineering model. Both material models were able to reproduce the principle behaviour of linear viscoelasticity as described in Section 2.2.3. The strain-nonlinearity of the quasi-static test could not be reproduced with this modelling. Deviations for the
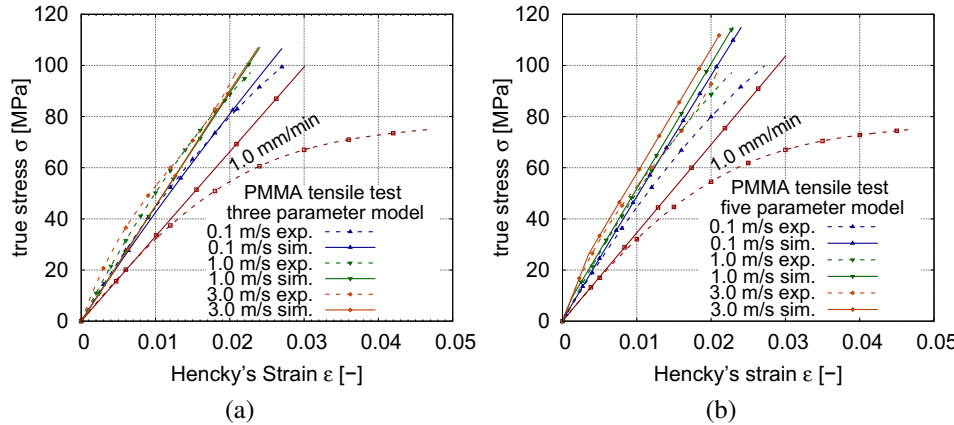
Figure 4.2 PMMA: tensile test. Simulation with a three- and a five-parameter engineering model compared to experimental results.

dynamic increased with higher strains because parameter identification and optimization was performed with respect to the initial stress-strain behaviour.

Bending and dart test at different velocities could be reproduced within this modelling technique likewise. Figure 4.3 shows that all velocities are in good agreement to experimental results. The simulation of quasi-static loadings reproduced the initial behaviour almost identical but deviated from experiments with higher strains. This behaviour is immanent of the applied model that uses a time-independent elastic spring that follows Hooke's law.
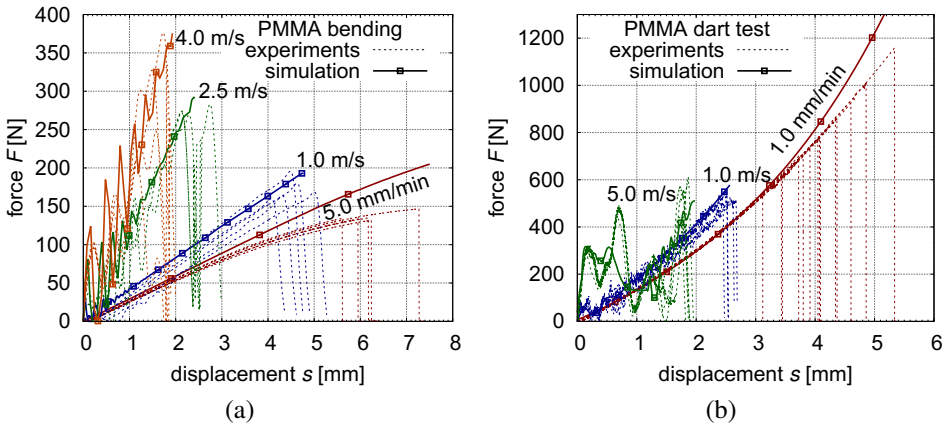
Figure 4.3   PMMA: Simulation of dart and bending test with the five-parameter engineering model.

With the addition of a second Maxwell-element to a five-parameter model, a more distinguished resolution of single velocities could be reached, but the effort for parameter determination was increased. However, differences in the stress-strain behaviour of PMMA under dynamic loading were comparatively small and both models proved to be sufficient for modelling the dynamic tensile behaviour of PMMA.

The kinematics of the experiments in form of oscillations at higher experiment velocities, are also approached by the FE-models. Corresponding to uniaxial tension, the non-linearity at higher strains can not be modelled with linear viscoelasticity. This effect can also be observed in the quasi-static bending and dart tests, where simulations overestimate the average experimental results slightly at higher strains.

Summarizing, the five-parameter engineering models are able to reproduce the elastic and viscoelastic behaviour of PMMA for different tensile-dominated load cases. The main deviation between model results and experiments stem from material nonlinearities that become significant with higher strains. For dynamic load cases, however, the model proved to be appropriate with small numerical effort and straightforward parameter identification.

Full Linear Viscoelastic Model

With parameters obtained from DMTA results in Section 3.2.2, a generalized Maxwell model with eighteen parallel Maxwell elements was created, which is referred to as the full viscoelastic model. The initial 28 Maxwell elements from Section 3.2.2.4, resulting from the premise that every Maxwell element roughly covers one decade of relaxation, were reduced because of current input limitation in the FE-solver LS-DYNA to a maximum number of 18 Maxwell elements.

Generally, only a small number of parallel Maxwell elements are usually used to consider linear viscoelasticity. The reduced number is due to limited numbers of input parameters within commercial FE-solver and validity of DMTA experiments for linear deformations only. As shown before, a small number of Maxwell elements is often sufficient for many problems. Furthermore, the parameter identification from DMTA experiments as presented is comparatively elaborate.

Maxwell elements with a decay constant β higher than 10^4 1/s had no visible influence on the mechanical response within the applied strain rates due to their fast relaxation. Corresponding to the previous section, bulk moduli were calculated for a quasi-static spring with $\nu=0.36$ and for the remaining seventeen springs with $\nu=0.3$ and were assumed to show the same relaxation behaviour as the corresponding shear moduli.

Figure 4.4 (a) shows that the obtained parameters, which are summarized in Table B.3, are able to reproduce the experimental master curve very well for a huge frequency range. In Figure 4.4 (b) the same parameters were used for dynamic simulations of uniaxial tensile tests. Simulation and experiments showed high agreement without any adjustment of parameters. Experiments at 1.0 mm/min and 0.1 m/s could be reproduced very well within the linearity limit. The experiment at 3.0 m/s was underestimated in its initial behaviour but showed high agreement to an average linear fit for the whole strain behaviour.
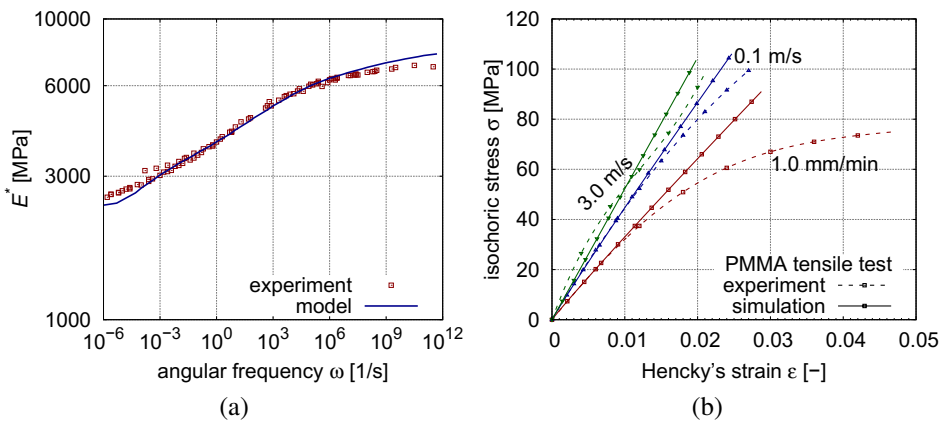
Figure 4.4   PMMA: Full linear viscoelastic model. (a) master curve and (b) dynamic tensile tests.

The elevation at very high and low angular frequencies showed to have no major influence on the uniaxial stress-strain behaviour and agreement between model and experimental was still high. Bending and dart tests were reproduced with an equivalent agreement to the engineering model in Figure 4.3.

The direct transfer from DMTA data to uniaxial tensile test proved to be applicable and described the principle strain rate dependent behaviour. However, minor deviations were observed, which are attributed to

- General measurement uncertainties of both tensile test and DMTA. Especially the temperature measurement of the DMTA experiments may contain some error because temperature could only be measured in the vicinity of the specimen but without contact.

- Difference between the (tensile) elastic modulus E and the tension-compression mixed flexural modulus E_{f}.

- Discrepancies from linear theory. The strain linearity limit for PMMA is located at approximately 0.6 % (OGORKIEWICZ, 1970).

- Deviation from thermorheological simplicity (PEREZ et al., 1999).

Furthermore, the effort for obtaining parameters is comparatively high. A simplified or automated approach to reduce these effort is therefore desirable and engineering models as presented in the previous sections are useful tools within their limitations. However, the full linear viscoelastic model follows a more physically motivation and is, in contrary to engineering models, able to represent a huge relaxation spectrum.

4.2 Hyper-Viscoelasticity

The presented linear viscoelastic models are not able to account for the nonlinearity of the quasi-static experimental results and the application of nonlinear hyperelastic approaches for the elastic spring appears reasonable. The combination of hyperelasticity with viscoelasticity is performed by replacing the linear spring element of the generalized Maxwell model by a nonlinear one, which is governed by a hyperelastic strain-energy function. In the present work, this function consists of a Mooney-Rivlin polynomial, given in Equation (2.52), of the third order combined with a hydrostatic work term $W_{\mathrm{h}}(J)$, which accounts for small dilatation, with

$$
\begin{aligned}
W(\bar{\mathrm{I}}_C, \bar{\mathrm{II}}_C, J) &= \sum_{i,j=0}^{n} C_{ij}(\bar{\mathrm{I}}_C - 3)^i (\bar{\mathrm{II}}_C - 3)^j + W_{\mathrm{H}}(J) \\
&= \sum_{i,j=0}^{n} C_{ij}(\bar{\mathrm{I}}_C - 3)^i (\bar{\mathrm{II}}_C - 3)^j + \frac{1}{2} K (J-1)^2.
\end{aligned}
\tag{4.2}
$$

To limit the parameters of Equation (2.48), all parameters except for C_{01}, C_{10}, C_{11}, C_{20}, C_{02} and C_{30} are set to zero. Parameter identification is performed by the comparison of experimental and numerical uniaxial stress-strain curves, which is performed with a least-square fit. Final parameters are given Table B.2.

Considering only the terms of first order in Equation (2.53), parameters for the hyper-elastic function lead to a shear modulus of $G = 1198$ MPa. With Poisson's ratio of 0.36, which was obtained in Section 3.2.3, E is calculated with 3259 MPa, which corresponds well to the elastic modulus given in Table 2.3 for Plexiglas® 8N.

It has to be noted that parameters obtained this way are only valid for uniaxial loading in the given strain area and their predicted mechanical behaviour may differ significantly from biaxial experiments or further triaxial loading situation.

Since the strain-energy from Equation (4.2) is a function of all three invariants, an isolated uniaxial parameter identification is not sufficient for global solutions. Hence, the hyperelastic parameter fit was undertaken with respect to different stress-states. The results at 5.0 mm/min from the bending test (Section 3.2.4) and the dart test (Section 3.2.5) were used, together with the tensile test results, for a simultaneous parameter fitting using the commercial optimization software LS-OPT (LS-OPT, 2008). This principle, however, is no adequate substitution for biaxial or shear tests, but it exhibited as a stabilizing factor for parameter identification.

The models for the bending and dart simulations are shown in Figure 4.5 with a fringe plot of their state of triaxiality, defined in Equation (2.31), for strains close to failure of the corresponding experiment. The triaxiality factor of the tensile test is very homogeneously time- and place-distributed at 0.33, except in the vicinity of the clamping. For the bending simulation triaxiality varies between -0.4 and 0.5, depending on the investigated integration point. The triaxiality factor for the simulated dart test varied between -0.4 and 0.8 mainly dependent on the thickness coordinate. For an adequate representation of the
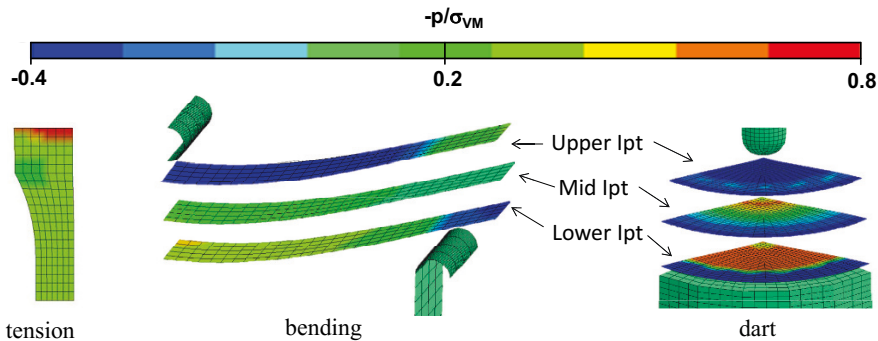
Figure 4.5 Quarter models of tensile, bending and dart test. Fringe plot of triaxiality for strains near fracture in experiment.

mixed tension-compression stress state seven integration point (Ipt) in thickness direction were used for all simulations with shell elements.

Figure 4.5 shows that bending and dart tests bear tensile as well as compressive regions. Due to the tensile dominated failure, the parameter identification is performed with respect to the tensile area predominantly. For small strains, it is assumed that the tensile and compressive stress-strain behaviour behaves identically viscoelastic. Simulation results of the tensile test compared to experimental results are shown in Figure 4.6 (a). Simulation and experiment agree very well for the whole strain area and the quasi-static strain-nonlinearities could be reproduced.

For the viscoelastic contribution, parameters of the five-parameter model, given in Table 4.1, are added to the hyperelastic model. The final set of parameters is given in Table B.2 and the corresponding simulations are compared to experimental results in Figure 4.6 (b). It is clearly visible that the simulations show excellent agreement to experimental results for every velocity.

Despite the very good correlation of experiments and simulations, the model is only valid for the depicted strain range $0 \leq \varepsilon \leq 0.05$. With the given parameter set, uniaxial strains above 0.05 deviate increasingly from realistic behaviour. This is typical for strain energy functions that depend on two or three invariants but their parameters are not identified with sufficient triaxiality data and only for a small strain area. However, the model shows the principle capability of modelling the nonlinear material behaviour accurately.

Results from the uniaxial tensile test can be transferred to the bending and dart test as well, which is depicted in Figure 4.7 (a) and (b). Quasi-static nonlinearities could be approximated significantly better than with the linear viscoelastic model. The dynamic area of both tests is approximated very well. The 1.0 m/s experiment of the dart test is
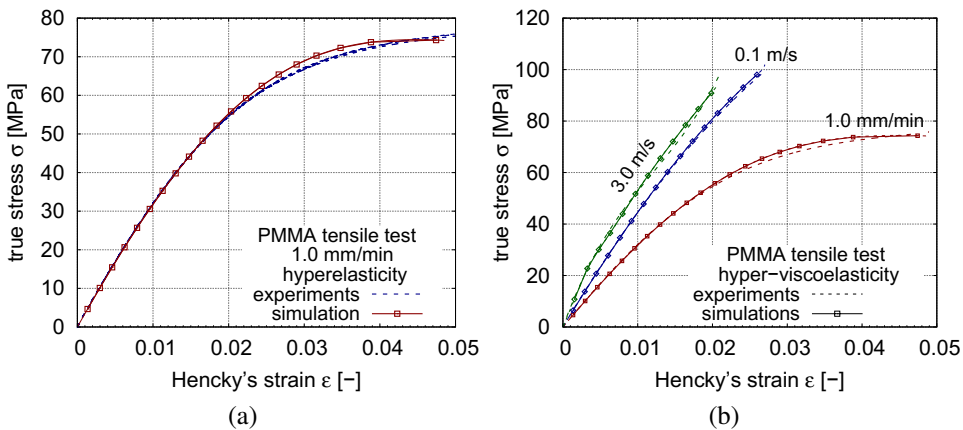
Figure 4.6   PMMA: tensile tests. Experiments and hyper-viscoelastic simulations compared.

also reproduced satisfactory, whereas the simulation the 5.0 m/s experiment shows already deviations in the initial stiffness.
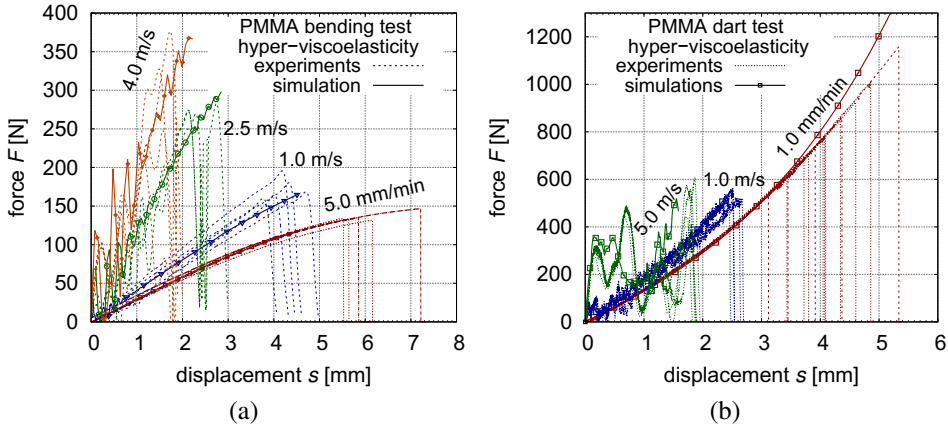
Figure 4.7   PMMA: bending and dart tests. Simulations and experiments compared.

With the presented material models, the mechanical characterization of PMMA is complete. Concluding, linear viscoelastic as well as hyper-viscoelastic models are able to represent the dynamic behaviour of PMMA under tension, bending, and dart impact loading. With the focus of the present work set on dynamic loading rates, both techniques can be applied with equal simulation results. The hyper-viscoelastic model, however, is accompanied by higher computational effort as well as an increased complexity in parameter identification. Thus, the linear viscoelastic model proved to be the most adequate for all presented dynamic load cases and was used henceforth.

4.3 Thermo-Hyperviscoelasticity

To consider the temperature dependence of PMMA, both parameters of the hyperelastic and viscoelastic models can be modelled as functions of temperature. As a first approach the hyperelastic constants C_{10} and C_{01} are applied as values of temperatures. According to Equation (2.53), this corresponds to a scaling of the first-order shear modulus. For this purpose, results from DMTA experiments obtained in Section 3.2.2 are used. Here, values for G represent the flexural shear modulus and scale factors are obtained referring to the flexural modulus at $25\,°C$. The resulting temperature dependent shear modulud G is depicted in Figure 4.8 (a) with the clearly visible glass transition at approximately $110\,°C$.

Simulation were then performed thermo-mechanically with the temperature dependent hyper-viscoelastic mechanical material model from Section 4.2 and an isotropic thermal material model. For the thermal material model. properties obtained in Section 3.2.1 were

used for modelling thermal conductivity k and heat capacity c as functions of temperature. The behaviour of this thermo-hyperviscoelastic model is shown for different temperatures in Figure 4.8 (b) for uniaxial tensile tests at different temperatures. The test at room temperature is compared to the uniaxial tensile test at $23\,°C$ and shows good agreement, except for small deviations at higher strains.

Simulations show to reproduce the temperature dependent behaviour well for all temperatures, especially at small strains. The deviations at higher strains do not play a major role in the subsequently performed crash analysis because failure occurs earlier at higher loading rates.

Summarizing, the temperature dependent modelling of the hyperelastic parameters appears as a very good phenomenological approach as the DMTA could be used directly without any further processing. However, the technique does not account the time-temperature shift and the overstress resulting from Maxwell-elements remains unaccounted by temperature.
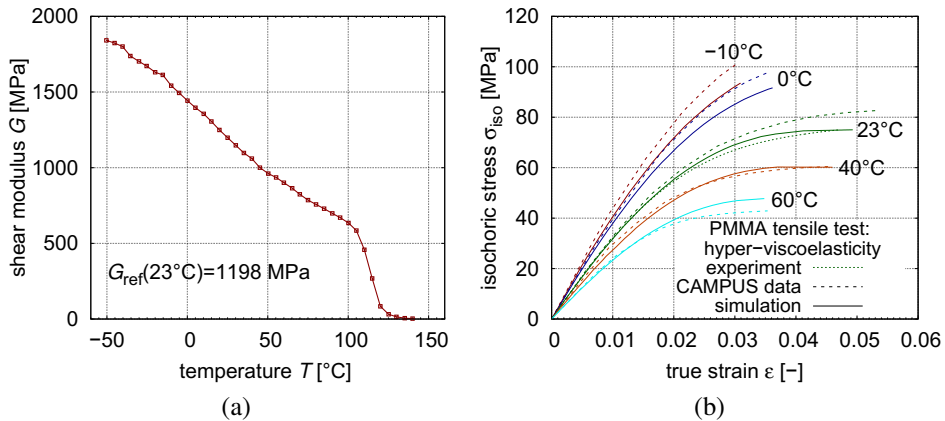
Figure 4.8 PMMA: (a) Model for temperature dependence of shear modulus G. (b) Temperature dependent simulations compared to data from CAMPUS® (2016).

4.4 Linear Thermoviscoelasticity Using the Arrhenius Shift Equation

A second approach to model temperature dependence is the time-temperature superposition correlation. A scaled time

$$t' = \int_0^t a_{\mathrm{T}}(T)\mathrm{d}t \tag{4.3}$$

is calculated within the FE solver using either the WLF or the Arrhenius function, and then used for the replacement of the physical time. This procedure corresponds to the master-curve shift performed in Section 3.2.2 and the Arrhenius shift approach is used likewise.

The elastic infinite elasticity G_∞ shows by definition no dependence on temperature because it is not coupled with a relaxation time. Following this approach, quasi-static calculations that effectively activate only the infinite spring will show no temperature dependence. Temperature-dependent experiments from CAMPUS® (2016) (Figure 4.8 b), however, show a temperature dependence at a quasi-static velocity that is significantly beyond a shift of overstress portions. The assumption that the elastic modulus is completely time- and temperature independent is therefore not sufficient.

Temperatures above the glass transition, which are usually beyond the application scope for glassy polymers in window applications, were not considered. The Arrhenius approach can only be seen valid up to temperatures of approximately $50\,°C$ (compare to Section 3.2.2). At higher temperatures, higher deviations are immanent.

Engineering Linear Viscoelastic Model

The simplified approach shows validity for a certain range of relaxation times only. Hence, this model is limited to temperature dependent dynamic tests. Arrhenius parameters from Table 3.2 are added to the five parameter Maxwell model from Section 4.1. For brevity, three different test temperatures are shown for the dart test of 1.0 m/s and 5.0 m/s in Figure 4.9. An apparent β-relaxation activation energy of 112.6 kJ/mol (Table 3.2) was applied at a reference temperature of $23\,°C$, which corresponds to the reference temperature for the master curve generation in Section 3.2.2.

Concluding, the Arrhenius shift function is not applicable on the engineering viscoelastic model in order to simulate temperature dependence of PMMA correctly. This is caused by insufficient resolution of the relaxation spectrum. For an adequate representation of temperature dependence the relaxation spectrum has to be considered more accurately resulting in a significantly higher amount of Maxwell elements.

Full Linear Viscoelastic Model

The full isothermal linear viscoelastic Maxwell model uses the structure from Section 4.1 combined with the Arrhenius shift function. Preliminary simulations exhibited that the physical β-relaxation energy of E_A=112.6 kJ/mol was insufficient to capture the temperature range between -30 °C and 60 °C adequately. A least-square fit for the uniaxial tensile test at different temperature was used to determine a phenomenological value of E_A=226.2 kJ/mol in order to reproduce experimental results best with the developed model. Furthermore, the relaxation spectrum had to be changed significantly, in order to
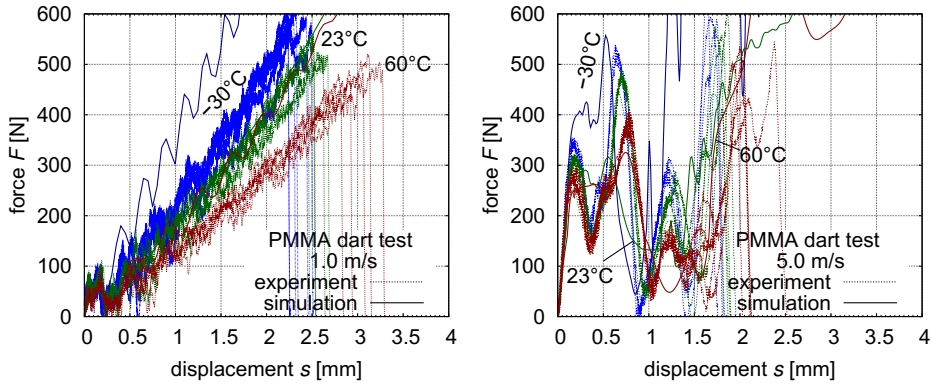
Figure 4.9 PMMA: dart test. Simulation of temperature dependence with the five-parameter engineering model.

capture the strain-rate dependent behaviour (Figure 4.10 a) and model the temperature dependence (Figure 4.11). This parameter adjustment led to a significant deviation from the relaxation master curve shown in Figure 4.10 (b).

The reasons for the deviating phenomenological value of E_A from its physical value are presumably the same as already stated in Section 4.1. Especially the limitation of DMTA experiments to small strains appears to be accountable for the deviation from the experimental activation energy as well as other literature values. Figure 4.11 depicts the result for uniaxial tensile tests and dart tests at 1 m/s compared to experimental results representatively. The results of uniaxial tensile tests at different temperatures are presented
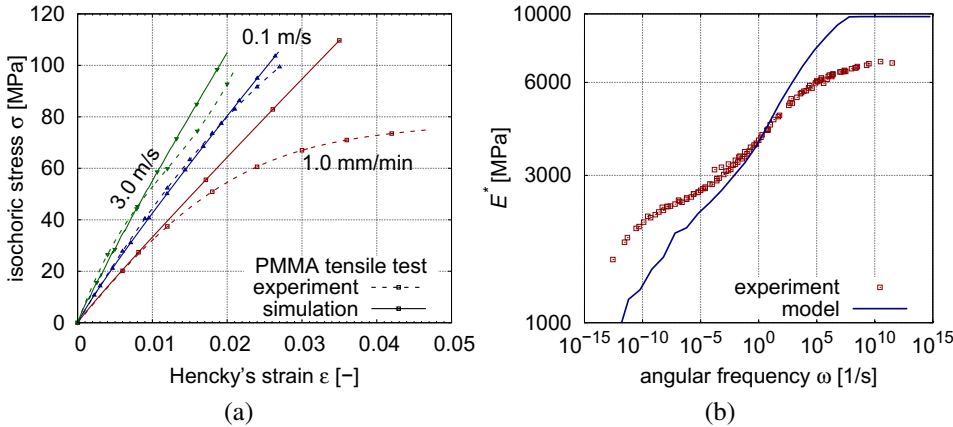
Figure 4.10 PMMA: tensile test. Full linear viscoelastic model with adjusted parameters for thermal simulations.
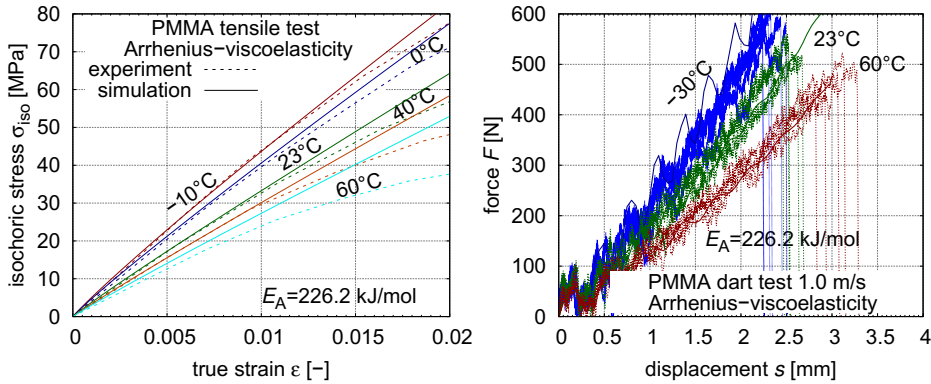
Figure 4.11 PMMA: simulation of temperature dependence with the full linear viscoelastic model. (a) Uniaxial tensile test. (b) Dart test at 1.0 m/s.

in Figure 4.11. As shown in Section 4.11, the Arrhenius function shows greater deviations from experimental results at temperatures above $40\,^\circ\mathrm{C}$.

The full linear viscoelastic model is able to cover temperature dependence of quasi-static and dynamic tests, but under time consuming parameter identification and cost-efficient simulations performed in Section 3.2.2. A direct transfer of the Arrhenius activation energy showed to be insufficient to model the full strain area behaviour and had to be adjusted with supplementary optimization. The same activation energy used for the uniaxial tensile test and the dart test, however, showed good results in modelling the temperature dependence. Therefore, the activation energy appears to transferable to other load cases.

4.5 A Simplified Failure Criterion

Conventionally, failure and pseudo-crack modelling in the explicit FEM is usually realized by element deletion. When an element is deleted, the energy of the element is removed from the calculation, which can be seen as an equivalent to the energy dissipation by crack propagation. A maximum principal stress criterion was chosen for PMMA causing the element to fail as soon as one integration point reaches the critical stress.

The failure behaviour was investigated using the linear viscoelastic model for reasons of calculation time efficiency and comparability to the PMMA-TPU laminate simulations from Chapter 6. Investigation regarding the influence of triaxiality on the failure behaviour have not been performed in the present work and a simplified approximation was chosen in this work. A failure stress of $132\,\mathrm{MPa}$ with a standard deviation of approximately $\pm 20\,\mathrm{MPa}$ would satisfy the stochastic failure for different strain rates at room temperature. However, for the deterministic simulation a constant value for the failure stress has to be

used for all experiments at room temperature, which covers the failure of every experiment satisfactory in average.

Related to the theory by REE and EYRING (1958), FLECK et al. (1990) used a strain rate and temperature dependent criterion for shear deformations, which gives the shear failure stress

$$\tau_{\text{fail}} = \frac{1}{V_{\text{fail}}}\left(E_{\text{fail}} + k_B T \ln\frac{\dot{\gamma}}{\dot{\gamma}_0}\right),\tag{4.4}$$

where E_{fail} represent an activation energy, V_{fail} a corresponding activation volume, k_B Boltzmann's constant, T the temperature, and $\dot{\gamma}$ as well as $\dot{\gamma}_0$ for the shear strain rate and reference shear strain rate respectively. ANTOINE et al. (2014) used this as maximum tensile stress based criterion according to

$$\sigma_{\text{fail}} = \frac{1}{V_{\text{fail}}}\left(E_{\text{fail}} + k_B T \ln\frac{\dot{\varepsilon}}{\dot{\varepsilon}_0}\right),\tag{4.5}$$

and gives corresponding parameters with $E_{\text{fail}}=2.95\cdot10^{-19}$ J, $V_{\text{fail}}=2.30\cdot10^{-18}$ mm^3, and $\dot{\varepsilon}_0=1.0$ 1/s. At room temperature failure stress is then calculated with 136.4 MPa for a strain rate of 100 1/s, 132.4 MPa for a strain rate of 10 1/s, and 128.3 MPa for a strain rate of 1 1/s. Therefore, a value of 132 MPa appears as a reasonable average value. However, a constant failure stress does not satisfy the real material behaviour and further failure criteria, including crack propagation have to be subject to further works. Calculations of the failure stress from Equation (4.4) are compared to experimental results of monolithic PMMA experiments in Figure 4.12. The failure stress was obtained by simulation of the experiments and iterative adjustment for the maximum principal stress criterion, so that the first failure of the simulation occurs at the maximum failure force or stress respectively of the corresponding experiment. It was observed for several simulations that an adjustment within ± 5 MPa had no influence on the failure, which is partially a result of a too small data acquisition rate. From Figure 4.12 can be deducted that the failure stress, modelled by a maximum principal stress element deletion criterion, is temperature- and rate dependent and shows additional dependence on the load case. Consequently, a constant failure stress can only be seen as a rough approximation.

Results of the simulation of the bending and dart tests are shown in Figure 4.13. Failure stress of dynamic uniaxial tensile test is overestimated by 21 %, while the failure stress of bending and dart test is within 13 % of the original failure value. The resultant crack velocity, however, is far below the real crack propagation velocity. Because the failure stress only applies to dynamic failure, quasi-static loading rates are not considered any further in the numerical part. The high scattering failure mechanisms occurring here would require further thorough investigation and stochastic criteria eventually.
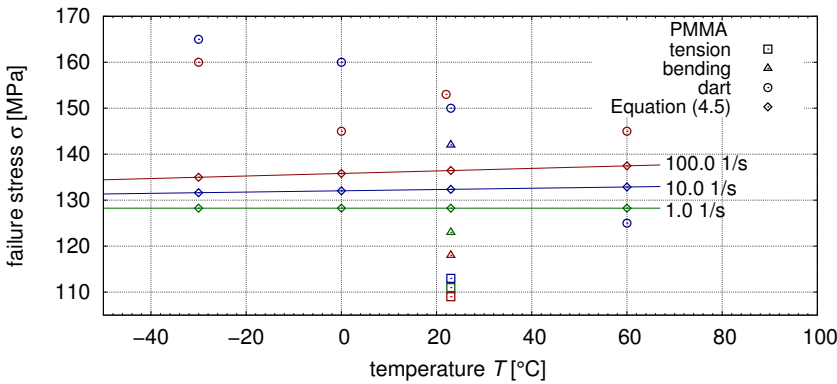
Figure 4.12 Maximum principal stress failure values determined from simulations compared to calculated values from Equation (4.5). For each experiment, the sort sequence starting with the highest velocity is red–blue–green. The corresponding velocities are documented in Section 3.2.
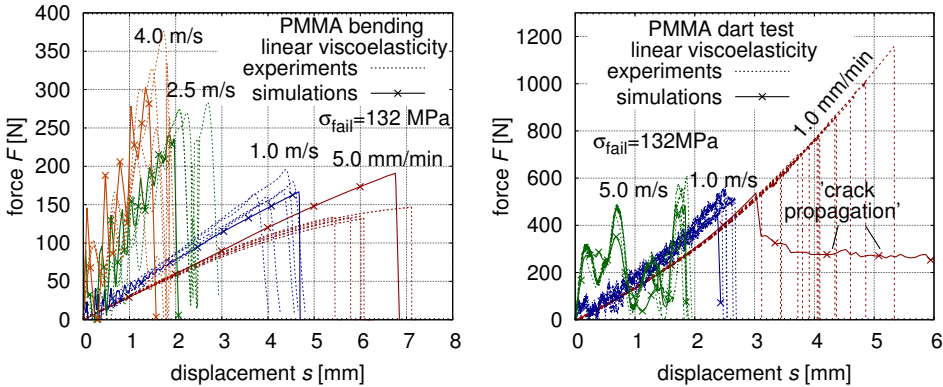
Figure 4.13 PMMA: bending and dart test, simulation of failure with a maximum principal stress criterion.

Element deletion is strongly affected by the mesh density and mesh convergence can only be reached by additional methods, for example regularization. The principle mesh dependence is shown the dart test at 5.0 m/s and three different mesh densities. The coarsest mesh is depicted in Figure 4.14, which corresponds to an average element edge length of 1 mm. Approaches like the XFEM, which uses discontinuous displacement approaches appears promising for further work regarding accurate failure modelling. The XFEM is based on the work by BELYTSCHKO et al. (1999), and has by now been treated and discussed in various other works (DOLBOW et al., 1999, FRIES et al., 2006).

Summarizing, local element deletion is a very cost-efficient, yet rudimentary and mesh-dependent approach for modelling material failure. Its application, however, is current
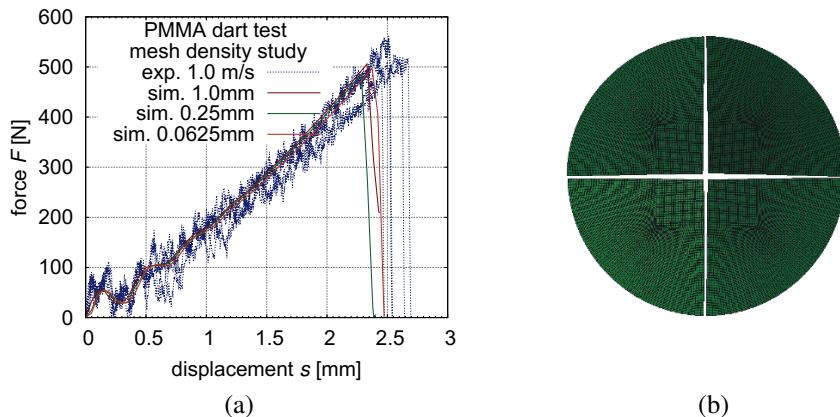
Figure 4.14   PMMA: (a) dart test simulation at 1.0 m/s for different element edge lengths (b) fracture pattern with 1 mm element edge length.

state of the art in many applications because of the lack of alternatives that combine easy applicability with cost-efficient calculation times.

4.6 Summary

Linear viscoelastic, hyper-viscoelastic and thermo-hyperviscoelastic models to represent the temperature and time dependent behaviour of PMMA were presented. All three models showed a good representation of the time-dependent mechanical behaviour. Additionally, the hyperelastic formulations enabled to model the nonlinear quasi-static behaviour accurately. Bending and dart tests revealed that the viscoelastic parameters obtained from uniaxial tensile tests could be successfully applied to other tensile dominated stress triaxialities.

Two approaches for modelling the temperature dependence of PMMA were shown and discussed. Temperature dependence was adequately modelled with scaling of hyperelastic parameters for a Mooney-Rivlin polynomial. For this, results from DMTA experiments were directly used for scaling of the linear hyperelastic parameters with very good correlation of simulations to experiments. A second approach, which used Arrhenius parameters obtained from DMTA results, showed to be able to model this behaviour, too, but with a significantly adjusted activation energy.

Failure was modelled using a maximum principal stress criterion with a fixed failure stress of 132 MPa. The high failure point scattering of PMMA under quasi-static loading rates was not approached in the present work. Stochastic methods and detailed crack modelling appear to be a promising tool for this problem.

5 Material Modelling of TPU

Experiments from Chapter 3 exhibited central material characteristics of TPU under tension that are summarized as

(1) large (elastic) strains until failure,

(2) nonlinear elastic behaviour,

(3) time- and temperature dependence (viscoelasticity),

(4) dependence on triaxiality, and

(5) adiabatic heating during deformation.

In the following sections these characteristics are considered in different material modelling techniques with an investigation of possibilities and limitations of the current available material models. With the focus on dynamic single-time crash events, the recovery behaviour, Mullins' effect (QI et al., 2005) or ageing are not considered. The focus is set on tensile dominated stress states only according the experiments from Section 3.3. For the FE simulation, solid elements with a reduced integration rule were used in combination with a stiffness-based hourglass formulation.

5.1 Hyperelasticity

Conventionally, interlayer materials were modelled with pure hyperelasticity. An overview of hyperelastic models that are used for laminated glass in crash analysis is given in DU BOIS et al. (2003). Typical hyperelastic strain energy functions show no time dependence and are therefore not capable of modelling strain rate dependence. Yet, experiments from Section 3.3 showed that the influence of time and temperature has significant effects and a consideration of strain-rate and temperature dependent behaviour is crucial.

Due to the general incapability to model viscoelastic behaviour, which includes temperature dependence and dissipation processes, pure hyperelastic models are not considered any further in the present work but are used within the hyper-viscoelastic model presented in Section 5.3.

5.2 Tabulated Hyperelasticity

An approach for the combination of hyperelasticity with rate effects was presented in KOLLING et al. (2007). Here, hyperelastic functions are used for different strain rates and an array of curves describes the strain rate dependence. The advantage of the model from KOLLING et al. (2007) is a direct input of uniaxial stress-strain curves for different strain rates obtained from uniaxial tensile tests into the FE solver. By this, extensive parameter identification can be omitted, while rate dependence is considered. The simplification to uniaxial data answers the frequent lack of biaxial and shear data in daily industrial practice. Hysteresis can additionally be modelled by a damage function. The model uses the strain energy function by HILL (1979), which is defined as

$$W(\lambda_1, \lambda_2, \lambda_3) = \sum_{i=1}^{3} \sum_{j=1}^{m} \frac{\mu_j}{\alpha_j} \left(\lambda_i^{\alpha_j} - 1 \right) + \frac{1}{n} \sum_{j=1}^{m} \frac{\mu_j}{\alpha_j} \left(J^{-n\alpha_j} - 1 \right), \qquad (5.1)$$

where μ and α are material parameters. With Hill's energy function Poisson's ratios between 0.0 and 0.5 are possible, and a more generalized formulation than with an Ogden energy function is reached. For ν close to 0.5 the Ogden energy function is obtained. With different strain energy functions for every strain rate, a set of constant strain rate curves (Figure 5.1 a) is required. The model is then able to interpolate between two curves but does not extrapolate beyond the limiting curves.

For obtaining stress-strain curves at constant strain rates, uniaxial tensile test results from Section 3.3.3 were used to determine the parameters of a polynomial function $\sigma(\varepsilon, \dot{\varepsilon})$, which describes the stress-strain-strain rate behaviour (RÜHL et al., 2012a). Experimental data from Section 3.3.3 were used to identify parameters for a function to describe the material behaviour using a phenomenological approach. For this, the Johnson-Cook model (JOHNSON et al., 1983) was modified to

$$\sigma(\varepsilon, \dot{\varepsilon}) = [A \ (\varepsilon - \varepsilon_0)^n] \left[1 + C \ln \left(\frac{\dot{\varepsilon}}{\dot{\varepsilon}_0} \right) \right] \qquad (5.2)$$

and parameter A, n, and C were determined with a least-square fit. With the obtained parameters stress-strain curves at constant strain rates could be created and were used as input curves for the tabulated hyperelastic model. The corresponding surface of Equation (5.2) is shown in Figure 5.1 (b) compared to experimental results of the uniaxial tensile test. Here, the strain rate dependence can be reproduced well for different strain rates and high strains. Dashed, black lines, represent engineering stress-strain curves at constant strain rates for every decade, where the lowest curve stands for a strain rate at 10^{-3} 1/s. However, the implemented version in LS-DYNA offers no possibility to model the temperature dependent behaviour, except for the usage of different isothermal material parameter sets.
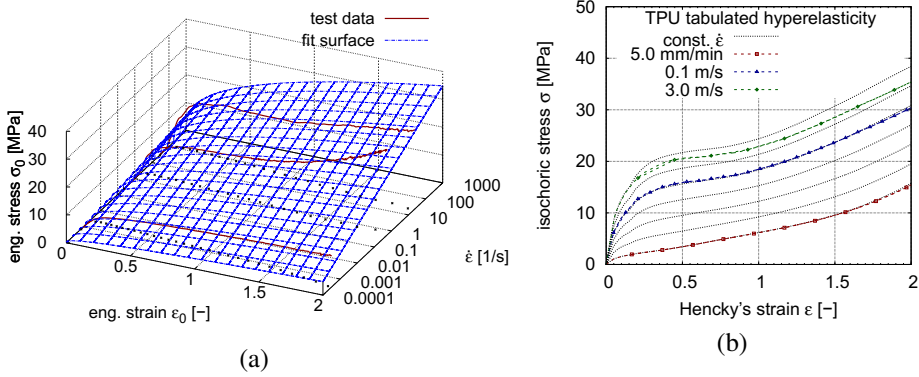
Figure 5.1 TPU: (a) fit surface for obtaining constant strain rates. (b) Simulation of uniaxial tensile test.

5.3 Hyper-Viscoelasticity

This modelling technique, which was already presented in Section 4.2 for PMMA, was used in ANTOINE et al. (2014), LOPEZ-RUIZ et al. (2015) and KOLLING et al. (2015) for the interlayer of polymeric laminates and LSG. ANTOINE et al. (2014) used an Ogden based energy function, while LOPEZ-RUIZ et al. (2015) and KOLLING et al. (2015) used a Mooney-Rivlin polynomial.

SCHYMANIETZ (2016) showed for PVB, a similar high-strain interlayer material as TPU that the Ogden and the Mooney-Rivlin model are capable of modelling the strain-rate independent mechanical behaviour very adequately. An additional consideration of biaxial stress-states confirmed these energy function as sufficient. The Arruda-Boyce model (ARRUDA et al., 1993) showed in preliminary studies to model the nonlinear behaviour PVB well under uniaxial and biaxial deformation. Furthermore, QI et al. (2005) applied a nonlinear hyperelastic part and a viscoelastic-plastic addition with parameters motivated from the molecular structure.

Limitations of the material models are in general nonlinear viscoelastic material behaviour and the resolution of single strain rate curves with a limited number of Maxwell elements. Parameter identification for TPU was reported by QI et al. (2005) to be hardly accountable for a phenomenological model.

KOLLING et al. (2015) showed that due to the highly nonlinear behaviour of the PVB interlayer, it was not possible to model both the quasi-static and the dynamic behaviour with one parameter set. Modified input parameters were used for the Mooney-Rivlin polynomial function that deviate from the quasi-static curve in order to represent the dynamic strain rate area exclusively. Another limitation is a quasi-isochoric assumption of most of these functions.

Corresponding to the modelling of PMMA in Section 4.2, the parameters of the polynomial given in Equation (4.2) are identified with uniaxial quasi-static tensile experiments from Section 3.3.3. Parameter identification showed to be more complex due to the high strains of the material. Furthermore, experiments at 0.1 m/s were excluded from the parameter identification process because of curve crossing (Section 3.3.3). Two sets of parameters were determined from uniaxial data for the hyperelastic function. The first one used the experimental data of the first 100 % of strain. The results of verification simulations are shown in Figure 5.2 (a). The velocity of 5.0 mm/min was simulated without Prony-terms as purely hyperelastic. A second parameter set was subjected to the overall strain behaviour until approximately 170 % of Hencky's strain.

Both parameter sets show to be capable of capturing the stress-strain relation of TPU very well until 100 % true strain, while the set from Figure 5.2 shows good results for higher strains, too. The second parameter set exhibited numerical stability issues at higher strains when using the full tensile bar specimen geometry or within the simulation of a laminated structure by a premature error termination. Therefore, the first parameter set was used henceforth for the interlayer simulation within a laminate. Additionally, it has to be pronounced that both parameter sets were obtained by uniaxial tensile test data only with no validation of biaxial stress states.

The viscoelastic response was modelled with six Maxwell elements for both hyperelastic parameter sets. The parameters of the Maxwell elements were optimized using dynamic uniaxial tensile tests. The results for both final parameter sets are shown in Figure 5.2 (a) and (b). The hyper-viscoelastic model shows to represent the isothermal uniaxial tensile behaviour including a strain-rate dependent behaviour well. Comparison of the simulation to experimental results both considered velocities are reproduced even for high strains.
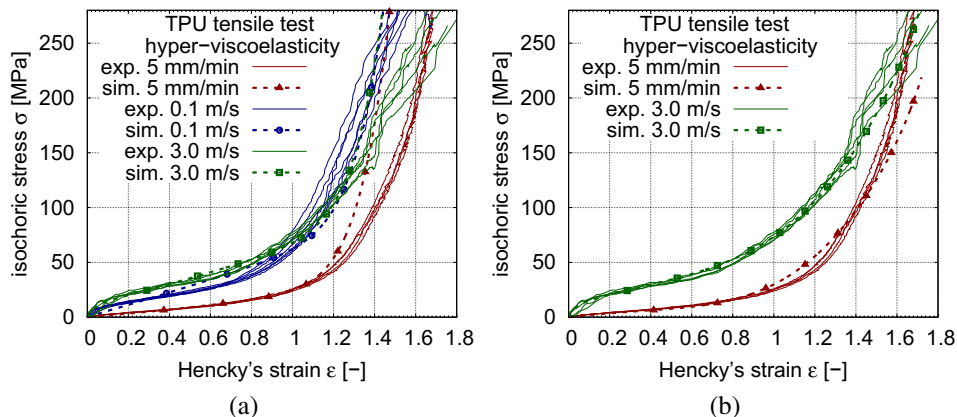
Figure 5.2 TPU: tensile test. Hyper-viscoelastic simulation (a) with respect to the first 100 % of strain and (b) for the whole strain area.

Concluding, the hyper-viscoelastic model could reproduce the uniaxial strain-rate dependent behaviour of TPU well. However, a validation of the material behaviour was only performed for the uniaxial tensile stress state. The reproduction of biaxial stress states would require further adjustment of the parameters, which would result in a simultaneous uniaxial and biaxial parameter identification. For clarity it is stated here, that for the simulation within the laminate, presented in Chapter 6 and 7, the parameter set determined for the first 100 % of strain was used. The difference between both parameter sets exhibited as only marginally influential on the overall laminate behaviour. This motivates the usage of simple and robust engineering models when solely the overall laminate behaviour is of interest.

5.4 Thermo-Hyperviscoelasticity

Modelling of temperature dependence was realized by using the hyper-viscoelastic model from Section 5.3. Here, data from DMTA experiments were used to scale the parameters C_{10} and C_{01} for the polynomial from Equation (4.2). This technique was successfully performed in Section 4.3 for PMMA with good agreement to experimental results. As a reference temperature 25 °C was chosen.

Considering this parameters study, a temperature of -85 °C would lead to a scale of C_{10} and C_{01} by 13.58 and a temperature of 135 °C to a factor of 0.03. Figure 5.3 shows the simulation of the uniaxial tensile test at different temperatures at 5.0 mm/min and 3.0 m/s.

However, temperature dependent uniaxial tensile tests were not performed in the present work and the models. An indirect validation will be performed by the temperature dependent simulations of the laminate. Furthermore, the qualitative form of the stress-strain curves of Figure 5.3 correspond well to experimental results from ZHANG et al. (2015). Therefore, the simulation model appears as a reasonable approach.

5.5 Adiabatic Heating

In order to investigate the influence of dissipative heating on the mechanical behaviour in terms of thermal softening, the hyper-viscoelastic model was extended to capture thermal effects additionally. The thermomechanical simulations are able to convert a constant fraction of the strain energy W into heat. The calculation is performed according to Equation (2.89), but also considers elastic parts and therefore the whole strain energy.

Figure 5.4 (a) shows the influence of the thermomechanical heating with a complete conversion of the strain energy into heat and the hyper-viscoelastic parameter set from Section 5.4. Due to thermal softening the stress-strain behaviour is reproduced worse than without heating. Therefore, a new optimization considering thermal softening was applied. The outcome is shown in Figure 5.4 (b). The obtained parameter set is able to capture
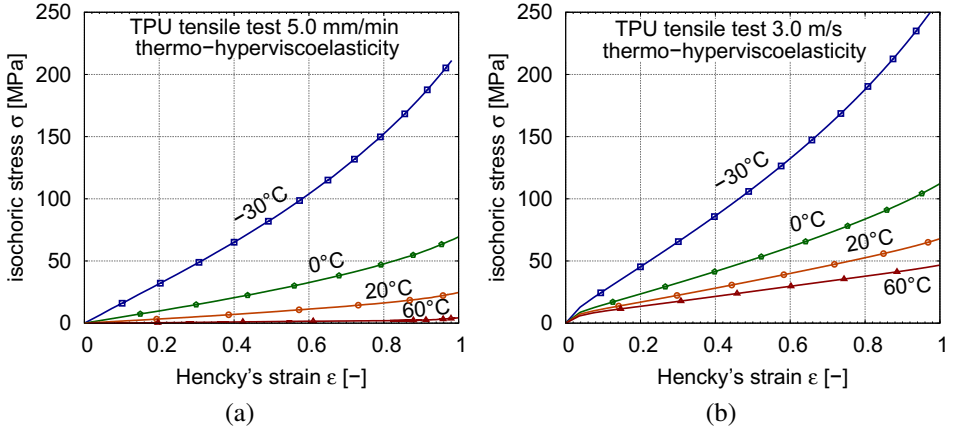
Figure 5.3 TPU: tensile test. Simulations at (a) 5.0 mm/min and (b) 3.0 m/s.

the stress-strain behaviour at all experimental velocities well. Moreover, a reasonable amount of heating is reached and crossing of both dynamic experimental curves is reached eventually. The simulations show that adiabatic heating can reproduce these curve crossing effects qualitatively, which suggests a temperature surveillance of future dynamic tensile tests for further investigation to resolve the role of thermomechanical heating.

The principle of the heating is performed by converting the full strain energy into heat, which includes the elastic as well as the viscoelastic and plastic ratios. For a further investigation, a model converting only the dissipative ratios of the strain would be a huge improvement.
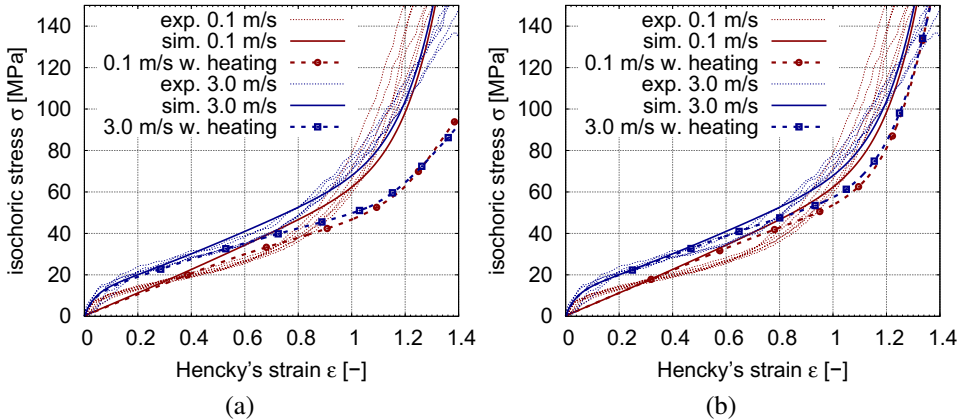
Figure 5.4 TPU: uniaxial tensile test. Strain based heating with (a) 100 % heat conversion and (b) 60 % heat conversion.

The presented model, however, is only a rough approach, especially the heating portion for different strain rates vary. The overstress at 3.0 m/s is higher than at 0.1 m/s and therefore the overall portion of strain energy dissipated into heat. Therefore, the dissipation mechanism based on portions of the complete strain energy is insufficient. A model considering the inelastic viscous and plastic dissipation of the material would improve the quality of further analysis.

5.6 Summary

A hyperelastic, a tabulated hyperelastic formulation, a hyper-viscoelastic and a thermo-hyperviscoelastic modelling technique were investigated. The pure hyperelastic formulation, which is frequently used for interlayer materials, is not sufficient to describe the material behaviour at dynamic loadings. The tabulated hyperelasticity showed to be a good engineering approach to model the strain rate dependence, but could not represent temperature dependence. The hyper-viscoelastic model was able to represent the nonlinear stress-strain behaviour, the viscoelastic behaviour, and the temperature dependent behaviour. Due to the addition of adiabatic heating effects, observed experimental stress-strain curve crossing could be reproduced qualitatively.

6 Simulation of PMMA-TPU Laminate

The following sections aim to find appropriate modelling techniques for the PMMA-TPU laminate considering the adhesion between the plies (Section 6.1.2) and different methods to model the fracture and failure behaviour of the laminated materials. The final models are validated using the clamped bending and the dart experiments at different velocities and temperatures. Quasi-static loading is not considered because focus is set on dynamic loading.

6.1 FE-Modelling

Modelling of laminates using finite elements can be performed in several ways. PMMA shows comparatively high bending stiffness and can be modelled with either shell or solid elements. To cover the bending behaviour with reduced-integrated solid elements adequately, at least three elements in thickness direction are required, which would raise the computation time significantly. Therefore, shell elements were chosen for the modelling of PMMA. The interlayer, on the other hand, has effectively no bending stiffness and a modelling technique with a single solid element row appears worthwhile.

Tup and support, depicted in Figure 6.1, were modelled as perfectly rigid materials because the elastic modulus of aluminium exceeds that of PMMA and TPU by more than one magnitude. Preliminary studies showed that the influence of friction within reason-
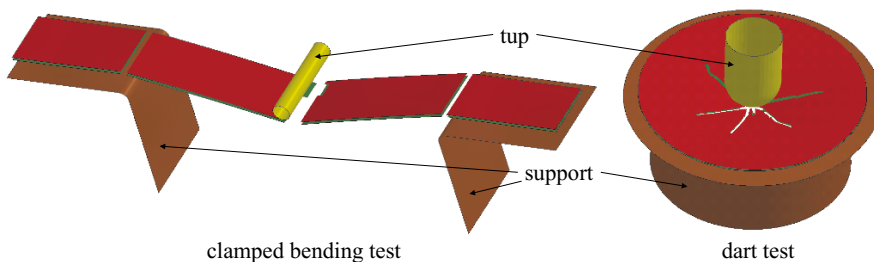
Figure 6.1   FE-models used for simulations. The interlayer elements are blanked for visibility.

able limits is marginal on the overall force-displacement behaviour, which corresponds to findings of HADAVINIA et al. (2011).

Corresponding to Chapters 4 and 5, the commercial FE-solver LS-DYNA was used (LS-DYNA, 2007). Here, fully integrated standard shell elements (type 16) were used for PMMA, while a reduced integration rule was applied for the solid TPU elements (type 1). Shell elements were calculated with seven integration point through thickness. Hourglass formulations for the reduced integration rule were stiffness based (type 5).

6.1.1 Mesh Structure and Element Types

Two different mesh types were investigated. A regular mesh, based on four-node quadrangular elements and an irregular mesh built with three-node triangular elements. Both mesh types are shown in Figure 6.2. KUNTSCHE (2015) reported an irregular mesh to show better agreement of the fracture pattern to experiments than a structured mesh. Furthermore, KHALILI et al. (2011) found better numerical performance of an unstructured mesh, where "unstructured" refers to a decrease of element size in the vicinity of the impact point. Similar characteristics were reported by ANTOINE et al. (2015).

| (a) | (b) |
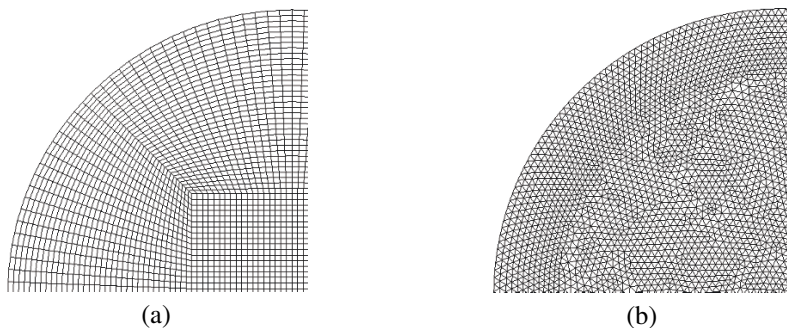
Figure 6.2 Different mesh structures with a nominal edge length of 1 mm under the impactor. (a) structured mesh with quadrangular elements and (b) unstructured mesh with triangular elements.

6.1.2 Coincident Element Modelling

The arrangement and connection of elements shows to have a crucial influence on stiffness of the numerical model of the laminate. KOLLING et al. (2015) showed similar influence of different modelling technique for laminated safety glass, which had a corresponding structure. They concluded that best approximation to the real specimen stiffness was obtained by using a shell-solid-shell model, where shell layers are PMMA and the solid layers TPU. However, this modelling techniques is only applicable to a three-layer laminate. At higher numbers of plies the shell thicknesses would lead to a mutual penetration of the plies and a smeared stiffness in their contact areas.

A three layer-structure (PMMA-TPU-PMMA) enables a physically motivated structure by assuming perfect adhesion of the single layers. The nodes of the upper and lower PMMA were merged with the upper respectively lower nodes of the TPU layer as depicted in Figure 6.3. As discussed in Section 3.4.1, delamination occurred in the direct vicinity of cracks only. The assumption of a perfect bonding between the layers can be seen as a first approximation to the real behaviour. Delamination modelling is not possible with this technique because of the perfect node bonding. Moreover, nodal temperature rise induced by thermomechanical heating is calculated as a smeared value of both adjacent plies.

Failure parameters of both materials within the coincident technique require a further discussion. For the coincident simulation of both materials, phenomenological values for the principal failure stress had to be used. For PMMA, σ_{fail}=111 MPa was determined, for TPU a failure stress of σ_{fail}=160 MPa showed the highest agreement to experimental results. Both values deviate from the monolithic failure stress values, which is caused by the coincident modelling technique. Due to the perfect bonding, a stiffer structure is modelled than it is observed in experiments. This is caused by an overestimation of the uniaxial PMMA failure stress and the absence of delamination. Therefore, coincident models are expected to show higher stiffness and smaller overall displacements due to a premature attainment of the failure stress. This was affirmed by preliminary simulations and is shown subsequently for simulations of the dart impact test. Therefore, the applied failure parameters are of phenomenological nature but are required for this modelling technique, especially to represent the post-breakage behaviour of the laminate.

The coincident technique is frequently applied due to its practicable and efficient handling (KOLLING et al., 2015; LOPEZ-RUIZ et al., 2015). For models that use element deletion, mass consistence is met longer than in non-coincident models because the mass of the PMMA shell elements is lumped in the nodes that are shared with the TPU. After failure of PMMA elements, their mass remains until the TPU solid element fails and is deleted from the calculation eventually. Failure values for both PMMA and TPU require adjustment, which is not physically based but a good engineering approach for the coincident technique.
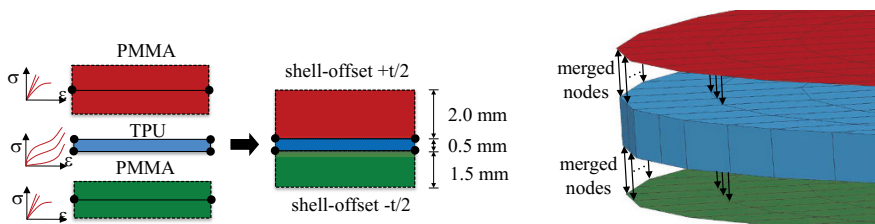
Figure 6.3   FE-model arrangement with coincident nodes.

6.1.3 Tied and Tiebreak Contacts for Delamination Modelling

The role of delamination in the impact performance of polymeric laminates and its modelling is discussed subsequently. A numerical investigation was performed to determine the differences between perfect bonding and delamination for the dart impact experiments. Two conventional ways to model delamination as a contact-based problem were examined. Either the contact is modelled together with a cohesive zone law (tiebreak contact) or by tied contacts with a failure criterion. Both criteria basically yield in a similar behaviour but differ in their contact formulation. Tiebreak contacts are penalty-based, which means that the nodes of the (slave) contact partner are checked for penetration of the master surface. If penetration is detected, a penalty-force

$$F = K_c \delta,$$ (6.1)

is applied on the node representing the contact reaction force. K_c then represents the contact stiffness and δ the penetration distance. Tied Contact act similar to beam elements that tie nodes to each other until failure is reached. In tied contacts, nodes of contact partners that are in close vicinity are tied to each other with varying nodal degree of freedom formulations until a failure criterion of the form

$$\left(\frac{\sigma}{\sigma_{fail}}\right)^2 + \left(\frac{\tau}{\tau_{fail}}\right)^2 \geq 1$$ (6.2)

is fulfilled, where the normal stress σ is greater than zero (tension) and τ is the shear stress. In the course of the present work, no experiments for obtaining delamination parameters were performed and value from literature are taken. HOESS et al. (2016) states excellent adhesion values for the PMMA-TPU laminates of the present work. σ_{fail}=56 MPa and τ_{fail}=44 MPa were used by DOGAN et al. (2012) as typical delamination values for epoxy adhesive. By numerical case studies of the dart and bending test, slightly higher values of σ_{fail}=62 MPa and τ_{fail}=48 MPa were found by comparing results of the simulations and experiments of the dart tests and are applied for tiebreak-contacts subsequently.

The described delamination criteria enable to model the failure of PMMA with a maximum principal stress failure criterion of σ_{fail}=132 MPa, as it was determined from monolithic experiments. In preliminary studies that considered the clamped bending test as well as the dart test, the failure stress of TPU was set to 275 MPa, which corresponds to experimental findings of the monolithic material.

6.2 Mechanical Behaviour

6.2.1 Dart Test

The simulation of the mechanical behaviour of the laminate is discussed by means of the dart test at 5.0 m/s and the clamped bending tests at 1.5 m/s as well as 2.0 m/s. The generalized Maxwell model from Section 4.1 was used for PMMA and the hyper-viscoelastic model from Section 5.3 was applied for the TPU interlayer. The final parameters for the coincident and tiebreak modelling are specified in Table 6.1.

Figure 6.4 (a) depicts the simulation results of triangular elements with coincident modelling compared to delamination modelling. Both techniques are not able to capture the first force peak, but show a very good overall correlation to experimental results. After first failure, a distinct higher stiffness of the coincident model can be observed, which confirms the assumptions from Section 6.1.2. Both techniques exhibit as equivalently capable to reproduce the principle behaviour. The coincident modelling is advantageous because of its simplicity in model assembly, computation time and stability. On the other hand, the delamination modelling with tiebreak contacts appears as the more physical approach, which is confirmed by the possibility to use directly the monolithic failure values for PMMA and TPU.

Figure 6.4 (b) shows the results of the simulation with a structured rectangle element mesh with delamination modelling compared to the triangular element mesh with delamination modelling likewise. The same input parameter were in these simulation. While the unstructured modelling exhibits a good overall correlation to experimental results, the structured mesh modelling showed a distinct deviation from this behaviour. This shows on the one hand the mesh dependence of the simulation, which occurs for conventional element deletion.

On the other hand, further differences can be deducted from both mesh types. First, the crack pattern of the structured mesh after 15 mm fin displacement, which is depicted in Figure 6.5, exhibits that the direction of crack propagation is enforced. This is avoided with the unstructured mesh, which exhibits a more realistic fracture pattern. In Figure 6.5 (a) and (b), cracks of the lower ply are illustrated with dark-green colour, while cracks of the

Table 6.1   Simulation parameters for coincident and delamination modelling.

	parameter	coincident model	tiebreak model
PMMA	σ_{fail}	111 MPa	132 MPa
TPU	σ_{fail}	160 MPa	275 MPa
delamination	σ_{fail}	-	62 MPa
delamination	τ_{fail}	-	48 MPa

upper ply are partly transparent. It is apparent, that cracks on both plies do not always follow the same path. Because of the more realistic fracture pattern, subsequently shown results are performed with unstructured mesh types of the form as shown in Figure 6.2 (b). It has to be noted that the better performance of the unstructured mesh only applies for the particular FE structure and mesh density. Further improvement by reducing the elements size may lead to better results for the structured mesh.

Further information can be deducted from the simulated fracture patterns. Failure of upper and lower PMMA does not occur contemporaneous. Cracks of both plies have roughly the same path but are sometimes slightly displaced, which could also be deducted from experimental fracture patterns. The circular crack pattern at the support edge, which is shown in Figure 6.5 (a) was reproduced in some simulations with the triangular and quadrangular elements and corresponds to experimental findings.
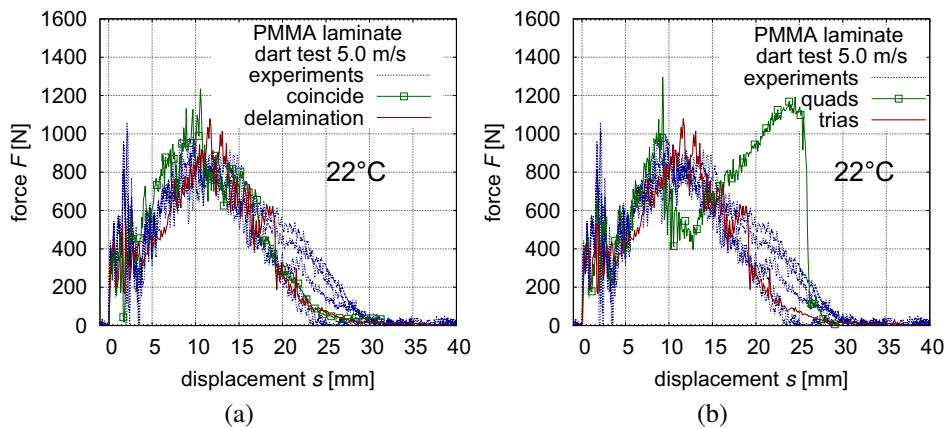
Figure 6.4   PMMA laminate: (a) Comparison of coincident and delamination modelling with triangular elements. (b) Comparison of triangular and quadrangular elements for the delamination model.

6.2.2 Global Energy Failure Threshold

The lack of reproducing the initial force peak is caused by a premature failure of elements under the fin and is a discretization problem. With different mesh densities, the initial force peak varies. Originating from the simulation of laminated safety glass, a nonlocal energy threshold criterion can be used to regularize the first point of failure. The investigated model is described in PYTTEL et al. (2011). Here, a circular area is defined, in which the strain energy must reach a critical energy before failure is activated. After that, the local element failure criterion, here the maximum principal stress, is used. The principle idea is shown in Figure 6.6 (a) and compared to conventional element deletion representatively for the dart impact test at 5.0 m/s in Figure 6.6 (b).
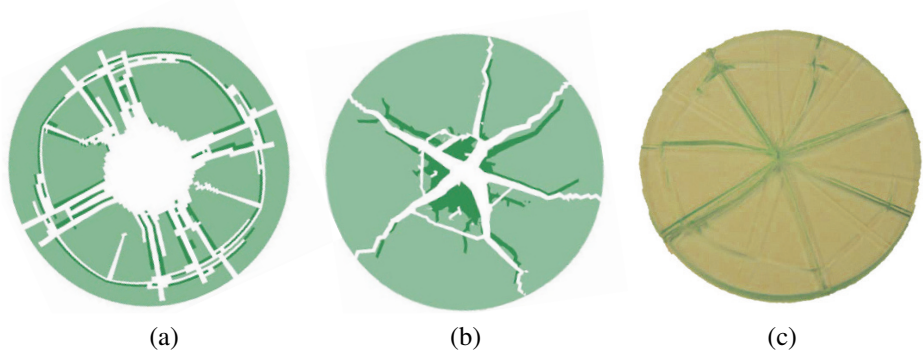
Figure 6.5 PMMA laminate: dart test fracture pattern of coincident structures at 5.0 m/s. (a) Structured mesh. (b) Unstructured mesh. (c) Experimental result.

The nonlocal failure criterion by PYTTEL et al. (2011) shows improvement compared to the conventional local failure criteria in terms of regularization of the first failure point, and because of that, a better reproduction of second force peaks. This way, an additional nonlocal force peak can be created, which is depicted in Figure 6.6 (b), that corresponds better to experimental results. However, the criterion remains dependent on the specimen geometry and can not be applied to other experimental setup without adjustment of the parameters. In the present work, a critical energy E_c=1 J within a critical radius R_c=40 mm was used for the dart impact tests.
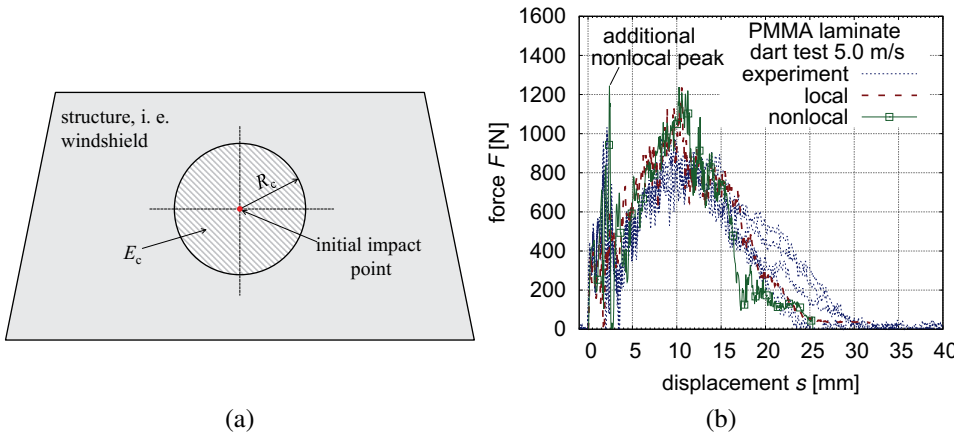
Figure 6.6 Global energy threshold element deletion criterion. (a) Principle idea by PYTTEL et al. (2011). (b) Comparison with and without nonlocal failure criterion for the dart test simulation at 5 m/s.

6.2.3 Clamped Bending Simulations

Observations from the dart test simulation can be principally transferred to the simulation of the clamped bending tests. Representative results for velocities at 1.5 m/s and 2.0 m/s are shown in Figure 6.7 for the coincident and delamination modelling. The behaviour of the laminate under clamped bending, which is characterized by multiple breakage, is represented well for both velocities. Furthermore, the force level of the breakage points corresponds to experimental results as well as the maximum displacement and hysteresis.

Figure 6.7 (a) shows this behaviour exemplary for the coincident model at 1.5 m/s. With the coincident maximum principal stress failure criterion for PMMA from Table 6.1 of 111 MPa, failure is reached too early and the surplus energy leads to a prolonged overall displacement. With higher values for the failure point, either reached by a nonlocal criterion (Section 6.2.2) or by an increased failure stress, similar results to the delamination model are reached. For 2.0 m/s, this behaviour is balanced by the stiffer behaviour of the laminate between 8 mm and 13 mm fin displacement, which is caused by the lack of delamination and the resulting stiffer post breakage behaviour.

The fracture pattern, as depicted in Figure 6.8 in comparison to a representative experimental result, is reproduced in its typical characteristics with breakage under the fin and at the support edges at both sides, which is represented by multiple force peaks. Though the mechanical behaviour of the laminate appears to be modelled sufficiently, main deviations result from the insufficient representation of failure points, which influences the post-breakage behaviour significantly.
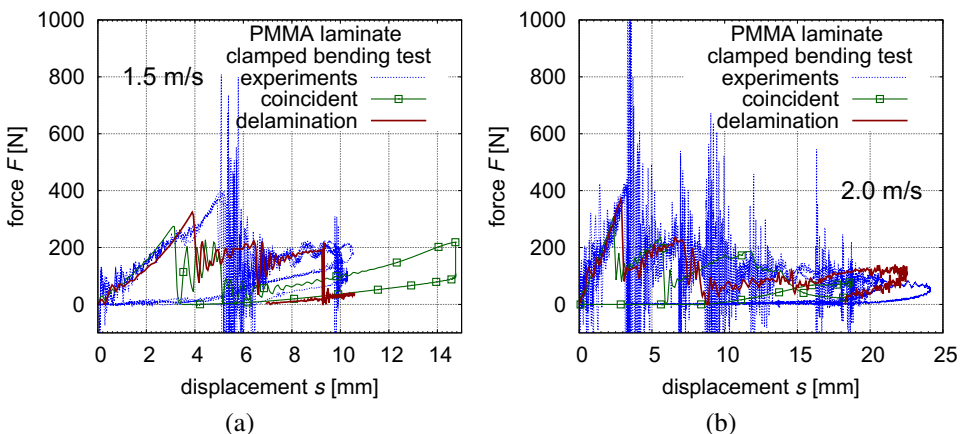
Figure 6.7   PMMA laminate: clamped bending test. Simulation at (a) 1.5 m/s and (b) 2.0 m/s with coincident and delamination modelling compared to experimental results.
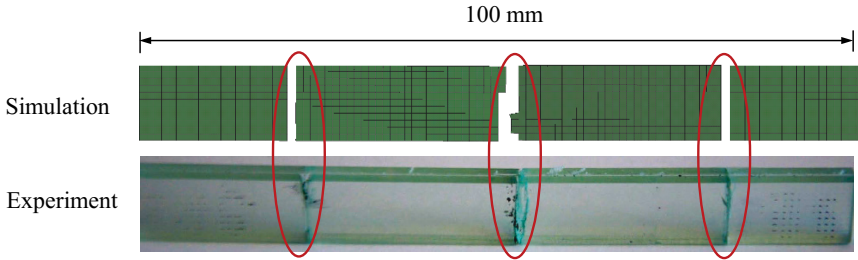
Figure 6.8   PMMA laminate: clamped bending test. Fracture pattern with coincident simulation compared to experimental results at 2.0 m/s.

6.3 Temperature Dependent Mechanical Behaviour

Temperature dependent simulations were performed with the coincident model and the nonlocal energy threshold, as defined in Table 6.1 for room temperature. For the other temperatures, failure criteria were adjusted according to Figure 6.9. Failure stress of PMMA was assumed to be constant at 111 MPa except for 60 °C, where a significant decrease in failure stress had to be used in order to represent experiments adequately. For TPU, the failure stress differed from the room temperature value only at -30 °C, where the material is in its glassy state. Here, it was assumed that TPU and PMMA both have a failure stress of 111 MPa.

Figure 6.10 shows the results for the temperature dependent dart impact simulations at 5.0 m/s. The nonlocal failure criterion proved to be able to delay the initial failure which leads to a reproduction of the second higher force peak.

The principle temperature-dependent behaviour is reproduced by the simulation for all four temperature, although some deviation are observed and require discussion. While the overall force-displacement behaviour at -30 °C, 0 °C, and 22 °C is capture quite ade-
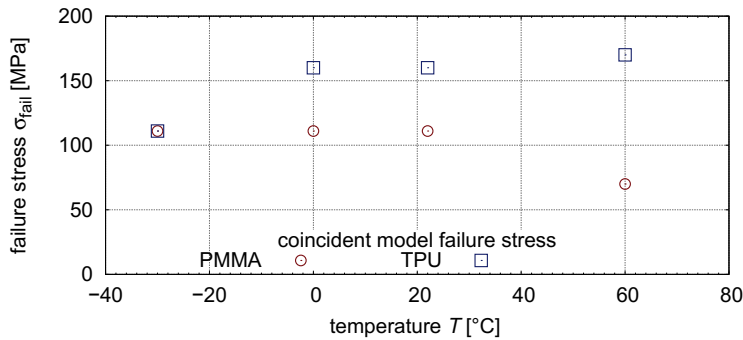
Figure 6.9   Temperature dependent failure stress used for PMMA and TPU in the simulation.
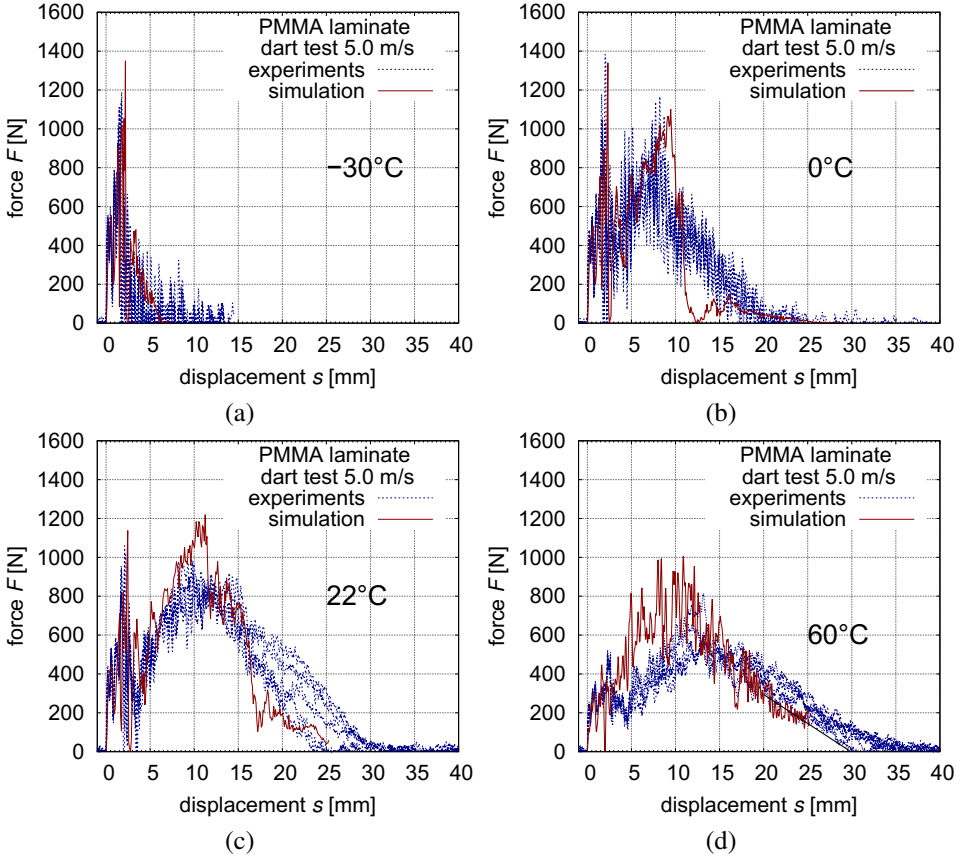
Figure 6.10   PMMA-TPU laminate simulation: Temperature dependent dart impact simulations.

quately. The simulation at 60 °C shows higher deviations compared to experimental results and a premature termination of the simulation. At 60 °C, the simulation overestimates on the one hand the maximum force, created by the nonlocal failure criterion. Therefore, the nonlocal criterion was not used at 60 °C, which corresponds to a reduction in the critical energy. On the other hand the simulated post-breakage behaviour shows higher deviation from experimental results, which is partially caused by the increasing deviations of the Arrhenius fit beginning at 50 °C, which was observed in Section 3.2.2. A comparison of the absorbed energies, as performed in Figure 6.11, shows very good correlation between simulation and experiments. Deviations observed in the force-displacement behaviour, like the insufficient reproduction of the force peak and deviations at higher strains, appear to have minor influence on the overall energy absorption behaviour. The energy absorption of the simulation at 60 °C was approached by an addition of a linear decreasing function
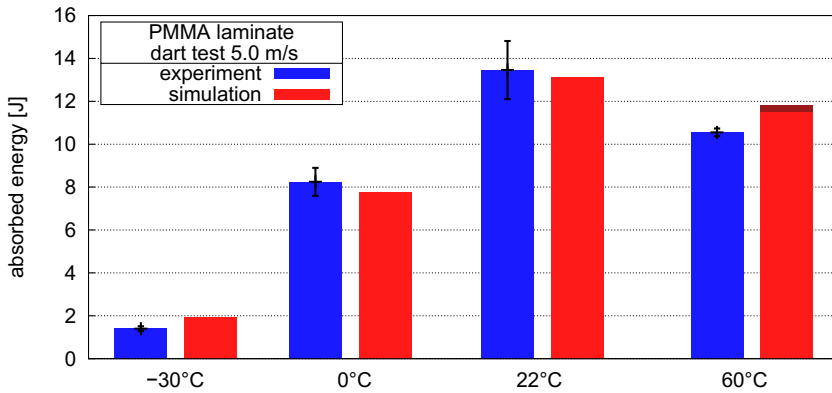
Figure 6.11 PMMA laminate: dart impact test. Simulation results for the impact energies at 5.0 m/s compared to experimental results. Errorbars represent the 95 % confidence interval.

of the force following a least square fit through the preceding data points. The calculated additional energy is depicted in dark-red in Figure 6.11.

Considering the fracture pattern, the PMMA plies were completely destroyed in the vicinity of the impactor, which was equivalently reproduced in the simulation. In all experiments, four to seven main crack lines formed, followed by a total laminate failure eventually. Furthermore, a second crack pattern, forming at the relatively sharp edges of the support is reproduced of a single element row directly above these edges.

6.4 Coupled Thermomechanical Behaviour

The adiabatic heating of the interlayer, as measured in Section 3.4.1, was subject to a basic investigation regarding feasibility using the clamped bending test at 2.0 m/s. The coincident model could not be used for this investigation because of the shared nodes of PMMA and TPU that results in a mixed temperature. Therefore, the delamination model with tiebreak contacts was used in a thermomechanical simulation. In the presented case study, the complete strain energy was assumed to be converted into heat in order to achieve the maximum possible heat generation.

Figure 6.12 (a) and (b) presents the force-displacement as well as the temperature time behaviour in comparison to experimental results. Temperatures represent the maximum temperatures measured within the relevant deformation area. The force-displacement behaviour is reproduced well and results in an interlayer failure, which corresponds to two of five experiments. A corresponding image series for experiments and simulation without experimental interlayer failure is shown in Figure 6.13. Without heating, interlayer failure was not predicted by simulations. The temperature development, however, is by
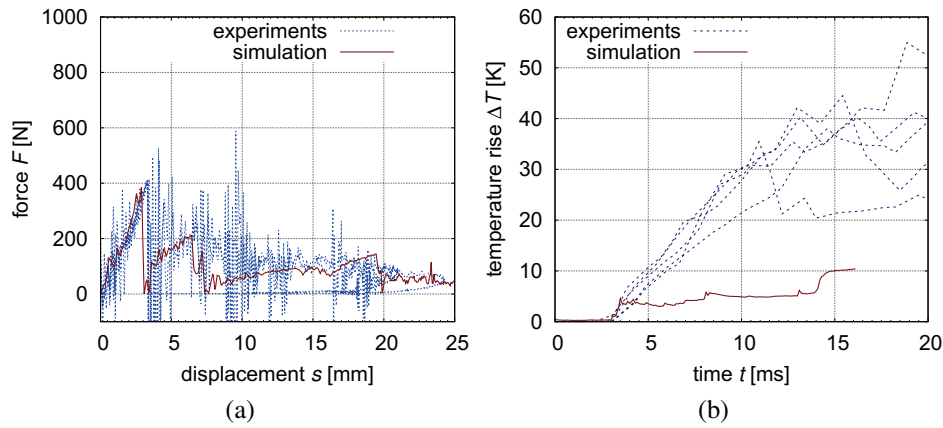
Figure 6.12 PMMA laminate: clamped bending test. Simulation and experiment at 2.0 m/s: (a) force-displacement and (b) adiabatic heating.

far underestimated although the whole strain of TPU is assumed to be converted in heat. A maximum temperature rise of $10\,°C$ is calculated compared to experimental results between $20\,°C$ and $50\,°C$. It is assumed that other effects like friction after and while delamination play a major role. This would contribute to a higher energy rise. However, with the presented simulation models the feasibility of adiabatic interlayer heating was shown.
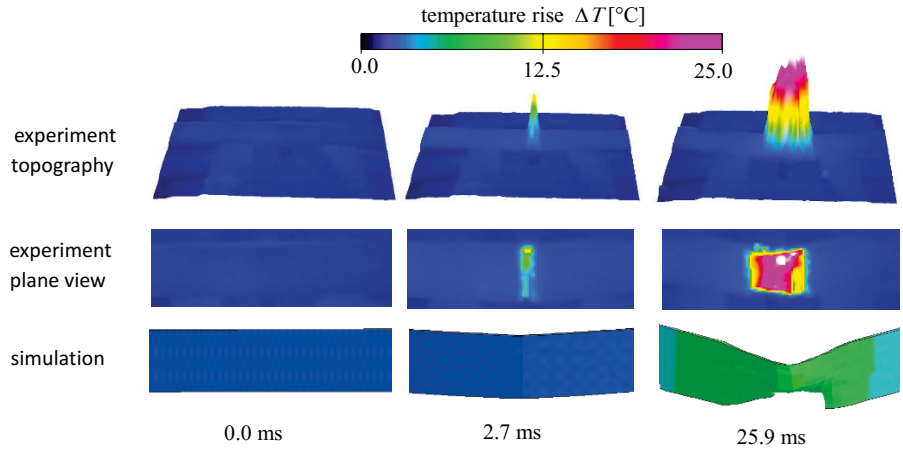
Figure 6.13 PMMA laminate: clamped bending test. Adiabatic interlayer heating: experiment and simulation. White fringe colours represent a temperature rise above $25\,°C$.

6.5 Summary

FE-simulation methods regarding a PMMA-TPU laminate under dynamic loading at different temperatures were presented. A structured mesh with quadrangular (PMMA) and hexahedron (TPU) elements and an unstructured mesh with triangular (PMMA) and pentahedron (TPU) elements were applied. For the main investigation the triangular and pentahedron mesh was used.

Simulations were performed with two models. The first was a coincident modelling technique that required a further adjustment of the failure criteria. The second a delamination modelling, which required tiebreak contacts. Here values from literature were used for the failure of the adhesion and failure parameters determined from tests with the monolithic materials could be applied directly. Both models could reproduce experimental findings at room temperature in terms of force-displacement behaviour, impact performance, and fracture pattern well.

For the temperature dependent experiments, the coincident modelling technique was used and required only adjustment of failure parameters. Experiments corresponded well to simulations results, with higher deviations at increased temperatures. Furthermore, the overall laminate simulation revealed to be crucially dependent on the failure of both materials. The temperature dependence of both materials could be applied as presented in Sections 4.4 and 5.4.

Areas of improvement are the fracture modelling of PMMA, which was only rudimentary approached with a constant principal stress value. Crack propagation models, like the XFEM (BELYTSCHKO et al., 1999), could greatly improve the reproducibility of these simulations. Conversion of a certain portion of strain energy into heat influenced the mechanical behaviour, but could not be reproduced in the simulations quantitatively. A thorough investigation of the heating mechanisms, however, was not performed in the presented model and should be subject to future research.

7 Component Tests and Validation

A final validation study of the presented models was undertaken with a head impact experiments, which is frequently used as an approval test in the automotive industry. A head dummy is accelerated to 10 m/s and impacts the window at a defined impact point. Head impact tests are based on the New Car Assessment Programme (NCAP) approval tests and were performed on an automotive side window consisting of monolithic PMMA and the PMMA-TPU laminate.

The test shows to be in step with actual practice and exhibits as a suitable validation method as it is a standard procedure in the automotive industry. Furthermore, it can be seen as a first approach towards the replacement of other glassy components like front or rear windows and basic conclusions may be transferred. Considering the structure of this chapter, the experimental setup and results are presented first. Concluding, simulations are compared and discussed.

7.1 Experimental Setup

Experiments were conducted on monolithic PMMA, the PMMA-TPU laminate as well as further materials for comparison. The specimens were adhered with a PU adhesive in combination with a corresponding primer material to the frame. Product names of the adhesive and the primer were Totalseal 110 and Totalseal respectively. The aluminium frame was provided by Evonik Industries AG and is shown in Figure 7.1.

Tests were either performed in horizontal (Figure 7.2) or vertical direction (Figure 7.3). For horizontal testing, a test bench was developed, which is shown in Figure 7.2 (a) and
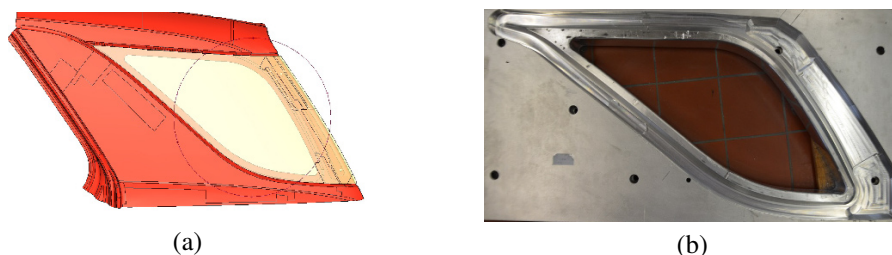
Figure 7.1 Frame used for head impact experiments. (a) CAD geometry (b) photography.

(b). The tests were performed at the company Advanced Car Technology Systems (ACTS) in Sailauf, Germany. Figure 7.3 shows a photograph of the experimental setup of the dynamic test. The three-channel acceleration sensor was positioned centric inside the head impactor.

(a)   (b)
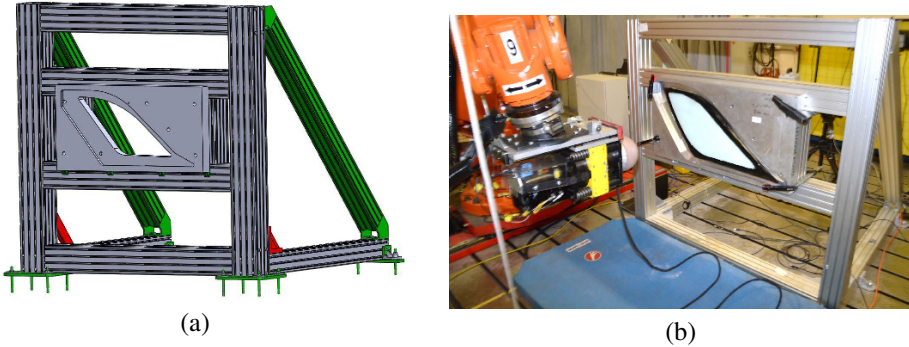
Figure 7.2   Test bench for horizontal head impact test: (a) CAD model, (b) constructed bench.
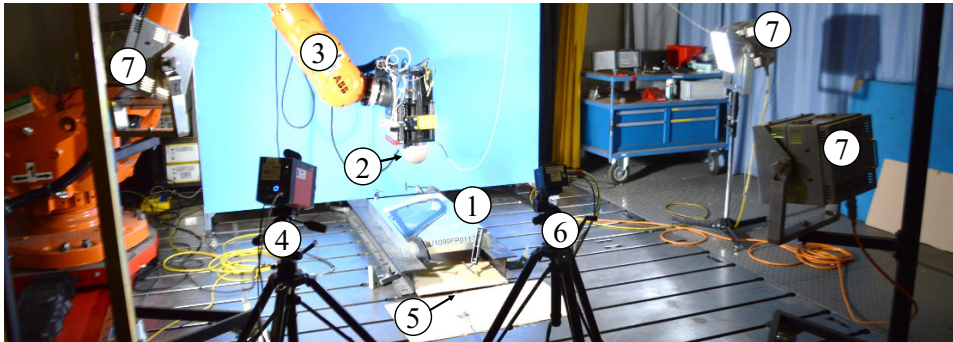
Figure 7.3   Experimental setup for vertical head impact test. The components are: specimen (1), head impactor (2), actuator (3), IR camera (4), thermocouple (5), high-speed camera (6), illumination (7).

In order to approach a standard automotive assessment test a standard NCAP head form was used as an impactor. The chosen impactor was a 3.5 kg Japan New Car Assessment Programme (JNCAP) head form based on the development presented in MATSUI et al. (2003). It is based on a spheric aluminium core coated by a poly(vinyl chloride) (PVC) layer. The overall outer diameter is 160 mm.

7.2 PU Adhesive

The adhesive Totalseal® 110 in combination with the Primer Totalseal® 5028 was used for mounting the windows to the aluminium frame. A simplified characterization with the pure adhesive material without primer was performed in order to respect the elasticity and deformation behaviour in the numerical simulation. The stress state at the adhesive is assumed to be dominantly compressive. At higher deformations of the window additional tensile states may occur, but are of minor importance for both investigated materials because of their brittle behaviour with small failure strains. For the laminate, the post breakage behaviour will not contribute significantly to uplifting the adhered edges of the window because of the localized failure behaviour.

Assuming a mainly compressive stress state, compression tests at different velocities and room temperature were performed in order to capture the rate dependent behaviour. For this purpose cubic specimens of the cured adhesive with 6 mm edge length were tested at 0.0000833 m/s (quasi-static) and 2.0 m/s. The quasi-static tests were performed on a servo-hydraulic machine, the three dynamic experiment series on the *4a* Impetus pendulum system. For each velocity, three experiments were repeated. Figure 7.4 shows the experimental results, where the unloading of the quasi-static test is not displayed. A rate dependence can clearly be observed from the comparison of the quasi-static and the 2.0 m/s experiment.

For simplicity, a numerically robust material model (KOLLING et al., 2009) based on the Hill functional was used to model the adhesive behaviour. This model was designed for modelling low and medium density foams and, unlike the real material behaviour, a Poisson's ratio of $\nu=0$ is applied here. Because of small deformations and no evaluation of the deformation or stress within the adhesive, this model can be used as a substitute model for the continuous elastic support. Figure 7.4 shows the result of the final optimization. Dynamic and quasi-static experiments and optimized simulation show a good agreement.
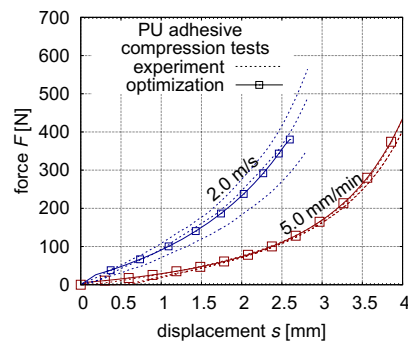
Figure 7.4 Adhesive: (a) Experimental setup. (b) Optimization of Hill's energy functional.

7.3 **Monolithic Materials**

The experimental results on monolithic PMMA are depicted in Figure 7.5. The acceleration measured by the sensor in the head's centre is multiplied by the mass $m = 3.5$ kg of the head impactor in order to compute the contact force. The process of the impact takes place within 4.0 ms. The point $t = 0$ s was determined by the first slope in z-acceleration above sensor noise that increases continuously. After first impact, the z-force rises steadily. At 1.0 ms the force stays at a level of approximately 1500 N and starts rising linearly at 1.5 ms until failure at approximately 2.9 ms. Here, a maximum z-force of 5000 N resulting from acceleration is reached. The other channels had to significant contribution to the resulting overall signals. Therefore, the acceleration as well as the impact was clearly performed in z-direction.

Further tests were performed on TSG (t=3 mm), PC (t=5 mm) as well as PMMA, which was impact modified (IM) (t=4 mm). The z-acceleration multiplied by the head impactor mass of $m = 3.5$ kg are depicted in Figure 7.5. All polymer materials showed a high agreement in their stiffness until failure. The overall concurrent behaviour of PC and the IM PMMA is noticeable, although they have different thicknesses. Both materials exhibited neither failure nor visible plastification. It may be noted that for automotive outdoor components, the application of a thin hardcoating layer is common practice, which was not investigated here. A change of failure mechanism by applying thin brittle layers was discussed in other works (GODART et al., 2007) that may influence this shown behaviour for PC and IM PMMA.

The significantly higher elastic modulus of TSG is represented in the higher forces within the first 2 ms compared to the polymers. The great disadvantage of this material is its small failure strain and the corresponding poor ability of energy absorption. TSG
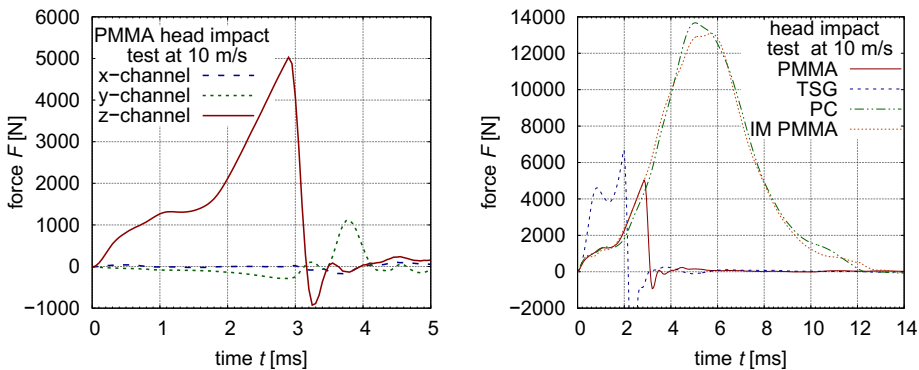
Figure 7.5   (a) Experimental results of the head impact on 4 mm PMMA. (b) Experimental results of the head impact on different materials.

TSG

| 0 ms | 2 ms | 3.2 ms | 8 ms |

PMMA

| 0 ms | 2 ms | 3.2 ms | 8 ms |
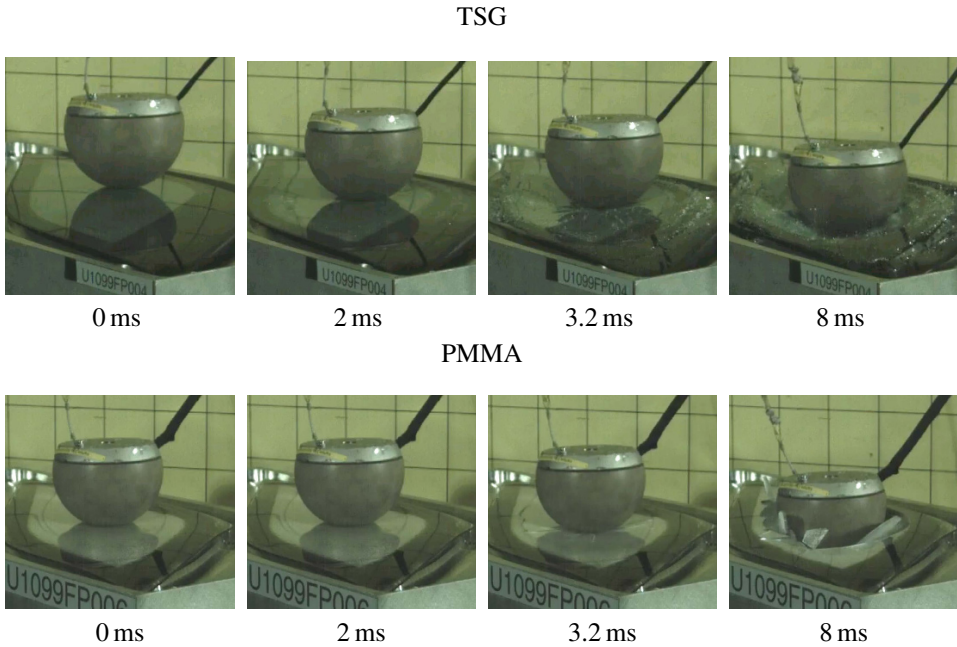
Figure 7.6 Image series of a head impact on TSG thickness of $t = 3$ mm and PMMA with $t = 4$ mm.

fulfills all requirements for side windows, including the scratch resistant and without any additional layers. For TSG and PMMA, image series of the impact development are shown in Figure 7.6. The brittle failure after small deformations is visible for both materials. Additionally, the global failure of TSG with significantly smaller fragments compared to PMMA can be observed.

The demanded characteristics like a scratch-resistant surface, a soft elastic response with high deformations and a stable or no breakage behaviour is not fulfilled by either of these materials. TSG shows good scratch resistance and weatherability, but its rapid failure makes insufficient for impact situations. Conventional PMMA shows a similar breakage behaviour but has a low scratch resistance performance compared to glass. To overcome the small failure strains inherent of conventional PMMA, an IM PMMA may be used, but, as well as for PC acceleration values are increased. Furthermore, all of the presented polymers can not undergo an equivalent procedure as the tempering for TSG.

Summarizing, the diversified requirements to a window material exclude conventional polymers for the most part. Therefore, a further look into laminated structures that combines high impact resistance with extended deformation and decreased accelerations is promising.

7.4 PMMA-TPU Laminate

Corresponding to the head impact test on the monolithic PMMA, the experiment was conducted at 10 m/s on the PMMA-TPU laminate of the present work. Three different tests were performed, two vertically and one horizontally with the corresponding setup from Section 7.1. Figure 7.7 depicts the force-time signals for all three tests, Figure 7.8 shows a corresponding series of images for one vertical head impact on the laminated side window. The two continuous lines in Figure 7.7 represent the z-acceleration curve for a laminate,
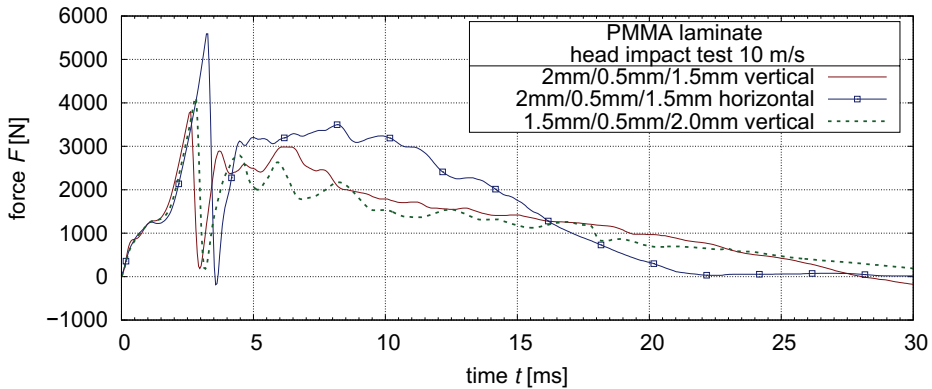
Figure 7.7   Head Impact at 10 m/s for PMMA-TPU laminates.

where the thicker ply (2 mm) is the impacted side. The dotted line depict a vice versa laminate structure, where the thinner 1.5 mm ply is the impacted side. All three experiments show a good agreement in total initial stiffness, which holds unto failure. The failure points of the single experiments scatter within a wide range of forces and displacements. Due to the unique character of each test, conclusions regarding the influence of gravity or laminate setup can not be drawn without further experiments. However, principle characteristics can be pointed out. The post breakage behaviour is characterized by a reduction of the force to almost 0 N, which is caused by the loss of contact between impactor and

| 0 ms | 2 ms | 8 ms | 16 ms |
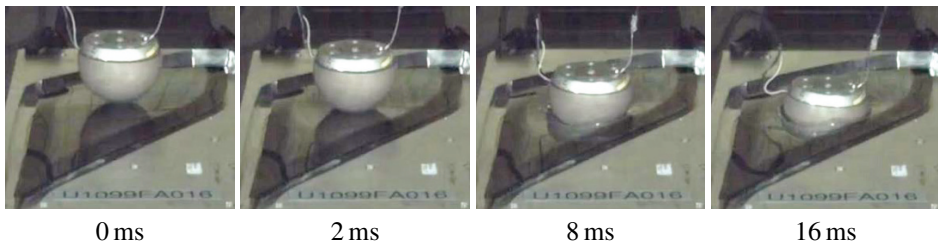
Figure 7.8   Image series of a head impact on PMMA-TPU laminate.

laminate. After that a significant post-breakage behaviour begins, with varying curve development. The laminate was able to withstand the impact and no splinters were detached from the laminate. The impactors showed little to none residual velocities, so the total kinetic energy was absorbed by the structure. In all three cases, the PMMA plates and the TPU layer failed locally and most likely simultaneously. Most cracks had the same path on the upper and the lower side and presumably cut through the PMMA layer.

The temperature increase due to illumination (halogen metal vapor lamps) was observed to be below 1 K and the influence on the mechanical behaviour of the specimen was negligible. However, a measurable rise in temperature of the interlayer was observed with IRT during the test, which confirms previous experimental result. Figure 7.9 shows a corresponding IR image of the impacted laminated side window directly after impact. Besides some planar temperature rises, which are probably caused by friction of the impactor, a distinct temperature rise can be observed at the cracks.
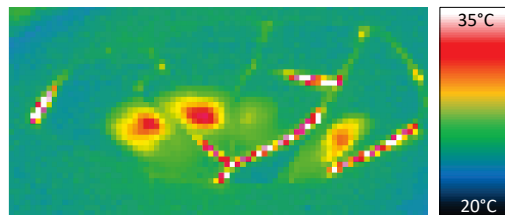
Figure 7.9   IR image of laminated window specimen after head impact experiment.

7.5 Validation of the Finite Element Model

FE Model

The final FE-model is shown in Figure 7.10 (a), a detailed view for the contact modelling is given in Figure 7.10 (b). The model is based on preliminary studies, which are summarized in Figure 7.12. The head impactor, which is a complex topic for accurate modelling was provided by the *LASSO Ingenieurgesellschaft mbH*. Information regarding the development and validation of the head impactor models are given in FRANK et al. (2003). The frame was modelled with rigid shell elements, the adhesive was given the material model from Section 7.2 and modelled with one solid element row. The lower nodes were connected coincident with the frame, while the contact with the window was performed by a contact modelling with contact-shells. Here, a shell element row is created upon the surface of the adhesive solid elements and connected with a tied contact to the window.
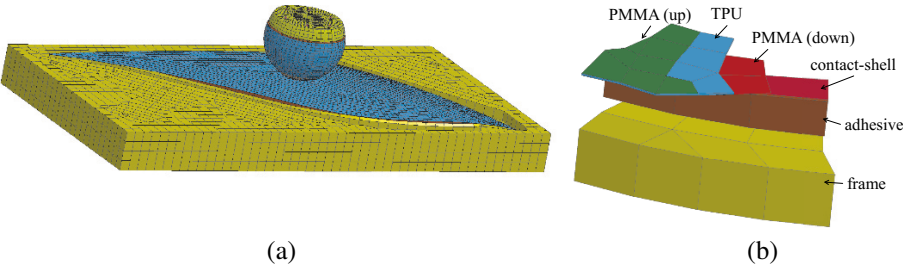
Figure 7.10 FE-model for the head impact simulation: (a) full model (b) detailed, exploded view for visualization of the structure.

Monolithic PMMA

Figure 7.11 (a) shows a mesh dependence study for the head impact on monolithic PMMA. All meshes show the same principle behaviour and only minor deviations even after failure of some elements, which, without remeshing, always leads to some mesh dependence. Therefore, a mesh with element edge lengths of 5 mm in average was used for the final validation simulations. Figure 7.11 (b) shows the head impact on monolithic PMMA simulation at 10.0 m/s with the nodes that were covered by adhesives assumed as totally rigid, which means that all translational and rotational nodes are restrained. The second simulation regarded the modelling of the adhesive as a continuous elastic support.

The rigid modelling overestimated the stiffness of the structure significantly, while with modelling of the adhesive material the stiffness of the experiment was captured very
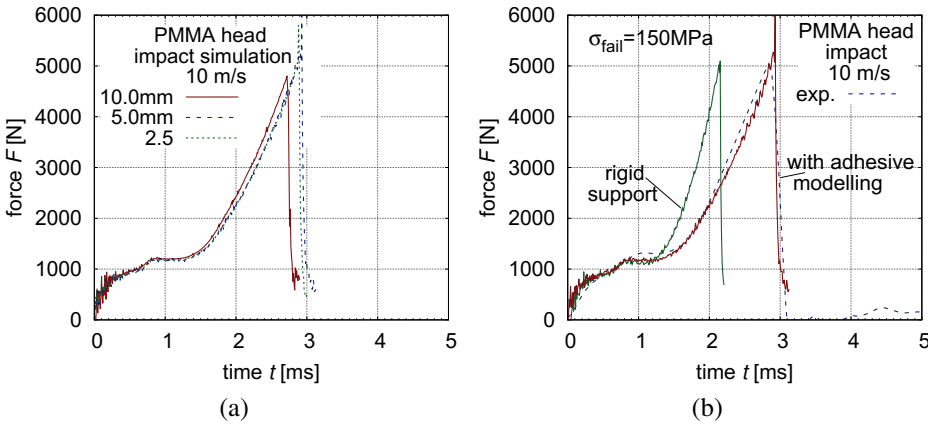
Figure 7.11 Head impact experiments: (a) mesh study and (b) support study for PMMA.

well. Failure was modelled with a monolithic first principal failure stress of σ_{fail}=150 MPa in order to represent the failure point adequately, which is within the scattering range of the monolithic PMMA discussed in Section 4.5.

PMMA-TPU Laminate

Figure 7.12 (a) shows a mesh dependence study for the head impact on the PMMA-TPU laminate. The findings from the monolithic mesh study can be confirmed. Furthermore, even after failure and deletion of PMMA and TPU elements, the resulting force-displacement behaviour corresponds well for all investigated meshes. In Figure 7.12 (b) the corresponding study to Figure 7.12 (b) is shown for the laminate. Again, the modelling of the adhesive enables a better reproduction of experimental results. Figure 7.13 shows the final simulation results using the full FE-model, which includes frame and adhesive modelling compared to experiments. Both simulations, the first one using the principal stress failure criteria (σ_{fail}=111 MPa) and the second one using the nonlocal energy failure threshold criterion additionally (E_{c}=13.0 J, R_{c} =40 mm), showed good correlation to the experimental results. E_{c} and R_{c}, however, were adjusted to meet the initial failure point.

Figure 7.14 shows the fracture pattern of the simulation (top) compared to experimental results (bottom). Here, the upper PMMA layer is depicted in green, the lower one in red. The interlayer is displayed in transparent blue. The typical star-shaped fracture pattern, which was observed in the experiments, was qualitatively reproduced in the simulations. Local interlayer failure occurred corresponding to experimental results. An improvement compared to the node-based Navier-support is observed. Similar results were obtained in LOPEZ-RUIZ et al. (2015) by using the engineering Maxwell model for PMMA (Section 4.1) and the hyper-viscoelastic model for TPU (Section 5.3).
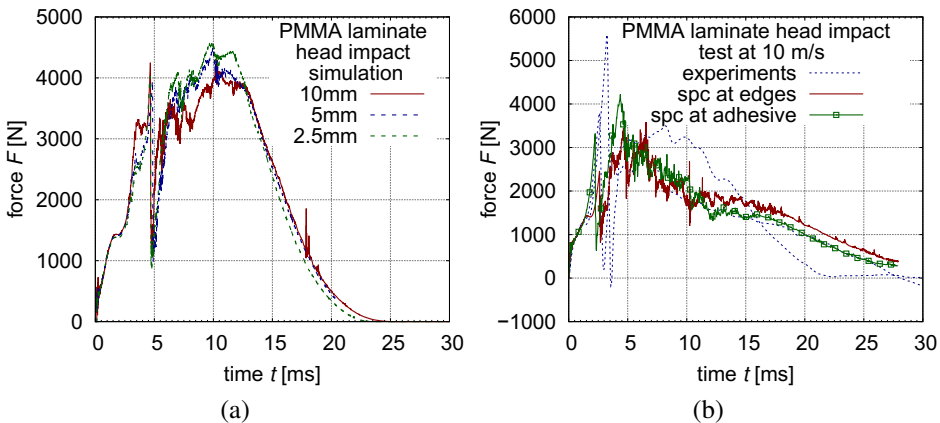
Figure 7.12 Head impact experiments: (a) mesh study and (b) support study for PMMA-TPU laminate.
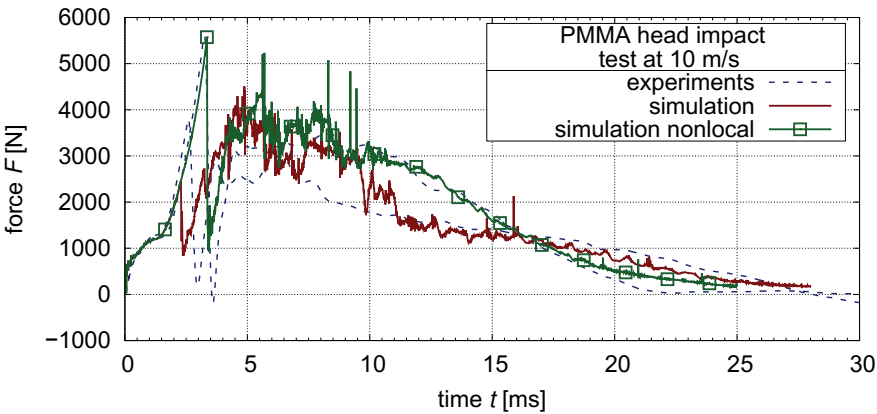
Figure 7.13   PMMA laminate: Simulation of head impact at 10 m/s compared to experiments.
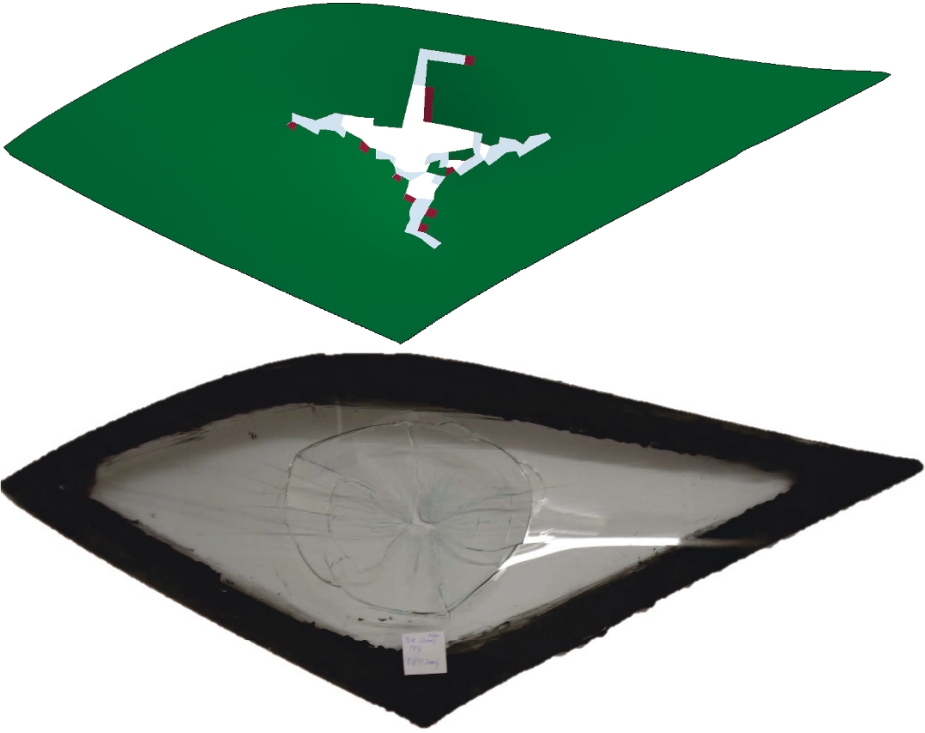
Figure 7.14   PMMA laminate head impact: fracture pattern. Comparison of simulation (top) and experiment (bottom). In the simulation result, the interlayer is depicted in transparent blue colour.

7.6 Summary

The head impact test on the side window exhibited typical characteristics for PMMA, TSG, PC, IM-PMMA, and PMMA-TPU laminates. The high energy absorption potential compared to monolithic PMMA and TSG for the laminate could be shown. Compared to PC and IM-PMMA, a distinct higher deformation respectively post-breakage behaviour of the laminate could be observed, which resulted in decreased accelerations on the impactor.

Experiments and simulations of both monolithic PMMA and the PMMA laminate were in good agreement. The material models for PMMA, TPU and the adhesive proved to be directly applicable for the applied load case. Modelling of the adhesive proved to be an important step to reproduce experimental results. With the application of a global energy threshold criterion, the maximum force peak could additionally be reproduced well. Furthermore, the coincident FE-modelling, which was already used for the simulation of dart and bending tests, was confirmed as an adequate engineering modelling technique.

The results revealed that qualitative and quantitative predictions with the presented FE-models of PMMA-TPU laminates are possible. The force-displacement behaviour as well as the fracture pattern and energy absorption showed high agreement to experiments, which qualifies the presented models as reliable prediction tool.

8 Summary and Outlook

An amorphous polymeric laminate consisting of two PMMA plies with a TPU interlayer was subjected to experimental and numerical research. For that purpose, theoretical fundamentals regarding continuum mechanics, polymer material theory and background information about the investigated materials were given.

In a first step, experiments regarding the monolithic materials were conducted. PMMA was subject to basic thermal measurements with the TPS method. The thermomechanical behaviour was characterized with DMTA experiments, uniaxial quasi-static and dynamic tensile and three-point bending tests, as well dart impact tests at different velocities and temperatures. The material exhibited as clearly rate- and temperature dependent with small strains until brittle failure. A thermomechanical characterization using the time-temperature superposition principle with the Arrhenius shift approach was undertaken to obtain viscoelastic parameters for the numerical simulation.

Measurements of TPU were performed with the TPS method, DMTA experiments, as well as uniaxial and biaxial tensile tests. The material showed to be rate- and temperature-dependent accompanied by a hyperelastic quasi-static behaviour. Elongations of several 100 % of engineering strain until failure were reached, which was subject to further DIC as well as IRT measurements. A significant adiabatic heating could be observed, which stems from viscoelastic and plastic material behaviour.

After the monolithic materials, a PMMA-TPU-PMMA laminate was subjected to low velocity impacts up to 5.0 m/s using three-point bending as well as dart impact tests. The principle behaviour, characterized by a distinct post-breakage load carriage capacity, was investigated. A significant interlayer heating was measured in the clamped bending tests after failure of PMMA plies.

On the basis of this experimental data, different material models were examined regarding their capability of simulating both materials and the laminate. For PMMA, a linear viscoelastic model proved to be adequate for simulation of the tensile dominated load cases of the present work. The parameters for this model were obtained by two ways: An engineering approach by a least-square optimization of uniaxial tensile curves and a more physically motivated approach based on DMTA experiments. With the second approach, a reproduction of the master curve and of dynamic tensile, bending and dart experiments was possible with the identified material parameter set.

Additionally to the conventional pure deviatoric modelling of viscoelasticity, a bulk relaxation was applied that enabled the consideration of the real Poisson's ratio in the

simulation. Temperature dependence was sufficiently modelled for a temperature area between -30 °C and 40 °C using the Arrhenius shift approach.

The quasi-static high strain behaviour of TPU was modelled adequately with a hyperelastic Mooney-Rivlin approach. A viscoelastic contribution was reached by the addition of a Prony-series, for which the parameters were obtained by least-square optimization with dynamic uniaxial tensile tests. By activating thermomechanical heating in the simulation, curve crossing of the corresponding experiments was reached qualitatively as observed in the experiments.

Different FE-modelling techniques for the laminate regarding element type, mesh structure, delamination, and failure were presented and discussed. The strain-rate dependent behaviour could be reproduced well for different load cases. The temperature dependent behaviour showed qualitatively promising results but requires further research. A final validation test consisting of head-dummy impacts on laminated windows showed very good correlation to experimental results and the proposed material and FE-modelling techniques revealed as powerful tools for predictive computational engineering.

The present work exhibited various research areas that require deeper insight for a better understanding of the presented experimental findings and an improvement of corresponding computational models. The **stochastic fracture behaviour of PMMA**, particularly under slow loading velocities, has significant influence on the behaviour of the laminate. Future simulation will most likely benefit from either stochastic failure criteria or detailed **crack modelling**. Furthermore, the **temperature dependence** of these criteria would improve the models' confidence.

For fully understanding the **thermomechanical behaviour of TPU**, particularly the adiabatic heating, further investigation are necessary. Thorough research will require the characterization of the wavelength dependent transmissivity of the interlayer, the contributing mechanisms and accurate calculation and modelling techniques.

The TPU interlayer showed significant influence on pre-conditioning in terms of **endothermic effects** (MACALONEY et al., 2007). A reproducible method of testing interlayers after the lamination process would contribute to a more accurate modelling of the laminate. Further heating of the interlayer appeared to stem from the **delamination**, which also bears potential for further development.

To keep pace with current development, comparison of different **production methods** like lamination or co-extrusion for laminated amorphous polymers appears to be a further promising field of improvement.

References and Regulations

References

ALTER, C., KOLLING, S., and SCHNEIDER, J. (2013): "Verhalten von Glas und Simulation des Nachbruchverhaltens von Verbundverglasung bei kurzzeitiger Beanspruchung", in: *2. Darmstädter Ingenieurkongress*, Shaker, pp. 395–399.

ANTOINE, G. O. and BATRA, R. C. (2014): Low speed impact of laminated polymethyl-methacrylate/adhesive/polycarbonate plates, in: *Composite Structures* vol. 116.1, pp. 193–210.

ANTOINE, G. and BATRA, R. (2015): Constitutive relations and parameter estimation for finite deformations of viscoelastic adhesives, in: *Journal of Applied Mechanics* vol. 82.2.

ARRUDA, E. M. and BOYCE, M. C. (1993): A three-dimensional constitutive model for the large stretch behavior of rubber elastic materials, in: *Journal of the Mechanics and Physics of Solids* vol. 41.2, pp. 389–412.

ARRUDA, E. M., BOYCE, M. C., and JAYACHANDRAN, R (1995): Effects of strain rate, temperature and thermomechanical coupling on the finite strain deformation of glassy polymers, in: *Mechanics of Materials* vol. 19.2, pp. 193–212.

BAASER, H. and GROSS, D. (1999): 3D-simulation of ductile crack growth, in: *Transactions on Modelling and Simulation* vol. 22, pp. 587–596.

BAUWENS-CROWET, C. (1973): The compression yield behaviour of polymethyl methacrylate over a wide range of temperatures and strain-rates, in: *Journal of Materials Science* vol. 8.7, pp. 968–979.

BAUWENS-CROWET, C., BAUWENS, J. C., and HOMES, G. (1969): Tensile yield-stress behavior of glassy polymers, in: *Journal of Polymer Science Part A-2: Polymer Physics* vol. 7.4, pp. 735–742.

BECKER, F. (2009): Entwicklung einer Beschreibungsmethodik für das mechanische Verhalten unverstärkter Thermoplaste bei hohen Deformationsgeschwindigkeiten, PhD thesis, Martin-Luther-Universität Halle-Wittenberg.

BECKER, W. and GROSS, D. (2013): *Mechanik elastischer Körper und Strukturen*, Springer.

BELYTSCHKO, T. and BLACK, T. (1999): Elastic crack growth in finite elements with minimal remeshing, in: *International Journal for Numerical Methods in Engineering* vol. 45.5, pp. 601–620.

BLATZ, P. J. and KO, W. L. (1962): Application of finite elastic theory to the deformation of rubbery materials, in: *Transactions of the Society of Rheology* vol. 6.1, pp. 223–251.

BLUMENTHAL, W. R. et al. (2002): Influence of temperature and strain Rate on the compressive behavior of PMMA and polycarbonate polymers, in: *AIP Journal Proceedings* vol. 620, pp. 665–668.

BOYCE, M. C., PARKS, D. M., and ARGON, A. S. (1988): Large inelastic deformation of glassy polymers. Part I: rate dependent constitutive model, in: *Mechanics of Materials* vol. 7.1, pp. 15–33.

BUCKLEY, C. P. and JONES, D. (1995): Glass-rubber constitutive model for amorphous polymers near the glass transition, in: *Polymer* vol. 36.17, pp. 3301–3312.

BUCKLEY, C., PRISACARIU, C., and MARTIN, C. (2010): Elasticity and inelasticity of thermoplastic polyurethane elastomers: Sensitivity to chemical and physical structure, in: *Polymer* vol. 51.14, pp. 3213–3224.

BURCHILL, P. (1989): Effect of absorbed water, temperature and strain rate on the yield strength of two methylmethacrylate-based plastics, in: *Journal of Materials Science* vol. 24.6, pp. 1936–1940.

BURZYNSKI, W. (1929): Über die Anstrengungshypothesen, in: *Schweizerische Bauzeitung* vol. 94.21, pp. 259–262.

CARLSON, J. et al. (2003): "Frequency and temperature dependence of acoustic properties of polymers used in pulse-echo systems", in: *Ultrasonics, 2003 IEEE Symposium on*, vol. 1, IEEE, pp. 885–888.

CHAUDHRI, M. (2004): Impact breakage of semi-brittle spheres, in: *Powder Technology* vol. 143-144, pp. 31–40.

CHEN, W., LU, F., and CHENG, M. (2002): Tension and compression tests of two polymers under quasi-static and dynamic loading, in: *Polymer testing* vol. 21.2, pp. 113–121.

DE DEUS, J. F. et al. (2004): Relaxations of poly (methyl methacrylate) probed by covalently attached anthryl groups, in: *Macromolecules* vol. 37.18, pp. 6938–6944.

DIONÍSIO, M. et al. (2000): Relaxation studies in PEO/PMMA blends, in: *Macromolecules* vol. 33.3, pp. 1002–1011.

DOGAN, F. et al. (2012): Delamination of impacted composite structures by cohesive zone interface elements and tiebreak contact, in: *Central European Journal of Engineering* vol. 2.4, pp. 612–626.

DOLBOW, J. and BELYTSCHKO, T. (1999): A finite element method for crack growth without remeshing, in: *International journal for numerical methods in engineering* vol. 46.1, pp. 131–150.

DOMININGHAUS, H. (1975): Kunststoff-handbuch, band ix: polymethacrylate, in: *Chemie Ingenieur Technik* vol. 47.19, pp. 807–807.

DU BOIS, P. A., KOLLING, S., and FASSNACHT, W. (2003): Modelling of safety glass for crash simulation, in: *Computational Materials Science* vol. 28.3, pp. 675–683.

EFFINGER, V. et al. (2014): "Nonlinear viscoelastic modeling of foams", in: *13th European LS-DYNA Forum*.

EKEREN, P. van and CARTON, E. (2011): Polyurethanes for potential use in transparent armour investigated using DSC and DMA, in: *Journal of thermal analysis and calorimetry* vol. 105.2, pp. 591–598.

ESTES, G. M., SEYMOUR, R., and COOPER, S. L. (1971): Infrared studies of segmented polyurethane elastomers. II. Infrared dichroism, in: *Macromolecules* vol. 4.4, pp. 452–457.

ESTEVEZ, R., TIJSSENS, M. G. A., and VAN DER GIESSEN, E. (2000): Modeling of the competition between shear yielding and crazing in glassy polymers, in: *Journal of the Mechanics and Physics of Solids* vol. 48.12, pp. 2585–2617.

FAN, J., WEERHEIJM, J., and SLUYS, L. (2015): High-strain-rate tensile mechanical response of a polyurethane elastomeric material, in: *Polymer* vol. 65, pp. 72 –80.

FERRY, J. D. (1980): *Viscoelastic properties of polymers*, John Wiley & Sons.

FINDLEY, W. N. and DAVIS, F. A. (2013): *Creep and relaxation of nonlinear viscoelastic materials*, Courier Corporation.

FINEBERG, J., SHARON, E, and COHEN, G (2003): Crack front waves in dynamic fracture, in: *International Journal of Fracture* vol. 121.1-2, pp. 55–69.

FITTIG, R. and PAUL, L. (1877): Über die aus der Citraconsäure und Mesaconsäure entstehende Crotonsäure, in: *Liebigs Annalen der Chemie* vol. 188, pp. 42–104.

FLECK, N., STRONGE, W., and LIU, J. (1990): "High strain-rate shear response of polycarbonate and polymethyl methacrylate", in: *Proceedings of the Royal Society of London A: Mathematical, Physical and Engineering Sciences*, vol. 429, 1877, The Royal Society, pp. 459–479.

FOUNTZOULAS, C. et al. (2009): "A computational study of laminate transparent armor impacted by FSP", in: *Proceedings of the 23rd International Symposium on Ballistics*, pp. 873–881.

FRANK, T. et al. (2003): "Development and validation of numerical pedestrian impactor models", in: *4th European LS-DYNA Users Conference*, pp. 1–18.

FRANZ, J. (2015): Untersuchungen zur Resttragfähigkeit von gebrochenen Verglasungen, PhD thesis, Technische Universität Darmstadt.

FRIES, T.-P. and BELYTSCHKO, T. (2006): The intrinsic XFEM: a method for arbitrary discontinuities without additional unknowns, in: *International Journal for Numerical Methods in Engineering* vol. 68.13, pp. 1358–1385.

GARWE, F. et al. (1996): Influence of cooperative α dynamics on local β relaxation during the development of the dynamic glass transition in poly (n-alkyl methacrylate) s, in: *Macromolecules* vol. 29.1, pp. 247–253.

GODART, M.-A. and LEEVERS, P. (2007): Effect of skin fracture on failure of a bilayer polymer structure, in: *International Journal of Fracture* vol. 148.4, pp. 315–329.

GREEN, A. E. and RIVLIN, R. S. (1997): The mechanics of non-linear materials with memory, in: *Collected Papers of RS Rivlin*, Springer, pp. 1192–1209.

GRELLMANN, W. and SEIDLER, S. (2015): *Kunststoffprüfung*, Carl Hanser Verlag GmbH Co KG.

GUNNARSSON, C. A., WEERASOORIYA, T., and MOY, P. (2011): Impact response of PC/PMMA composites, in: *Dynamic Behavior of Materials, Volume 1*, Springer, pp. 195–209.

GUSTAFSSON, S. E. (1991): Transient plane source techniques for thermal conductivity and thermal diffusivity measurements of solid materials, in: *Review of scientific instruments* vol. 62.3, pp. 797–804.

GUSTAVSSON, M., KARAWACKI, E., and GUSTAFSSON, S. E. (1994): Thermal conductivity, thermal diffusivity, and specific heat of thin samples from transient measurements with hot disk sensors, in: *Review of Scientific Instruments* vol. 65.12, pp. 3856–3859.

HADAVINIA, H. et al. (2011): Modelling of low velocity impact of laminated composite substructures, in: *International Journal of Vehicle Structures and Systems* vol. 3.2, pp. 96–106.

HAGAN, R. S., SCHMITZ, J. V., and DAVIS, D. A. (1961): "Impact Testing of High Impact Thermoplastic Sheet", in: *Technical Papers, 17th Annual Technical Conference of SPE, SPPPB*, vol. 7.

HAMOUDA, A. M. S. (2002): The influence of humidity on the deformation and fracture behaviour of PMMA, in: *Journal of Materials Processing Technology* vol. 124.1-2, pp. 238–243.

HAUPT, P. (2002): *Continuum mechanics and theory of materials*, Springer.

HAWARD, R. N. (2012): *The physics of glassy polymers*, Springer.

HILL, R. (1979): Aspects of invariance in solid mechanics, in: *Advances in applied mechanics* vol. 18, pp. 1–75.

HODOWANY, J. et al. (2000): Partition of plastic work into heat and stored energy in metals, in: *Experimental Mechanics* vol. 40.2, pp. 113–123.

HOESS, W., SCHMIDT, A., and MANIS, A. (2016): Elastomer PMMA layered composites having improved properties, US Patent US20160101607 A1.

HOESS, W. et al. (2009): Transparent plastic composite, US Patent US20090226730 A1.

HOLZAPFEL, G. A. (2000): *Nonlinear solid mechanics*, vol. 24, Wiley.

HSIEH, A. J. et al. (2004): The effects of PMMA on ballistic impact performance of hybrid hard/ductile all-plastic-and glass-plastic-based composites, Army Research Laboratory.

ILLINGER, J. L., LEWIS, R. W., and BARR, D. B. (1975): Effect of Interlayer on Impact Resistance of Acrylic/Polycarbonate Laminates, in: *Polymer Preprints.* Vol. 16.1, pp. 545–550.

IMAI, Y. and BROWN, N. (1976): Environmental crazing and intrinsic tensile deformation in polymethylmethacrylate, in: *Journal of Materials Science* vol. 11.3, pp. 417–424.

IONITA, D., CRISTEA, M., and BANABIC, D. (2015): Viscoelastic behavior of PMMA in relation to deformation mode, in: *Journal of Thermal Analysis and Calorimetry* vol. 120.3, pp. 1775–1783.

JOHLITZ, M. and DIEBELS, S. (2011): Characterisation of a polymer using biaxial tension tests. Part I: Hyperelasticity, in: *Archive of Applied Mechanics* vol. 81.10, pp. 1333–1349.

JOHNSON, A. R. and CHEN, T.-K. (2005): Approximating thermo-viscoelastic heating of largely strained solid rubber components, in: *Computer methods in applied mechanics and engineering* vol. 194.2, pp. 313–325.

JOHNSON, G. R. and COOK, W. H. (1983): "A constitutive model and data for metals subjected to large strains, high strain rates and high temperatures", in: *Proceedings of the 7th International Symposium on Ballistics*, vol. 21, The Hague, The Netherlands, pp. 541–547.

KELLY, P. M. (2001): "Lightweight transparent armour systems for combat eyewear", in: *The proceedings of the 19th international symposium of balllistics, Interlaken, Switzerland*, pp. 7–11.

KHAJEHSAEID, H. et al. (2014): A visco-hyperelastic constitutive model for rubber-like materials: A rate-dependent relaxation time scheme, in: *International Journal of Engineering Science* vol. 79, pp. 44–58.

KHALILI, S. et al. (2011): Finite element modeling of low-velocity impact on laminated composite plates and cylindrical shells, in: *Composite Structures* vol. 93.5, pp. 1363–1375.

KINLOCH, A. J. (2013): *Fracture behaviour of polymers*, Springer Science & Business Media.

KNAPPE, W., LOHE, P., and WUTSCHIG, R. (1969): Kettenaufbau und Wärmeleitfähigkeit bei amorphen Linearpolymeren, in: *Die Angewandte Makromolekulare Chemie* vol. 7.1, pp. 181–193.

KOLLING, S. et al. (2007): A tabulated formulation of hyperelasticity with rate effects and damage, in: *Computational Mechanics* vol. 40.5, pp. 885–899.

KOLLING, S. et al. (2012): "Simulation of PMMA-TPU-laminates under impact loading", in: *11. German LS-DYNA Forum*.

KOLLING, S. et al. (2009): Simulation of recoverable foams under impact loading, in: *Predictive Modeling of Dynamic Processes*, Springer, pp. 9–25.

KOLLING, S., ALTER, C., and RÜHL, A. (2015): Experimentelle und Numerische Untersuchungen von Windschutzscheiben unter stoßartiger Belastung zur Verbesserung des Fußgänger- und Insassenschutzes, Abschlussbericht BMBF Projekt 17N1111, doi: 10.2314/GBV:858609622.

KOLSKY, H. (1949): An investigation of the mechanical properties of materials at very high rates of loading, in: *Proceedings of the Physical Society. Section B* vol. 62.11, p. 676.

KUNTSCHE, J. K. (2015): Mechanisches Verhalten von Verbundglas unter zeitabhängiger Belastung und Explosionsbeanspruchung, PhD thesis, Technische Universität Darmstadt.

LAMBROS, J. and ROSAKIS, A. J. (1995): Shear dominated transonic interfacial crack growth in a bimaterial-I. Experimental observations, in: *Journal of the Mechanics and Physics of Solids* vol. 43.2, pp. 169–188.

LEADERMAN, H. (1941): Elastic and creep properties of filamentous materials, PhD thesis, Massachusetts Institute of Technology.

LEONHARDT, F. and SCHLAICH, J. (1973): *Vorgespannte Seilnetzkonstruktionen: Das Olympiadach in München*, na.

LI, Z. and LAMBROS, J. (2001): Strain rate effects on the thermomechanical behavior of polymers, in: *International Journal of Solids and Structures* vol. 38.20, pp. 3549–3562.

LIU, Y. and LIAW, B. (2009): Drop-weight impact tests and finite element modeling of cast acrylic plates, in: *Polymer testing* vol. 28.6, pp. 599–611.

LOPEZ-RUIZ, D. et al. (2015): "CAE validation study of a side window impact using plexiglas materials", in: *10th European LS-DYNA Users Conference*.

MACALONEY, N. et al. (2007): Viscoelastic characterization of aliphatic polyurethane interlayers, Army Research Laboratory.

MATSUI, Y. et al. (2003): "Development of JAMA-JARI pedestrian child and adult headform impactors", in: *Proceedings: International Technical Conference on the Enhanced Safety of Vehicles*, vol. 2003, National Highway Traffic Safety Administration, 9–p.

MICHAELI, E. W. et al. (2006): Simulation des nicht-linear viskoelastischen Werkstoffverhaltens von Kunststoffen mit dem 3D-Deformationsmodell, in: *Journal of Plastics Technology* vol. 2.5.

MOONEY, M. (1940): A theory of large elastic deformation, in: *Journal of applied physics* vol. 11.9, pp. 582–592.

MULLIKEN, A. and BOYCE, M. (2006): Mechanics of the rate-dependent elastic–plastic deformation of glassy polymers from low to high strain rates, in: *International journal of solids and structures* vol. 43.5, pp. 1331–1356.

MULLINS, L. and TOBIN, N. R. (1957): Theoretical model for the elastic behavior of filler-reinforced vulcanized rubbers, in: *Rubber Chemistry and Technology* vol. 30.2, pp. 555–571.

OGDEN, R. (1972): "Large deformation isotropic elasticity-on the correlation of theory and experiment for incompressible rubberlike solids", in: *Proceedings of the Royal Society of London A: Mathematical, Physical and Engineering Sciences*, vol. 326, 1567, The Royal Society, pp. 565–584.

OGDEN, R. W. (1997): *Non-linear elastic deformations*, Courier Corporation.

OGIHARA, S., ISHIGURE, T., and KOBAYASHI, A. (1998): Study on impact perforation fracture mechanism in PMMA, in: *Journal of Materials Science Letters* vol. 17.8, pp. 691–692.

OGORKIEWICZ, R. M. (1970): *Engineering properties of thermoplastics: a collective work produced by imperial chemical industries ltd., plastics division. edited by r. m. ogorkiewicz*, John Wiley & Sons.

PATEL, P. J., HSIEH, A. J., and GILDE, G. A. (2006): "Improved low-cost multi-hit transparent armor", in: *25th Army Science Conference*.

PATERSON, M. and WHITE, J. (1992): Effect of water absorption on residual stresses in injection-moulded nylon 6, 6, in: *Journal of materials science* vol. 27.22, pp. 6229–6240.

PEARSON, J. et al. (2007): Measurement of low velocity and quasi-static failure modes in PMMA, in: *Polymer Composites* vol. 28.3, pp. 381–391.

PEREZ, J, CAVAILLE, J., and DAVID, L (1999): New experimental features and revisiting the α and β mechanical relaxation in glasses and glass-forming liquids, in: *Journal of Molecular structure* vol. 479.2, pp. 183–194.

PIZZI, A. and MITTAL, K. L. (2003): *Handbook of adhesive technology, revised and expanded*, CRC press.

PYTTEL, T., LIEBERTZ, H., and CAI, J. (2011): Failure criterion for laminated glass under impact loading and its application in finite element simulation, in: *International Journal of Impact Engineering* vol. 38.4, pp. 252–263.

QI, H. and BOYCE, M. (2005): Stress–strain behavior of thermoplastic polyurethanes, in: *Mechanics of Materials* vol. 37.8, pp. 817–839.

RADIN, J. and GOLDSMITH, W. (1988): Normal projectile penetration and perforation of layered targets, in: *International Journal of Impact Engineering* vol. 7.2, pp. 229–259.

RANZ, T. (2007): *Elementare Materialmodelle der linearen Viskoelastizität im Zeitbereich*, Universität der Bundeswehr München.

RAVI-CHANDAR, K. et al. (2000): Failure mode transitions in polymers under high strain rate loading, in: *International Journal of Fracture* vol. 101.1-2, pp. 33–72.

REE, T. and EYRING, H. (1958): The relaxation theory of transport phenomena, in: *Rheology: theory and applications* vol. 2, p. 83.

RÜHL, A. et al. (2012a): "Characterization and modelling of polymer interlayers for laminated glass", in: *11th German LS-DYNA Forum*.

RÜHL, A. et al. (2012b): "Simulation of PMMA-TPU-laminates under impact loading", in: *Forschungskolloquium Baustatik-Baupraxis 2012*.

RÜHL, A. et al. (2016): Computational design of a heated PMMA window validated by infrared thermography, in: *Glass Structures & Engineering* vol. 1.2, pp. 375–383.

RICHARDS, M., CLEGG, R., and HOWLETT, S. (1999): "Ballistic performance assessment of glass laminates through experimental and numerical investigation", in: *Proceedings of the 18th international symposium on ballistics*, pp. 1123–1130.

RICHETON, J. et al. (2006): Influence of temperature and strain rate on the mechanical behavior of three amorphous polymers: characterization and modeling of the compressive yield stress, in: *International journal of solids and structures* vol. 43.7, pp. 2318–2335.

RICHETON, J. et al. (2007): Modeling and validation of the large deformation inelastic response of amorphous polymers over a wide range of temperatures and strain rates, in: *International journal of solids and structures* vol. 44.24, pp. 7938–7954.

RITTEL, D. (1999): On the conversion of plastic work to heat during high strain rate deformation of glassy polymers, in: *Mechanics of Materials* vol. 31.2, pp. 131–139.

RITTEL, D. (2000): An investigation of the heat generated during cyclic loading of two glassy polymers. Part I: Experimental, in: *Mechanics of Materials* vol. 32.3, pp. 131–147.

RITTEL, D. and RABIN, Y. (2000): An investigation of the heat generated during cyclic loading of two glassy polymers. Part II: Thermal analysis, in: *Mechanics of Materials* vol. 32.3, pp. 149–159.

RIVLIN, R. (1948): Large elastic deformations of isotropic materials. I. Fundamental concepts, in: *Philosophical Transactions of the Royal Society of London. Series A, Mathematical and Physical Sciences* vol. 240.822, pp. 459–490.

RIVLIN, R. S. and SAUNDERS, D. (1951): Large elastic deformations of isotropic materials. VII. Experiments on the deformation of rubber, in: *Philosophical Transactions of the Royal Society of London A: Mathematical, Physical and Engineering Sciences* vol. 243.865, pp. 251–288.

SARVA, S. S. et al. (2007): Stress–strain behavior of a polyurea and a polyurethane from low to high strain rates, in: *Polymer* vol. 48.8, pp. 2208–2213.

SCHAPERY, R. A. (1969): On the characterization of nonlinear viscoelastic materials, in: *Polymer Engineering & Science* vol. 9.4, pp. 295–310.

SCHWARZL, F. R. (1990): *Polymermechanik: Struktur und mechanisches Verhalten von Polymeren*, Springer.

SCHYMANIETZ, D. (2016): Modellierung des visko-hyperelastischen Materialverhaltens von PVB unter großen Deformationen, Master thesis, TH Mittelhessen, Gießen.

SHARMA, A., SHUKLA, A., and PROSSER, R. A. (2002): Mechanical characterization of soft materials using high speed photography and split Hopkinson pressure bar technique, in: *Journal of Materials Science* vol. 37.5, pp. 1005–1017.

SONG, J.-H., WANG, H., and BELYTSCHKO, T. (2008): A comparative study on finite element methods for dynamic fracture, in: *Computational Mechanics* vol. 42.2, pp. 239–250.

STENZLER, J. S. and GOULBOURNE, N. C. (2011): The effect of polyacrylate microstructure on the impact response of PMMA/PC multi-laminates, in: *International Journal of Impact Engineering* vol. 38.7, pp. 567–576.

STICKLE, A. and SCHULTZ, P. (2011): Exploring the role of shear in oblique impacts: A comparison of experimental and numerical results for planar targets, in: *International Journal of Impact Engineering* vol. 38.6, pp. 527–534.

SWALLOWE, G. and LEE, S. (2003): "A study of the mechanical properties of PMMA and PS at strain rates of 10^{-4} to 10^3 over the temperature range 293–363 K", in: *Journal de Physique IV (Proceedings)*, vol. 110, EDP sciences, pp. 33–38.

TAYLOR, G. I. and QUINNEY, H (1934): The latent energy remaining in a metal after cold working, in: *Proceedings of the Royal Society of London. Series A, Containing Papers of a Mathematical and Physical Character* vol. 143.849, pp. 307–326.

TEKALUR, S. A., ZHANG, W., and HUYNH, L. (2010): "Dynamic failure of monolithic and layered PMMA and PC plates", in: *Proceedings of the IMPLAST 2010 Conference*.

TETSUTANI, T., KAKIZAKI, M., and HIDESHIMA, T. (1982): Relaxation spectroscopy of the dielectric β-relaxation in poly (n-alkyl methacrylate) s by absorption-current measurements. II. Dielectric relaxation spectrum for isotactic poly (methyl methacrylate), in: *Polymer Journal* vol. 14.6, pp. 471–476.

TOQUEBOEUF, W., MORTAIGNE, B., and COTTENOT, C. (1997): Dynamic behaviour of polycarbonate/polyurethane multi-layer for transparent armor, in: *Le Journal de Physique IV* vol. 7.C3, pp. C3–499.

TRELOAR, L. R. G. (1944): Stress-strain data for vulcanised rubber under various types of deformation, in: *Transactions of the Faraday Society* vol. 40, pp. 59–70.

VOGEL, H. (1921): Das Temperaturabhängigkeitsgesetz der Viskosität von Flüssigkeiten, in: *Phys. Z* vol. 22, pp. 645–646.

WANG, F. and YUE, Z. (2010): Numerical simulation of damage and failure in aircraft windshield structure against bird strike, in: *Materials & Design* vol. 31.2, pp. 687–695.

WANG, L. L. and YANG, L. M. (1992): A class of nonlinear viscoelastic constitutive relation of solid polymeric materials, in: *The progress in impact dynamics*, pp. 88–116.

WEERASOORIYA, T. et al. (2006): "Fracture toughness of PMMA as a function of loading rate", in: *Proceedings of the 2006 SEM annual conference on experimental mechanics*, pp. 5–7.

WILLIAMS, M. L., LANDEL, R. F., and FERRY, J. D. (1955): The temperature dependence of relaxation mechanisms in amorphous polymers and other glass-forming liquids, in: *Journal of the American Chemical society* vol. 77.14, pp. 3701–3707.

WINTER, D. (1993): Optische Verschiebungsmessung nach dem Objektrasterprinzip mit Hilfe eines Flächenorientierten Ansatzes, PhD thesis, TU Braunschweig.

WOICKE, N. et al. (2004): Three-dimensional thermorheological behavior of isotactic polypropylene across glass transition temperature, in: *Journal of Applied Polymer Science* vol. 94.3, pp. 877–880.

WRIGGERS, P. (2013): *Nichtlineare Finite-Element-Methoden*, Springer.

Wu, H., Ma, G., and Xia, Y. (2004): Experimental study of tensile properties of PMMA at intermediate strain rate, in: *Materials Letters* vol. 58.29, pp. 3681–3685.

Xibao, L. et al. (2014): Mechanical properties of thermoplastic polyurethanes laminated glass treated by acid etching combined with cold plasma, in: *Plasma Science and Technology* vol. 16.10, p. 964.

Yeoh, O. (1990): Characterization of elastic properties of carbon-black-filled rubber vulcanizates, in: *Rubber chemistry and technology* vol. 63.5, pp. 792–805.

Yi, J et al. (2006): Large deformation rate-dependent stress–strain behavior of polyurea and polyurethanes, in: *Polymer* vol. 47.1, pp. 319–329.

Zhang, L. et al. (2015): Temperature-and strain rate-dependent constitutive modeling of the large deformation behavior of a transparent polyurethane interlayer, in: *Polymer Engineering & Science* vol. 55.8, pp. 1864–1872.

Standards

ASTM D4065 (2012): Standard Practice for Plastics: Dynamic Mechanical Properties: Determination and Report of Procedures.

ASTM D5628-10 (2010): Standard Test Method for Impact Resistance of Flat, Rigid Plastic Specimens by Means of a Falling Dart (Tup or Falling Mass).

ASTM D638 - 02a (2003): Tensile testing ASTM D638 for Thermoplastics.

BS 903-5 (2004): Physical testing of rubber - Part 5: Guide to the application of rubber testing to finite element analysis.

DIN 53441 (1984): Testing of plastics; stress relaxation test.

DIN EN 1288-1 (2000): Glass in building – Determination of the bending strength of glass – Part 1: Fundamentals of testing glass.

DIN EN 6032 (2016): Aerospace series – Fibre reinforced plastics – Test method – Determination of the glass transition temperatures.

DIN EN ISO 178 (2013): Determination of flexural properties.

DIN EN ISO 22007-1 (2012): Determination of thermal conductivity and thermal diffusivity – Part 1: General principles.

DIN EN ISO 527 - 1 (2012): Plastics – Determination of tensile properties – Part 1: General principles.

DIN EN ISO 527 - 2 (2012): Plastics – Determination of tensile properties – Part 2: Test conditions for moulding and extrusion plastics.

DIN EN ISO 53504 (2015): Testing of rubber – Determination of tensile strength at break, tensile stress at yield, elongation at break and stress values in a tensile test.

DIN EN ISO 62 (2008): Plastics – Determination of water absorption.

DIN EN ISO 6603-2 (2002): Plastics - Determination of puncture impact behaviour of rigid plastics.

DIN EN ISO 6721-1 (2011): Plastics - Determination of dynamic mechanical properties - Part 1: General principles.

DIN EN ISO 899-1 (2003): Plastics - Determination of creep behaviour - Part 1: Tensile creep.

DIN ISO 7765-2 (2009): Plastics film and sheeting – Determination of impact resistance by the free-falling dart method – Part 2: Instrumented puncture test (ISO 7765-2:1994).

UNECE No. 43 (2012): Uniform provisions concerning the approval of safety glazing materials and their installation on vehicles, online, retrieved via http://www.unece.org.

Manuals and Data Sheets

BASF Polyurethanes GmbH (2011): Thermoplastic polyurethane elastomers (TPU): Elastollan® - material properties.

BASF Polyurethanes GmbH (2013): Thermoplastic polyurethane elastomers (TPU): Elastollan® - product range.

Campus® (2016): Datasheet Plexiglas® 8N, retrieved: 20.10.2016 from campusplastics.com.

Evonik Industries AG (2008): Plexiglas® GS/Plexiglas® XT product description.

Evonik Industries AG (2015): Plexiglas® 8N product description.

GOM Aramis (2013): theory and user manual.

Hot Disk (2015): Thermal constants analyser - instruction manual.

LS-DYNA (2007): keyword user's manual.

LS-DYNA (2016): theory manual.

LS-OPT (2008): LS-OPT user's manual.

Mettler Toledo (2004): STARe Software with Solaris operating system.

Appendix A

Experiments

A.1 Materials used in Experiments

Table A.1 Materials used in monolothic experiments.

experiment	PMMA	t [mm]	TPU	t [mm]
TPS	Plexiglas® 7H	25.0	Elastollan® 785 A10[a]	$n \cdot$ 0.35
DMTA	Plexiglas® 8N	3.0	Elastollan® 785 A10	0.35
uniaxial tension	Plexiglas® 8N	3.0	Elastollan® 785 A10	0.35
biaxial tension			Elastollan® 785 A10	0.35
bending	Plexiglas® 8N	3.0		
dart	Plexiglas® 8N	3.0		
head impact	Plexiglas® 7H	3.0		

[a] n represents the stacking of multiple plies

Table A.2 Materials used in laminate experiments.

experiment	PMMA	t [mm]	TPU	t [mm]
bending	Plexiglas® 7H and 8H	1.5, 2.0	Elastollan® 785 A10	0.5
bending (clamped)	Plexiglas® 7H and 8H	1.5, 2.0	Elastollan® 785 A10	0.5
dart	Plexiglas® 7H and 8H	1.5, 2.0	Elastollan® 785 A10	0.5
head impact	Plexiglas® 7H and 8H	1.5, 2.0	Elastollan® 785 A10	0.5

A.2 Transient Plane Source Method

For each temperature between 8 and 15 experiments were conducted. Results are given with their standard deviation.

Table A.3 Parameters and results of TPS measurements for PMMA and TPU.

T [°C]	P [mW]	t [s]	Δt [min]	$k \pm$ SD [W/(mK)]	$c_{vol} \pm$ SD [J/(m^{3}K)]	$\kappa \pm$ SD [mm^2/s]
PMMA						
-50	80	320	120	0.1889 ± 0.0011	1.3742 ± 0.0111	0.1375 ± 0.0019
-40	80	320	120	0.1905 ± 0.0009	1.4040 ± 0.0203	0.1357 ± 0.0039
-30	80	320	120	0.1954 ± 0.0008	1.4439 ± 0.0065	0.1354 ± 0.0011
-20	80	320	120	0.1991 ± 0.0009	1.5033 ± 0.0076	0.1324 ± 0.0012
-10	80	320	120	0.2029 ± 0.0005	1.5693 ± 0.0032	0.1293 ± 0.0006
0	80	320	120	0.2047 ± 0.0009	1.6140 ± 0.0068	0.1269 ± 0.0010
10	80	320	120	0.2037 ± 0.0012	1.6349 ± 0.0112	0.1246 ± 0.0016
20	80	320	120	0.2013 ± 0.0006	1.6575 ± 0.0072	0.1214 ± 0.0009
30	80	320	120	0.2052 ± 0.0019	1.7432 ± 0.0158	0.1177 ± 0.0016
40	80	320	120	0.2056 ± 0.0015	1.8284 ± 0.0122	0.1124 ± 0.0014
50	80	320	120	0.2078 ± 0.0006	1.8744 ± 0.0060	0.1108 ± 0.0006
60	80	320	120	0.2085 ± 0.0014	1.9389 ± 0.0120	0.1076 ± 0.0013
70	80	320	120	0.2101 ± 0.0007	1.9860 ± 0.0155	0.1058 ± 0.0011
80	80	320	180	0.2126 ± 0.0025	2.0429 ± 0.0253	0.1041 ± 0.0024
90	100	640	180	0.2088 ± 0.0003	2.0137 ± 0.0009	0.1037 ± 0.0005
100	120	640	180	0.2169 ± 0.0016	2.0670 ± 0.0182	0.1049 ± 0.0017
110	120	320	180	0.2082 ± 0.0004	2.5743 ± 0.0074	0.0809 ± 0.0002
120	120	640	180	0.2043 ± 0.0003	2.5257 ± 0.0041	0.0809 ± 0.0002
130	120	640	180	0.2027 ± 0.0006	2.5520 ± 0.0013	0.0794 ± 0.0006
TPU						
-50	80-140	640	180	0.2402 ± 0.0008	1.2962 ± 0.0145	0.1858 ± 0.0019
-40	80-140	640	180	0.2373 ± 0.0012	1.7174 ± 0.0200	0.1382 ± 0.0023
-30	100,120	640	180	0.2331 ± 0.0007	1.7433 ± 0.0017	0.1337 ± 0.0017
-20	100-160	640	180	0.2333 ± 0.0005	1.8035 ± 0.0066	0.1294 ± 0.0006
-10	80,100,120	640	180	0.2335 ± 0.0003	1.8248 ± 0.0066	0.1279 ± 0.0006
0	80,100,120	640	180	0.2389 ± 0.0007	1.9333 ± 0.0146	0.1236 ± 0.0011
10	80,100,120	640	180	0.2370 ± 0.0018	1.9257 ± 0.0200	0.1231 ± 0.0019
20	80,100,120	640	180	0.2261 ± 0.0011	1.9343 ± 0.0100	0.1169 ± 0.0009
30	80,100,120	640	180	0.2231 ± 0.0004	1.9973 ± 0.0147	0.1117 ± 0.0009
40	80,100,120	640	180	0.2223 ± 0.0005	2.0211 ± 0.0011	0.1100 ± 0.0007
50	80,100,120	640	180	0.2219 ± 0.0004	2.0675 ± 0.0064	0.1073 ± 0.0003
70	80,100,120	640	180	0.2242 ± 0.0005	2.1259 ± 0.0063	0.1055 ± 0.0004
80	80,100,120	640	180	0.2230 ± 0.0004	2.1674 ± 0.0050	0.1029 ± 0.0003
90	80,100,120	640	180	0.2216 ± 0.0009	2.2448 ± 0.0122	0.0987 ± 0.0005
100	80 - 140	640	180	0.2219 ± 0.0004	2.2743 ± 0.0086	0.0976 ± 0.0004
100	120	320	180	0.2220 ± 0.0004	2.2532 ± 0.0057	0.0985 ± 0.0003

A.3 Dynamic Mechanical Thermal Analysis

For both PMMA and TPU two representative experimental results were chosen: A temperature sweep and a temperature-frequency sweep. For these four experiments the parameters are given in Table A.4. Table A.5 gives the viscoelastic parameters obtained from DMTA experiments.

Table A.4 Experimental parameters for DMTA experiments.

PMMA	unit	temperature sweep	master curve		
setup	[-]	bending	bending		
temperature T	[°C]	−80 to 145	−100 to 145		
temperature steps ΔT	[°C/min]	1.5	−100.0 °C to	0.0 °C:	10
			0.0 °C to	90.0 °C:	5
			90.0 °C to	145.0 °C:	2.5
			145.0 °C to	172.5 °C:	15
frequency f	[Hz]	1.0	0.01 to 100.0		
pre-load F_{pre}	[N]	3	3		
load amplitude F_{amp}	[N]	0.8	0.8		
length l	[mm]	66.32	65.34		
width b	[mm]	10.12	10.1		
thickness t	[mm]	3.1	3.1		
support distance	[mm]	60	60		
TPU	unit	temperature sweep	master curve		
setup	[-]	double-shear	double-shear		
temperature T	[°C]	−80 to 79	−80 to 70		
temperature steps ΔT	[°C/min]	0.5	−80.0 °C to	−20.0 °C:	10
			−20.0 °C to	0.0 °C:	5
			0.0 °C to	50.0 °C:	2.5
			50.0 °C to	70.0 °C:	10
frequency f	[Hz]	1.0	0.01 to 100.0		
load amplitude F_{amp}	[N]	4	8		
displacement s	[mm]	50	50		
diameter d	[mm]	3.0	3.0		
thickness t	[mm]	0.35	0.35		
geometry factor[a]	[1/m]	24.75	24.75		

[a] recommended to be between 20 and 100 (METTLER TOLEDO, 2004)

Table A.5   PMMA: viscoelastic parameters from DMTA experiments.

i	E_i [MPa]	G_i [MPa]	β_i [1/s]	i	E_i [MPa]	G_i [MPa]	β_i [1/s]
1	450.0	173.0	10^{-14}	15	320.0	123.0	10^{+00}
2	450.0	173.0	10^{-13}	16	360.0	139.0	10^{+01}
3	170.0	65.0	10^{-12}	17	380.0	146.0	10^{+02}
4	190.0	73.0	10^{-11}	18	450.0	173.0	10^{+03}
5	160.0	61.0	10^{-10}	19	410.0	158.0	10^{+04}
6	155.0	60.0	10^{-09}	20	360.0	139.0	10^{+05}
7	155.0	60.0	10^{-08}	21	250.0	96.0	10^{+06}
8	155.0	60.0	10^{-07}	22	250.0	96.0	10^{+07}
9	150.0	58.0	10^{-06}	23	250.0	96.0	10^{+08}
10	160.0	62.0	10^{-05}	24	250.0	96.0	10^{+09}
11	210.0	81.0	10^{-04}	25	220.0	85.0	10^{+10}
12	260.0	100.0	10^{-03}	26	200.0	77.0	10^{+11}
13	280.0	108.0	10^{-02}	27	200.0	77.0	10^{+12}
14	290.0	110.0	10^{-01}	28	100.0	30.0	10^{+13}

A.4 Uniaxial Tensile Tests

Uniaxial tensile tests at 0.1 m/s, 1.0 m/s, and 3.0 m/s were performed at German Institute of Polymers (DKI), Darmstadt. Average values are provided with their standard deviation (SD).

Table A.6   PMMA tensile test: evaluation for strains between 0.05% 0.25%

test	E [MPa]	v [-]	σ_{fail} [MPa]	$\varepsilon_{\text{fail}}$ [-]
1.0 mm/min	3391.43	0.3522	75.90	0.0531
1.0 mm/min	3454.26	0.3572	68.34	0.0321
1.0 mm/min	3460.62	0.3704	76.65	0.0545
1.0 mm/min	3445.01	0.3675	72.12	0.0377
1.0 mm/min	3424.94	0.3518	76.81	0.0471
average	3435.25 ± 27.96	0.3597 ± 0.0087	73.96 ± 3.68	0.0471 ± 0.0114

Table A.7 PMMA: dynamic tensile test results. Evaluation for strains between 0.05% and 0.25%.

test	E [MPa]	ν [-]	σ_{fail} [MPa]	$\varepsilon_{\text{fail}}$ [-]
0.1 m/s	4881.81	0.2919	101.63	0.0270
0.1 m/s	4710.65	0.2553	98.74	0.0273
0.1 m/s	4641.67	0.3275	101.06	0.0272
0.1 m/s	4857.53	0.3676	101.38	0.0279
0.1 m/s	5519.24	0.3332	100.70	100.70
average	4922.18 ± 348.47	0.3151 ± 0.0429	100.70 ± 1.15	0.0272 ± 0.0004
1.0 m/s	6112.05	0.4735	106.28	0.0234
1.0 m/s	4251.25	0.2544	97.71	0.0224
1.0 m/s	3692.20	0.3177	104.20	0.0245
1.0 m/s	7427.56	0.2602	104.25	0.0226
1.0 m/s	4693.53	0.1376	105.39	0.0241
1.0 m/s	5084.94	0.2701	103.41	0.0232
average	5210.2546 ± 1359.16	0.2856 ± 0.1096	103.54 ± 3.03	0.0232 ± 0.0008
3.0 m/s	6550.05	0.2451	95.96	0.0203
3.0 m/s	5080.08	0.2641	96.97	0.0210
3.0 m/s	6174.25	0.3142	91.62	0.0211
3.0 m/s	6772.83	0.3085	100.0312	0.0205
3.0 m/s	5278.31	0.1944	104.85	0.0209
average	5971.10 ± 757.15	0.2645 ± 0.0496	97.89 ± 4.92	0.0208 ± 0.0003

Table A.8 TPU: tensile test. Evaluation for strains between 10% and 20%.

test	E [MPa]	ν [-]
5.0 mm/min	7.90	0.4948
5.0 mm/min	8.17	0.4926
5.0 mm/min	9.29	0.4797
5.0 mm/min	8.29	0.4812
average	8.41 ± 0.61	0.4870 ± 0.0077

Table A.9 TPU: temperature rise at 500 mm/min.

rectangle	1	2	3	4	5	6
average	8.97 K	7.53 K	7.01 K	8.29 K	9.26 K	9.32 K
maximum	7.98 K	10.04 K	9.32 K	9.24 K	8.29 K	7.63 K

line	1	2	3	4	5	6
average	10.51 K	9.45 K	10.21 K	8.26 K	7.49 K	7.95 K
maximum	10.23 K	10.15 K	10.37 K	10.01 K	9.21 K	9.38 K

A.5 Three-Point Bending Test

Average values are provided with their standard deviation (SD). Temperatures from Table A.12 represent pixel-evaluation within a rectangle around the relevant area.

Table A.10   PMMA and PMMA laminate: geometries and temperatures in bending experiments.

experiment	free length l_{free}	length l	height b	thickness t	temperature T
5.0 mm/min	50.0 mm	60.0 mm	10.0 mm	3.0 mm	24.6 °C
500.0 mm/min	50.0 mm	60.0 mm	10.0 mm	3.0 mm	24.6 °C
1.0 m/s	50.0 mm	60.0 mm	10.0 mm	3.0 mm	28.1 °C
2.5 m/s	35.0 mm	45.0 mm	10.0 mm	3.0 mm	26.8 °C
4.0 m/s	30.0 mm	40.0 mm	10.0 mm	3.0 mm	24.6 °C

Table A.11   PMMA laminate clamped bending: geometries and temperatures.

experiment	free length l_{free}	length l	height b	thickness t	temperature T
1.0 m/s	80.0 mm	120.0 mm	10.0 mm	4.0 mm	28.1 °C
2.0 m/s	60.0 mm	100.0 mm	10.0 mm	4.0 mm	28.1 °C
3.0 m/s	80.0 mm	120.0 mm	10.0 mm	4.0 mm	28.1 °C

Table A.12   PMMA laminate bending: maximum temperature rise.

free bending	1	2	3	4	5	6	7
1.0 m/s	5.2 K	4.7 K	20.1 K	24.9 K	10.7 K	9.8 K	11.3 K
2.0 m/s	27.7 K	23.5 K	6.4 K	14.0 K	16.7 K	18.1 K	
clamped bending	1	2	3	4	5		
1.5 m/s	23.4 K	25.5 K	26.9 K	25.2 K	23.2 K		
2.0 m/s	55.0 K	36.5 K	44.5 K	40.2 K	39.7 K		
3.0 m/s	58.6 K	38.7 K	42.8 K	41.6 K	50.0 K		

Table A.13   PMMA bending: failure displacement and force.

experiment	s_{fail}	F_{fail}	experiment	s_{fail}	F_{fail}
500.0 mm/min	6.07 mm	164.55 N	5.0 mm/min	7.27 mm	138.92 N
500.0 mm/min	6.17 mm	160.63 N	5.0 mm/min	6.17 mm	134.95 N
500.0 mm/min	5.53 mm	152.13 N	5.0 mm/min	6.23 mm	130.82 N
500.0 mm/min	6.60 mm	170.17 N	5.0 mm/min	5.61 mm	134.19 N
500.0 mm/min	5.90 mm	169.52 N	5.0 mm/min	5.95 mm	133.43 N
500.0 mm/min	5.43 mm	162.31 N	5.0 mm/min average	6.24 mm	141.68 N
500.0 mm/min	5.87 mm	161.56 N	5.0 mm/min SD	0.56 mm	14.16 N
500.0 mm/min	5.47 mm	162.22 N			
500.0 mm/min	4.50 mm	136.37 N	1.0 m/s	4.48 mm	195.54 N
500.0 mm/min	5.37 mm	151.52 N	1.0 m/s	4.07 mm	159.86 N
500.0 mm/min	4.47 mm	130.99 N	1.0 m/s	4.31 mm	164.08 N
500.0 mm/min	5.70 mm	140.60 N	1.0 m/s	5.00 mm	168.54 N
500.0 mm/min	5.73 mm	147.31 N	1.0 m/s	4.62 mm	180.14 N
500.0 mm/min	5.50 mm	144.71 N	1.0 m/s average	4.50 mm	173.63 N
500.0 mm/min	5.20 mm	142.77 N	1.0 m/s SD	0.31 mm	12.88 N
500.0 mm/min average	5.57 mm	153.16 N			
500.0 mm/min SD	0.55 mm	11.91 N			
			2.5 m/s	2.12 mm	237.16 N
4.0 m/s	7.27 mm	146.64 N	2.5 m/s	2.14 mm	274.07 N
4.0 m/s	6.17 mm	134.96 N	2.5 m/s	2.29 mm	269.56 N
4.0 m/s	6.24 mm	130.82 N	2.5 m/s	2.16 mm	256.59 N
4.0 m/s	5.61 mm	134.19 N	2.5 m/s	2.12 mm	262.50 N
4.0 m/s	5.95 mm	113.82 N	2.5 m/s	2.44 mm	228.47 N
4.0 m/s average	6.25 mm	132.09 N	2.5 m/s average	2.21 mm	260.72 N
4.0 m/s SD	0.62 mm	11.83 N	2.5 m/s SD	0.13 mm	17.15 N

A.6 Dart Impact Tests

Table A.14 PMMA dart test: statistical evaluation of failure displacements.

velocity v	temperature T	average fail. disp. s	standard deviation
1.0 m/s	-30 °C	2.349 mm	0.100 mm
5.0 m/s	-30 °C	1.780 mm	0.050 mm
1.0 m/s	0 °C	2.445 mm	0.052 mm
5.0 m/s	0 °C	1.830 mm	0.029 mm
1.0 m/s	23 °C	2.574 mm	0.088 mm
5.0 m/s	22 °C	1.885 mm	0.052 mm
1.0 m/s	60 °C	3.058 mm	0.176 mm
5.0 m/s	60 °C	2.162 mm	0.181 mm

Appendix B

Material Modelling

B.1 Material Parameters for PMMA

Table B.1 Parameters of the five parameter generalized Maxwell model for PMMA.

element number	shear modulus G_i	bulk modulus K_i	decay constant β_i
three parameter model	1.84 GPa	2.75 GPa	
2	1.27 GPa	2.75 GPa	$0.129\,\mathrm{ms}^{-1}$
five parameter model	1.27 GPa	4.09 GPa	
2	0.55 GPa	1.19 GPa	$0.01891\,\mathrm{ms}^{-1}$
3	2.92 GPa	6.33 GPa	$60.5913\,\mathrm{ms}^{-1}$

Table B.2 Parameter set of the hyper-viscoelastic model for PMMA.

$C10$ [GPa]	$C01$ [GPa]	$C11$ [GPa]	$C20$ [GPa]	$C02$ [GPa]	$C30$ [GPa]
-4.122	4.758	68267.0	-33609.3	-34699.0	3427.0

G_1 [GPa]	β_1 [ms^{-1}]	G_2 [GPa]	β_2 [ms^{-1}]		
0.55128	0.01891	2.92347	60.5913		

Table B.3   PMMA: viscoelastic parameters of full viscoelastic model.

i	DMTA parameters				adjusted parameters for thermal simulation			
	E [MPa]	G [MPa]	K [MPa]	β [1/s]	E [MPa]	G [MPa]	K [MPa]	β [1/s]
1	2400.0	923.1	2000.0	0.0	800.0	307.7	666.7	10^{-13}
2	180.0	69.2	150.0	10^{-5}	400.0	153.8	333.3	10^{-12}
3	300.0	115.4	250.0	10^{-4}	300.0	115.4	250.0	10^{-10}
4	290.0	111.5	241.7	10^{-3}	460.0	176.9	383.3	10^{-8}
5	270.0	103.8	225.0	10^{-2}	250.0	96.2	208.3	10^{-6}
6	290.0	111.5	241.7	10^{-1}	180.0	69.2	150.0	10^{-5}
7	330.0	126.9	275.0	10^{+0}	210.0	80.8	175.0	10^{-4}
8	410.0	157.7	341.7	10^{+1}	290.0	111.5	241.7	10^{-3}
9	430.0	165.4	358.3	10^{+2}	290.0	111.5	241.7	10^{-2}
10	460.0	176.9	383.3	10^{+3}	390.0	150.0	325.0	10^{-1}
11	450.0	173.1	375.0	10^{+4}	590.0	226.9	491.7	10^{+0}
12	390.0	150.0	325.0	10^{+5}	760.0	292.3	633.3	10^{+1}
13	300.0	115.4	250.0	10^{+6}	780.0	300.0	650.0	10^{+2}
14	270.0	103.8	225.0	10^{+7}	850.0	326.9	708.3	10^{+3}
15	270.0	103.8	225.0	10^{+8}	880.0	338.5	733.3	10^{+4}
16	220.0	84.6	183.3	10^{+9}	780.0	300.0	650.0	10^{+5}
17	200.0	76.9	166.7	10^{+10}	800.0	307.7	666.7	10^{+6}
18	200.0	76.9	166.7	10^{+11}	790.0	303.8	658.3	10^{+7}

B.2 Material Parameters for TPU

Table B.4   Uniaxial parameter set for the hyperelastic simulation of TPU for true strains up to 100%.

$C10$ [GPa]	$C01$ [GPa]	$C11$ [GPa]	$C20$ [GPa]	$C02$ [GPa]	$C30$ [GPa]
$9.00 \cdot 10^{-4}$	$1.7999 \cdot 10^{-3}$	$-3.0 \cdot 10^{-6}$	$-2.0764 \cdot 10^{-4}$	$6.0 \cdot 10^{-4}$	$1.51 \cdot 10^{-5}$

Table B.5   Uniaxial parameter set for the hyperelastic simulation of TPU for true strains up to 170%.

$C10$ [GPa]	$C01$ [GPa]	$C11$ [GPa]	$C20$ [GPa]	$C02$ [GPa]	$C30$ [GPa]
$1.963 \cdot 10^{-4}$	$3.196 \cdot 10^{-3}$	$2.819 \cdot 10^{-3}$	$-5.26 \cdot 10^{-4}$	$-3.48 \cdot 10^{-3}$	$2.306 \cdot 10^{-6}$

Table B.6 Final hyper-viscoelastic material parameter for TPU.

ρ [kg/m^3]	ν [-]				
1190	0.499				

$C10$ [GPa]	$C01$ [GPa]	$C11$ [GPa]	$C20$ [GPa]	$C02$ [GPa]	$C30$ [GPa]
$9.00 \cdot 10^{-4}$	$1.7999 \cdot 10^{-3}$	$-3.0 \cdot 10^{-6}$	$-2.0764 \cdot 10^{-4}$	$6.0 \cdot 10^{-4}$	$1.51 \cdot 10^{-5}$

G_1 [GPa]	β_1 [ms^{-1}]	G_2 [GPa]	β_2 [ms^{-1}]		
$1.8428 \cdot 10^{-6}$	0.8765578	0.04411212	6.79308878		
G_3 [GPa]	β_3 [ms^{-1}]	G_4 [GPa]	β_4 [ms^{-1}]		
$5.0 \cdot 10^{-5}$	5.0	0.06	2.997		
G_5 [GPa]	β_5 [ms^{-1}]	G_6 [GPa]	β_6 [ms^{-1}]		
$5.0 \cdot 10^{-4}$	$6.0 \cdot 10^{-2}$	$1.3015 \cdot 10^{-2}$	$6.4383 \cdot 10^{-5}$		